GEODYNAMICS, DEFORMATION AND MATHEMATICAL ANALYSIS OF METAMORPHIC BELTS, NW HIMALAYA

A THESIS

Submitted in partial fulfilment of the requirements for the award of the degree of

DOCTOR OF PHILOSOPHY

in

EARTH SCIENCES

by

SOUMYAJIT MUKHERJEE

DEPARTMENT OF EARTH SCIENCES
INDIAN INSTITUTE OF TECHNOLOGY ROORKEE
ROORKEE-247 667 (INDIA)

JULY, 2007

INDIAN INSTITUTE OF TECHNOLOGY ROORKEE
ROORKEE

CANDIDATE'S DECLARATION

I hereby certify that the work which is being presented in this thesis entitled **GEODYNAMICS, DEFORMATION AND MATHEMATICAL ANALYSIS OF METAMORPHIC BELTS, NW HIMALAYA** in partial fulfillment of the requirements for the award of the Degree of Doctor of Philosophy and submitted in the Department of Earth Sciences of the Indian Institute of Technology Roorkee, Roorkee is an authentic record of my own work carried out during a period from July 2003 to July 2007 under the supervision of Dr. A.K. Jain, Professor, Department of Earth Sciences, Indian Institute of Technology Roorkee, Roorkee.

The matter presented in this thesis has not been submitted by me for the award of any other degree of this or any other Institute.

Soumyajit Mukherjee

(SOUMYAJIT MUKHERJEE)

This is to certify that the above statement made by the candidate is correct to the best of my knowledge.

AK Jain

Date: 23/7/2007

(Prof. A.K. Jain)
(Supervisor)

The Ph.D. Viva-Voce examination of **Mr. Soumyajit Mukherjee**, Research Scholar has been held on .....

Signature of supervisor

Signature of External Examiner

Acknowledgements

I express my gratitude to my Supervisor **Prof. A.K. Jain** for introducing me Himalayan Geology, and the channel flow model in particular, comments on different chapters and discussions at every stage of this work.

I sincerely thank **Prof. R.P. Gupta-** the present Head of the Department; and **Prof. V. N. Singh** and **Prof. B. Parkash** -the ex- Heads of the Department for extending Departmental facilities in my work. **Prof. A.K. Choudhuri** (IITR) is thanked for posing critical questions on my research. I express my special thanks to **Dr. S. Singh** (IITR) for introducing me the geology of the Sutlej section, and for giving most of the colour prints-outs of this thesis during the slog hours.

The **Council of Scientific & Industrial Research** (New Delhi) is acknowledged for funding this research in terms of **Junior Research Fellowship** (grant number: 2-48/2001IIEU.II) and **Senior Research Fellowship** (grant number: 9/143(441)/2003-EMR-I).

Swedish Institute's (Stockholm) 'Guest Studentship' is acknowledged that enabled me to run analogue models in the Hans Ramberg Tectonic Laboratory, Uppsala University, Sweden during 2005-2006.

Dr. R. Govindarajan and **Dr. K.C. Sahu** (JNCASR, India) are thanked for teaching me fluid mechanics.

I am indebted to **Prof. D.K. Mukhopadhyay** and **Prof. D.C. Srivastava** (IITR) for their comments on this work.

I heartily thank my lab mates- **Dr. R. Kumar**, **Nikunja** and **James** for their support, and to **Chawla-ji**, and **Bhim** for numerous help in the research.

Soumyajit Mukherjee

(SOUMYAJIT MUKHERJEE)

ABSTRACT

Intra-continental collision between the Indian- and the Eurasian Plates since ~ 55 Ma remobilized the Indian crust and resulted in the exhumation of different parts of the mountain in various episodes. The Higher Himalayan Shear Zone (HHSZ), a part of the Himalayan Metamorphic Belt, was deformed and exhumed as a delayed response to the post-collisional crustal shortening. The ductile extensional shearing at the top of the HHSZ took place simultaneously with the ductile compressional shearing at the lower boundary of this shear zone. Based on structural geology, mathematical analyses and analogue modelling, models of exhumation of the HHSZ are proposed taking the Zanskar- and the Sutlej sections of the shear zone in the NW Indian Himalaya as the study areas. Additionally, flanking structures in micro-scales from the Sutlej section of the HHSZ are studied and their compatibility with the proposed exhumation model is addressed.

Thin-section studies of the rocks of the Zanskar Shear Zone (ZSZ) reveal (a) an initial top-to-SW sense of ductile shearing; (b) subsequent top-to-NE sense of ductile shear coeval with the ongoing top-to-SW sense of ductile shearing; (c) top-to-NE sense of ductile synthetic secondary shearing; (d) brittle-ductile extension; (e) top-to-SW sense of brittle shear; (f) northeasterly steeply dipping brittle faults; and (g) brittle extension. A two-phase model of exhumation of the HHSZ is proposed. The first phase represented top-to-SW sense of non-coaxial shearing same as the Couette flow during the Neo-Himalayan Period. The second phase was guided by combined top-to-SW sense of simple

shear and the channel flow during the Middle Miocene Period. This simulated a thin ZSZ characterized by a top-to-NE sense of ductile shearing. Variation in the ratio of relative velocity of the boundaries of the HHSZ to the pressure gradient explains the variable thickness of the ZSZ.

Fieldwork and micro-structural studies of the HHSZ in the Sutlej section reveal (a) initial top-to-SW sense of ductile shearing; (b) late stage top-to-NE sense of ductile shearing in two zones- the 'Himalayan Detachment-1' (HD1) and the 'Himalayan Detachment-2' (HD2); (c) uniform top-to-SW sense of brittle shearing; and (d) brittle-ductile extension. A three-phase model of exhumation of the HHSZ is proposed. The first phase represented top-to-SW sense of non-coaxial shearing, similar to what is proposed for the Zanskar section of the HHSZ, during the Neo-Himalayan Period. The second phase was guided by combined top-to-SW sense of simple shear and channel flow in two pulses. One of the pulses took place throughout the HHSZ during the Middle Miocene Period; the other pulse was restricted within the lower sub-channel. Thin HD1 and HD2 were produced during the respective pulsed flows. The third phase of exhumation is idealized by brittle slip of markers in a top-to-SW sense.

The channel flow component had differentially acted in various sections of the HHSZ. For example, while a single pulse of channel flow is deciphered from the Zanskar section; two distinct spatially and temporally separated pulses acted in the Sutlej section. The models of exhumation of the HHSZ for both these sections predict that (i) the base of

the ZSZ (or the HD1) exhumed with highest rate; and (ii) the ZSZ (or the HD1) might be missing in certain sections of the HHSZ even if channel flow was active.

The exhumation mechanism of the HHSZ is studied with 10 analogue models of channel flow initiating from a horizontal channel and extrusion through a linked inclined channel. The inclined channel is the model HHSZ and is of parallel, gently diverging-up and strongly diverging-up geometries in different considerations. In these experiments, Polydimethylsiloxane (PDMS) is used as the model material and only geometric similarity is maintained with the prototype. Six flow zones are deciphered in the two channels. The flow zone-4, formed nearly at the middle of the inclined channel, reveals a single zone of ductile extensional shearing similar to that in the South Tibetan Detachment System (or the HD1). This indicates that, in certain sections of the HHSZ, exhumation of the HHSZ took place by channel flow in two distinct pulses and gave rise to two ductile extensional shear zones, even when non-parallel geometry of the walls of the inclined channel is considered. A blind ductile secondary thrust, formed in zone-4, rotates while moving up and finally crops to the surface. In Sutlej section of the HHSZ, this thrust may be correlated with the Chaura Thrust with the recorded activation at least 13 Ma after the ongoing extrusion of the HHSZ by channel flow mechanism 18 Ma ago. The analogue models generate intrafolial folds within the ductile extensional shear zone, which is similar to the field observations from the detachments from different sections of the HHSZ.

Ductile sheared rocks of the HHSZ in Sutlej section outside the HD1and the HD2, in

micro-scale, reveal 'microflanking structures' (MFS) defined by the nucleated minerals (the crosscutting elements- CEs), and deflected cleavages and grain margins (the host fabric elements- HEs). Depending on whether the drag of HEs across the CE is different or same, the MFS are grouped into the Type-(i) and the Type-(ii) varieties, respectively. The Type-(ii) MFS indicates directional growth of the CE. The Type-(i) MFS indicates non-coaxial shearing, where the external HEs bounding the CEs act as the C-plains, and that the CE minerals undergo crystal-plastic deformation. Salient morphological variations in the MFS are: (1) variable intensity and senses of drag along the single- and the opposite CE margins; (2) HE defined only at one of the sides of the CE; and (3) presence of thin hazy zone at the HE-CE contact. The HEs are dragged even in absence of rheological softening at the CE boundaries. The Type-(i) MFS from the HHSZ reveals top-to-SW sense of shearing, which matches with other shear sense indicators. This also supports a channel flow model of exhumation of the studied shear zone. Rheological possibilities, except for a weaker CE mineral within a stronger host grain, have been encountered in the present study, and are represented in a graph of its constitutive equation.

CONTENTS

LIST OF FIGURES

LIST OF TABLES

Chapter 1

INTRODUCTION

1.1 THE HIMALAYA

1.1.1. General Introduction

The majestic mountain chain of Himalaya is an archetypical product of continent-continent collision between the Indian- and the Eurasian plates since ~ 55 Ma. It is the youngest and the longest mountain chain on the Earth with a number of very high peaks located in it. The collision resulted in the closure of the Tethyan Ocean, progressive southward thrusting of the remobilized Indian crust, subduction of India plate beneath Eurasian plate and thickening of the Eurasian crust to ~ 70 km (Godin et al., 2006 and references therein). The subject of Himalayan Geology is more than 150 years old but continues to intrigue Earth Scientists for many a unique unresolved problems.

General geology and tectonics of the Himalaya in different sectors, and also as a whole, has been reviewed in various research papers and edited books. The most exhaustive and up to date review is by Yin (2006). The Himalayan orogen is delimited by the Indus Suture Zone (ISZ) in the north, the Chaman fault in the west, the Sagaing fault in the east and the Main Frontal Thrust in the south. From south to north, the main lithologies in the Himalayan orogen occur as longitudinal strips and consist of (i) Neogene Sub-Himalayan sediments, (ii) Proterhozoic Lesser Himalayan sequence, (iii) Proterozoic Higher Himalayan Crystallines (HHC), and (iv) Paleozoic-Mesozoic Tethyan Sedimentary Zone. These litho-units are separated from each other by major thrusts (Figs. 1.1, -1.2),

Figure Captions

Fig. 1.1 Simplified map of the Himalayan mountain chain. Major faults are the Main Boundary Thrust (MBT), Main Central Thrust (MCR) and South Tibetan Detachment System (STDS). Reproduced from Hodges (1998).

Fig. 1.2 A NE-SW cross-section of the Himalaya. 1: Indo Gangetic plain; 2. Sub Himalayan Cenozoic foreland basin (SH); 3. Lesser Himalayan Sedimentary Zone (LHSZ); 4. Himalayan Metamorphic Belt including Lesser Himalayan Jutogh Nappe (JN); 4 Higher Himalayan Crystalline (HHC) belt and Tso Morari Crystalline (TMC); 5. Tethyan Sedimentary Zone (TSZ); Subduction related zones: 6. Indus Tsangpo Suture Zone and Spongtang Klippe (SK); 7. Ladakh Batholith Complex (LB); 8. Shyok Suture Zone (SSZ); Eurasian plate: 9. Karakoram Batholith Complex (KMC); 10. Partially molten crust (PMC); 11. Subducting Indian crust (IC). Symbols: MFT: Main Frontal Thrust; MBT: Main Boundary Thrust; MCT: Main Central Thrust; GSB: Garhwal Seismic Belt; ZSZ: Zanskar Shear Zone (equivalent to the South Tibetan Detachment System); MHT: Main Himalayan Thrust. Note that the vertical scale above the '0 km' has been exaggerated to show the topography. Reproduced from Jain et al. (2002).

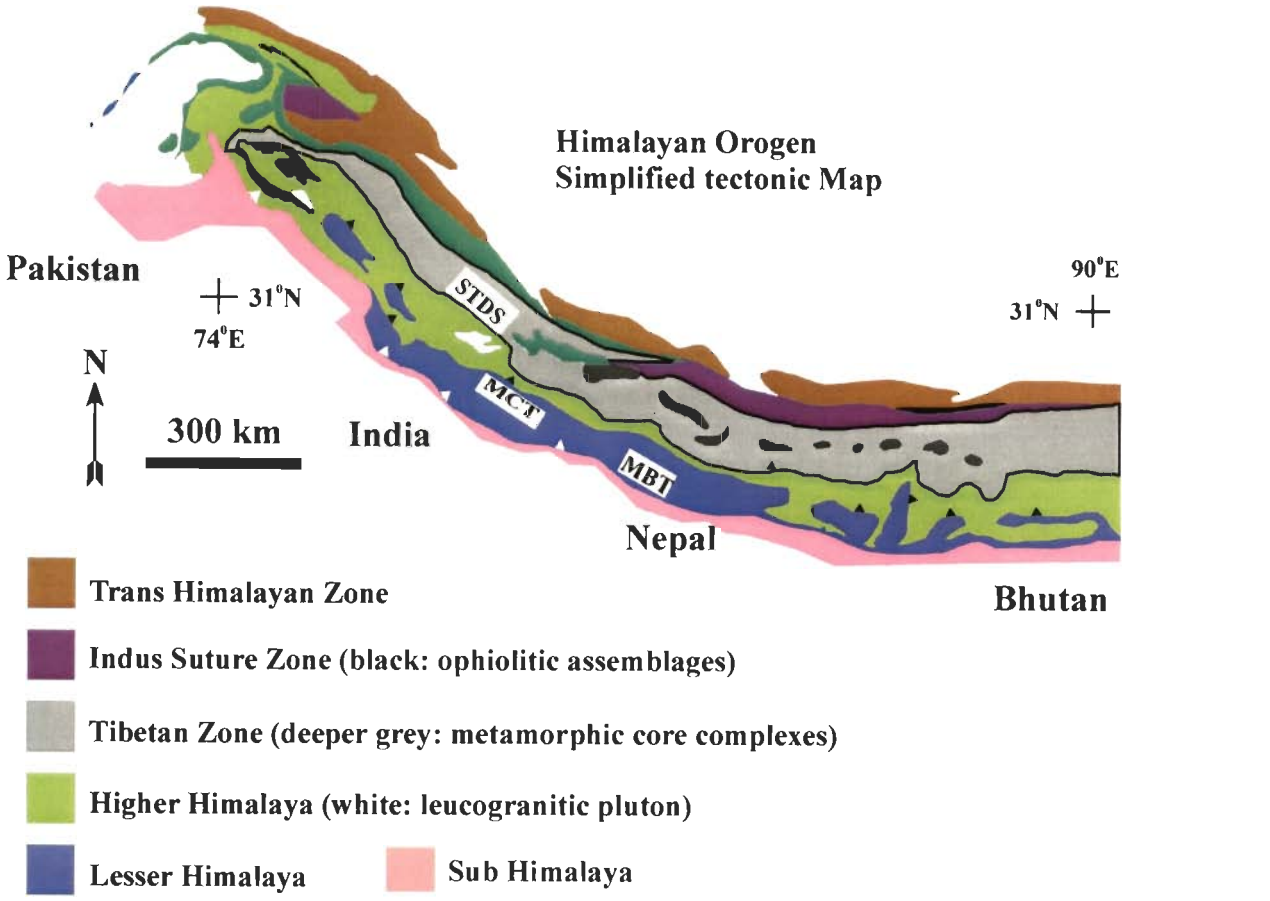
Himalayan Orogen
Simplified tectonic Map
Pakistan
31°N
74°E
90°E
31°N
N
300 km
India
STDS
MCT
MBT
Nepal
Bhutan
Trans Himalayan Zone
Indus Suture Zone (black: ophiolitic assemblages)
Tibetan Zone (deeper grey: metamorphic core complexes)
Higher Himalaya (white: leucogranitic pluton)
Lesser Himalaya
Sub Himalaya

Fig. 1.1

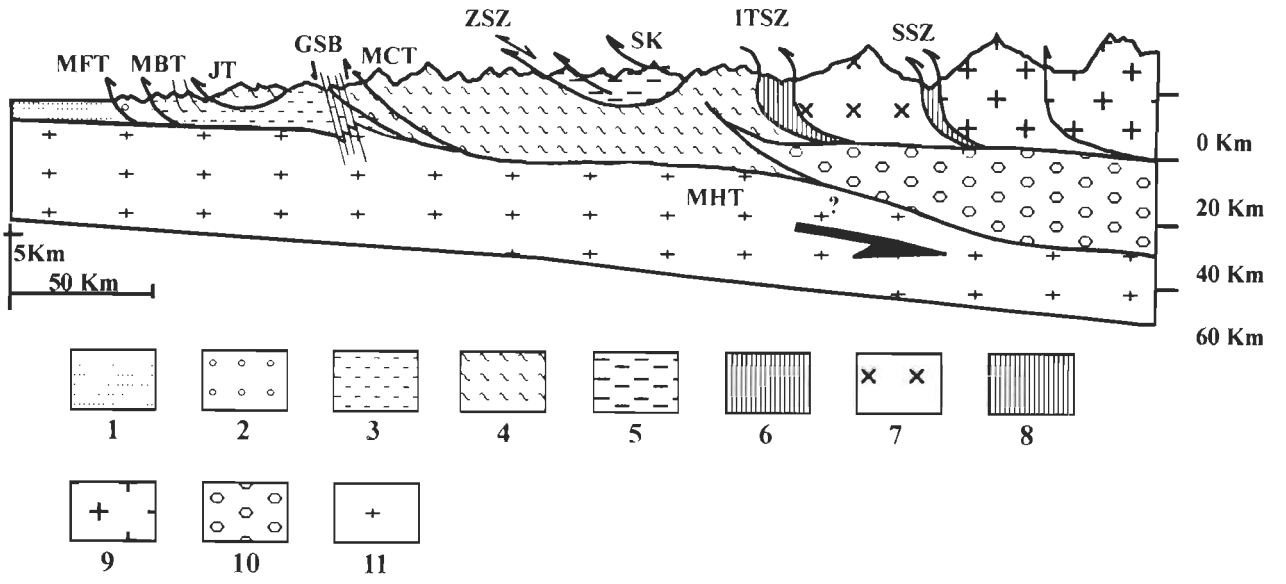
MFT
MBT
JT
GSB
MCT
ZSZ
SK
ITSZ
SSZ
MHT
5Km
50 Km
0 Km
20 Km
40 Km
60 Km
1
2
3
4
5
6
7
8
9
10
11

Fig. 1.2

which are northeasterly dipping, listric in regional-scale, and merge at depth with the Main Himalayan Thrust. (Figs 1, -2; Hodges et al., 2000; Jain et al., 2002; Yin, 2006 and references therein).

1.1.2 Himalayan Metamorphic Belt

The HHC is delimited by the Main Central Thrust (MCT) in the south and the South Tibetan Detachment System (STDS) in the north. The exact location of the MCT has been debated (Thakur, 1993 and references therein). The STDS has been recognized in various sections of the Himalaya by different local names. The HHC rocks are thrust southward- by a secondary thrust, which is named as the Jutogh Thrust in the western Himalaya. The rocks at the frontal part of the Indian plate, immediately south to the ISZ, is exposed as the Tso Morari Crystallines (TMC). The Lesser Himalayan Jutogh Nappe, the HHC and the TMC together define the Himalayan Metamorphic Belt (HMB) (Fig. 1.3). The Jutogh thrust sheet consists of medium grade (semi)pelitic rocks and metasediments of biotite and garnet grade. The HHC is the central core of the Himalaya- a ~ 30 km thick package consisting of (i) pelitic and psammitic rocks of Precambrian age metamorphosed into greenschist- to amphibolite facies, and (ii) (leuco)granites not younger than 400 Ma age. The rocks of the TMC underwent ultra-high pressure eclogite facies metamorphism around 53 Ma ago (Jain et al., 1999 and references therein; Mukherjee and Sachan, 2001; Jain et al., 2002 and references therein; Godin et al., 2006; Yin, 2006).

Figure Captions.

Fig. 1.3. Simplified geological map of the NW Himalaya. 1 – Sub-Himalayan (SH) Cenozoic foreland basin. 2 – Lesser Himalayan Sedimentary Zone (LHSZ). 3 – Himalayan Metamorphic Belt (HMB): (a) Higher Himalayan Crystalline (HHC) Belt/Higher Himalayan Shear Zone and Jutogh Nappe (JN) with ca. 500 Ma granitoid (b) and Cenozoic leucogranite (c). 4 – Tethyan Sedimentary Zone (TSZ). 5 – Tso Morari Crystalline (TMC) Belt. 6 – Trans-Himalayan tectonic units. Other abbreviations: MBT – Main Boundary Thrust. JT – Jutogh Thrust. MCT – Main Central Thrust. HDZ – Himalayan Detachment Zone including ZSZ – Zanskar Shear Zone and MF – Martoli Fault. ITSZ – Indus Tsangpo Suture Zone (ITSZ). Ki – Kishtwar. S – Shimla. UK – Uttarkashi. G – Gangotri. Reproduced from Jain et al. (2005).

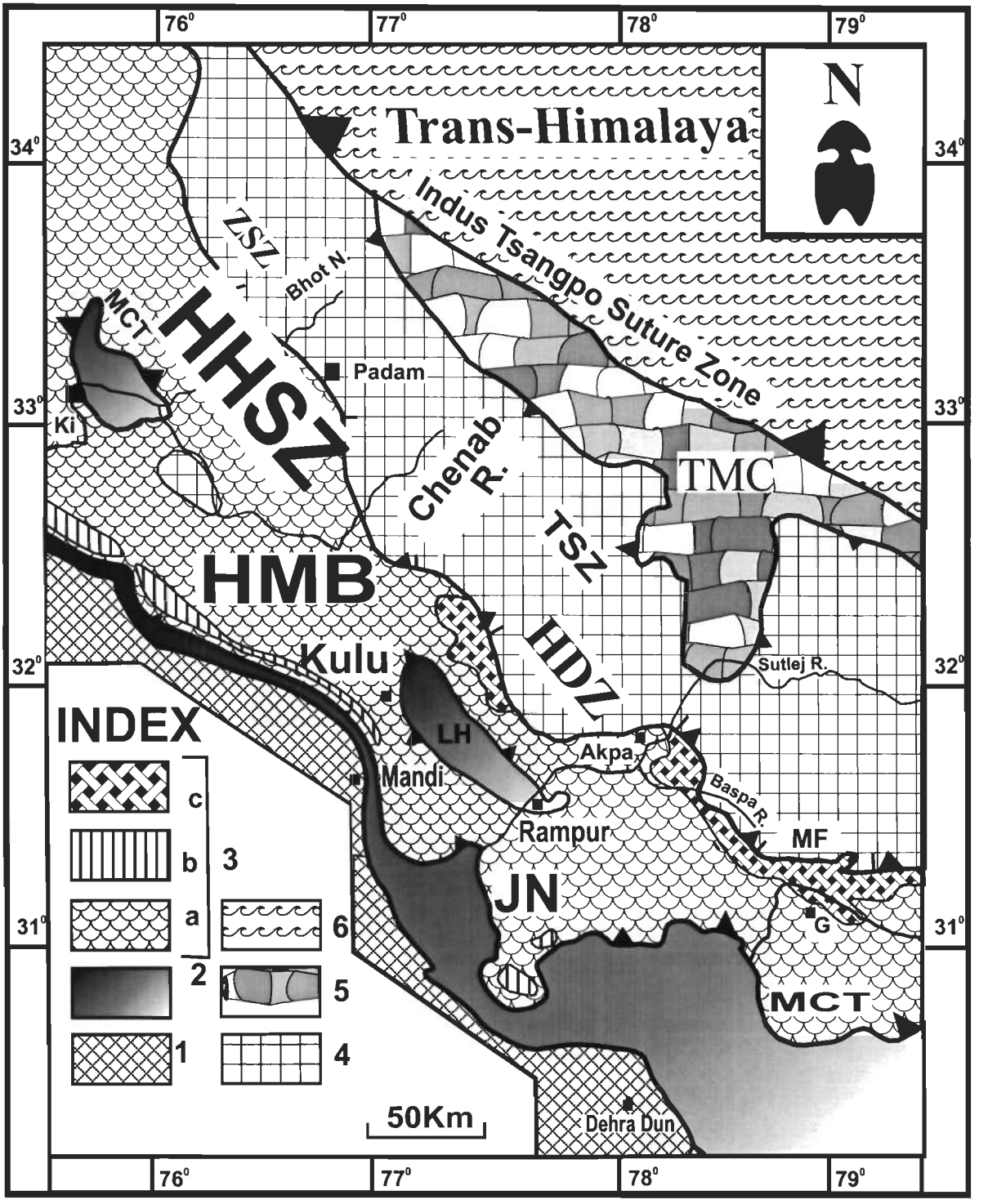
76°
77°
78°
79°
34°
33°
32°
31°
N
Trans-Himalaya
Indus Tsangpo Suture Zone
ZSZ
Bhot N.
MCT
HHSZ
Padam
Ki
Chenab R.
TSZ
TMC
HMB
HDZ
Kulu
Sutlej R.
INDEX
c
b
a
3
2
1
6
5
4
LH
Akpa
Mandi
Baspa R.
Rampur
MF
JN
G
MCT
50Km
Dehra Dun

Fig. 1.3

1.1.3 Higher Himalayan Shear Zone

Jain and Anand (1988) described the HHC as a ductile shear zone with ubiquitous top-to-SW sense of shearing, and referred it as the 'Higher Himalayan Shear Zone' (HHSZ). From now onward in the thesis, 'HHSZ' will be used to denote the 'HHC'. The STDS is structurally characterized by top-to-NE sense of extensional ductile shearing. Compiled data from different sectors of the Himalaya indicates that the MCT and the STDS were active between 25-14 Ma and 24-12 Ma, respectively with an overlapping period of activation between 24-12 Ma (Godin et al., 2006 and references therein).

The inverted metamorphic sequence in the HHSZ is one of the most discussed aspects in Himalayan geology. Models that have been proposed to explain this peculiar feature vis-à-vis the exhumation of the HHSZ are: (i) overthrusting of hot material, (ii) imbricate thrusting, (iii) folding of isograds, (iv) (heterogeneous) simple shearing, (v) general shear of foreland dipping isograds, and (vi) shear heating (Godin et al., 2006 and references therein). However, these models need reappraisal in the light of the present understanding of simultaneous activation of the ductile extensional shearing within the STDS and the ductile compressional shearing of the MCT during 24-12 Ma.

Four phases of exhumation have been worked out from the Himalaya (Jain and Anand, 1988; Jain et al., 2002 and references therein). Out of these, exhumation of the HHSZ was during the Neo-Himalayan period (25-15 Ma). Four phases of deformation have been documented from the HHSZ. Amongst these, the D2 deformation has been most pervasive and is indicated by top-to-SW sense of ductile shearing along northeasterly

dipping main foliation planes/ C-planes and northeasterly plunging lineations. This deformation has been a delayed response to the India-Asia collision that initiated ~ 55 Ma ago, and might have taken place during the Neo-Himalayan exhumation period (Hodges, 2000; Jain et al., 2002 and references therein). Three phases of metamorphism have been documented from the HMB in the NW Himalaya. Amongst them, the M2 metamorphism took place during the D2 deformation phase, and is most prominent in the HHSZ from its base up to the top. The M2 phase is characterized by the syntectonic growth of staurolite, kyanite, sillimanite and hornblende porphyroblasts both along the S- and the C-planes (Jain and Manickavasagam, 1993; Manickavasagam et al., 1999).

A number of rivers in the Himalaya flow toward southwest direction, which is (fortunately) nearly perpendicular to the main foliation and sub-parallel to the stretching lineation in the HHSZ. These rivers had created natural XZ-sections, which are ideally suited to study the true sense of ductile shearing of the HHSZ. In many places of the HHSZ, these sections are the only suitable sites to undertake geological investigations.

1.2 THE CHANNEL FLOW

Recently, the channel flow model has been considered as an efficient mechanism of exhumation of the HHSZ. The relevant terminologies existing in literature, and those used in the thesis are as follows.

In fluid mechanics, 'open channel flow' is defined as "fluid motion in which a liquid in a conduit has part of its boundary exposed to atmospheric pressure. The conduit may be

completely open to the atmospheric pressure, as in a natural river beds or artificial canals and channels, or it may be closed in drainage and sewage pipes that are not running full" (John and Haberman, 1971). In a different language, 'open channel flow' is "any flow with a free surface, whether a conduit, river, canal, sewage line or any other conveying system..." (Manohar and Krishnamachar, 1982). The term, "Poiseuille flow", has been used for laminar flows through a pipe of uniform diameter, which is governed by pressure gradient (Langlois, 1964; Batchelor, 1967; John and Haberman, 1971; Rogers, 1978). For a flow maintained by pressure gradient through non-parallel walls, the term "Poiseuille flow" has still been used, although "Jeffery-Hamel flow" is a more appropriate term (e.g. Eagles, 1966). The flow through an inclined channel is described as "Poiseuille flow through inclined plates" (Papanastasiou et al., 2000; Pozrikidis, 2001). The terms 'Couette flow' (Langlois, 1964; Schlichting and Gersten, 1999) or 'simple shear flow' (Liu, 1977) stand for the laminar flow with no pressure gradient but only guided by the shear of the boundary wall(s). Schlichting and Gersten (1999) have used the term 'Couette Poiseuille flow' to denote the flow through a parallel wall horizontal channel by a combination of the shear of the wall(s) and the pressure gradient. The lack in strict terminologies to describe fluid flow patterns is well demonstrated by usage of the terms 'plane Couette Poiseuille flow' (Papanastasiou et al., 2000), 'Couette flow' (Schlichting, 1955; Broadkey, 1967; Munson et al., 2002); 'generalized plane Couette flow' (Pai, 1956); and 'plane Couette flow' (Rogers, 1978) to represent the 'Couette Poiseuille flow' of Schlichting and Gersten (1999).

In this thesis, 'channel flow'/ 'plane Poiseuille flow' has been used to denote laminar flow of incompressible Newtonian viscous fluid through a channel with parallel infinitely long horizontal walls.

1.3 THE DETACHMENT FAULT

Ramsay and Huber (1987) defined 'detachment fault' as the low-angle major base to a complex normally faulted terrain that runs at low-angle to the contact between the crystalline metamorphic basement and the overlying sedimentary cover. On the other hand, Davis and Reynolds (1996) gave a generalized definition of the 'detachment fault' as a low angle normal fault. In Nepal Himalaya, the upper boundary of the HHSZ was identified as a zone of extensional shearing, and was named 'South Tibetan Detachment System' (Caby et al., 1983; Burg and Chen, 1984; Burchfiel and Royden, 1985; Burchfiel et al, 1992). The use of the word 'detachment' in this case is more akin to that defined by Davis and Reynolds (1996). In this work, extensional ductile shear zones are reported from Sutlej section of the HHSZ. The main foliations within these zones dip moderately and are sub-parallel with those outside the extensional shear zone. Such shear zones in the HHSZ have been described in this thesis as 'detachments' keeping similarity in use of the term by the recent workers from other sections of the HHSZ (Edwards et al., 1996; Searle, 1999).

1.4 FLANKING STRUCTURES

Flanking structures are deflections of planar markers around a planar discontinuity (Fig. 1.4.), and are encountered in various sheared rocks (Passchier, 2001). Till date, almost all

flanking structures have been described from field-scales. A number of analogue- (Exner, 2005) and numerical models (Kocher, 2006) have emphasized the role of different shear regimes and anisotropy in the rock matrix, respectively, in the genesis of flanking structures. The inclination of the cross-cutting discontinuity (the 'cross-cutting element') to the primary shear plane has been demonstrated to be an unreliable indicator of ductile shear sense in macro-scales (Fig. 1.5) (Grasemann et al., 2003).

1.5 OBJECTIVES

This work aims at field- and micro-structural studies in selected sections of the HHSZ in the NW Indian Himalaya to establish the tectonic model of exhumation of the shear zone. Mathematical analyses and analogue models have been performed to establish the exhumation model. Additionally, microflanking structures, a new kind of micro-structure, have been reported in detail, and have been selectively used in deducing the ductile sense of shearing of the HHSZ.

1.6 ORGANIZATION OF THE THESIS

Chaper-2 includes micro-structural studies of the rocks of the Zanskar Shear Zone, presents the dominant deformation structures in a schematic cross-section, and proposes a model of exhumation of the HHSZ in the Zanskar section. The model is based on structures, mathematical analyses of slow flow, and physical boundary conditions obtained from the literature. The mathematical analyses assume the shear zone to be bounded by parallel walls.

Figure Captions.

Fig. 1.4 Diagrammatic representation of flanking structure. The dragged part of the host fabric element (HE), near the crosscutting element (CE), is called the 'internal HE'. Away from the internal HE is the straight and undisturbed 'external HE' Reproduced from Fig. 1 of Passchier (2001).

Fig. 1.5 The development of different flanking structures under simple shear conditions, depending on the initial angle of the cross-cutting element (CE) to the shear zone boundary (after Grasemann et al., 2003). This diagram is valid exclusively for a top-to-right sense of shearing (the case of a top-to-left shear is mirror symmetric across the vertical plane). Note that the sense of shear along the CE is reversed as its orientation passes through that of the instantaneous stretching axes at 45^0 (ISA_2) and 135^0 (ISA_1), respectively. If one tries to interpret the bulk ductile sense of shearing from the orientation of the CE at the left half of the half circle, it is top-to-left; whereas at the right half it is top-to-right. Flanking structures, for these reasons, are not considered reliable shear sense indicators in many cases.

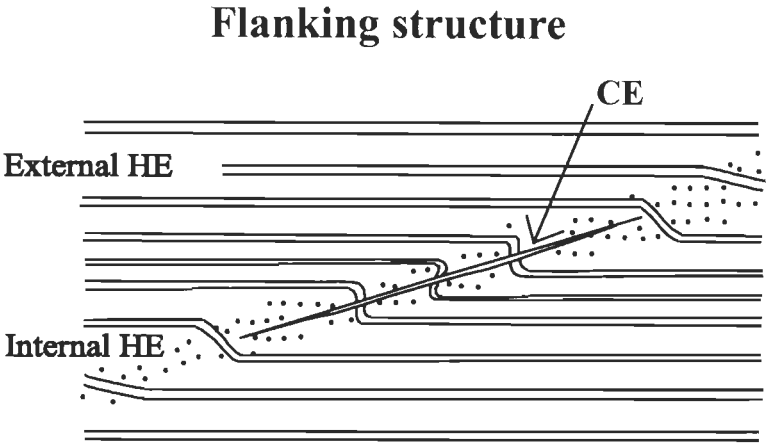
Flanking structure
CE
External HE
Internal HE

Fig. 1.4

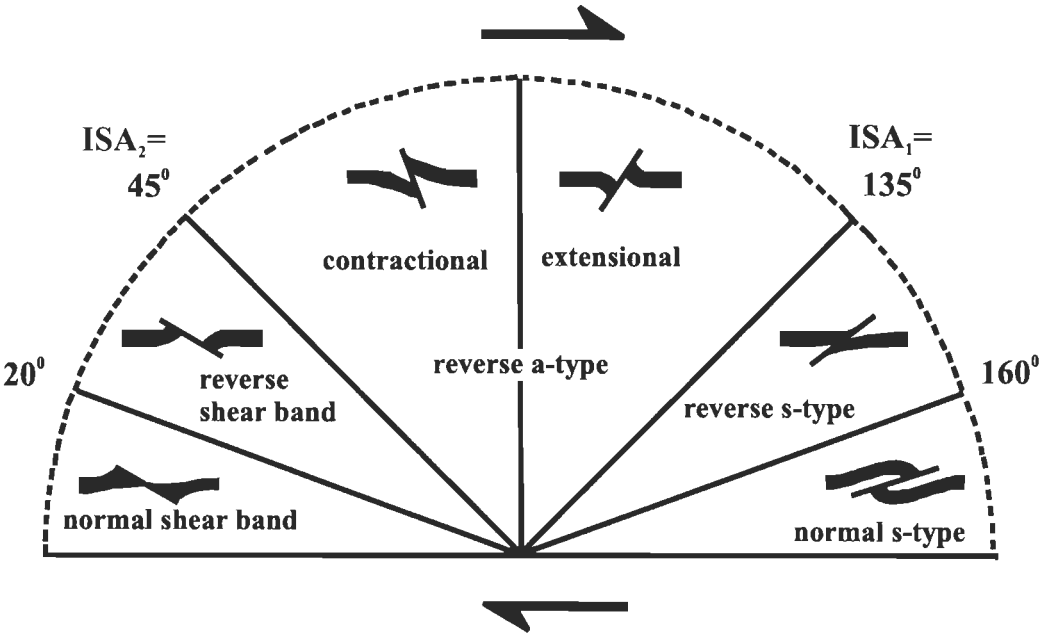
ISA2= 45°
ISA1= 135°
contractional
extensional
20°
reverse shear band
reverse a-type
reverse s-type
160°
normal shear band
normal s-type

Fig. 1.5

Chapter-3 presents lithologic- and structural data from fieldwork and thin-section studies of the HHSZ rocks in the Sutlej river section. These studies lead to a model compliant subdivision of the shear zone. The kinematics of shear zone is analyzed mathematically, which is a sequel to that of the previous chapter. The boundary walls of the shear zone in this case are also considered parallel. Finally, a three-stage exhumation model of the HHSZ for this section is proposed.

Chapter-4 raises the key question- whether exhumation of the HHSZ through a channel with non-parallel walls can simultaneously produce two detachments. 10 analog models of channel flow were performed with a 'channel flow box' consisting of a horizontal channel and a linked inclined model HHSZ. Going beyond the key question, the other kinematics of the flow has also been partially explored.

Chapter-5 reports and describes in detail the flanking structures in micro-scales. These structures are documented under very high magnification in an optical microscope. 'Microflanking structures' are classified and their limited but reliable use as ductile shear sense indicators is discussed taking examples from the Sutlej river section of the HHSZ.

Conclusions of the previous chapters have been drawn in Chapter-6. The main points involve the model of exhumation of the HHSZ and the microflanking structures.

Chapter 2

HIGHER HIMALAYAN SHEAR ZONE, ZANSKAR SECTION- MICRO-STRUCTURES & EXHUMATION MODEL

2,1. INTRODUCTION & OBJECTIVES

The Zanskar Shear Zone (ZSZ) (Fig. 2.1a) is a NW-SE trending zone with top-to-NE sense of ductile shearing, a continuation of the South Tibetan Detachment Systems (STDS) and is located in the Suru Doda valleys of the NW Indian Himalaya. The STDS and the ZSZ have been designated as the Himalayan Detachment-1 (HD1) in the next chapter of this thesis. The top boundary of the ZSZ separates the Tethyan Sedimentary Zone in the north and the Higher Himalayan Shear Zone (HHSZ) in the south. The lower boundary of the HHSZ is the Main Central Thrust (MCT). The HHSZ in the Zanskar section consists of gneisses and schists containing sillimanite, kyanite, muscovite and K-feldspar; metapelites, metapsammites, mylonites, leucogranites, granitoids, aplites, pegmatites, and migmatites with greenschist to amphibolite facies metamorphism. The HHSZ rocks are Precambrian and Proterozoic in age (Patel et al., 1993; Jain and Patel, 1999, Jain et al., 2002 and references therein).

Field-work has revealed four phases of deformation of the HHSZ in the Zanskar section. Amongst them, top-to-SW sense of ductile shearing along northeasterly ~30^0 dipping primary shear planes (C-planes, S_2 or S_m of Jain and Patel, 1999) throughout the HHSZ belongs to the D_2 deformation phase. This deformation was initiated possibly during the early phase of Neo-Himalayan Period 25Ma back, and was a delayed response to the intense crustal shortening due to India-Asia collision (Patel et al., 1993; Jain et al., 2002).

Figure Captions.

Fig. 2.1a Geological map of the Higher Himalayan Shear Zone and the Zanskar Shear Zone (ZSZ) in the Zanskar valley, NW Indian Himalaya. Reproduced from Patel et al (1993). The studied thin-sections are from rocks within the ZSZ near the place Padam.

Fig. 2.1b A schematic cross-section of the Zanskar Shear Zone along the NE-SW geographic direction. The structures reported by Patel et al. (1993) are shown- 1: top-to-SW sense of ductile shearing; 3: top-to-NE (down) extensional ductile shearing; $1'$: Top-to-SW sense of brittle shearing represented by duplexes; and $2'$: Steeply northeasterly dipping brittle faulting. Ductile shearing represented by '1' and '3' are subsequently referred as 'shearing-1' and 'shearing-3', respectively. Primary shear plains of 'shearing-1' define the 'main foliations'. Stretching lineations plunge northeasterly. The orientation of the thin-sections, studied in this work, is perpendicular to the main foliations and parallel to the stretching lineations, and is shown. The cross-section is neither to scale nor to angle.

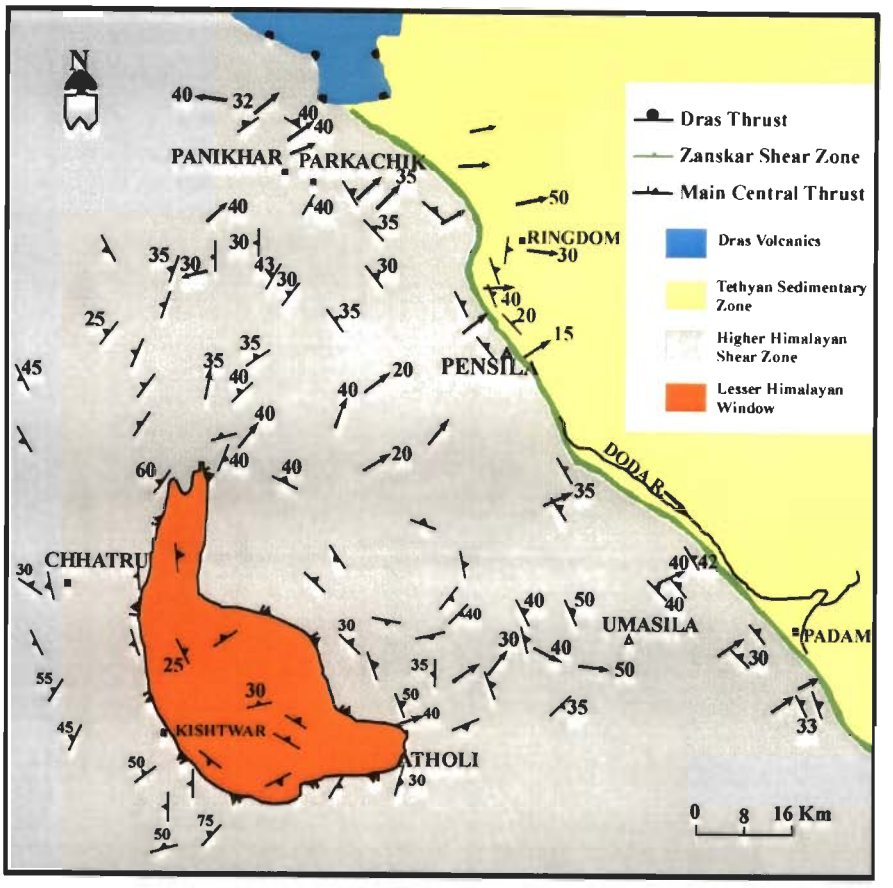

Fig. 2.1a

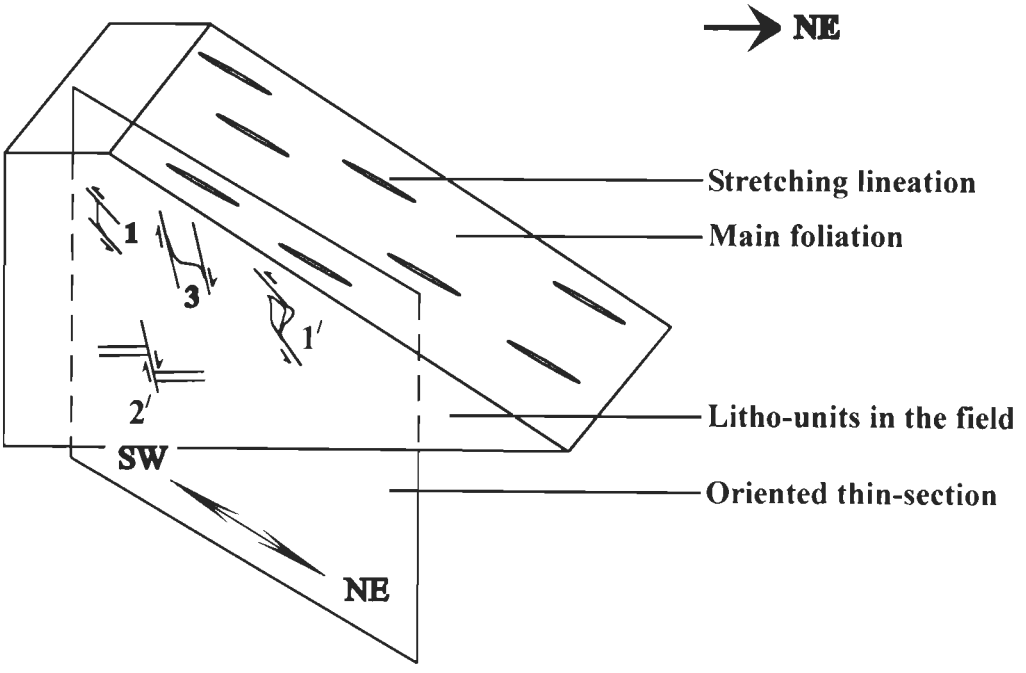

Fig. 2.1b

Within the ZSZ, stretching lineations (L_2 or L_m of Jain and Patel, 1999) plunge 25-38^0 northeasterly and define this SW direction of movement. The northeasterly ~40^0 dipping ductile shear fabrics cut across the C-planes of the D_2 deformation phase. The top-to-NE sense of ductile shearing, associated with these C-planes, is henceforth referred as the *top-to-NE (down) shearing*. Brittle normal faults, northeasterly steeply dipping to ~40-50^0, cut across C-planes of the ductile fabrics (walker et al., 1999). Another brittle phase of top-to-SW sense of shearing is represented by duplexes (Patel et al., 1993). These structures are represented in a schematic cross-section of the ZSZ in Fig. 2.1b.

Ar-Ar hornblende data has indicated that peak metamorphism in the ZSZ occurred before 30.7 ± 2.0 Ma. After this event, a rapid cooling took place until 19 Ma. On the other hand, the peak metamorphism in the middle of the HHSZ occurred before 22.0 ± 1.0 Ma. This was followed by a rapid cooling till 15 Ma (Searle et al., 1992). The extensional shearing within the ZSZ was active between 22-19 Ma, and ceased by 11-9 Ma (Yin, 2006 and references therein). The lower boundary of the HHSZ, i.e. the MCT, was active between 20-23 Ma in general in the Central Himalaya; a much longer span of 13-41 Ma in the Nepal Himalaya; 22-14 Ma in the western Himalaya in general; 22-16 Ma along the Kishtwar Window; 11-16 Ma and 14-22 Ma in the Garhwal Himalaya; 13-15 Ma from central Nepal; 11-14 Ma from Bhutan Himalaya; and 22-14 Ma or still younger in the Sikim Himalaya (Jain et al., 2002 and references therein; Yin, 2006 and references therein). A Middle Miocene timing of the ductile top-to-NE sense of shearing within the ZSZ simultaneous to the top-to-SW sense of shearing of the MCT has broadly been accepted for different sections of the HHSZ (Dèzes et al., 1999; Robyr et al., 2002). Combined slip at its boundaries gave rise to

fast exhumation of the HHSZ along with anatexis, migmatization and leucogranite injection within the ZSZ (Walker et al., 1999, Yin, 2006 and references therein). The melt activity may also be in pulses starting from as early as the Eocene Period, 45 Ma back (Jain et al., 2005). The presence of rocks in a hot partially molten stage at mid-crustal depth has been ascertained from south Tibet (Nelson 1996). These suggest that at least during a part of its exhumation in the ductile regime, the HHSZ had oozed up like a fluid. The pressure gradient responsible for this fluid flow has been estimated to be 1-2 $kbar.km^{-1}$ in the Nepal Himalaya (Grujic et al., 1996, as referred in Vannay and Grasemann, 2001). A much lower value of pressure gradient of 0.28 ±0.17 $kbar.km^{-1}$ has been estimated that for the Zanskar section (Searle et al., 1992). On the other hand, the rate of slip of the MCT was in the order of few mm per year in Nepal Himalaya (e.g. Kohn et al., 2004). For the ZSZ, the rate was about ten times faster i.e. in the order of few cm per year (Dèzes et al., 1999). The ZSZ is much thinner than the reminder of the HHSZ. The thickness of the ZSZ varies along its length-.from 2.5 to 0.5 km (Jain and Patel 1999). Walker et al. (1999) reports that the ZSZ has a thickness of around 1-2 km. On larger scales as well, the thickness of the continuation of the ZSZ along the trend of the Himalaya, is spatially variable (Vannay and Grasemann 2001). The inverted metamorphism within the HHSZ and the top-to-NE sense of ductile shearing in the ZSZ/STDS has been explained by different models for the exhumation of the HHSZ, but each of them has been challenged (see Hodges, 2000 for review).

This chapter aims at (i) micro-structural documentation of the dominant deformation patterns of the ZSZ rocks; (ii) compilation of the structures of the HHSZ in the Zanskar

section based on the present- and the previous studies; and (iii) proposing a model for the exhumation and the ductile deformations of the HHSZ in this section.

2.2. MICRO-STRUCTURAL STUDIES

2.2.1. Ductile deformations

Thin-sections (Fig. 2.1b), oriented perpendicular to the northeasterly dipping C-planes, or the 'main foliation', of the top-to-SW sense of shearing of D_2 deformation and parallel to the northeasterly plunging stretching lineations, are studied. The top-to-NE (down) sense of shearing cutting the preexisting shear fabrics is found to be the most prominent deformation event, and is revealed by mineral fishes (ten Grotenhuis et al., 2002) defined by minerals of high- (Fig. 2.2a, -b) and low-grades (Fig. 2.3a), elongated (recrystallized) quartz grains (Figs. 2.2b, 2.3b-d) defining S-fabrics (Berthè et al., 1979) and intrafolial folds of aggregate of quartz and sillimanite (Fig. 2.4a). Some of these mineral fishes have undergone dynamic recrystallization at their boundaries. The fine grained minerals probably boudinaged from the tip of the mineral fishes define fish trails, which are also the C-planes. The S-fabrics become sigmoidally curved as they approach the C-planes. The intrafolial folds are rootless types and their enveloping surfaces define the C-planes. The angle between the S- and the C- fabrics is around 47^0. The axial traces of these folds in the oriented thin-sections make high-angle of around 70^0 to the SW direction of the C-planes.

Figure Captions

Fig 2.2a. Intensely ductile sheared gneissose rock showing early top-to-SW sense of ductile shearing (marked by half arrow '1', henceforth referred as 'shearing-1'), and late top-to-NE sense of ductile shearing (marked by half arrow '2', henceforth referred as 'shearing-2'). The most prominent and latest top-to-NE sense of ductile shearing (marked by half arrow '3', henceforth referred as 'shearing-3') cut the primary shear plains of the first two shearing events. 'Shearing-1' occurs as relict. Its S-fabrics are defined by quartz grains, some of which are nearly sigmoid shaped (grain 'P'), and some are at very low-angle to the primary shear plain (grain 'Q'). Short and straight C-plains, bounding these quartz grains, are defined by biotite grains. Sigmoid and single-mouth quartz grains ('R' and 'U') define the S-plains for the 'shearing-2'. The C-plains for the 'shearing-2' are parallel to, therefore the same as, that for the 'shearing-1'. These C-plains are cut by the thick C-plains of the 'shearing-3', at $\theta=25^0$. Top-to-NE (down) extensional shearing is also referred as the 'shearing-3'. A composite sigmoid mineral fish with muscovite surrounding the staurolite core (grain aggregate 'T') defines the S-fabric of 'shearing-3'. 'Shearing-1' is correlated with the Main Himalayan D_2 deformation of Jain et al. (2005); 'shearing-2' with extensional shearing typical of the Himalayan detachments; and 'shearing-3' as synthetic to 'shearing-2', respectively. Photo in plane polarized light. XZ oriented thin-section from Zanskar Shear Zone. Photo length: 10mm. Thin-section number: P9/A.

Fig 2.2b. Recrystallized quartz grains revealing top-to-NE (down) extensional shearing ('shearing-3' of caption of Fig. 2.2a). Relict top-to-SW ductile shearing ('shearing-1' in caption of Fig. 2.2a) is deciphered from a sigmoid fish defined by an aggregate of biotite, and a quartz fish (pointed out by an arrow). θ (defined in caption of Fig. 2.2a) is measured as 41^0. Photo in plane polarized light. XZ oriented thin-section from Zanskar Shear Zone. Photo length: 4.0mm. Thin-section number: P9/D.

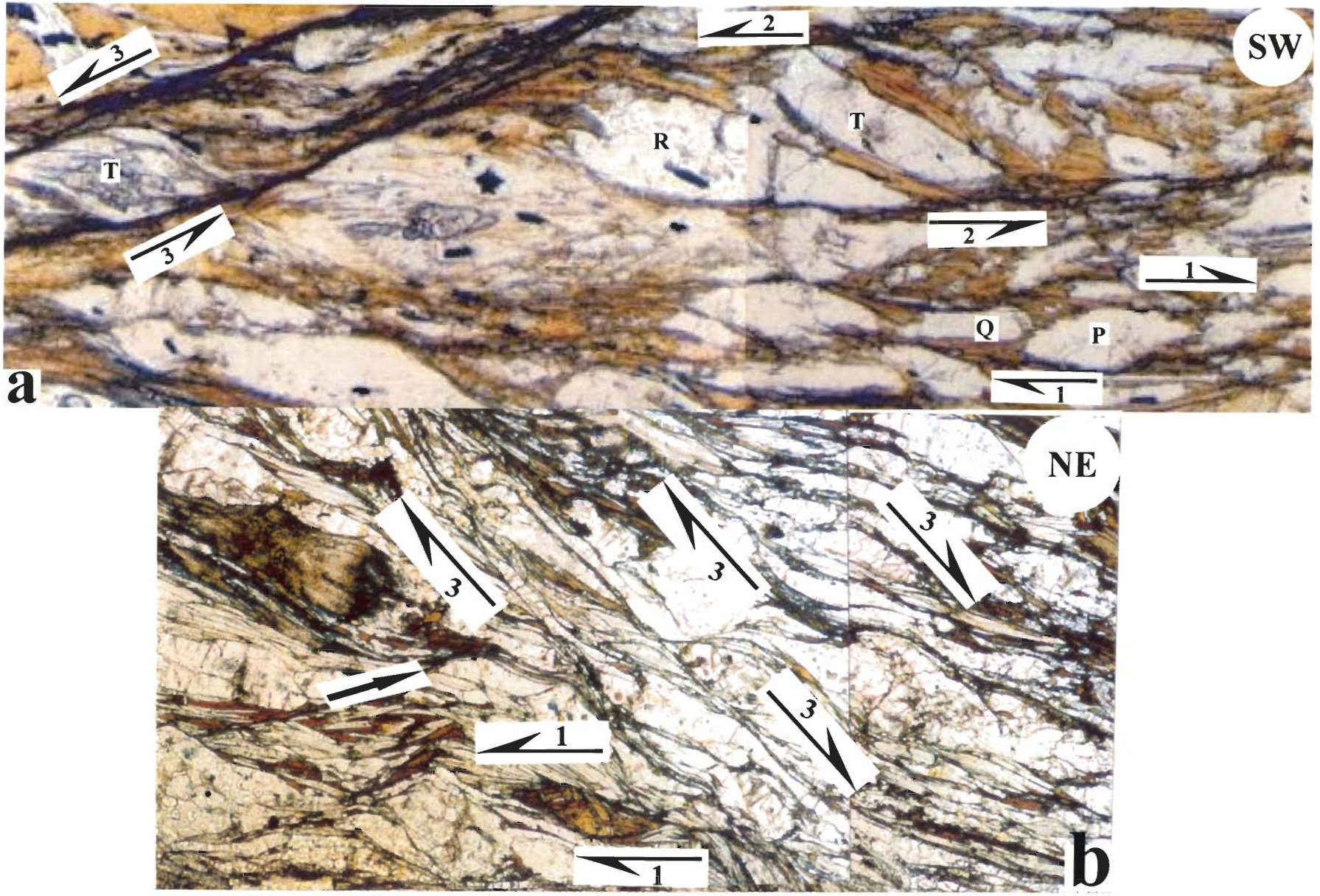

Fig. 2.2

Figure Captions.

Fig. 2.3a. Intensely ductile sheared gneissose rock showing three senses of ductile shearing, viz. top-to SW, top-to-NE and top-to-NE (down), which are 'shearing-1', '-2' and '-3', respectively of Fig. 2.2a. The first two senses of shearing are represented by sigmoid fishes defined by an aggregate of muscovite grains. The last one is defined by individual micas defining the S-fabric, and also by sigmoid quartz grains (pointed out by an arrow) that are partly wrapped by muscovite. θ (defined in caption of Fig. 2.2a) is measured as 40^0. Photo in cross polarized light. XZ oriented thin-section from Zanskar Shear Zone. Photo length: 5.0mm. Thin-section number: P9/O.

Fig. 2.3b. Top-to-NE (down) extensional shearing (same as 'shearing-3' of caption of Fig. 2.2a) has sheared recrystallized quartz grain into long tail along the shear plain. This indicates that the 'shearing-3' event has been pervasive. θ (defined in caption of Fig. 2.2a) measured elsewhere in the thin-section gives an amount of 53^0. Photo in plane polarized light. XZ oriented thin-section from Zanskar Shear Zone. Photo length: 5.0mm. Thin-section number: P9/B.

Fig. 2.3c. Sigmoid quartz grains of different thicknesses define the S-fabric and top-to-NE (down) extensional shearing (same as 'shearing-3' of caption of Fig. 2.2a) with decipherable thick and nearly straight C-plains. Top-to-NE sense of shearing ('shearing-2' of caption of Fig. 2.2a) is deciphered from intrafolial folds of quartz grains. θ (defined in caption of Fig. 2.2a) measured elsewhere in the thin-section gives an amount of 43^0. Photo in plane polarized light. XZ oriented thin-section from Zanskar Shear Zone. Photo length: 5.0mm. Thin-section number: P9/C.

Fig. 2.3d. Recrystallized quartz grains showing the S- and the C-fabrics. The S-fabric demonstrates top-to-NE (down) extensional shearing ('shearing-3' of caption of Fig. 2.2a). Interestingly, the S-fabric is defined, only at their contacts to the C-plain, by strongly swerved quartz grains. Instead of a pair of C-plains, a single C-plain is found in this view. Orientations of the S- and the C- plains are shown by thin white lines. The angle between the S-plains and the C-plains of 'shearing-3' is $\sim 47^0$. θ (defined in caption of Fig. 2.2a) is measured elsewhere from the thin-section as 36^0. Photo in cross polarized light. XZ oriented thin-section from Zanskar Shear Zone. Photo length: 5.0mm. Thin-section number: P9/K.

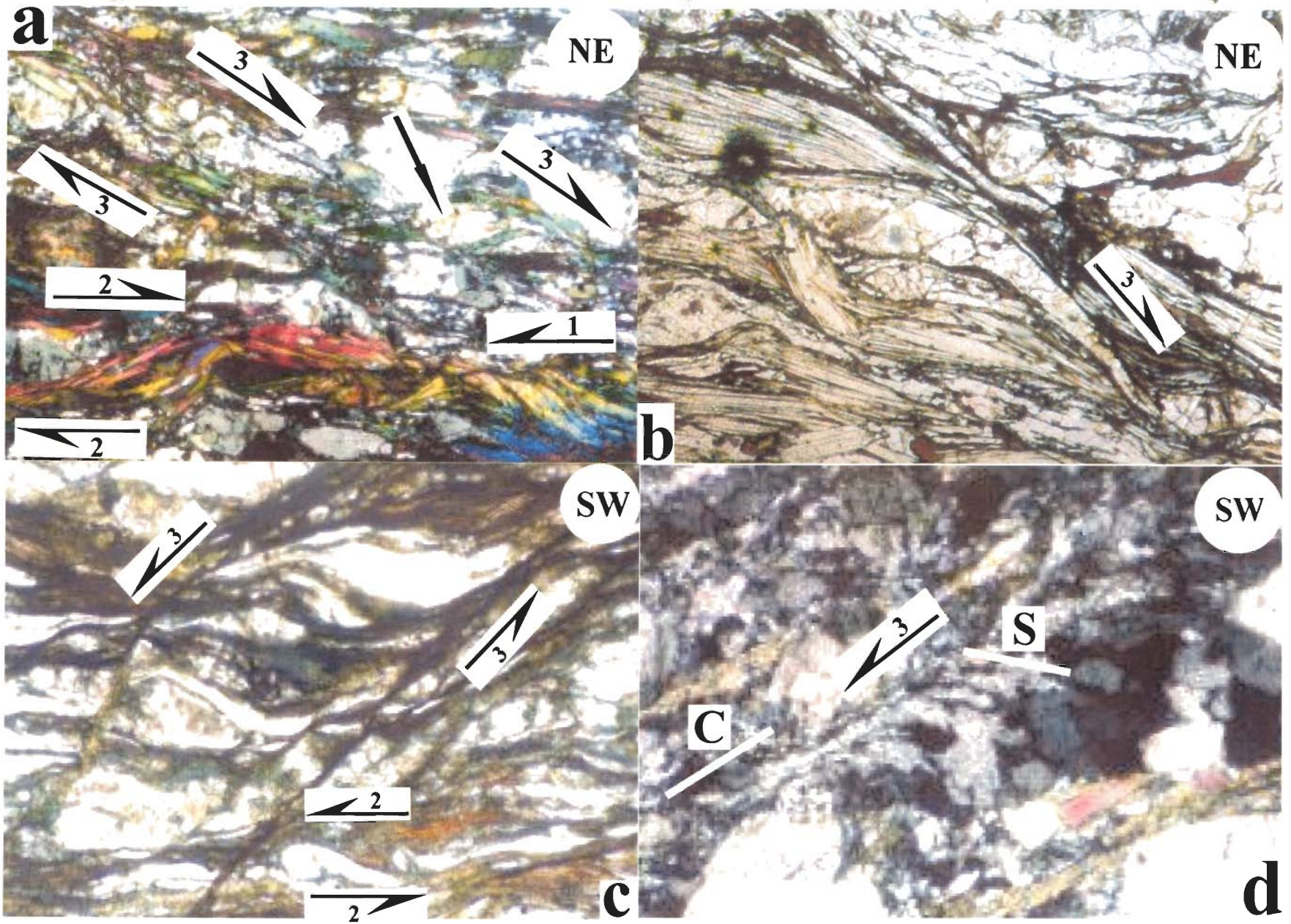

Fig. 2.3

Figure Captions.

Fig 2.4a. Broad hinge intrafolial fold defined by aggregate of quartz and staurtolite with markedly different limb thicknesses. The fold gives top-to-NE (down) extensional shearing ('shearing-3' of caption of Fig. 2.2a) along NE dipping thick and straight shear plain. The axial trace is marked by a white line. The angle between the axial trace and the C-plain of 'shearing-3' is 70^0. Photo in plane polarized light. XZ oriented thin-section from Zanskar Shear Zone. Photo length: 3.0mm. Thin-section number: P9/G.

Fig. 2.4b. Biotite aggregate and quartz grains strongly sheared in distinct zones into top-to-NE direction (the 'shearing-2' of caption of Fig. 2.2a) defining the S-fabric. XZ oriented thin-section from Zanskar Shear Zone. Photo in plane polarized light. Photo length: 2.5mm. Thin-section number: P9/F.

Figs. 2.4c & -d. Top-to-NE shearing ('shearing-2' of caption of Fig. 2.2a.) are displayed by recrystallized quartz grains, which is a sigmoid shaped fish (Fig. 2.4c), or an overturned fold with unequal thicknesses- and lengths of the limbs (Fig. 2.4d). For Fig. 2.4c, the shear sense given by the fish-shaped quartz is confirmed by smaller muscovite fishes, shown by a white arrow. Photos in cross polarized light. For Fig. 2.4d, the angle between the S- and the C-plains is measured as 25^0. XZ oriented thin-section from Zanskar Shear Zone. Photo length: 3.0mm. Thin-section number: P9/I.

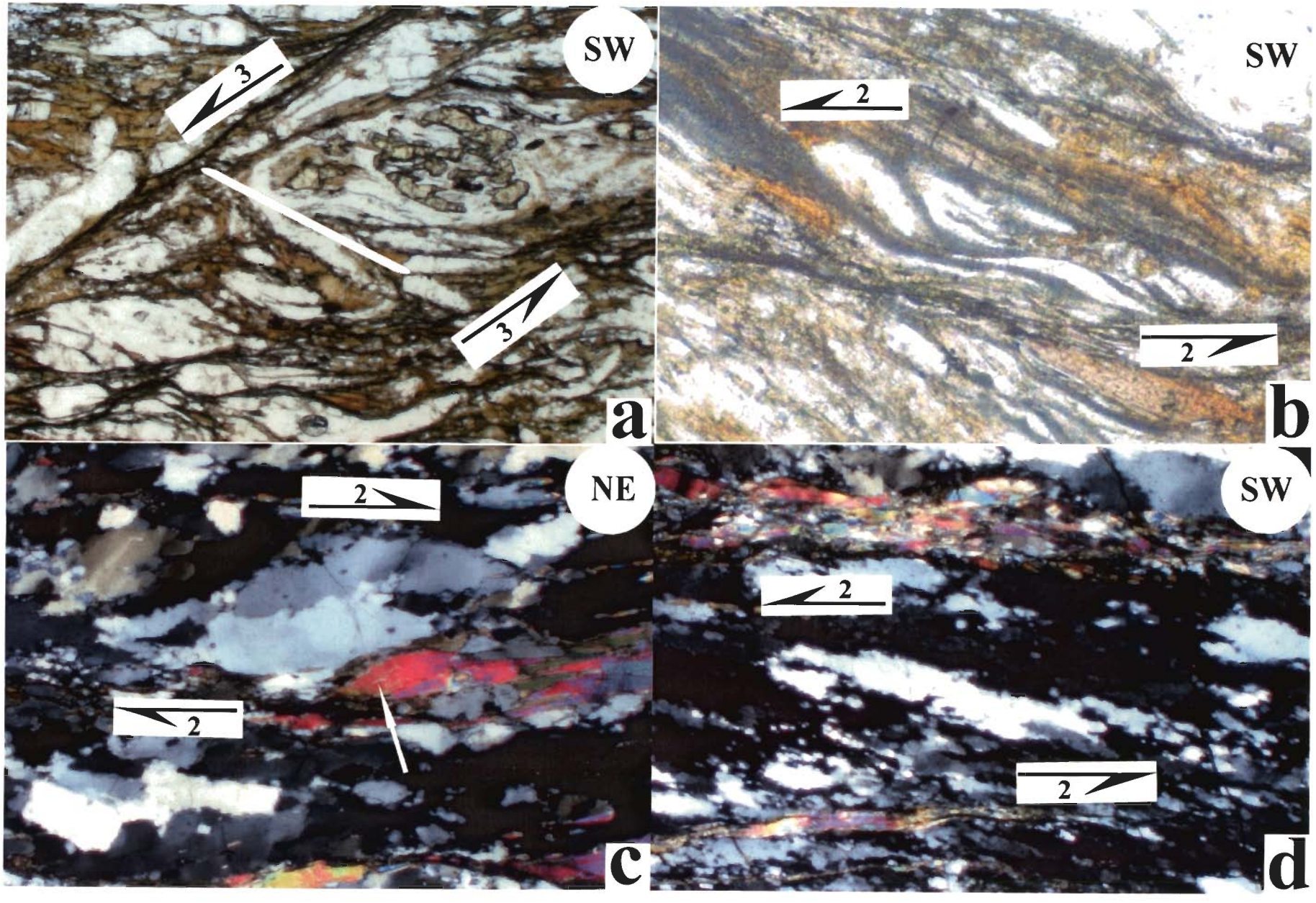

Fig. 2.4

The second dominant deformation event is the top-to-NE sense of ductile shearing ('shearing-2' in figure captions) typical of the Himalayan detachment. This is documented using sigmoid quartz fishes (Figs. 2.2a, 2.4b-c) and intrafolial folds of aggregates of quartz (Figs. 2.3c, 2.4d). Where overturned folding of a quartz vein is not sufficient to deduce the ductile shear sense (Fig. 2.5a), the preferred orientation of the quartz grains (Vernon, 2004) constituting such folds is used (Fig. 2.5b). Intrafolial folds of high-grade minerals are also used as a shear sense indicator (Fig. 2.6a). The axial traces of these folds are usually at low-angle- 13-21^0 to the NE direction of the C-planes of the 'shearing-2' (Figs. 2.5b, 2.6a). Besides, S-fabrics define by preferred orientation of quartz grains (Figs. 2.6b, 2.6c), and mica fishes of different morphological varieties (Figs. 2.3a, 2.6d, 2.7a, -b) are indicative of this sense of shear. The angle between the S- and the C- fabrics is around 30^0. Mica fishes with their long axes parallel to the primary shear planes are not useful in shear sense determination (Fig. 2.7c). Top-to-NE sense of ductile shearing ('shearing-2') is a new observation in the ZSZ.

The less frequent and sometimes obscure is the remnant top-to-SW sense of shearing ('shearing-1' in figure captions). These are deciphered from different morphologies of mineral fishes defined by single- and aggregate of mineral(s) (Figs. 2.2a, -b, 2.3a) and Type-1 microflanking structures (Figs. 2.8a-d). Type-2 microflanking structures indicative of directional growth of minerals are also documented (Fig. 2.9a), which have no implication in regional tectonics. Those types of microflanking structures were, therefore, not considered in modeling the exhumation. Microflanking structures (Mukherjee and Koyi, 2007) have been defined, classified, and their restricted use in

determining ductile shear sense has been discussed in detail in the Chapter-5 in this thesis. Summarily, microflanking structures are flanking structures (Passchier, 2001) in micro-scales. Here nucleated minerals define the 'cross-cutting elements'. Deflected cleavages and grain margins of the host mineral gains around the nucleated minerals define the 'host fabric elements'. Hook-shaped minerals have rarely been observed within the ZSZ (Figs. 2.9b, -c), which indicates reversal of the ductile shear sense initially from top-to-SW into finally top-to-NE sense (Fig. 2.9d, also see Wennberg, 1996 for details). The recrystallized quartz grains associated with different micro-structures (Figs. 2.3d, 2.4c, -d, 2.5b, 2.6b, -c) might be the result of the M_3 phase of metamorphism of Pognante et al. (1990).

Indicators of the three ductile shear senses imply different stages of non-coaxial shearing within the ZSZ. The C-planes for the top-to-SW shearing 'shearing-1') are parallel with those of the top-to-NE shearing ('shearing–2'). The former shearing event is least abundant in the thin-sections. Therefore, 'shearing-1' is interpreted as the earliest deformation episode. Indicators of this shear sense might get destroyed and rarely reactivated into hook shapes by the later 'shearing-2' event. The C-planes for the top-to-NE (down) shearing ('shearing-3') are at angle between 25-53^0 to the primary shear plane of '–2'. 'Shearing-3' is interpreted in this work as the synthetic secondary synthetic shearing (Passchier and Trouw, 2005) related to 'shearing-2'. It is important to note that the 'shearing-1' and the '-3' have previously been reported from field (Patel et al., 1993).

2.2.2. Brittle deformations

Throughout the HHSZ, a consistent top-to-SW sense of brittle shearing is deciphered from asymmetric duplexes defined by stacked-up minerals of low- and high grades (Figs. 2.10a-c). These micro-duplexes are identified by their morphological resemblance with different well established geometries of duplexes from field-scales (e.g. McClay and Insley, 1986 and references therein). To the knowledge of the author, this is the first report of duplexes from micro-scales. Some of the micro-duplexes are typically hat- or trapezium shaped with straight boundaries indicating no migration. No migration of the boundaries of the thrust grains is indicated by their straight margins. It is interesting to note that duplexes with nearly trapezium-shapes have been reported from field and subsequently idealized (Figs. 6.93 & 6.96 of Davis and Reynolds, 1996). The thrust planes bounding the micro-duplexes are traced in thin-sections and are found to be the C-planes for the 'shearing-1' and '–2' events. In other words, the pre-existing ductile primary shear planes acted later as the brittle primary shear planes. Nearly symmetric stacks of minerals (Figs. 2.10d, 2.11b) do not reveal any sense of shear. Similar duplexes from field-scales are diagrammatically represented by Davis and Reynolds (1996). Thrust slices of mineral grains that detached and away from the underthrust counterpart grains are not used for shear sense determination (Fig. 2.11c). Few grains with irregular boundaries even though they have an overall hat shape (Figs. 2.11a, -d) indicate migration of boundaries of adjacent grains (see Figs. 3.32 and -3.33 and their captions- of Passchier and Trouw, 2005). These grains are not taken as indicators of any thrust movement.

Figure Captions.

Fig. 2.5a. Overturned round hinge fold of Q-domain of quartz (shown by 'Q' in the photograph) with limbs of nearly equal thickness, and southwesterly dipping axial plain. Thinner foliation plains, defined by alternate biotite- and quartz-rich layers, are tightly folded with sharp hinges and nearly straight limbs. These are located at both the sides of the folded Q-domain, and are shown by 'm' and 'n' in the photograph. Since the enveloping surface (Ghosh, 1993) of this fold is not defined by straight foliation plains, the fold is probably not of intrafolial type. Therefore, no attempt is made to decipher the shear sense from this fold. Photo in plane polarized light. XZ oriented thin-section from Zanskar Shear Zone. Photo length: 2.0 mm. Thin-section number: P9/M.

Fig. 2.5b. Overturned fold of an aggregate of quartz grains. The sense of shearing deciphered from the fold vergence, and also from the shape preferred orientation of individual recrystallized grains, is ubiquitously top-to-NE ('shearing-2' of caption of Fig. 2.2a). The axial trace of the fold is marked by a white line. The angle between the axial trace to the C-plain of 'shearing-2' is 21^0. Photo in cross polarized light. XZ oriented thin-section from Zanskar Shear Zone. Photo length: 3.0mm. Thin-section number: P9/H.

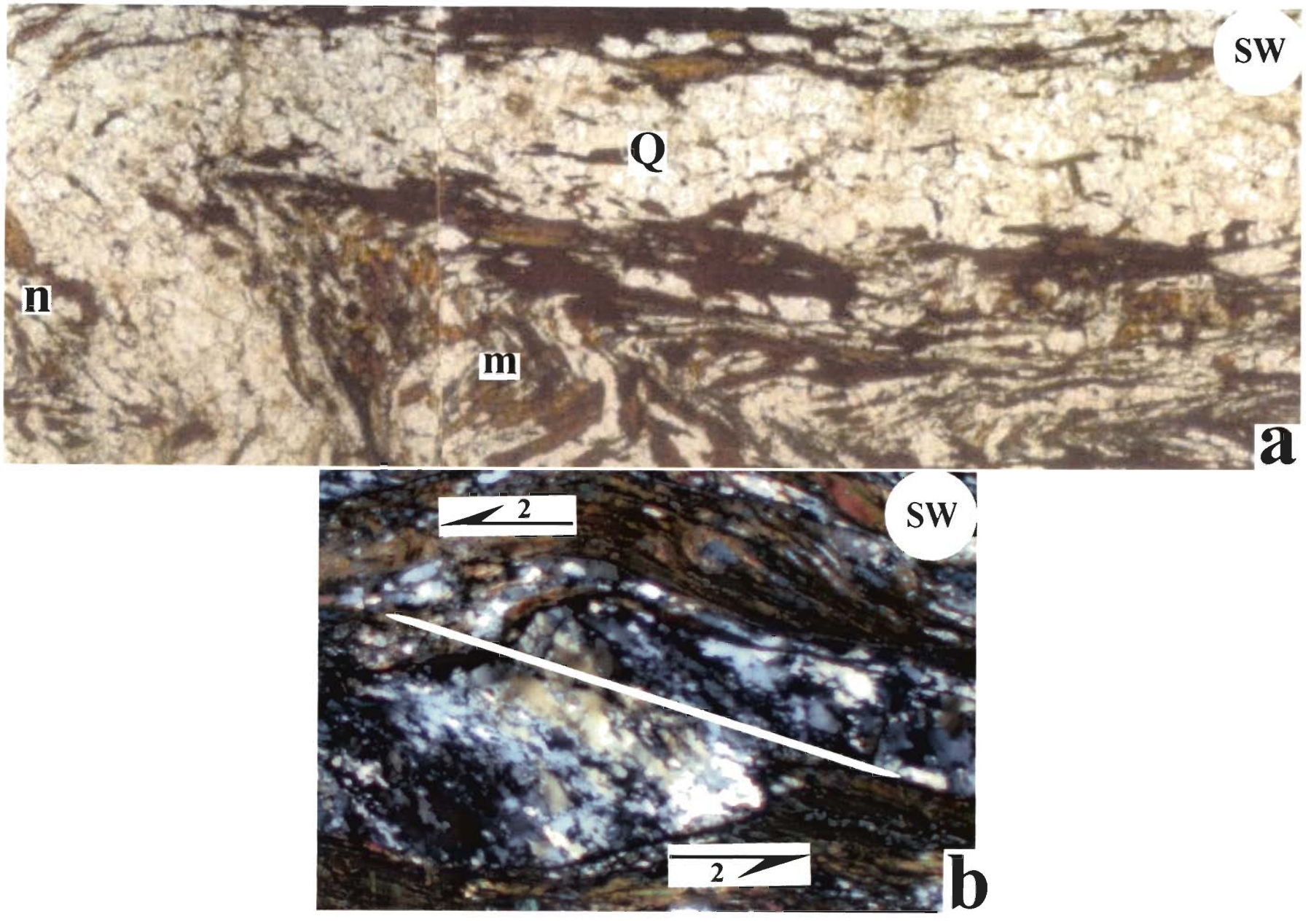

Fig. 2.5

Figure Captions.

Fig. 2.6a. Rootless intrafolial fold of an aggregate of quartz (qz), biotite (bt) and sillimanite (silli) within the gneissose rock giving top-to-NE sense of shear ('shearing-2' of caption of Fig. 2.2a). The axial trace makes an angle of 13^0 with the primary shear plain. Photo in plane polarized light. XZ oriented thin-section from Zanskar Shear Zone. Photo length: 1mm. Thin-section number: P9/S.

Figs. 2.6b & -c. Recrystallized quartz grains showing S-C fabric indicating top-to-NE shearing ('shearing-2' of caption of Fig. 2.2a). The grains defining the C-plains are finer compared to those defining the S-plains. The C-plain is undulatory in Fig. 2.6c, and is thicker than that in Fig. 2.6b. Orientations of the S- and the C- plains are shown by thin white lines. The angles between them are measured as 43^0 and $\sim 44^0$, for Figs. 2.6b and 2.6c, respectively. XZ oriented thin-section from Zanskar Shear Zone. Photos in cross polarized light. Photo length: 5.0mm. Thin-section numbers: P9/J.

Fig. 2.6d. Top-to-NE extensional shearing ('shearing-2' of caption of Fig. 2.2a) indicated by sigmoidal fish defined by a number of muscovite grains. The angle between the S- and the C-plains is measured as 30^0. Photo in cross polarized light. XZ oriented thin-section from Zanskar Shear Zone. Photo length: 5.0mm. Thin-section number: P9/L.

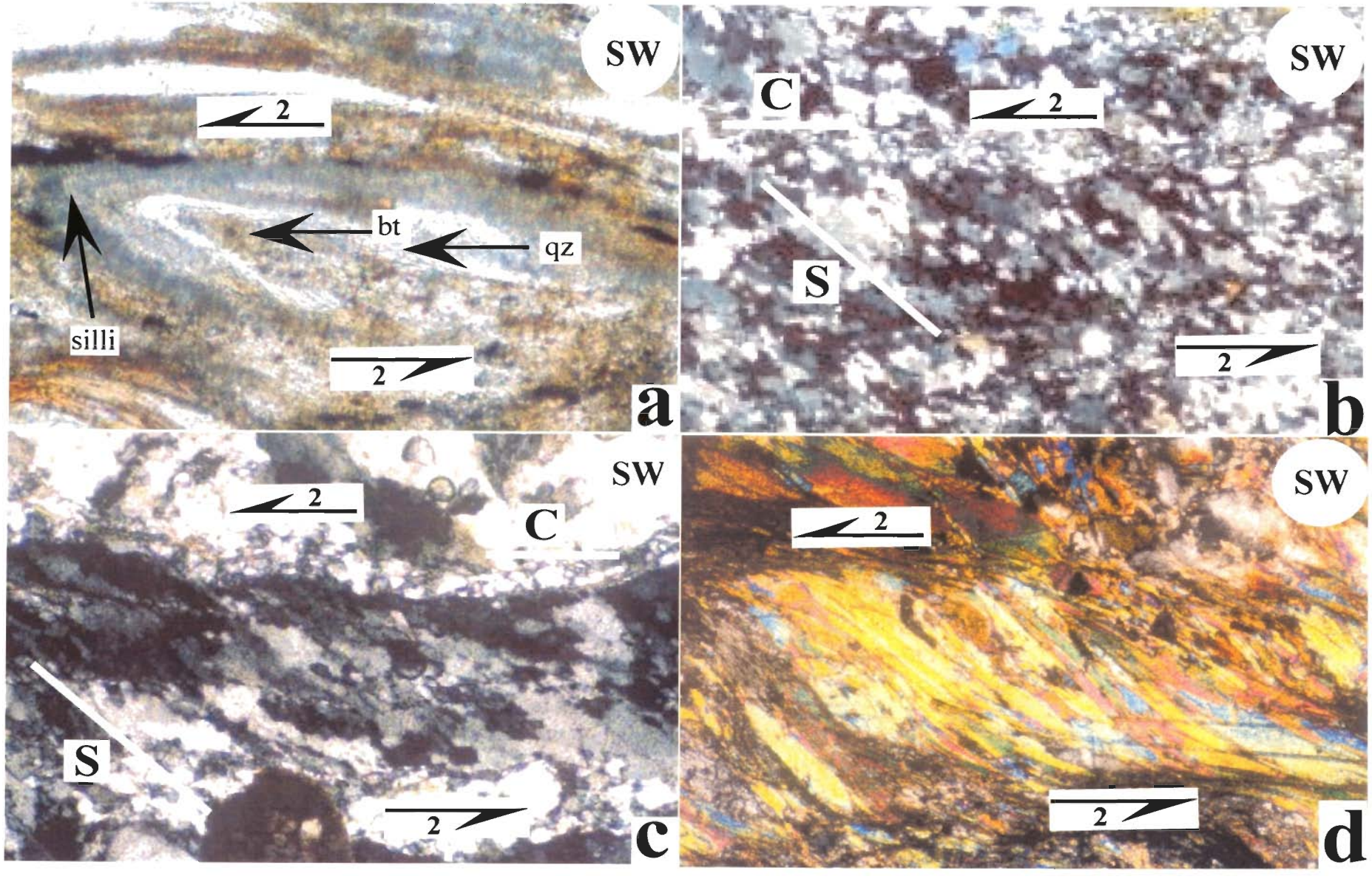

Fig. 2.6

Figure Captions

Fig. 2.7a. A sigmoid muscovite fish giving top-to-NE sense of shear ('shearing-2'of caption of Fig. 2.2a). Extensive dynamic recrystallization at the boundaries of the fish has partly destructed its true shape. Photo in cross polarized light. XZ oriented thin-section from Zanskar Shear Zone. Photo length: 10mm. Thin-section number: P9/P.

Fig. 2.7b. Two parallelogram-shaped muscovite fishes giving top-to-NE sense of shearing ('shearing-2' of caption of Fig. 2.2a). Dynamic recrystallization at the boundaries of the fishes has partly obliterated their accurate parallelogram shapes. Photo in cross polarized light. XZ oriented thin-section from Zanskar Shear Zone. Photo length: 5.0mm. Thin-section number: P9/R.

Fig. 2.7c. A lenticular muscovite fish with mouth (notches) at both the sides. The long axis of this grain is shown by a white line. The main foliation (outside the photograph) is sub-parallel with the long axis of the grain. Therefore, this mineral grain cannot be used to decipher the ductile shear sense..

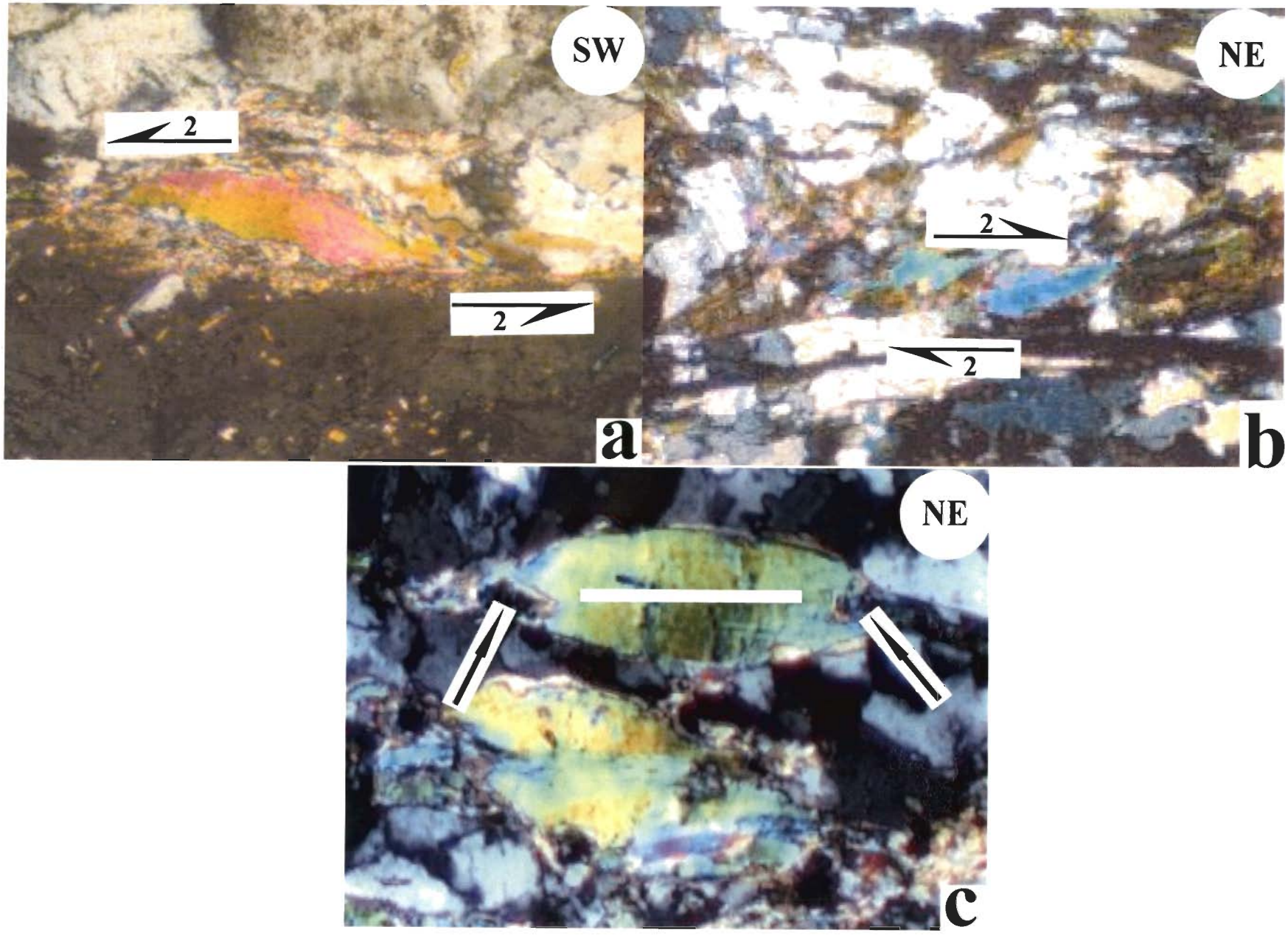

Fig. 2.7

Captions

Fig. 2.8. Microflanking structures.

Fig. 2.8a Type-(i) microflanking structure with biotite mineral as the crosscutting element (CE). The cleavage plains, of the biotite grain hosting the CE, are the host fabric elements (HEs). At the present position of the photograph, the left- and the right margins of the CE show that the HEs are concave-up and convex-up, respectively, and are pointed out by arrows. The parallelogram shape of the CE indicates top-to-SW sense of ductile shearing ('shearing-1' of caption of Fig 2.2a). Photo in plane polarized light. XZ oriented thin-section from Zanskar Shear Zone. Photo length: 0.5mm. Thin-section number: P9/A12.

Fig. 2.8b Type-(i) microflanking structure with muscovite as the crosscutting element. The cleavage plains, of the biotite grain hosting the CE, are the host fabric elements (HEs). At the present position of the photograph, the left margin of the CE shows concave-up HE. The HE, at the right margin of the CE, is not distinct. The parallelogram shape of the CE indicates top-to-SW sense of ductile shearing ('shearing-1' of caption of Fig 2.2a). Photo in plane polarized light. XZ oriented thin-section from Zanskar Shear Zone. Photo length: 0.5mm. Thin-section number: P9/A13.

Fig. 2.8c Type-(i) microflanking structure with muscovite as the crosscutting element (CE). The cleavage plains, of the biotite grain hosting the CE, are the host fabric element (HE). The parallelogram shape of the CE indicates top-to-SW sense of ductile shearing ('shearing-1' of caption of Fig 2.2a). This demonstrates that the cleavage plains of the host grains bounding the CE efficiently act as the ductile shear plains as well. At the present position of the photograph, the left margin of the CE shows that some of the HEs are strongly convex-up (pointed out by an arrow). The right margin of the CE shows straight HEs, and is also pointed out by an arrow. Photo in plane polarized light. XZ oriented thin-section from Zanskar Shear Zone. Photo length: 0.5mm. Thin-section number: P9/A14.

Fig. 2.8d Type-(i) microflanking structure defined by a muscovite grain as the 'cross-cutting element' (CE) and the cleavages of mineral grain hosting the CE as the 'host fabric element' (HE). At the present position of the photograph, the left margin of the CE shows that few of the HEs are concave-up, and is pointed out by an arrow. The parallelogram shape of the CE indicates top-to-SW sense of ductile shearing ('shearing-1' of caption of Fig 2.2a). Photo in plane polarized light. XZ oriented thin-section from Zanskar Shear Zone. Photo length: 0.5mm. Thin-section number: P9/A15.

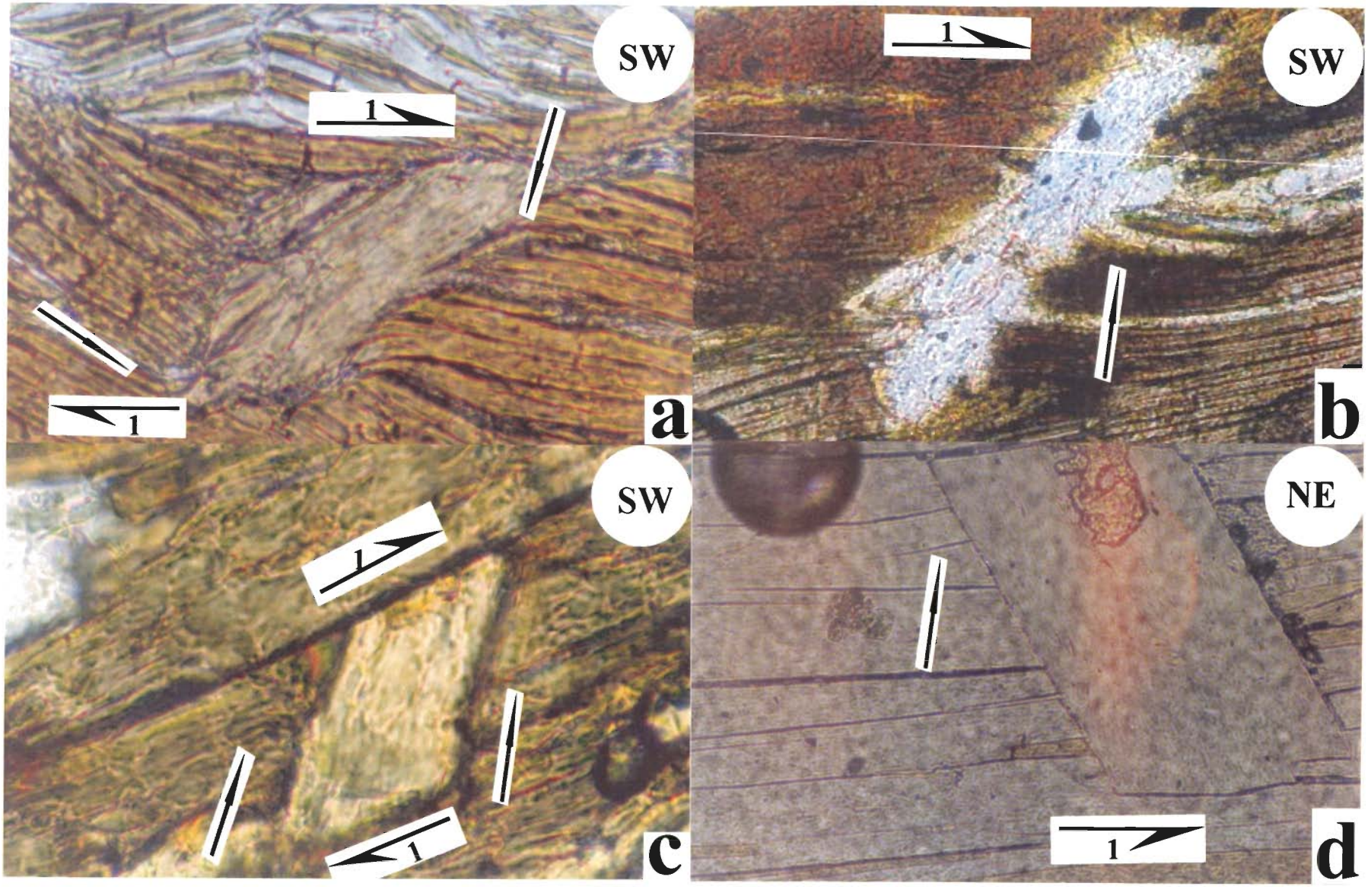

Fig. 2.8

Figure Captions.

Fig. 2.9a. Type-(ii) microflanking structure defined by a biotite grain as the 'crosscutting element' (CE) and the foliation defined by quartzofeldspathic layer (pointed out by arrow '1' at the both sides of the CE). At the present orientation of the CE, curvature of the foliation plains defined by micas around it are concave-up at the upper right and the left sides, and convex-up at the bottom right and the left sides. These curvatures of foliations are pointed out by arrows. Inferred growth directions of the CE grain are shown by white arrows, which are perpendicular to the main foliation/ C-plain of 'shearing-1'. Photo in cross polarized light. XZ oriented thin-section from Zanskar Shear Zone. Photo length: 5mm. Thin-section number: P9/T.

Fig. 2.9b. Dense intergrowth of sillimanite and biotite. Sillimanite occurs as fibrous and hazy aggregate, but the hook shape is still decipherable. The prominent curvatures of the sillimanite, which define the hook, are pointed out by arrows. The hook-shaped fabric is typically generated by reversal of the ductile shear sense and is illustrated in Fig. 2.9d and in its caption. Photo in plane polarized light. XZ oriented thin-section from Zanskar Shear Zone. Photo length: 1.0mm. Thin-section number: P9/N.

Fig. 2.9c. Line drawing of the aggregate of sillimanite grains of Fig. 2.9b. The prominent curvatures defining the hook geometry are pointed out by arrows.

Fig. 2.9d. The fabric produced by the reversal of ductile shear sense is displayed: (I) An S-fabric produced by the top-to-left sense of shearing. The shearing is represented by hollow half arrows. (II) Reactivation of this fabric by top-to-right sense of shearing. The shearing is represented by thick half arrows. (III) Continuation of top-to-right sense of shearing orients the fabric at low-angle with the primary shear plain, and results in the hook shape. (I) to (III) are reproduced from Wennberg (1996). The fabric in (III) is comparable with what has been documented for the natural example of sillimanite in Fig. 2.9b.

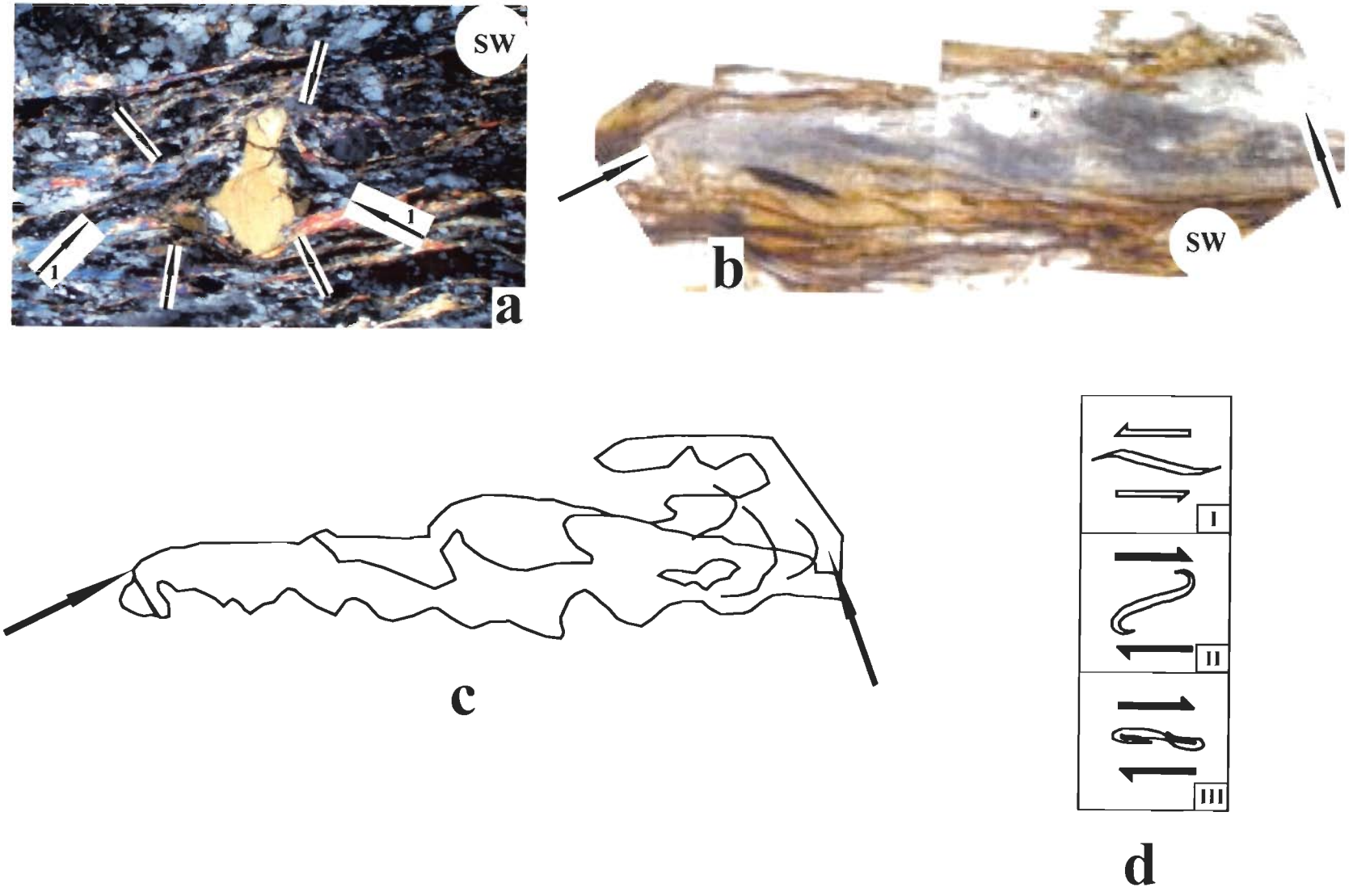

Fig. 2.9

Figure Captions

Fig. 2.10a A muscovite grain is thrust over quartzofeldspathic grains, and gives top-to-SW brittle sense of shear in grain-scale. Note that the thrust-up muscovite grain is trapezium- or hat shaped with dynamic recrystallization at certain parts of its boundary. Just above the muscovite hat, and below the white lines demarcated in the photograph, the quartzofeldspathic minerals also take part in thrust movement as revealed by concordance between their longest grain boundaries and the muscovite grain. Above the white lines, such concordance is not observed. The thrust plain delineating the lower boundary of the muscovite grain is marked by a white arrow. This plain is traced in the thin-section and was found to be the same as the ductile shear plain for the 'shearing-1' and '–2' events. Photo in cross polarized light. XZ oriented thin-section from Zanskar Shear Zone. Photo length: 5mm. Thin-section number: P9/U.

Fig. 2.10b A muscovite grain 'p' is thrust over quartzofeldspathic grains. A larger muscovite grain, 'q', which is hat shaped and with extensive dynamic recrystallization at the grain boundary, is thrust over the grain 'p'. Both these muscovite grains give top-to-SW sense of brittle movement. Such inter-thrusting pattern of the grains match with that for thrust slices reported from field-scale. Photo in cross polarized light. XZ oriented thin-section from Zanskar Shear Zone. Photo length: 5mm. Thin-section number: P9/V.

Fig. 2.10c A number of stacked muscovite grains are demarcated by broken white lines. These are the 'thrust slices', which demonstrate top-to-SW sense of brittle shearing. The thrust plain at the boundary of the muscovite, pointed out by a white arrow, is traced in the thin-section and is found to be the same as the ductile shear plain for the 'shearing-1' and '–2' events of the caption of Fig. 2.2a. Photo in cross polarized light. XZ oriented thin-section from Zanskar Shear Zone. Photo length: 2.5mm. Thin-section number: P9/W.

Fig. 2.10d Duplex structure defined by four staurolite grains (numbered in the photograph) stacked one above another, and sillimanite (grain '5') wraps the staurolite grain '4' at the top. Due to the overall symmetric shape of this antiformal stack, the brittle sense of shear cannot be deciphered. A part of the sillimanite grain projects like a long horn rendering question on its textural/micro-structural significance. In the photograph, a question mark is placed where the horn originates. Photo in cross polarized light. XZ oriented thin-section from Zanskar Shear Zone. Photo length: 2.5mm. Thin-section number: P9/X.

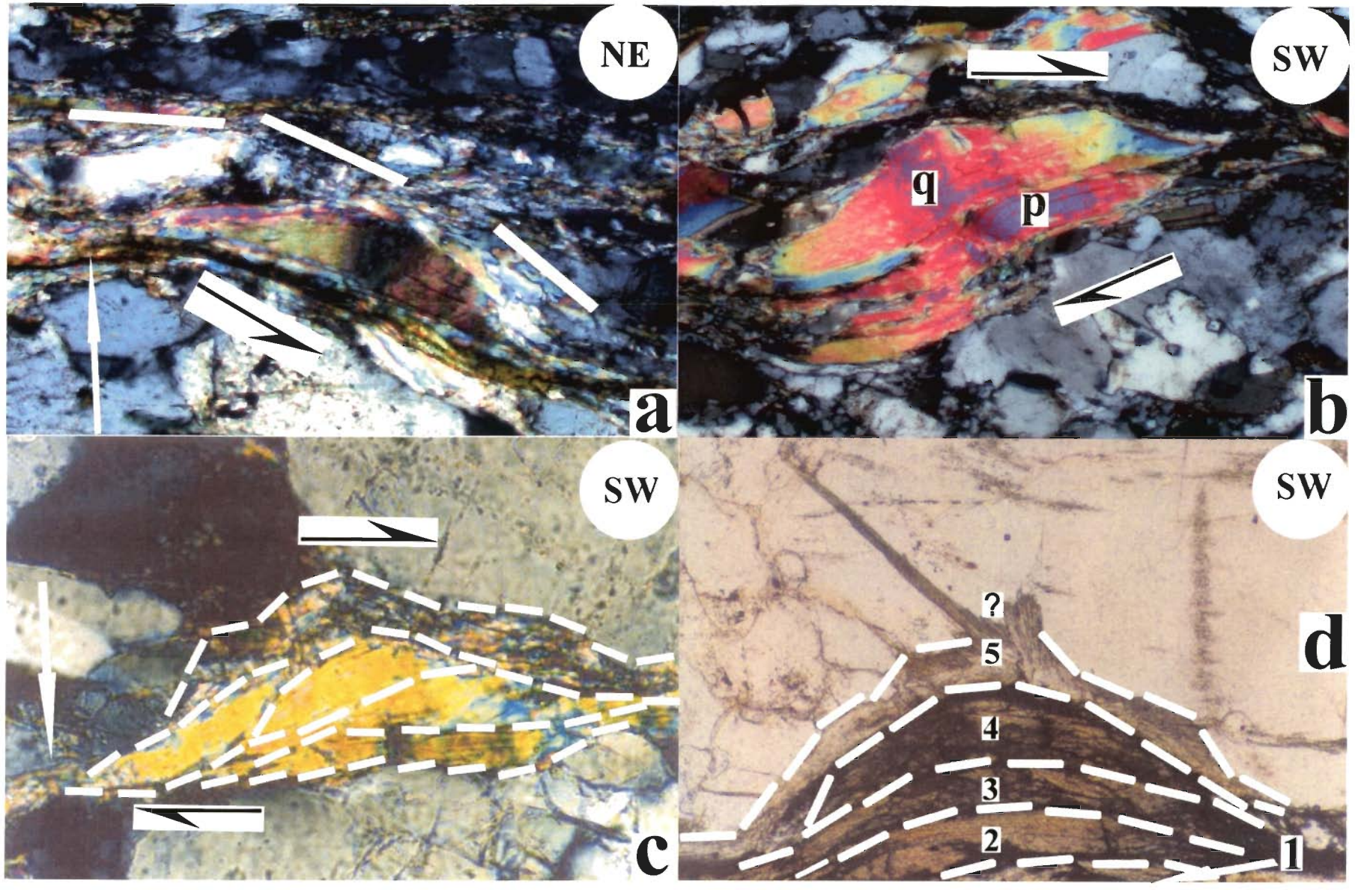

Fig. 2.10

Figure Captions.

Fig. 2.11a. A number of biotite grains stacked one above another and resembles a duplex. However, it cannot be called a duplex unambiguously since migration of adjacent grain boundaries of quartz, pointed out by arrows, might also give rise to the hat shape of few biotite grains. In the present study, such ambiguous grains were exempted in brittle shear sense determination. Photo in plane polarized light. XZ oriented thin-section from Zanskar Shear Zone. Photo length: 5.0mm. Thin-section number: P9/Y.

Fig. 2.11b. A staurolite grain, marked by 'p', is possibly stacked over another staurolite grain (marked by 'q'). The boundary between grains 'p' and 'q' is marked by a broken white line. Since the overall geometry of this suspected stacking does not match well with any of the accepted morphologies of duplexes, the aggregate in this case is not called as a duplex and no attempt has been made to decipher the brittle shear sense. Photo in plane polarized light. XZ oriented thin-section from Zanskar Shear Zone. Photo length: 5.0mm. Thin-section number: P9/Z.

Fig. 2.11c. A muscovite grain is surrounded by quartz grains. The muscovite looks like a thrust slice. The broken line demarcating a part of its boundary is most probably the thrust plane. The counterpart underthrust grain is not seen in the photograph. The grain might be overthrust and transported to a longer distance and crossed the underthrust grain. No attempt is made to find out the brittle sense of shearing from this muscovite grain. Photo in plane polarized light. XZ oriented thin-section from Zanskar Shear Zone. Photo length: 5.0mm. Thin-section number: P9/A1.

Fig. 2.11d. A number of biotite grains stacked one above another and resembles a duplex. However, it cannot be called a duplex unambiguously since migration of adjacent grain boundaries of quartz, pointed out by arrows, might also give rise to the hat shape of few biotite grains. In the present study, such ambiguous grains were exempted in brittle shear sense determination. Photo in cross polarized light. XZ oriented thin-section from Zanskar Shear Zone. Photo length: 5.0mm. Thin-section number: P9/Y.

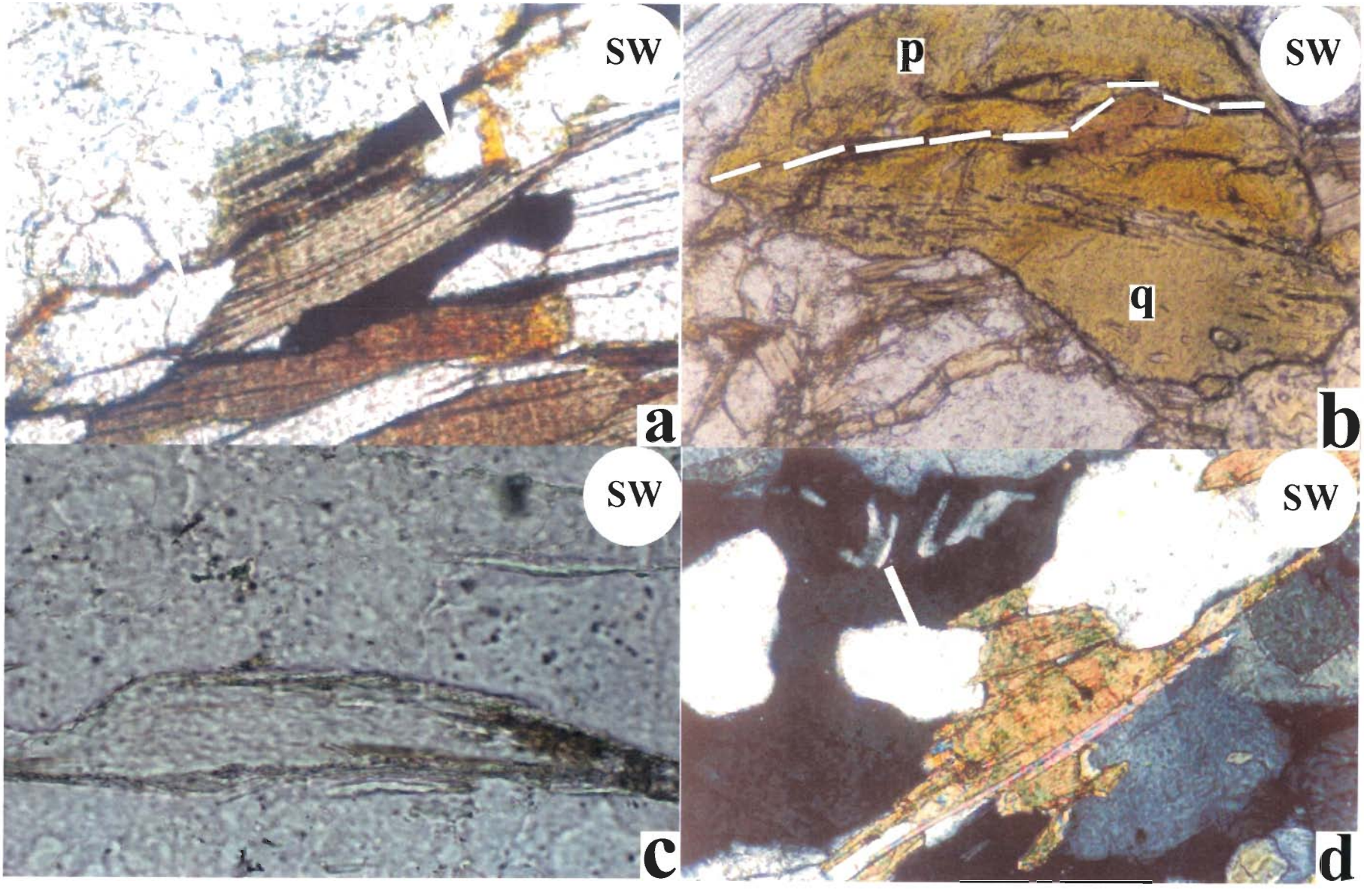

Fig. 2.11

The V-pull apart micro-structures of minerals (Hipperitt, 1993) indicate top-to-SW sense of brittle shearing (Figs. 2.12a, -c, -d). Both more competent- (Fig. 2.12a) and less competent minerals (Fig. 2.12c) undergo V-pull apart. The gap created by the brittle separation of the clast into the 'V' is filled in by passive folding of the foliation planes. Geometric analyses of these folds reveal that they belong to the Class-3 geometry (Mukherjee and Chakraborty, 2007).

Brittle extension, parallel to the main foliation (the C-planes of 'shearing-1' and '-2'), is deciphered by series of parallel pull aparts (Hipperitt 1993) of originally single mineral grains (Fig 2.12d).

Northeasterly dipping steep brittle normal fault planes are deciphered by sharp slip of the individual minerals (Figs. 2.13a, -b), and sometimes by the slip of main foliation (Fig. 2.13c), across them. In few cases, however, a lack of disrupted markers hinders recognition of the sense of slip along the brittle faults (Fig. 2.13c). In the present study, the relative time relation between the top-to-SW brittle shearing and the brittle normal faulting could not be established.

At higher magnifications, boudins of different varieties e.g. pinch and swell structures (Fig. 2.14a), lenticular boudins (Fig. 2.14b, -c) and foliation boudins (Fig. 2.14d) are documented indicating intense penetrative deformation (Ghosh, 1993).

Figure Captions.

Fig. 12a. A V-pull apart of garnet with chlorite infilled and passive folded at the V-opening, pointed out by an arrow. Sense of brittle shear is top-to-SW. Photo in plane polarized light. XZ oriented thin-section from Zanskar Shear Zone. Photo length: 5mm. Thin-section number: P9/A4.

Fig. 12b. A V-pull apart of alkali feldspar showing top-to-SW sense of brittle shearing. Photo in cross polarized light. XZ oriented thin-section from Zanskar Shear Zone. Photo length: 10mm. Thin-section number: P9/A5.

Fig. 12c. A lenticular muscovite fish, which has been V-pull apart, and demonstrates top-to-SW sense of brittle shearing. Photo in cross polarized light. XZ oriented thin-section from Zanskar Shear Zone. Photo length: 10mm. Thin-section number: P9/A7.

Fig. 12d. A set of parallel pull aparts of alkali feldspar grain with extension direction (shown by white arrows) nearly parallel to the main foliation/ C-plain of 'shearing-1'. The main foliation is not within the photograph. Photo in cross polarized light. XZ oriented thin-section from Zanskar Shear Zone. Photo length: 2.5mm. Thin-section number: P9/A6.

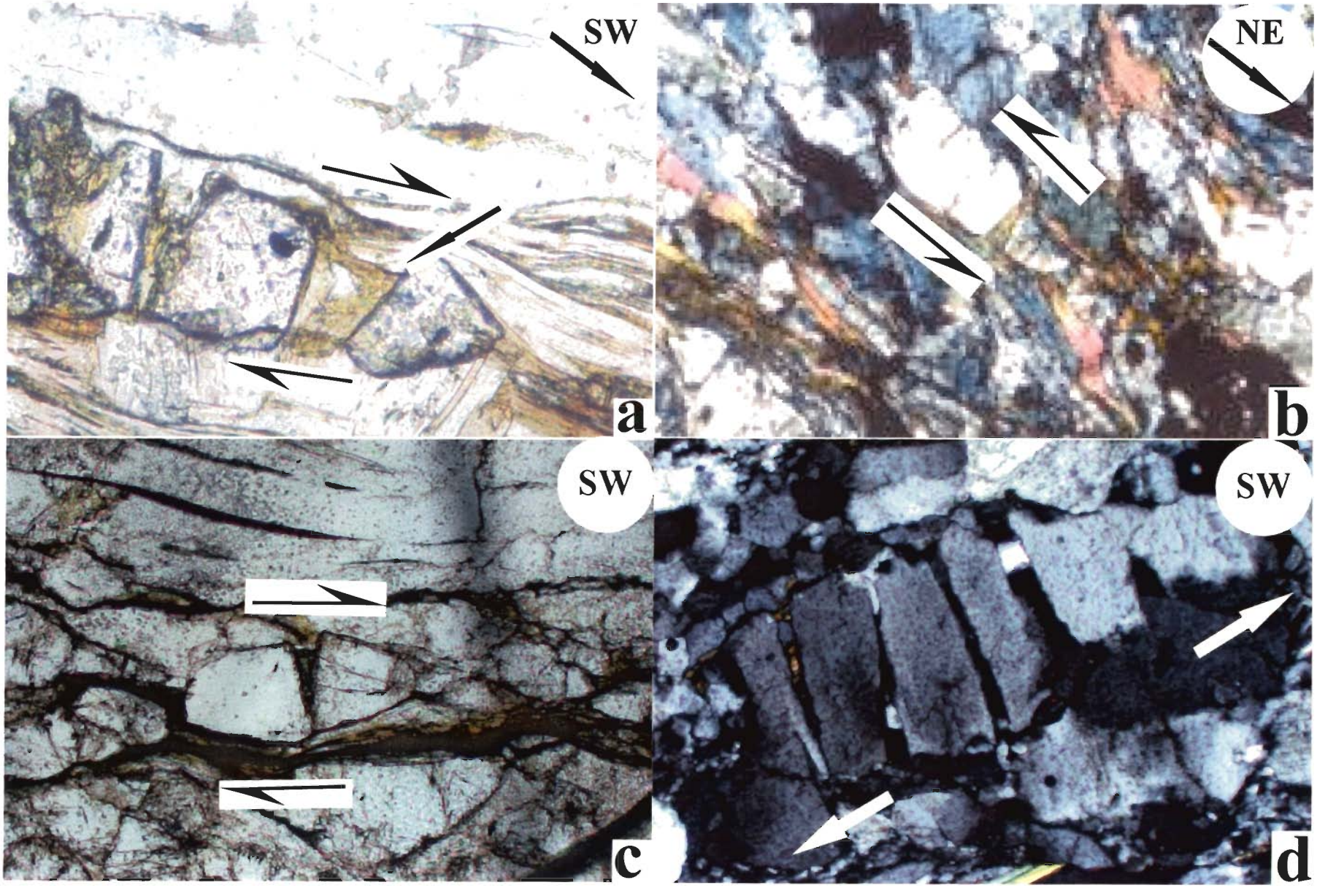

Fig. 2.12

Figure Captions.

Fig. 2.13a. Sharp brittle normal fault, northeasterly steeply dipping and at 70^0 to the main foliation. Shows prominent slip and weak drag of the biotite aggregate across it. The biotite aggregate is pointed out by arrow at one of the sides of the fault. Photo in cross polarized light. XZ oriented thin-sections from Zanskar Shear Zone. Photo lengths: 5mm. Thin-section numbers: P9/A2.

Fig. 2.13b. Sharp brittle normal fault cutting the main foliation at steep angle at $\sim 90^0$. Prominent slip but no drag of a quartz grain across the fault is noted. The quartz grain is pointed out by an arrow at one of the sides of the fault. Photo in cross polarized light. XZ oriented thin-sections from Zanskar Shear Zone. Photo length: 5mm. Thin-section number: P9/A2.

Fig. 2.13c. A sharp brittle fault northeasterly steeply dipping to 70^0 with the main foliation. Abrupt termination of grains across this fault is noted but no disrupted marker could be established. This makes it intangible whether the fault is normal or reverse in this particular case. Photo in cross polarized light. XZ oriented thin-section from Zanskar Shear Zone. Photo length: 5mm. Thin-section number: P9/A3.

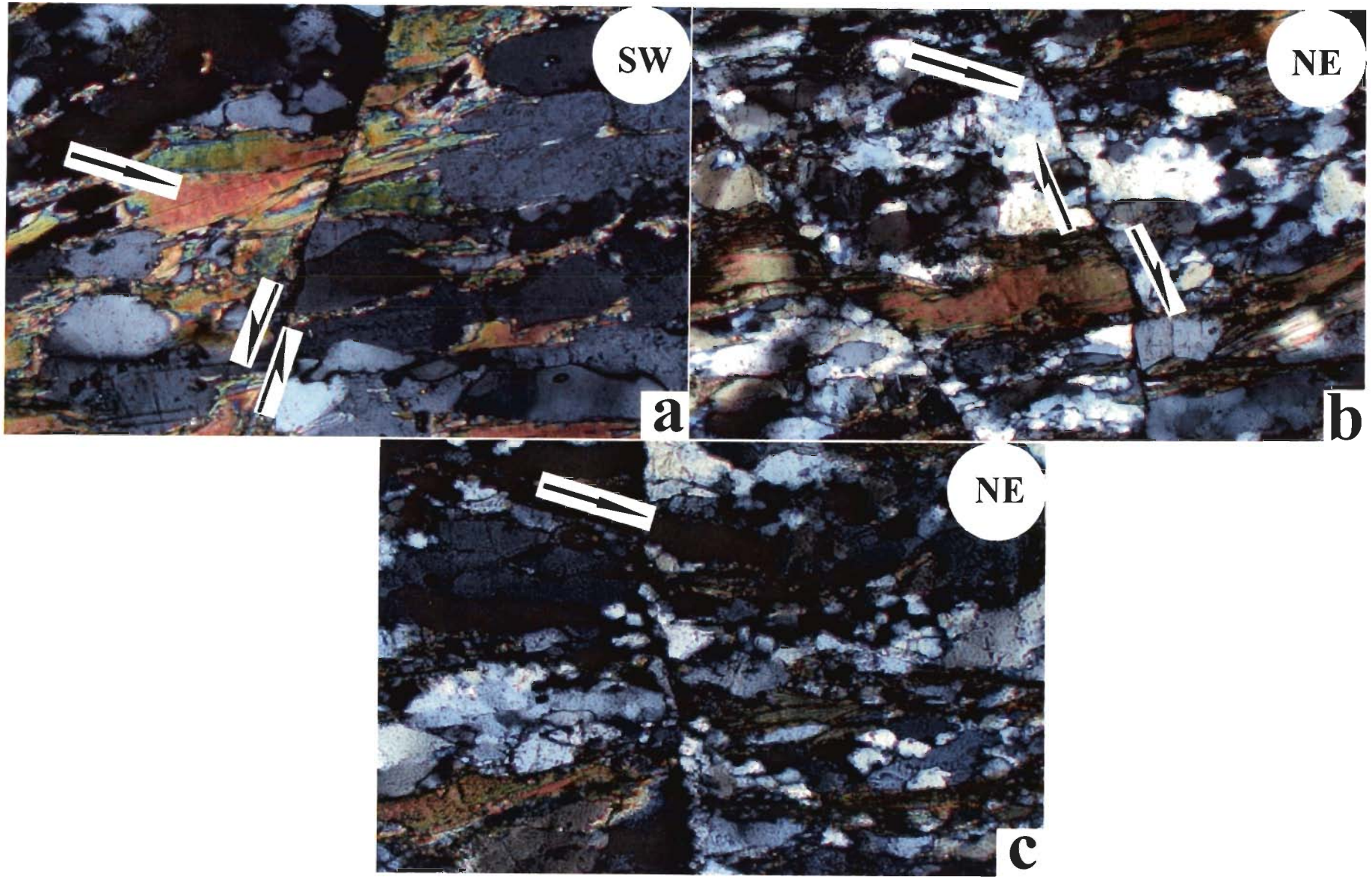

Fig. 2.13

Individual minerals (Figs. 2.14a-c) and also mineral aggregates (fig. 2.14d) of the main foliation are boudinaged. Some of these boudins are not surrounded by any foliation planes, hence scar folds are not defined. Individual clasts may be connected (Fig. 2.14b) or they can separated into decipherable distance (Fig. 2.14c). These indicate differential local brittle-ductile extension parallel to the main foliation.

2.3. STRUCTURAL COMPILATION

The summary of the present micro-structural observations from the ZSZ, along with the structures reported from the reminder of the HHSZ in the Zanskar section by Jain and Anand (1988) and Patel et al. (1993), are summarized in Fig. 2.15. Different phases of ductile deformations, in this structural compilation, are utilized to propose a model for the exhumation of the HHSZ in the Zanskar section as follows.

2.4. FORMULATION OF THE MODEL

The following constraints are chosen to propose the model for exhumation during the ductile deformation phases of the HHSZ, Zanskar section.

(I) Inverted metamorphism of the rocks of the HHSZ.

(II) Top-to-SW sense of ductile shearing within the HHSZ started from Neo-Himalayan Period (25 Ma).

(III) Within the ZSZ, top-to-NE sense of ductile shearing continued ~18 Ma ago with the ongoing top-to-SW sense of ductile shearing of the MCT.

(IV) The ZSZ is thinner than the reminded of the HHSZ. The thickness of the ZSZ varies along its length.

Figure Captions.

Fig. 2.14 Different geometric types of boudins. The direction of extension is shown with arrows, which are parallel to the main foliation/ C-plain of 'shearing-1'. Note that the main foliation is not within the field of view for Fig. 2.14a and -b.

Fig. 2.14a Pinch and swell structure of alkali feldspar, indicating that the extensional force has not been strong enough to separate the single clast into two completely separated pieces. Photo in cross polarized light. XZ oriented thin-section from Zanskar Shear Zone. Photo length: 0.5mm. Thin-section number: P9/A8.

Fig. 2.14b Lenticular boudin of alkali feldspar with individual clasts having point contact. Note the absence of any passive folds in between the two clasts. This is due to the unavailability of any foliation surrounding the boudin. The extensional force has been strong enough to break the single clast and separate them. Photo in plane polarized light. XZ oriented thin-section from Zanskar Shear Zone. Photo length: 0.5mm. Thin-section number: P9/A9.

Fig. 2.14c Lenticular boudin of alkali feldspar with tips of individual clasts more widely separated than that of Fig. 2.14b. Note the absence of any passive folds is due to the unavailability of any foliation surrounding the boudin. Photo in cross polarized light. XZ oriented thin-section from Zanskar Shear Zone. Photo length: 0.5mm. Thin-section number: P9/A10.

Fig. 2.14d Lenticular foliation boudin of an aggregate of muscovites. The aggregate at the right side is much bigger in size than that at the left side. A thin white line demarcates the main foliation/ C-plain of 'shearing-1'. Photo in cross polarized light. XZ oriented thin-section from Zanskar Shear Zone. Photo length: 2.5mm. Thin-section number: P9/A11.

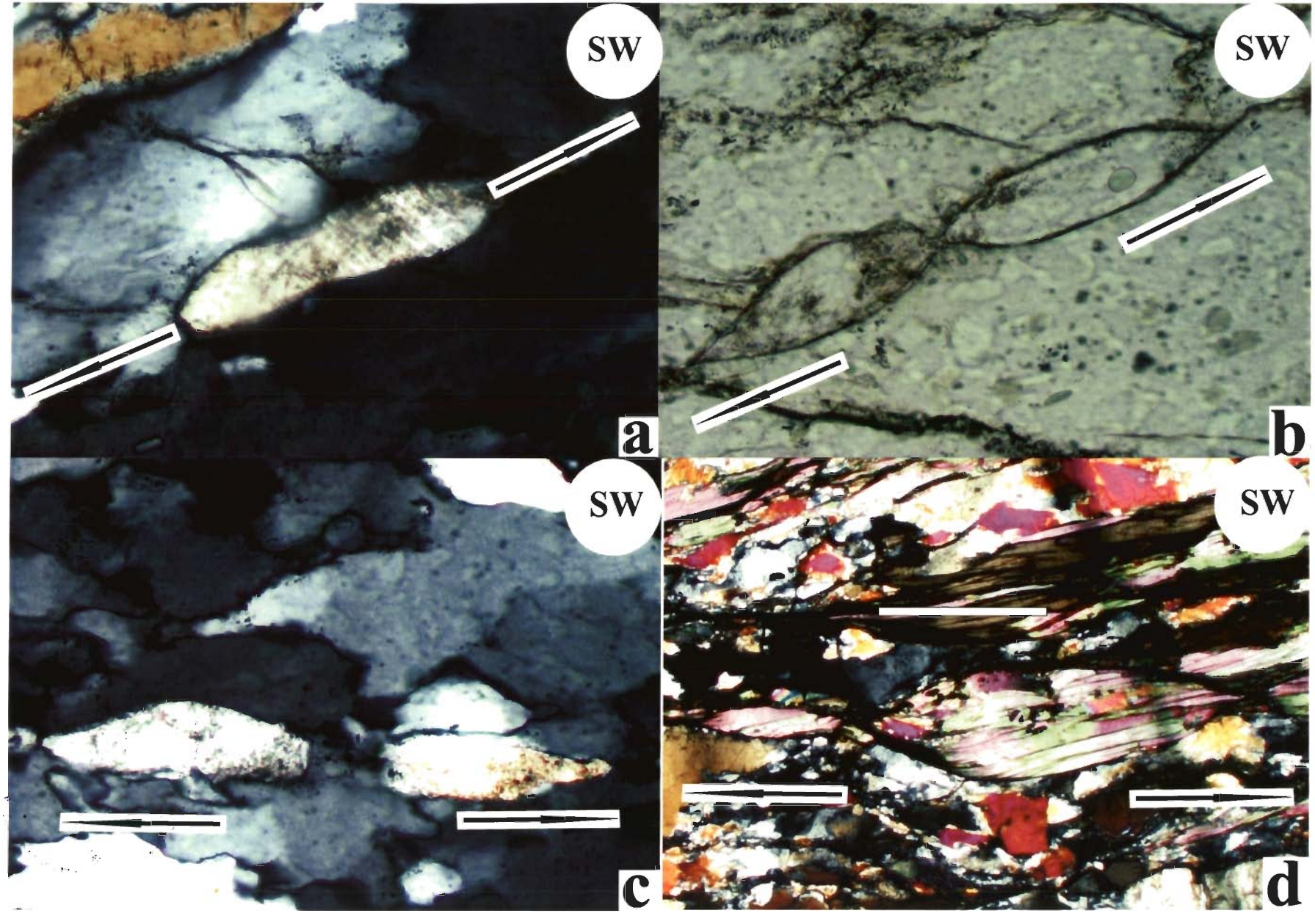

Fig. 2.14

Figure Captions.

Fig. 2.15 The dominant structures within the HHSZ, Zanskar section, observed in the NE-SW cross-section, are summarized from the present micro-structural studies, and the previous work- mainly from Jain and Anand (1988). The HHSZ is bounded by northeasterly dipping Main Central Thrust (MCT) and the Lesser Himalaya (LH) at the south, and the top of the Zanskar Shear Zone (ZSZ) and the beginning of the Tethyan Sedimentary Zone (TSZ) at the north. The half arrows, marked by '1', imply top-to-SW compressional ductile shearing. The half arrows, marked by '2' represent top-to-NE extensional ductile shearing. The half arrows, marked by '3', denotes steeper top-to-NE (down) extensional ductile shearing. Half arrows 1, -2 and -3 correspond to the 'shearing-1', '-2' and '–3' events, respectively. Different shear sense indicators have been used to decipher these shear senses, but only the S-C fabrics are used in this sketch to represent them. The number '(i)' represents a hook-shaped fabric, within the ZSZ, produced due to superposition of shearing-2 on the preexisting S-fabric of 'shearing-1'. The half arrows, marked by $1'$, imply top-to-SW sense of brittle shearing (duplex movement). The half arrows, marked by $2'$, imply northeasterly steeply dipping brittle normal fault. The number $3'$ imply boudinaging. Boudins of different types (lenticular-, pinch and swell and foliation varieties) are observed within the ZSZ, and are represented by the lenticular variety in the sketch. The number $4'$ imply parallel pull apart. $3'$ and $4'$ imply brittle-ductile- and brittle extension, respectively. Both these extensions are parallel to the main foliation and are shown by arrows. Microflanking structures are not shown in this cross-section. 'Shearing-2', and possibly also 'shearing-3' and $2'$, are exclusively confined within the ZSZ. The Diagram is neither to scale nor angle.

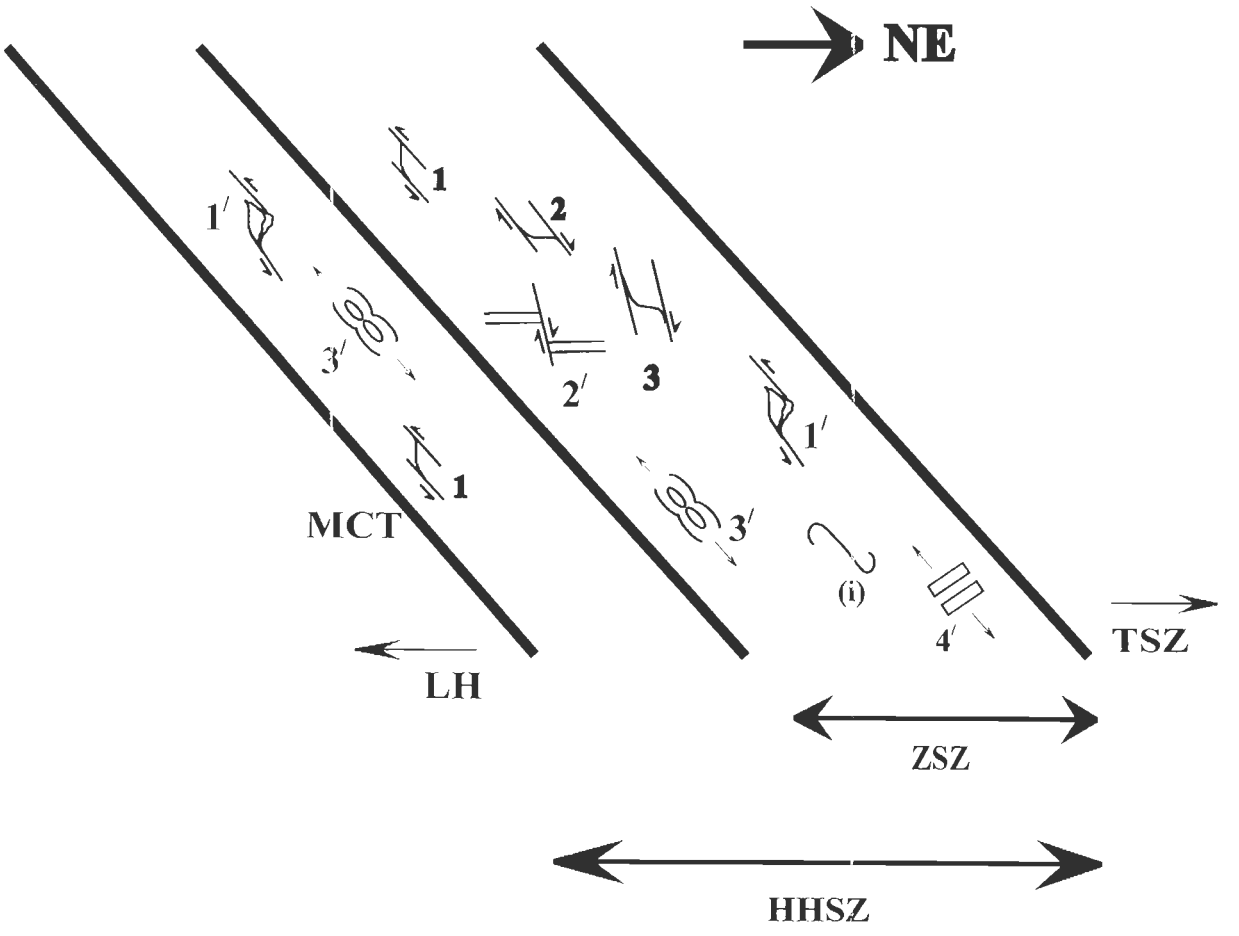

Fig. 2.15

(V) At least during a part its phase of exhumation, the HHSZ oozed up like a fluid.

2.5. EXISTING MODELS

2.5.1. Summary

A number of models of exhumation have been proposed for the HHSZ in the Zanskar- and also for the other sections of the Himalaya. These models have been categorized as (i) thermal models, (ii) coupled thermo-mechanical models, (iii) post-metamorphic deformation models, and (iv) syn-metamorphic deformation models (Yin, 2006). The drawbacks of these models are summarized by Hodges (2000). Two important models, relevant to the present work, are discussed below.

2.5.2. The ductile shear model

The 'ductile shear model' (Jain and Manickavasagam, 1993) explains inverted metamorphism within the Zanskar section of the HHSZ by considering consistent top-to-SW sense of non-coaxial/simple shearing, or Couette flow, along numerous discrete shear planes, giving rise to its exhumation. The metamorphic isograds became overturned folded in the regional scale (Fig. 2.16) giving rise to inverted metamorphism. Along with the P-T data, millimeter- to decimeter scale displacement along the C-planes has been calculated to exhume cumulatively the rocks of the HHSZ from a depth of at least 30-35 km. Further works (Manickavasagam et al 1999; Jain et al 1999, Jain et al 2002) from other sections of the HHSZ have provided structural- and thermo-barometric data that support this model. Besides, this model has also been fitted with other shear zones in the Himalaya with similar structural- and P-T constraints, e.g. from part of the Garhwal

nappe (Tripathi and Gairola, 1999). The main shortcoming of this model is that it cannot explain the top-to-NE sense of ductile shearing within the ZSZ (constraint III of Section-4.1).

2.5.3. The channel flow model

During 'channel flow'/'plane Poiseuille flow' (curve 2 of Fig. 2.20), an incompressible Newtonian viscous fluid undergoes laminar flow through infinitely long parallel horizontal static channel walls, due to a pressure gradient (equation 6 in Appendix) giving rise to a parabolic velocity profile (Pai, 1956). The vertex of this profile is equidistant from the channel walls. A line passing through the vertex and parallel to the walls divide the channel into two zones of equal thickness with opposite senses of ductile shearing. The thickness of these zones remain constant whatever the value of the pressure gradient and the viscosity of the fluid. The velocity increases across the channel from zero at one wall, attains the maximum value at the middle of the channel, and drops symmetrically to zero at another wall. Shearing at any instant is zero on the line equidistant from the walls, and increases symmetrically towards the walls.

Following its less stringent meaning, the channel flow model has been used for exhumation of the HHSZ through its wedge-shaped geometry, in the Bhutan Himalaya (Grujic et al., 1996; Grujic et al., 2002) (Fig. 2.17), implicitly for the HHSZ in the Zanskar

Figure Caption.

Fig. 2.16. Distributed 'ductile shear model' of exhumation of the HHSZ showing northeasterly/northerly dipping S-plains and the isograds. Possible superposed effects of post-metamorphic overturned and/or recumbent folding (A), and thrusting like the MCT (B) and zones of ductile high strains (C) on isograds, causing inverted metamorphism are shown. Double thick arrows, single arrows and double open arrow represent early ductile compressional shearing, discrete thrusts and late extensional ductile shearing, respectively. Symbols- LH: Late Proterozoic sedimentary sequence of the Kishtwar Window (KW); TSZ: Tethyan Sedimentary Zone; CC: continental crust of the Indian plate; M: upper mantle; T: Thatri; K: Kishtwar; A: Atholi; UL: Umasi La; P: Padam. Metamorphic isograd boundaries are represented by dash-dot lines. Reproduced from Jain et. al. (2002), and Jain and Manickavasagam (1993).

Fig. 2.17. Channel flow model for exhumation/extrusion of the HHSZ through its wedge-shaped geometry, in Bhutan Himalaya. Note that the parabolic velocity profile of extrusion of partially molten HHSZ crust gives rise to megascopic telescoping of the metamorphic isograds. Symbols- MCT: Main Central Thrust; STDZ: South Tibetan Detachment Zone (a continuation of the Zanskar Shear Zone). Subduction of the Indian shield below the Tibetan plate is shown by a thick arrow. Reproduced from Grujic et al. (1996).

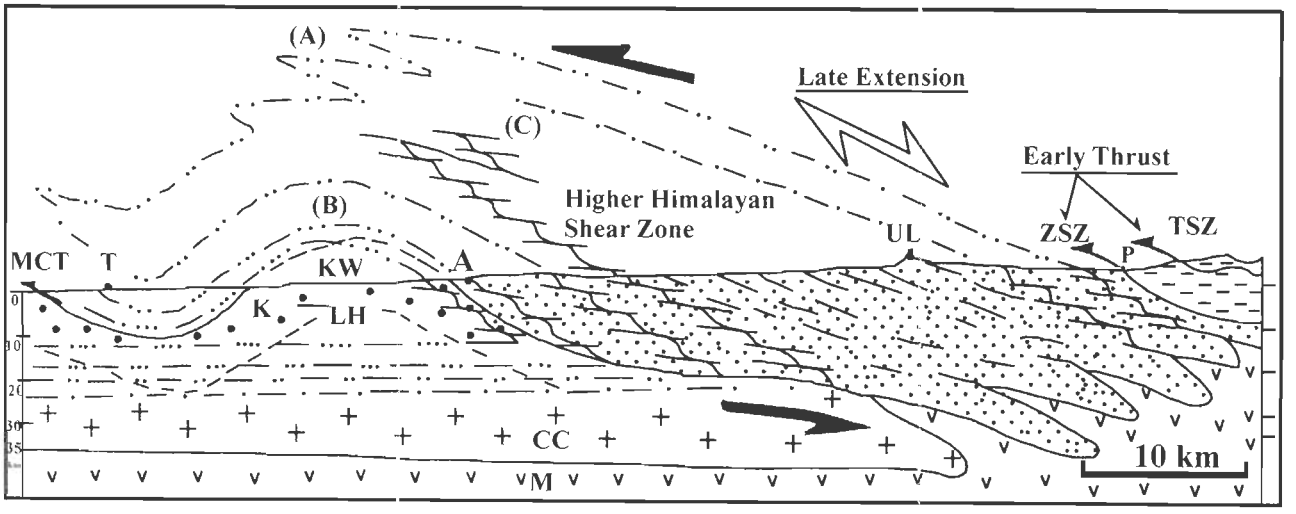

Fig. 2.16

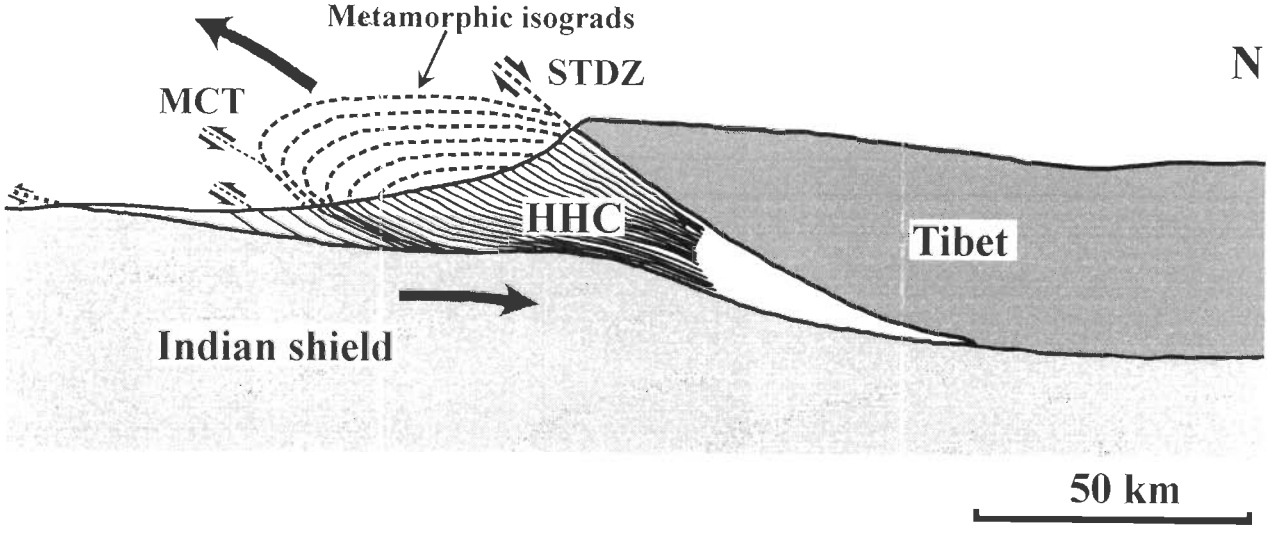

Fig. 2.17

section (Stephenson et al., 2001), and subsequently for the HHSZ in all the sections of the Himalaya (Beaumont et al., 2001; Jamieson et al., 2002; Beaumont et al., 2004; Jamieson et al., 2004). However, the drawbacks of this model are that it cannot take into account the ubiquitous top-to-SW sense of shearing throughout the HHSZ including the ZSZ, and the variable thickness of the thin ZSZ (constraints (III) and (IV), respectively, of Section 2.4).

2.6. THE PROPOSED COMBINED MODEL

To satisfy all the constraints listed in the Section 2.4, the following model of combined ductile shear and channel flow (henceforth referred as the 'combined flow') is proposed as the mechanism that accounts for the exhumation within the ductile regime of the HHSZ in the Zanskar section. The MCT and the top of ZSZ are considered as the parallel walls of a very long channel. Incompressible Newtonian viscous fluid behaviour of the rocks of the HHSZ is assumed. The brittle- and the brittle-ductile deformations are not incorporated in this model. The exhumation of the HHSZ, Zanskar section, within the ductile regime, is divided into two phases: $E=E_1+E_2$.

The E_1 phase: (Fig. 2.18) The top-to-SW sense of ductile non-coaxial shearing of the boundaries of the HHSZ is represented by a linear velocity profile (equation 3 of Appendix). At any instant, angle between the discrete ductile shear planes developed parallel to the boundaries of the HHSZ and the velocity profile remain the same. The velocity of different layers within the HHSZ falls linearly across it, attains a zero value, and rise again linearly towards the other wall. Any marker, assumed to be perpendicular

Figure Captions.

Fig. 2.18 The E_1 phase of exhumation, or the "ductile shear model". An inactive marker 'AB' is initially perpendicular to the boundary walls of a channel/shear zone. The walls are parallel, horizontal, infinitely long, NE-SW oriented and define the flow domain. The channel is assumed to be full of incompressible Newtonian viscous fluid. Orthogonal coordinate axes are chosen with the X-axis parallel to-, and equidistant from, the channel walls. The walls of the channel are top-to-SW sheared with the velocities U_1 and $-U_2$. The velocity profile ($A'B'$) is a straight line (equation 3 of Appendix). The intersection between $A'B'$ and the Y-axis is the pivot point 'P' over which the marker AB rotates. If the AP part of the channel undergoes exhumation, the BP part undergoes subduction, and vice versa. The angles, between the marker line with the discrete C-plains (H, K. L) produced at any instant in the simple shear history, remain the same. This means that the sense- and the magnitude of ductile shearing, at any instant within the channel, remain constant.

Fig. 2.19 Structural significance of the E_1 phase of exhumation is presented by S-C fabrics. The HHSZ demonstrates consistent top-to-SW sense of ductile shearing. The isograds are kinked into top-to-SW sense giving rise to inverted metamorphism within the HHSZ. This is demonstrated with a single isograd. Not to scale.

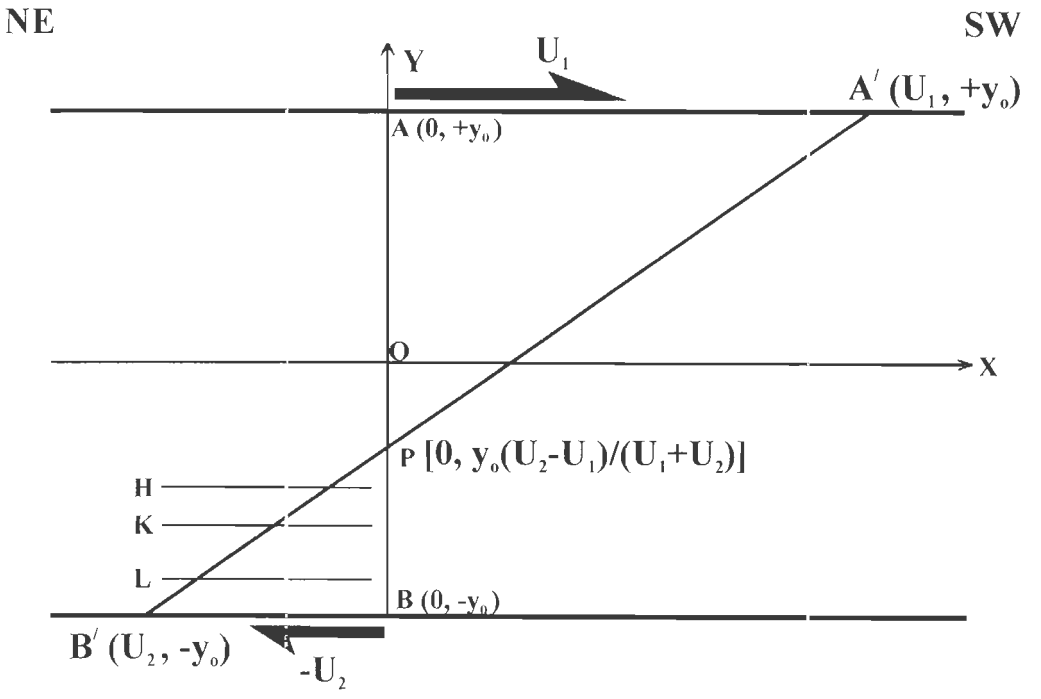

Fig. 2.18

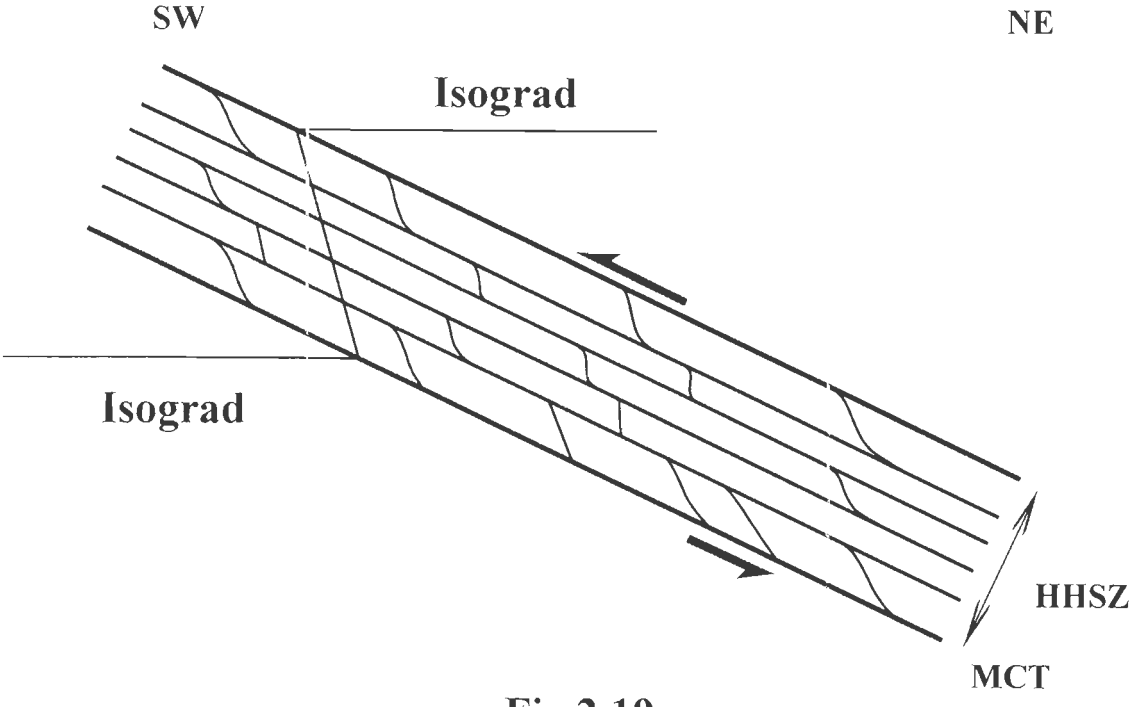

Fig 2.19

to the MCT, rotates about a pivotal point. The position of this pivot depends on the velocity of the boundaries and the thickness of the HHSZ (see the expression after equation 4 of Appendix). This phase took place during the early phase of Neo-Himalayan Period, or during the Himalayan D_2 deformation phase of Jain et al. (2002). In other word, the E_1 phase is modeled in the same way as the 'ductile shear model' (Jain and Manickavasagam, 1993; Manickavasagam et al., 1999; Jain et al., 2002).

The E_1 phase gave rise to intense crustal shortening within the HHSZ giving rise to the top-to-SW sense of shearing. This was manifested by the S-C fabric and other shear sense indicators (Figs. 2.2a, -b, 2.3a, 2.8a-d). The isograds within the HHSZ were also sheared to top-to-SW sense giving rise to inverted metamorphism inside it. These structural significances of the E_1 phase are idealized in Fig. 2.19. The angle between the S- and the C fabric in different parts of the HHSZ is determined by (i) the angle between these two foliations before shearing took place; (ii) whether the S-fabrics are strain sensitive or -insensitive (Davis and Reynolds, 1996); and (iii) probable strain partitioning within the shear zone. For these reasons, the angles between them should not be unequivocal indicators of the magnitude of strain, and therefore should not be considered for the validation of this, and the next phase of exhumation model.

The E_2 phase: (curve 3 of Fig. 2.20) During this phase of exhumation, viscosities of the rocks of the HHSZ were significantly reduced to the extent that it acted like fluid and underwent faster exhumation towards the southwest by a combination of the pressure gradient (channel flow/plane Poiseuille flow) and ongoing top-to-SW ductile shearing of

Figure Captions.

Fig. 2.20. With the same choice of the channel, its geographic orientation, the coordinate axes and the marker as in Fig. 2.18; line 1 represents the velocity profile of the simple shear deformation (the E_1 phase). The top and the bottom boundaries of the channel are sheared with velocities U_1 and $-U_2$, respectively in the top-to-SW sense and are shown by half arrows. In this case, $(dp/dx)=0$, and U_1 and/or $U_2 \neq 0$. Parabola-2 represents the channel flow, for which $U_1=U_2=0$. The flow direction is indicated by the solid arrow. Parabola-3 represents the combined ductile/simple shear and channel flow during the E_2 phase, when either or both $U_1, U_2 \neq 0$, and $(dP/dx) \neq 0$. The vertex V' of this parabola is located within the upper part of the channel. The line 'Z' passing through V', and parallel to the walls of the channel, demarcates the lower boundary of the ZSZ. T and T' stand for the thickness of the ZSZ and that of the rest of the HHSZ, respectively. Not to scale.

Fig. 2.21. Structural significance of the E_2 phase of exhumation is presented with the use of S-C fabric. The HHSZ undergoes consistent top-to-SW sense of ductile shearing. Within the ZSZ, top-to-NE sense of ductile shearing is produced even within the regime of bulk southwestward flow. Isograds inside the HHSZ attain parabolic geometries giving rise to inverted metamorphism. This is demonstrated with a single isograd. Not to scale.

Fig. 2.22. Reorientation of the ductile shear fabric during the E_2 phase, which was initially with top-to-SW sense within the ZSZ. The fabric showing top-to-SW sense of shear was produced during the E_1 phase. The upper- and the lower boundaries of the ZSZ move with velocities U_1 and U_3, respectively. The expression of U_3 is given between equations (9) and –(10) in the Appendix. Bulk southwestward flow reorients this fabric from MN into M_1N_1, into M_2N_2, and into M_3N_3. This gives rise to the top-to-NE sense of shearing at the final M_3N_3 position. Not to scale.

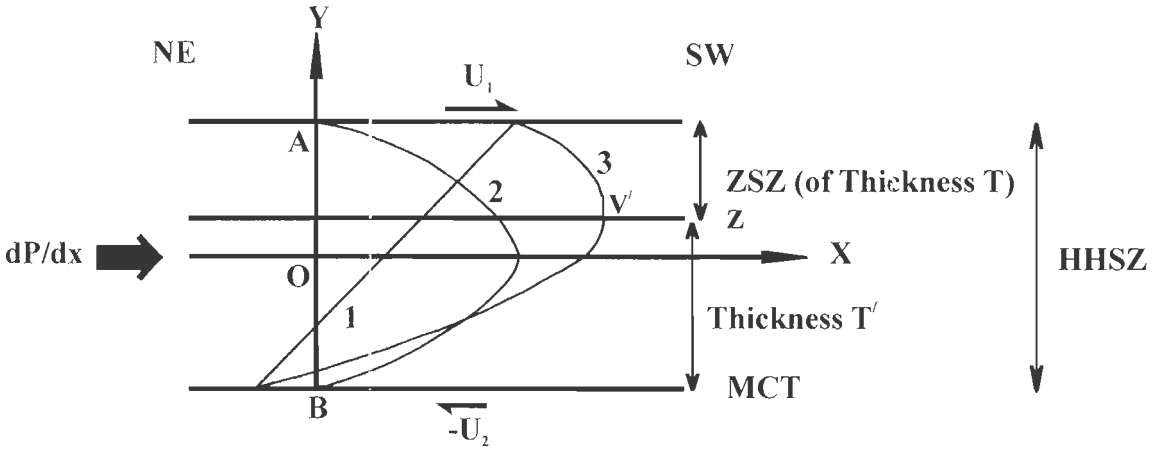

Fig. 2.20

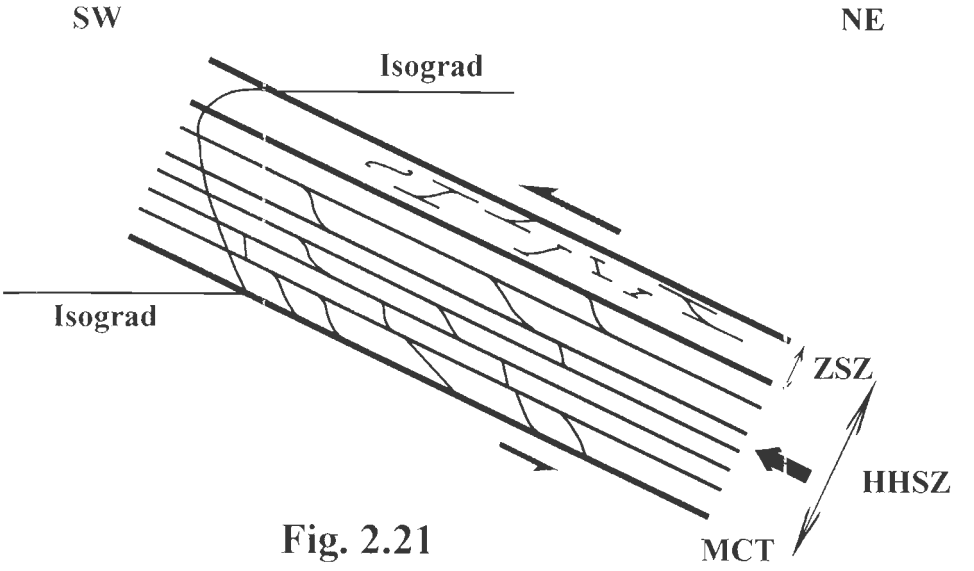

Fig. 2.21

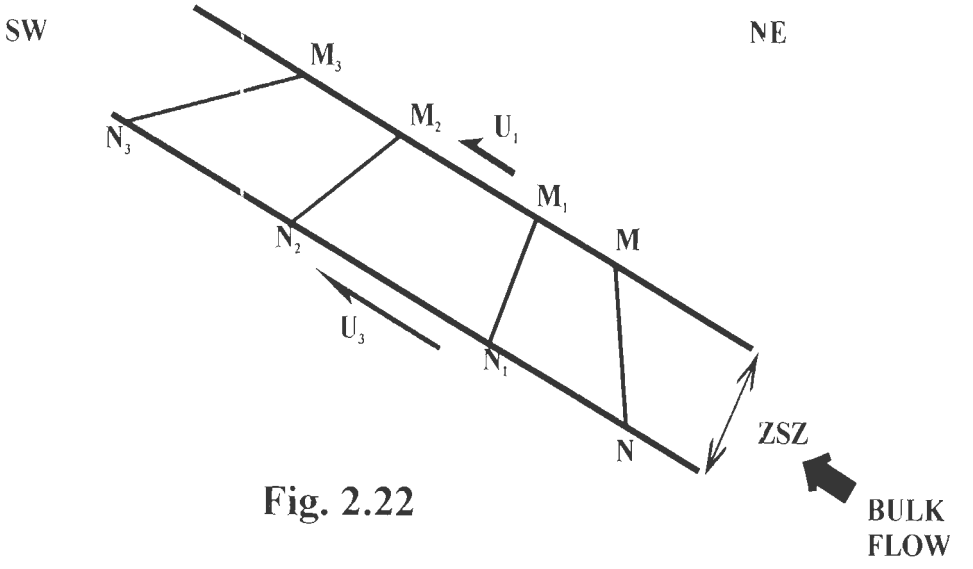

Fig. 2.22

the MCT and the top of the ZSZ. The fluid behaviour is evidenced by protracted partial melting, anatexis, migmatization and leucogranite injection within the structurally higher parts of the HHSZ. The flow is represented by a parabolic velocity profile (equation 7 in Appendix), which, incidentally, turns out to be the addition of the E_1 and the channel flow components (see the expression immediately after equation 7 in Appendix). This phase continued during the Middle Miocene Period. The vertex of the velocity profile is located within the upper part of the channel (see the expression after equation 9 in the Appendix). Across the line passing through the vertex and parallel to the MCT, the sense of ductile shearing is opposite. This line is taken as the lower boundary of the ZSZ. The E_2 phase predicts that the base of the ZSZ was characterized by the fastest rate of exhumation (see expressions after equation 9 of Appendix). The simulated ZSZ is thinner than of the reminder of the HHSZ (from equations 10a and -b of Appendix).

The structural significance of the E_2 phase is represented in Figs. 2.21 and -2.22. During this phase, some of the S-fabrics of the earlier E_1 phase were reoriented within the ZSZ, and some possibly created, giving rise to a top-to-NE sense of ductile shearing (Figs. 2.2a, 2.3a, 2.4b-d, 2.5b, 2.6a-d) during the bulk top-to-SW sense of flow. However, some shear fabrics escaped this retro-shear along the same C-planes, due to strain partitioning, and survived as remnants (Figs. 2.2a-b, 2.3a, 2.8a-d). Rarely, shear fabrics that enjoyed reversal of the ductile shear sense were preserved as isolated hooks (Figs. 2.9b, -c). The metamorphic isograds within the HHSZ were sheared in the same way as the parabolic flow profile giving rise to inverted metamorphism within the shear zone (Fig. 2.21).

Referring to equation 10a and case-'A' of Appendix, the thickness of the ZSZ is dependent on the following parameters: (i) the pressure gradient driving the channel flow, (ii) thickness of the HHSZ, (iii) the viscosities of the rocks of the HHSZ and (iv) the relative velocity of the boundaries of the HHSZ. For particular thickness- and viscosity of the rocks of the HHSZ, variation in the thickness of the ZSZ can be explained by varying the ratio of the relative velocity of the walls to the pressure gradient driving the channel flow. Additionally, for certain combinations of the four parameters mentioned above, the vertex of the combined flow lies on the upper boundary or even outside the HHSZ (Fig. 2.23; cases 'F' and 'G', respectively of Appendix). In these situations, the HHSZ undergoes uniform top-to-SW sense of ductile shearing. Thus, the E_2 phase predicts that the ductile shear zone with a top-to-NE sense of shearing might be lacking in some sections of the HHSZ even when the component of channel flow was active. In the former special case of E_2 phase (profile 1 in Fig. 2.23), the velocity profile for the combined flow is independent of viscosity (equation 12 of Appendix). Cases 'B' to 'E' are presented in order to cross-check the derivation of the combined flow in equation 7.

2.7. APPENDIX

Derivations & discussions

(I) Simple shear flow (line 1 in Fig. 2.18): With the choice of axes as of Fig. 2.18 and for a steady plane laminar flow of an incompressible Newtonian viscous fluid within an infinitely long channel with parallel- and horizontal walls, the Navier Stokes equation simplifies to:

$dP/dx = \mu (d^2x/dy^2)$ (vide p. 60 of Schlichting, 1955) ..... (1)

Figure Caption.

Fig. 2.23. Two special cases of the E_2 phase of exhumation are represented by the parabolic velocity profiles 1 and -2. Within the flow domain of the HHSZ, the profiles are represented by solid lines. The profiles are extrapolated by dashed lines outside the flow domain in order to show that they are parabolas and the location of their vertices. The top-to-SW sense of simple shearing is shown with half arrows at the boundaries of the NE-SW cross-section of the HHSZ. The pressure gradient is shown by a solid arrow. For profile-1, the vertex of the parabola lies on the upper boundary of the HHSZ. This is the situation (F) of the Appendix. For profile-2, the vertex lies outside the HHSZ, which is the situation (G) of the Appendix. For both these situations, consistent top-to-SW sense of ductile shearing persists throughout the HHSZ and is manifested by S-C fabric and other shear sense indicators. The diagram is neither to scale nor angle.

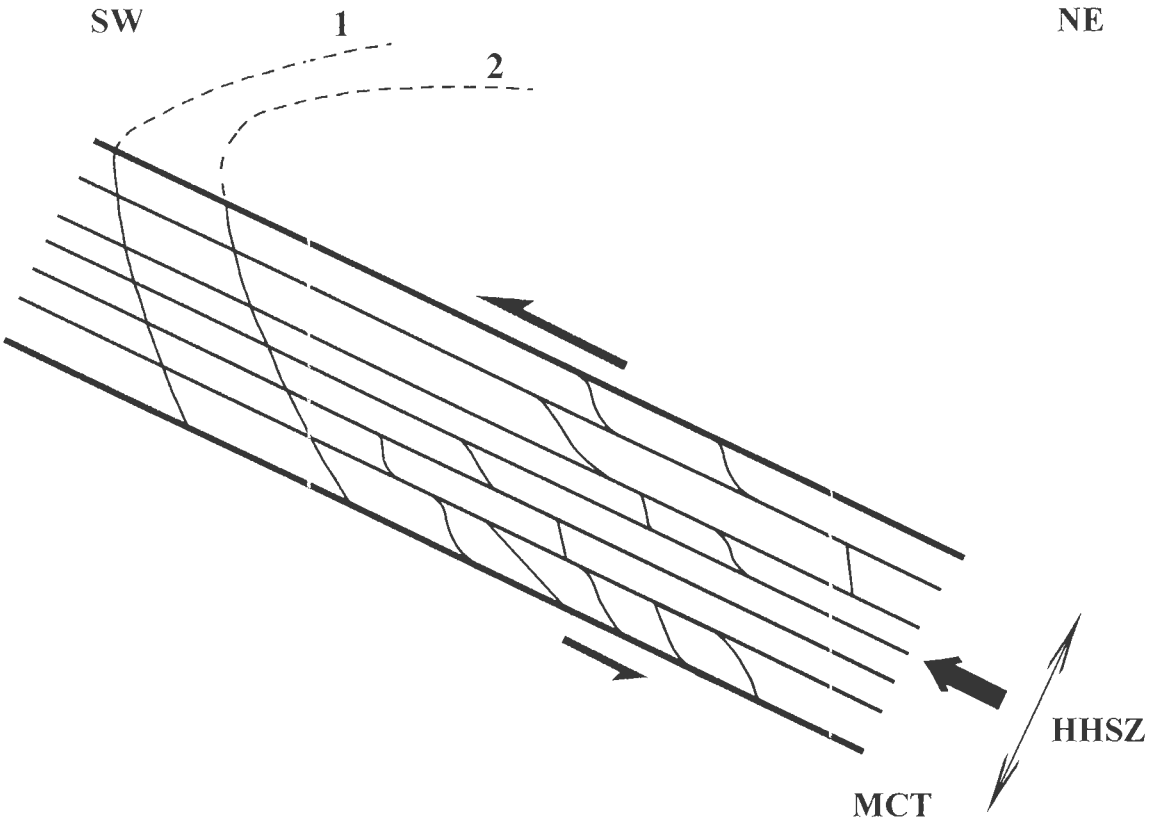

Fig. 2.23

Where P: pressure, and x: the distance along the X-axis. Therefore, dP/dx: pressure gradient in the X-direction.

μ: viscosity of the fluid

For simple shear flow, the velocities of either or both the walls of the channel U_1, $U_2 \neq 0$, and $dP/dx=0$.

Putting $dP/dx=0$ in equation 1:

$\mu (d^2x/dy^2) = 0$

or, $(d^2x/dy^2) = 0$; since $\mu \neq 0$

Integrating,

$dx/dy = C_1$

Integrating again:

$x = C_1y + C_2$ ... ... (2)

where C_1 and C_2 are the integration constants. Taking the thickness of the channel is '$2y_o$' units with the X-axis equidistant from, and parallel to, the walls of the channel, the boundary conditions are given by:

$x = -U_2$, for $y = -y_0$; and $x = +U_1$, for $y = + y_0$

Applying these boundary conditions in equation 2 and the integration constants are solved as:

$C_1 = 0.5. y_0^{-1}.(U_1+U_2)$

$C_2 = 0.5. (U_1-U_2)$

Putting these values in equation 2, the velocity profile for simple shear deformation (or the 'ductile shear model') is obtained as follows:

$x = 0.5.(U_1-U_2) + 0.5.y. y_0^{-1} (U_1+U_2)$ ... ... (3)

Note that the ratio of velocities, $(U_1 . U_2^{-1}) = (AP.BP^{-1})$ ... ... (4)

Putting x=0 in equation 3, the coordinate of pivot (P), or the intersection between the Y-axis and the velocity profile, is given by:

$P \equiv [0, y_o.(U_1-U_2).(U_1+U_2)^{-1}]$

Note that for $U_1=U_2$, 'P' is located equidistant from the walls of the channel. With progressive decrease of U_2 towards zero, 'P' keeps shifting towards the wall which is sheared with the velocity U_2. Finally for $U_2=0$, 'P' coincides with that wall.

(II) Channel flow or Plane Poiseuille flow (curve 2 in Fig. 2.20): Here U_1, U_2 =0, and $dP/dx \neq 0$. With the choice of axes and symbols as of Fig. 2.20, the Navier Stokes equation simplifies to equation 1. For channel flow/plane Poiseuille flow, the boundary conditions are:

$x = 0$, for $y = + y_0$; and $x = 0$, for $y = - y_0$

Assuming that (dP/dx) is constant, equation 1 is integrated,

$(dx/dy) = (dP/dx). Y + C_1$

Integrating again,

$x = 0.5.(dP/dx)\, y^2 + C_1.y + C_2$ ... ... (5)

where C_1 and C_2 are the integration constants. Applying the boundary conditions, the integration constants are solved,

$C_1 = 0$; $C_2 = -0.5.\, y_0^2.(dP/dx)$

Putting these values in equation 2, the equation for plane Poiseuille flow is derived as follows:

$$x = -0.5\mu.(dP/dx).(y_0^2 - y^2) \quad \ldots\ldots\ldots (6)$$

(As in many fluid mechanics texts e.g. Pai 1956)

The co-ordinate of the vertex of this parabolic profile is given by $[0.5\mu.y_0^2.(dP/dx), 0]$, which lies on the X-axis.

(III) Combination of simple shear and channel flow (curve 3 in Fig. 2.20): Here either or both of U_1, $U_2 \neq 0$, and also $dP/dx \neq 0$. With the choice of axes as of Fig. 2.20, the Navier Stokes equation simplifies to equation 1. Solving equation 1, equation 5 is reached.

The boundary conditions are:

$x = -U_2$, for $y = -y_0$; and $x = +U_1$, for $y = +y_0$

Putting these values in equation 4 and solving integration constants:

$C_1 = 0.5.(U_1+U_2)$

$C_2 = 0.5.\{\mu.(U_1-U_2) - (dP/dx).y_0^2\}$

Putting these values in equation 5, the velocity profile is obtained as:

$$x = 0.5[(U_1-U_2) + (U_1+U_2)\,y_0^{-1}.y - \mu^{-1}.(dP/dx).(y_0^2-y^2)] \quad \ldots\ldots\ldots (7)$$

From equations 3 -6 and -7,

x(of combined flow)=x(of simple shear)+x(of channel flow)

Equation 7 can be rewritten as,

$$x = \{0.5.\mu^{-1}.(dP/dx)\}y^2 + \{0.5.y_0^{-1}.(U_1+U_2)\}y + \{0.5(U_1-U_2) - 0.5.\mu.(dP/dx)\,y_0^2\}$$

$\ldots\ldots\ldots (8)$

which is in the form of:

$X=A.Y^2+B.Y+C$

where $X \equiv x$;

$Y \equiv y$;

$A \equiv 0.5.\mu^{-1}.(dP/dx)$;

$B \equiv 0.5.y_0^{-1}.(U_1+U_2)$; and

$C \equiv 0.5(U_1-U_2) - 0.5.\mu.(dP/dx)\, y_0^2$

Therefore, equation 7 represents a parabola.

Representing equation 8 in the following form:

$$[y-\{-0.5.(U_1+U_2).y_0^{-1}.\mu.\,(dP/dx)^{-1}\}]^2$$

$$=-4.(-0.5.\mu.(dP/dx)^{-1}.[x-\{0.5.(U_1-U_2)-0.125.y_0^{-2}(U_1+U_2)^2.\mu.(dP/dx)^{-1}-0.5.\mu^{-1}.(dP/dx).y_0^2\}] \quad \ldots\ldots\ldots (9)$$

and comparing with the standard form of a parabola:

$(Y-P)^2 = -4.Q.(X-R)$

where $X \equiv x$;

$Y \equiv y$;

$P \equiv - 0.5.(U_1+U_2).y_0^{-1}.\mu.(dP/dx)^{-1}$;

$Q \equiv -0.5.\mu.(dP/dx)^{-1}$

$R \equiv 0.5.(U_1-U_2) - 0.125.\, y_0^{-2}(U_1+U_2)^2.\mu.(dP/dx)^{-1} - 0.5.\mu^{-1}.\,(dP/dx).y_0^2$

the coordinate of its vertex (R,P) is obtained as:

x- ordinate: $0.5.(U_1-U_2)-0.125.\ y_0^{-2}(U_1+U_2)^2.\mu.(dP/dx)^{-1}-0.5.\mu^{-1}.y_0^2.(dP/dx)$

y- ordinate: $-0.5.y_0^{-1}.\mu.(U_1+U_2).(dP/dx)^{-1}$

The maximum value of the x-ordinate on the parabolic profile given by equation 7 is obtained at the vertex. Therefore, the highest velocity of the fluid attained inside the channel is given by U_3= x- ordinate at the vertex. Geologically speaking, the vertex denotes the location of the fastest rate of exhumation.

For $(dP/dx)<0$, i.e. for a flow from negative- towards the positive side of the X- axis, the absolute value of the Y-ordinate of the vertex is given by:

$0.5.\mu.y_0^{-1}(U_1+U_2).(dP/dx)^{-1}$, which is > 0.

A line passing through the vertex separates the whole flow domain into two zones with opposite senses of ductile shearing.

The thickness of the upper zone is given by:

$$T=[y_0-0.5.y_0^{-1}(U_1+U_2).\mu.(dP/dx)^{-1}] \quad \ldots\ldots\ldots (10a)$$

The thickness of the lower zone is given by

$$T'=[y_0+0.5.y_0^{-1}(U_1+U_2).\mu.(dP/dx)^{-1}] \quad \ldots\ldots\ldots (10b)$$

From equations 10a and –10b, it is noted that $T<T'$

From equation 10a, the following statements can be made:

(A) For a channel with constant thickness (of '$2.y_0$' units) and full with an incompressible Newtonian viscous fluid of constant viscosity (μ), T depends on the ratio of the relative velocity of the walls to the pressure gradient i.e. $(U_1+U_2).(dP/dx)^{-1}$. For a constant (dP/dx), with increasing relative velocity of the walls i.e. U_1+U_2, T becomes progressively thinner.

(B) For constant parameters y_0, μ and (dP/dx), T depends on the relative velocity of the walls, and not on the absolute velocities of the walls i.e. U_1 and U_2.

(C) For constant pressure gradient (dP/dx), T decreases with increasing amount of the relative velocity of the walls.

(D) For no ductile shear active on the channel walls, i.e., $U_1=U_2=0$, which gives $(U_1+U_2)=0$, T attains its maximum value=y_0. In this case, the vertex of the parabola lies on the X-axis. This is the situation for plane Poiseuille flow given by equation 6.

(E) For (dP/dx)=0, there is no pressure gradient and the fluid movement is guided solely by U_1 and U_2. This is the simple shear mode of deformation of the channel and the velocity profile is given by equation 3. Uniform shear sense is displayed throughout the channel. 'T' remains undefined.

(F) For $(U_1+U_2).(dP/dx)^{-1}=(2.y_0^2.\mu^{-1})$, i.e. for

$(dP/dx)=0.5.\mu.y_0^{-2}\ (U_1+U_2)$ ... ... (11)

T is =0. The situation is represented by profile-1 of Fig. 2.23. The vertex of the parabolic profile of the combined flow lies on the channel wall which undergoes shearing in the same direction as that of the plane Poiseuille flow. The sense of shear remains the same throughout the channel. Putting this value of (dP/dx) from equation 11 into equation 7 of the velocity profile of combined flow, the velocity profile for T=0 situation is deduced as follows:

$x=0.5.(U_1-U_2)+0.5.y_0^{-1}.(U_1+U_2).\{y-0.5.y_0^{-1}).(y_0^2-y^2)\}$ ... ... (12)

It is noted that the equation is independent of viscosity (μ).

(G) For $(U_1+U_2).(dP/dx)^{-1}>(2.y_0^2.\mu^{-1})$, T is <0. The situation is represented by profile-2 of Fig. 2.23. The vertex of the parabola lies outside the channel, and uniform sense of shearing is displayed throughout the channel. The situation, therefore, is equivalent with the simple shear deformation. However, the difference between them is that in case of simple shearing, at any instant the angle between the shear fabric and the primary shear plane remains everywhere the same. On the other hand, for the combined flow with T= or < 0, the angle would vary.

Chapter 3

HIGHER HIMALAYAN SHEAR ZONE, SUTLEJ SECTION- STRUCTURES & EXHUMATION MODEL

3,1 INTRODUCTION

The Higher Himalayan Shear Zone (HHSZ) is a ductile sheared crustal slice in the Himalaya, and is bounded by the Main Central Thrust (MCT) in the south and the continuation of the South Tibetan Detachment System (STDS) in the north. The HHSZ in the Sutlej section is characterized by compressional top-to-SW sense of ductile shearing. This deformation was prevalent during the early phase of Neo-Himalayan Period ~25Ma back, and was a result of the intense crustal shortening produced by the collision between the Indian- and the Eurasian plates (Jain et al., 2002 and references therein; Godin et al., 2006 and references therein; Yin 2006, and references therein). The STDS is structurally characterized by prominent top-to-NE sense of extensional ductile shearing even within the compressional collisional domain of the Himalaya (Godin et al., 2006 and references therein). The ductile extensional shearing within the STDS was simultaneous with the ongoing compressional ductile shearing of the MCT during the middle Miocene Period ~18 Ma before the present (Yin, 2006 and references therein). In certain sections of the NW Himalaya, top-to-SW sense of ductile shearing has also been reported from the continuation of the STDS, e.g. from the Zanskar Shear Zone in the Suru Doda valleys in India (Patel et al., 1993; Dèzes et al., 1999; Chapter-2 in this thesis), and the Main Mantle Thrust from Pakistan (Argles and Edwards, 2002).

From most sections of the HHSZ, a single detachment equivalent to the STDS have been reported, e.g. the Zanskar Shear Zone in the Suru Doda valley, the Annapurna Detachment along the Kali Gangdaki section, the Bhote Koshi Detachment along the Bhote Koshi valley, the Nyalam Detachment north of Nayalam, the Dinghye Detachment at Dinghye area, the Lhozhang Detachment in the Lhozhang area, the Jhala Normal fault in the Bhagirathi valley and the Malari Fault or the Trans-Himadri Fault in the Garhwal Himalaya (Jain et al., 2002 and references therein; Yin, 2006 and references therein). However, in particular sections of the eastern Himalaya, a second detachment inside the HHSZ has also been documented, e.g. at Gonto La in southern Tibet (Edwards et al., 1996) and at the Everest massif, Nepal Himalaya (Searle, 1999). In the Qomolangma- and the Lhoste- detachments, the upper- and the lower detachments respectively at the Everest massif, extensional shearing took place before 16 Ma and between 18-16 Ma, respectively (Searle et al., 2003; Law et al., 2004). Therefore, it can be concluded that the second detachment inside the HHSZ is discontinuous along the trend of the Himalaya.

3.2 OBJECTIVES

Taking the HHSZ in the Sutlej section as the study area, this chapter aims at (i) documentation and compilation of first order ductile- and brittle deformations from field- and thin-section studies; and (ii) proposing a model of exhumation of the ductile and the brittle deformations of the HHSZ based on these structures and mathematical analyses.

Figure Captions

Fig. 3.1 Tectonic map of the Higher Himalayan Shear Zone, Sutlej section and nearby areas. Compiled from Jain and Anand (1988), Singh (1993) and Vannay and Grasemann (2001). Location of the Main Central Thrust (MCT), as given by Jain and Anand (1988), has been followed. The Jhakri Formation and the Wangtu Gneissic Complex have been considered as parts of the HHSZ. The speculated position of the MCT below the Jutogh Thrust has been shown by dashed line TT'. Perpendicular to TT' is the line MM' along which ratios of thicknesses of the parts of the HHSZ have been calculated in Fig. 3.12. Abbreviations: LKRW: Larji Kulu Rampur Window; SD: Sangla Detachment; JD: Jhala Detachment; MCT: Main Central Thrust; JT: Jutogh Thrust; MBT: Main Boundary Thrust; LH: Lesser Himalaya.

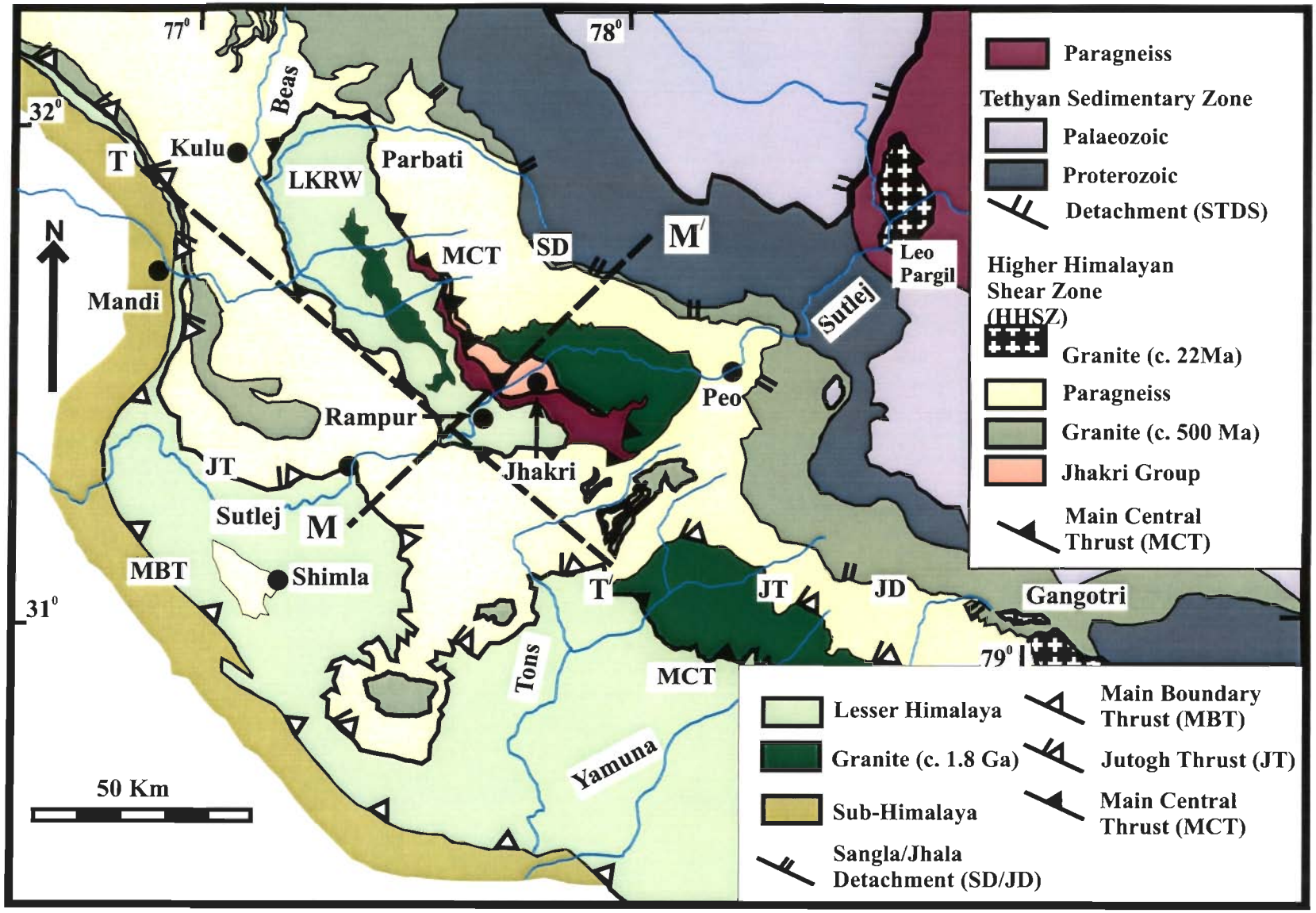
77°
78°
32°
31°
Beas
Kulu
T
LKRW
Parbati
MCT
SD
M′
Leo
Pargil
Sutlej
N
Mandi
Rampur
Peo
Jhakri
JT
Sutlej
M
MBT
Shimla
T′
JT
JD
Gangotri
79°
Tons
MCT
Yamuna
50 Km
Paragneiss
Tethyan Sedimentary Zone
Palaeozoic
Proterozoic
Detachment (STDS)
Higher Himalayan
Shear Zone
(HHSZ)
Granite (c. 22Ma)
Paragneiss
Granite (c. 500 Ma)
Jhakri Group
Main Central
Thrust (MCT)
Lesser Himalaya
Granite (c. 1.8 Ga)
Sub-Himalaya
Sangla/Jhala
Detachment (SD/JD)
Main Boundary
Thrust (MBT)
Jutogh Thrust (JT)
Main Central
Thrust (MCT)

Fig. 3.1

Figure Captions.

Fig. 3.2 Geological map of the HHSZ, Sutlej section. Compiled and simplified from Singh (1993), Srikantia and Bhargava (1998) and Vannay and Grasemann (1998). Location of the MCT as assigned by Singh et al. (1993) has been followed. Based on the present field studies, the boundary between the rocks with different viscosities (prevalent during the dominant ductile deformations in the HHSZ), the attitude of the main foliations and that of the primary brittle shear plains, and the two Himalayan Detachments named here as- the HD1 and the HD2, are delineated/ plotted in this map. Note that (i) the HD2 nearly coincides with the Vaikrita Thrust passing through Karcham; and (ii) the HD2 is much thinner compared to the HD1.

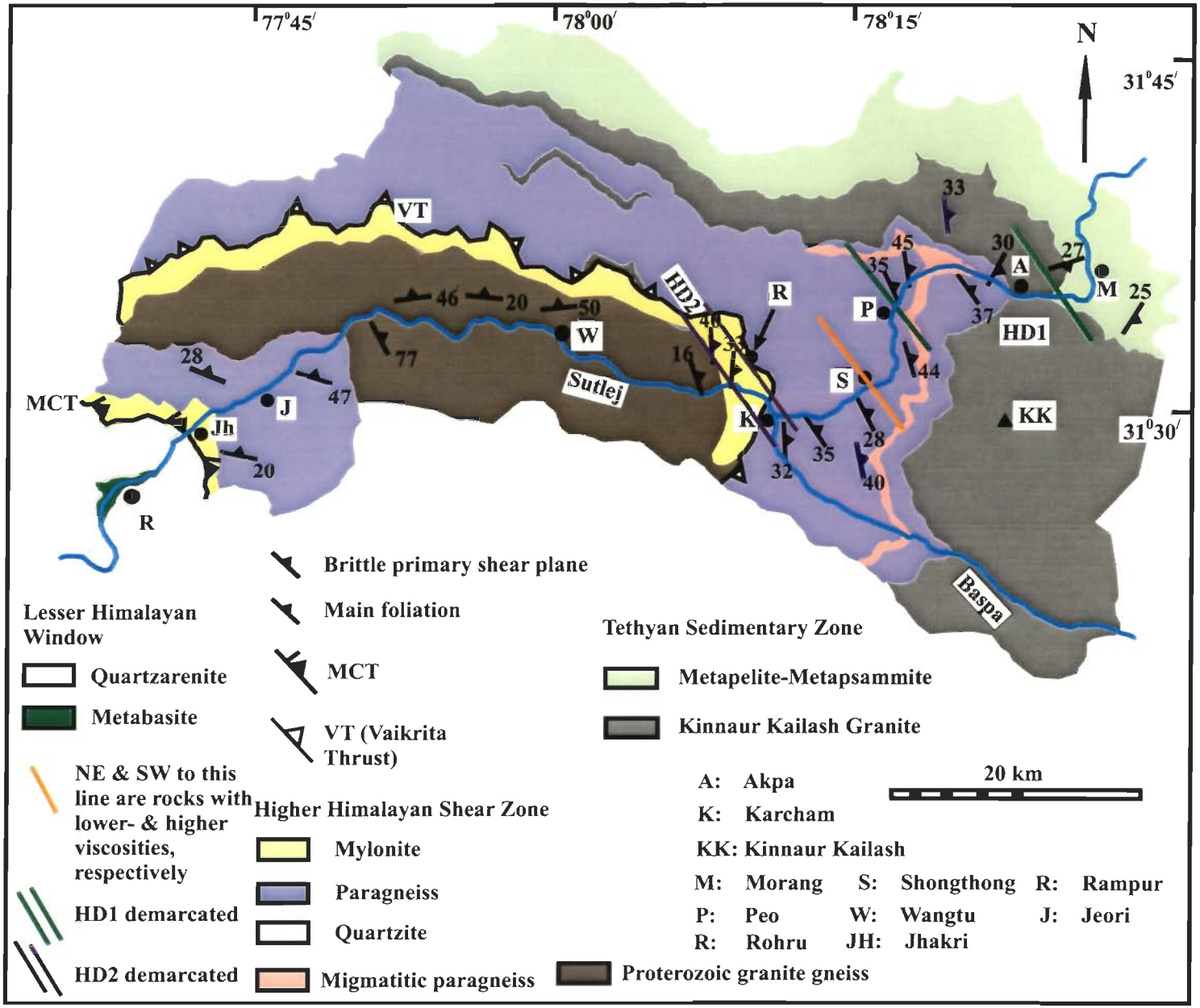
77°45′
78°00′
78°15′
N
31°45′
31°30′
VT
HD2
HD1
MCT
Sutlej
Baspa
W
P
R
S
K
A
M
J
Jh
KK
46
20
50
77
28
47
20
16
35
32
28
40
45
35
30
27
25
37
44
33
Brittle primary shear plane
Main foliation
MCT
VT (Vaikrita Thrust)
Lesser Himalayan Window
Quartzarenite
Metabasite
NE & SW to this line are rocks with lower- & higher viscosities, respectively
HD1 demarcated
HD2 demarcated
Higher Himalayan Shear Zone
Mylonite
Paragneiss
Quartzite
Migmatitic paragneiss
Tethyan Sedimentary Zone
Metapelite-Metapsammite
Kinnaur Kailash Granite
Proterozoic granite gneiss
20 km
A: Akpa
K: Karcham
KK: Kinnaur Kailash
M: Morang
S: Shongthong
R: Rampur
P: Peo
W: Wangtu
J: Jeori
R: Rohru
JH: Jhakri

Fig. 3.2

3.3 GEOLOGICAL FRAMEWORK

The HHSZ in the Sutlej river section (Figs 3.1, 3.2) in Rampur- and Kinnaur Districts of Himachal Pradesh, India is accessible for fieldwork from National Highway-22A (NH-22A) which runs parallel to the Sutlej river. The HHSZ is subdivided by three secondary thrusts. From south to north, these are the Jutogh Thrust (JT), the Chail Thrust and the Vaikrita Thrust (VT), respectively. These thrusts demarcate contrasting metamorphic grades across them (Thakur, 1993). The MCT is cut by the JT (Fig. 3.1).The Jutogh Thrust Sheet skirts around the MCT-bounded Lesser Himalayan rocks of the Larji-Kulu-Rampur Window (LKRW).

There have been different opinions on the location and designation of the different structural discontinuities in this section. For example, Vannay and Grasemann (2001) identified the VT of Srikantia and Bhargava (1998) as the MCT. A significantly different, and less accepted view in the designation of major tectonic litho-units, is that the VT has been considered as the southern boundary of the 'Tethyan Himalayan Tectogens' and the northern boundary of the 'Lesser Himalayan Tectogens' with the absence of Higher Himalaya in this section (Srikantia and Bhargava, 1998).

Fission track zircon-apatite ages reveal that the HHSZ in the Sutlej section acted like a number of wedges within the brittle deformation regime. These wedges moved differentially towards the southwest and northeast during the Plio-Pliestocene Peroid as a part of the late tectono-thermal evolution of the HHSZ (Jain et al., 2000). The Karcham Normal Fault passing through Karcham with a top-to-east sense of brittle shearing, has been recognized as a major brittle structure in this area (Vannay, et al., 2004 and references therein).

The rocks of the HHSZ are dominantly gneisses and schists with greenschist- amphibolite facies metamorphism and are of Precambrian and Proterozoic in age (Thakur, 1993; Jain et al., 2002; Yin 2006 and references therein). Northeast to the LKRW, the HHSZ is exposed as the Jeori Formation and consists mainly of pelitic- and psamitic schists, and is separated from the 1870-2070 Ma old Wangtu Gneissic Complex (Singh and Jain, 1993). From the localities- Karcham up to Akpa, psamitic- and pelitic schists, quartzites, mylonites, migmatites, leucogranites, pegmatites, and occasional bands of amphibolites, calc-silicates and aplites are present. These belong to the Vaikrita Group of Srikantia and Bhargava (1998).

From the lower part of the HHSZ up to the VT, the peak metamorphism is characterized by an increase in temperature from 610 to 700^{0}C and drop in pressure from 900 to 700 MPa (Vannay et al., 1999). Northward from the VT, the temperature increases from 570 to 750^{0}C at nearly constant pressure of 8 MPa. These thermo-barometric data, along with the presence of the staurolite zone at the base- and profound melt activities at the top of the HHSZ indicate inverted metamorphism (Vannay and Grasemann, 2001). Reviewing the P-T data of this terrain, Vannay and Grasemann (2001) concluded that: (i) the peak metamorphism of the HHSZ was achieved at 30 km depth; and (ii) the P-T evolution of the terrain matches with the geochronologic constraints suggesting that the HHSZ was exhumed by simultaneous thrusting of the MCT and extensional shearing of the STDS.

3.4. FIELD- & THIN-SECTION STUDIES

3.4.1. Lithologic grouping

The lithologies of the HHSZ that was deformed during the D2 deformation and onwards, after the India-Asia collision ~ 55 Ma ago, is grouped into the following two rheological categories (Fig. 3.2). The first category is *(1) rocks with higher viscosity.* These are

located in the lower part of the HHSZ- from the MCT to the locality Shongthong. The lithologies dominantly include pelitic- and psamitic schists, quartzites and pre-collisional 1866±10 Ma old Wangtu Granite (Singh, 1993). These rocks were presumably in solid states during the post-collisional deformation. The second category is *(2) rocks with lower viscosity.* These are located within the upper part of the HHSZ- northward from Shongthong. These rocks are dominantly migmatites, gneisses and in places are (leuco)granites and pegmatites. Within this zone, the extruding granitic melt might have migmatized the preexisting rocks, and occasionally accumulated giving rise to (leuco)granites and pegmatites. Section 3.4.2 deciphers the melting activity and extrusion to be syntectonic in nature. At least a part of the rock must be in a molten stage during the deformation. The contact between these two rock-types at the locality Shongthong is a 'spot observation', and is extrapolated for the sake of presentation in the map (Fig. 3.2). The Lesser Himalayan rocks of the LKRW are not included in these categories since it was exhumed by doming during the Pliocene-Quaternary periods (Jain et al., 2002) much later to the deformation episodes in the HHSZ.

On the Akpa-Ashrang road (not shown in Fig. 3.2), the upper boundary of the HHSZ is marked as the contact between the psammitic- and pelitic schists of the Tethyan Sedimentary Zone at the north and granites at the south. This boundary is extrapolated for similar reasons and onto the Sutlej section, which passes between the locations- Akpa and Morang (Fig. 3.2).

The dynamic viscosity of a granitic melt at 700^0C is 10^5-10^{12} Pa s. The viscosity of the schistose rocks at 500-700^0C is 10^{18}-10^{19} Pa s, which is 6 to 13 order of magnitude higher

than that for the granitic melt (Druguet and Carreras, 2006 and references therein). Therefore, the upper zone of rocks of the HHSZ was rheologically weakened compared to the lower zone at least during a part of the ductile deformation event. This inference has been tested in one of the mathematical analyses of the possible exhumation of the HHSZ (Fig. 3.18; equations 31 to 53 in the Appendix).

3.4.2. Field structural geology

Except a few local folds or crenulations, the foliations dominant within the HHSZ are planar and dip northeasterly with moderate dips. Stretching lineations are defined on the main foliation planes/primary shear planes and plunge moderately northeast. Within the zone of rocks with lower viscosity, the main foliations are defined by migmatitic foliations with granitic melts/leucosomes (Figs. 3.3a, -d, 3.4a, -b) indicating syn-shearing/syntectonic migmatization (Brown, 2001). It is expected that the rheological softening might have facilitated the ductile deformation.

For the different shear sense indicators, the northeasterly dipping main foliation planes act as the primary shear planes (the C-planes). Throughout the HHSZ, S-C fabrics (Berthè et al., 1979) (Fig. 3.3a), sigmoid quartz veins and leucosomes (Figs. 3.3b, -d, 3.4d, 3.5c, -d), and intrafolial folds (Fig. 3.3c) denote the top-to-SW sense of ductile shearing. Nearer to the C-planes which bound them, the S-planes become sigmoid and attain progressively lower angles. In places, the C-planes are sub-horizontal (Fig. 3.3a, -d) indicating that they undulate on a regional scale. The S-fabrics vary in thickness, length and curvature. The top-to-SW sense of shearing is identified as the Himalayan D_2 deformation, which took place during the early phase of

Figure Captions

Fig. 3.3 Top-to-SW sense of ductile shearing given by different shear sense indicators from the HHSZ outside the two detachments (the HD1 and the HD2).

Fig. 3.3a S-C-C$^{/}$ fabric defined by thicker leucosome and thinner melanosome layers within migmatite, at Shongthong. Prominent secondary synthetic shear plane (C$^{/}$) sharply cuts the S-fabric. The C-plane is discontinuously occupied by leucosomes (shown by an arrow) indicating migmatization syntectonic to this S-C shearing event.

Fig. 3.3b Sigmoid quartz vein defining the S fabric within gneiss. Sharp, straight and discrete C plane. At Jeori.

Fig. 3.3c Intrafolial fold in migmatitic gneiss. The main foliation planes or the C-planes above and below this fold are straight and parallel. Inclination of axial trace (marked by dashed lines) of the fold to the main foliation gives the shear sense. At Powari.

Fig. 3.3d A train of sigmoid leucosomes in migmatite indicate the sense of primary shearing. The C-plane is sub-horizontal. Comparing the inclination of this C-plane with that of Fig. 3.3a-c, it can be said that the C-plane is undulating in regional scale. Near Pangi.

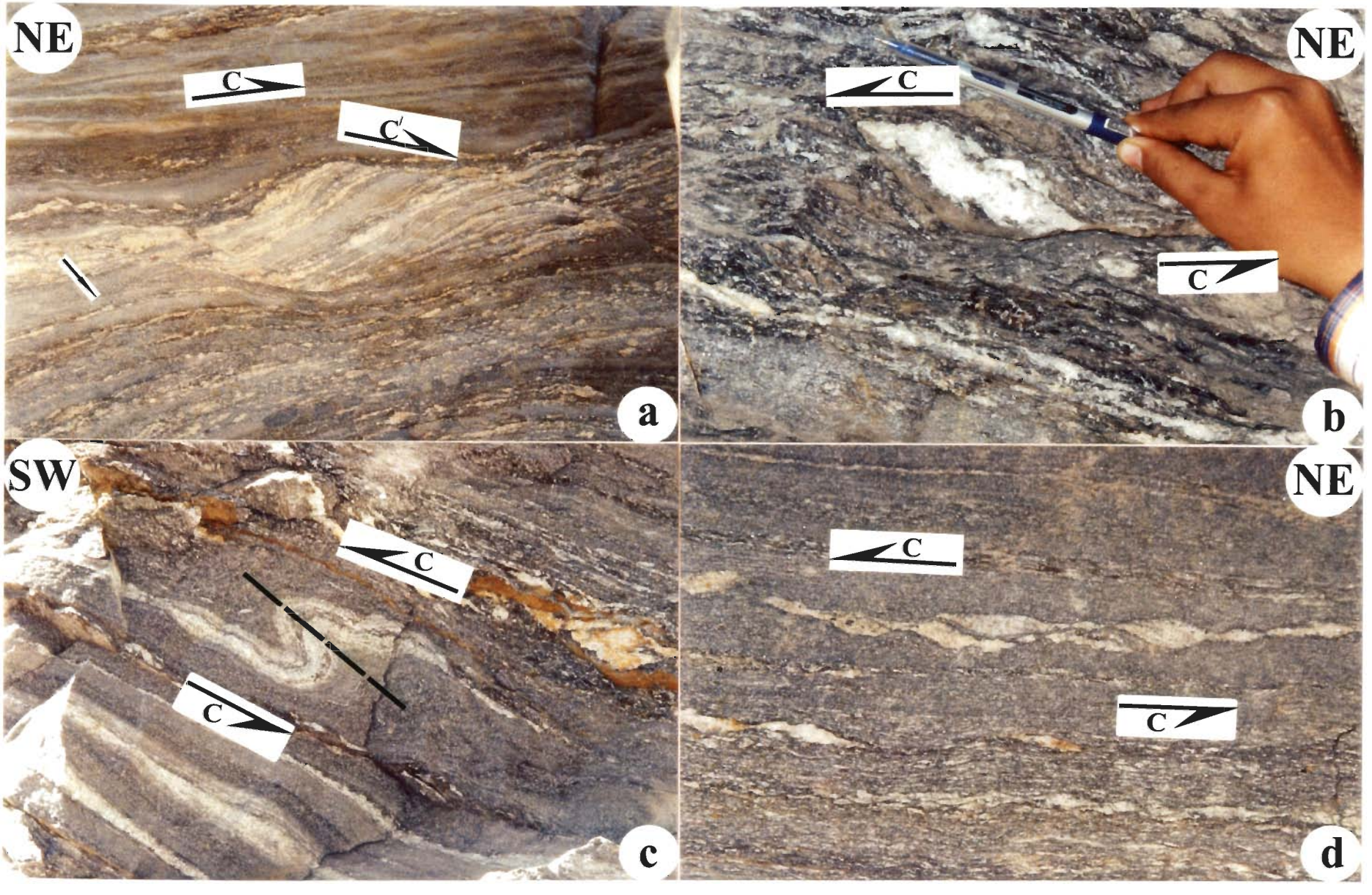

Fig. 3.3

Figure Captions

Fig. 3.4 Dominant top-to-NE extensional ductile shearing and rare top-to-SW compressional ductile shearing are noted from the HD1, host rock: migmatite.

Fig. 3.4a S-C fabric defined by thicker leucosomes and thinner melanosomes, giving top-to-NE extensional ductile shearing. Located between Pangi- and Kashang bridges.

Fig. 3.4b Thick sigmoid leucosome giving top-to-NE extensional ductile shearing. Near Kashang bridge.

Fig. 3.4c S-C fabric giving relic top-to-SW ductile shearing. S-planes defined by alternate layers of thicker leucosome- and thinner melanosome layers. The C-plane is defined by thin and straight melanosomes. Located between Kashang and Kharo bridges.

Fig. 3.4d S-C fabric defined by leucosomes and melanosomes giving top-to-NE extensional shearing. Thin leucosome layer locally defines secondary C′ shearing synthetic to top-to-NE primary shear. Near Kharo bridge.

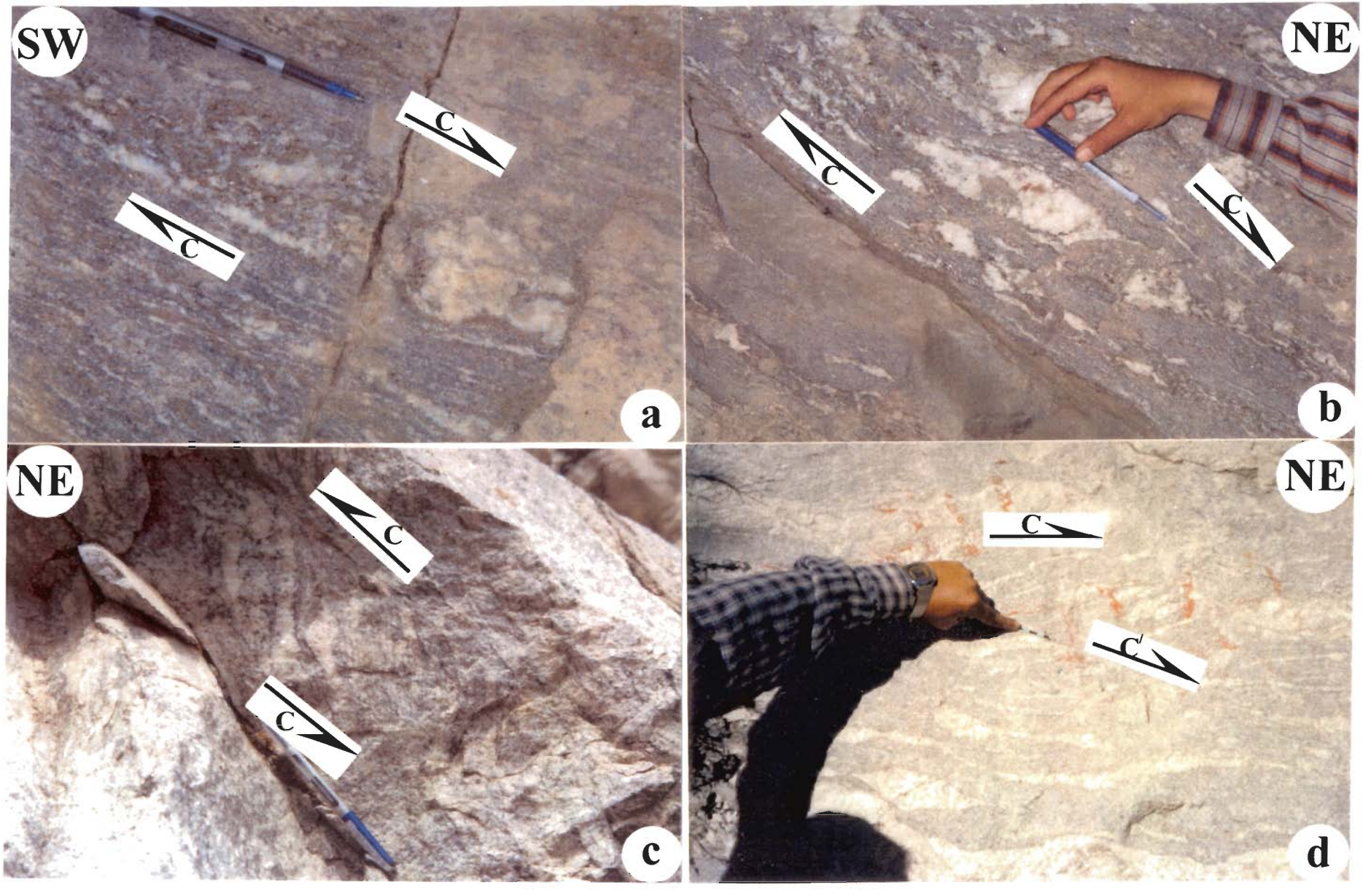

Fig. 3.4

Figure Captions

Fig. 3.5. Both top-to-NE extensional and top-to-SW compressional ductile shearing are documented from the HD2, located near Karcham. Host rock: gneiss.

Fig. 3.5a Intrafolial fold of quartz vein with thick hinges and thin limbs giving top-to-NE sense of extensional ductile shearing. Note that the primary shear planes act as the enveloping surfaces of the fold.

Fig. 3.5b A number of sigmoid quartz veins giving top-to-NE extensional ductile shearing. One of these veins is much elongated along the C-plane indicating intense shearing in this geographic direction.

Fig. 3.5c Sigmoid- and elongated veins of quartz indicate top-to-SW sense of compressional ductile shearing. Prominent synthetic C' shearing, at low angle to the C-plane, is also displayed.

Fig. 3.5d Sigmoid- and lenticular quartz veins indicate top-to-SW sense of compressional ductile shearing.

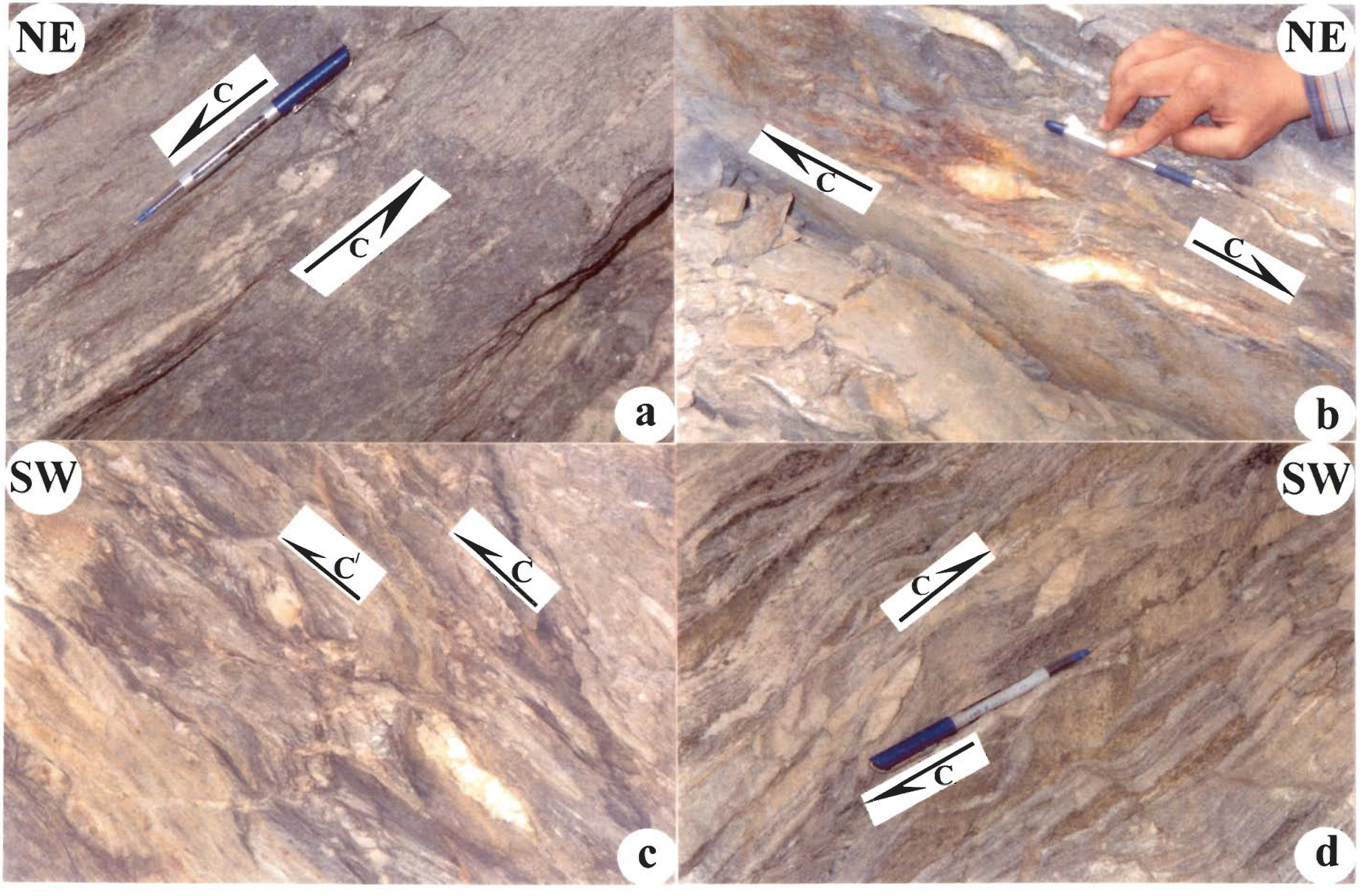

Fig. 3.5

Neo-Himalayan Period. Some of the S-fabrics are occasionally affected by secondary shearing synthetic to the main shearing event (Figs. 3.3a, 3.4d). These are the C' shear planes along which shearing took place probably simultaneous with the C shearing event (Passchier and Trouw, 2005). In this work, the C' shearing is not considered while defining the detachments nor is it used in modeling the mechanism of exhumation of the HHSZ. The same approach was adopted for modeling the exhumation of the HHSZ, Zanskar section, as discussed in Chapter-2.

Interestingly, an additional phase of top-to-NE sense of extensional ductile shearing, deciphered from intrafolial folds (as referred in Ghosh, 1993), S-C fabrics (Berthè, et al., 1979), and quartz veins and leucosomes of sigmoid shapes, is found to be confined within two zones. This sense of shearing is defined within the northeasterly dipping C-planes parallel to, hence the same as, that for the top-to-SW sense. In these two zones, compressional top-to-SW sense of shearing occurs less frequently. One of these zones, designated as the Himalayan Detachment-2 (HD2), is delineated at the locality Karcham (Fig. 3.2). At the same locality, the 'Vaikrita Thrust' (Srikantia and Bhargava, 1998) and the 'Karcham Normal Fault' (Vannay and Grasemann, 2001) have also been delineated. Identification of the HD2, mainly based on intrafolial folds from field, is crucial. Lack of any large-scale folds in this area and uniformly dipping foliation planes confirm that these intrafolial folds are definitely not secondary parasitic folds. The ductile shear sense indicators within the HD2 are presented in Figs. 3.4a-d. The other zone is designated as the Himalayan Detachment-1 (HD1) (Fig. 3.2). The lower boundary of the HD1 is delineated between the locations Pangi- and Kashang. The upper boundary of the HD1 is

the same as the contact between the HHSZ and the overlying Tethyan Sedimentary Zone. The ductile shear sense indicators within the HD1 and the HD2 are presented in Figs. 3.4 and -3.5, respectively. The HD1 and the HD2 lie within the rock-of lower- and higher viscosities, respectively. The HD1 and the STDS bear the same structural geology of top-to-NE sense of shearing. In addition, due to its occurrence within the topmost part of the HHSZ, same as that of the STDS delineated in other sections of the Himalaya, the HD1 in this section is considered to be the continuation of the STDS. The fact that the top-to-NE sense of ductile shearing took place later than the top-to-SW sense of shearing within the HD1 and the HD2 is indicated by the abundance of the former shear sense indicators within these detachments.

Throughout the HHSZ, including the HD1 and the HD2, a phase of brittle-ductile extension parallel to the main foliation is deciphered from different varieties of boudins e.g. lenticular boudins (Fig. 3.6a), pinch and swell structures (Figs. 3.6b, -c), and foliation boudins (Fig. 3.6d). Calc silicate layers (Fig. 3.6a), quartz veins (Fig. 3.6c) and migmatitic foliations (Fig. 3.6d) on different scales are boudinaged. These boudins indicate widespread intense penetrative deformation (Ghosh, 1993) with brittle-ductile extension parallel to the main foliation. The foliation planes are drawn towards the gap created by partly or completely separated clasts, and define prominent scar folds. In some lenticular- and foliation boudins, the inter-boudin partition is filled with quartz (Fig. 3.6a). This indicates accumulation of the melt fraction at sites of low stress (Marchildon and Brown, 2003), which took place possibly during the brittle-ductile extension.

Figure Captions

Fig. 3.6 Different varieties of boudins from the HHSZ indicating brittle-ductile phase of extension. Main foliation showing prominent scar fold at inter-boudin separations. Away from the separated clasts, the main foliations are straight and sub-parallel. Arrows indicate extension parallel to the main foliation.

Fig. 3.6a Lenticular boudin of calc-silicate layer. The inter boudin partition is filled with quartz, and is shown by a smaller arrow. Located within the HD2 near Karcham. A pen, marked with a black ellipse, is the marker.

Fig. 3.6b Pinch and swell structure of quartz vein within psamite schist. Located outside the HD1 and the HD2, near Shongthong.

Fig. 3.6c Very large pinch and swell structure of quartz vein within the host rock of migmatitic gneiss at Powari. A hammer, marked with a black ellipse, is the marker.

Fig. 3.6d Foliation boudin of thick leucosome- and thin melanosome layers within migmatite. Located within the HD1, near Kashang.

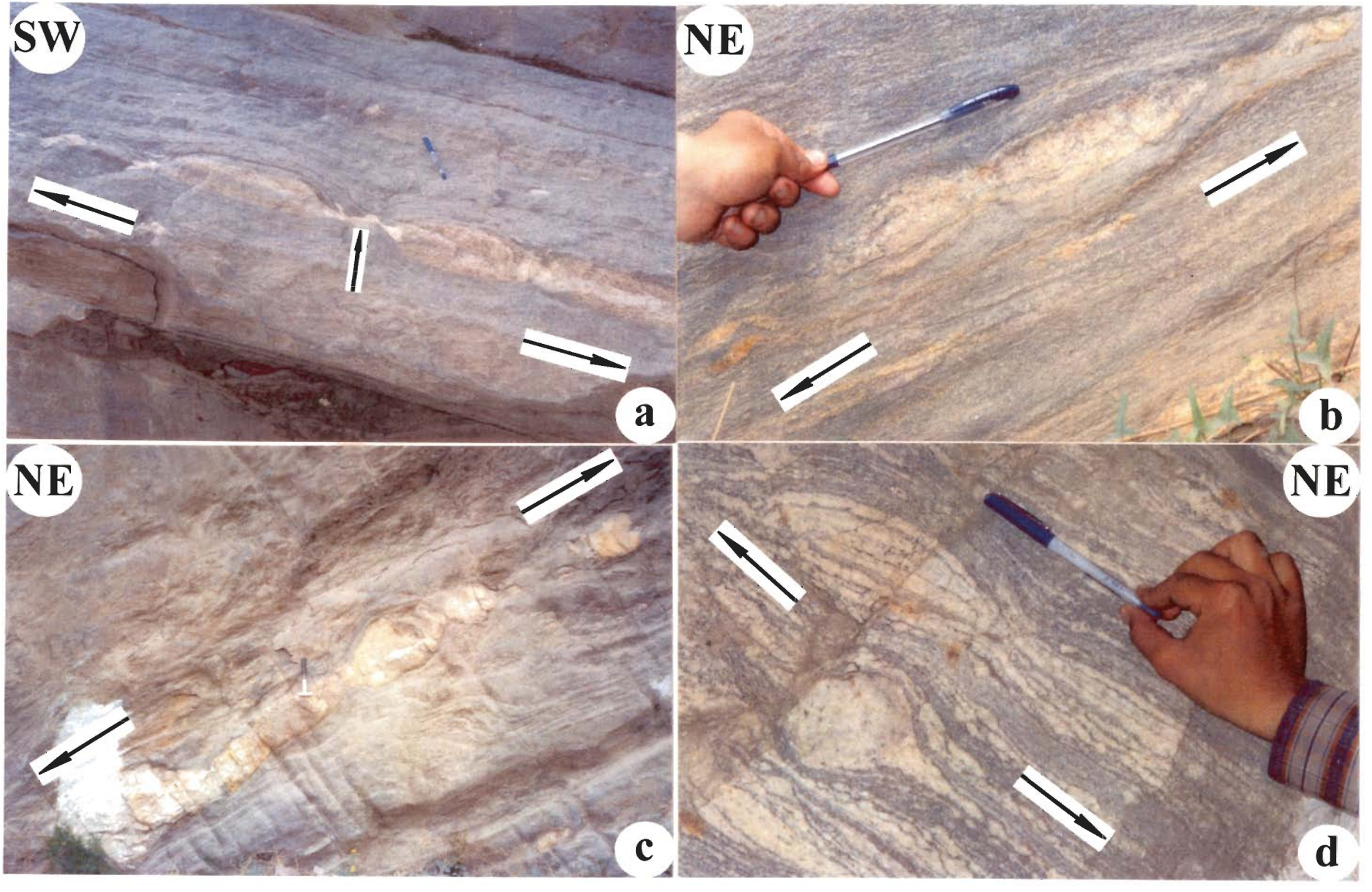

Fig. 3.6

Figure Captions

Fig. 3.7. Duplexes of different sizes from the HHSZ showing consistent top-to-S/SW brittle sense of shear. Some of these duplexes are also affected by secondary brittle shearing. Primary- and secondary brittle shear senses are shown by half arrows '1' and '2', respectively.

Fig. 3.7a Near Samej village, outside the HD1 and HD2.

Fig. 3.7b Within the HD2. Long straight pair of primary brittle shear plains deciphered. At Karcham.

Fig. 3.7c. In migmatitic gneiss. Note that the S-C fabric is also defined by the migmatitic/gneissic foliation, which are parallel to the primary brittle shear plain. Above the C-plane marked, two thrust blocks are pointed out with arrows. Near Shongthong bridge, outside the HD1 and the HD2.

Fig. 3.7d. Synthetic secondary brittle shearing is very prominent. Within the HD1. At Kharo bridge,

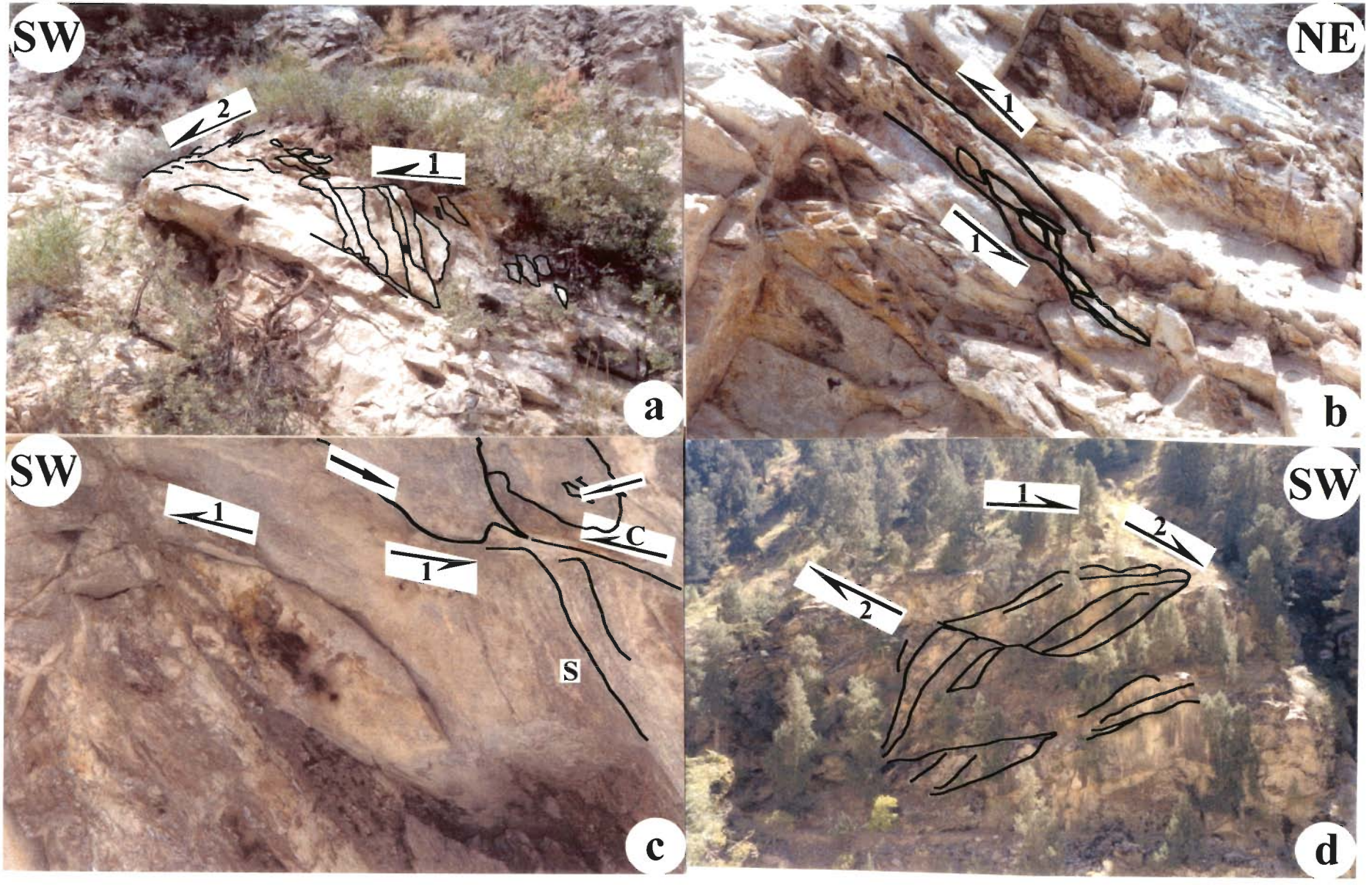

Fig. 3.7

In the HHSZ, including the HD1 and the HD2, late stage brittle shearing with consistent top-to-SW sense is deciphered from sigmoid-shaped duplexes of different dimensions (Figs. 3.7a-d). The roof- and the sole thrusts dip gentle- to moderately steep northeasterly. These thrust planes were traced and were found to be the C-planes for the top-to-SW and the top-to-NE sense of shearing (e.g. Fig. 3.7c). In other words, the pre-existing ductile primary shear planes subsequently acted as the brittle primary shear planes. At places, southwesterly dipping strong synthetic brittle shear planes affect the duplexes (Figs. 3.7a, -d). The secondary brittle shearing event has been excluded from modeling the brittle phase of exhumation (Fig. 3.20, equations 63 to 66 in the Appendix of this chapter).

3.4.3. Micro-structural studies

Thin-sections of rocks of the HD1 and the HD2, oriented perpendicular to the main foliations and parallel to the stretching lineations, were studied. These thin-sections reveal dominantly top-to-NE sense of ductile shearing displayed by S-C fabrics (Berthè et al., 1979) (Fig. 3.8a), mineral fishes (ten Grotenhuis et al., 2002) of sigmoid (Fig. 3.9a) and parallelogram geometries (Fig. 3.9b). The spiral shaped inclusion trails inside the porphyroblasts (Fig. 3.8b) were excluded in deciphering ductile the sense of shearing due to the prevailing controversy of their actual tectonic implications (Bozkurt, 2007 and references therein). Pronounced extension parallel to the main foliation is deciphered from crystal-plastic/ductile deformation indicated by stretching of rigid mineral such as garnet from the HD2 (Fig. 3.8d). At higher magnification, rare and relic top-to-SW sense of shearing is displayed in the rocks of the HD1 as revealed from parallelogram-shaped biotite fishes (Fig. 3.9b)

Figure Captions

Figs. 3.8a-c Shear sense indicators from XZ oriented thin-sections from the HD2 give extensional ductile shearing.

Fig. 3.8a. S-C fabric displayed by micas. C-planes are almost straight. The S-plane is defined by discrete mica grains, and is shown by a broken black line. Curvature of the S-fabric is more prominent only at the contacts with the C-planes. Photo in cross polarized light. Photo length: 5.0mm. Thin-section number: SJ24.

Fig. 3.8b Garnet porphyroblast with prominent tail and inclusions oriented in a sigmoid pattern. In deciphering the sense of shear from this porphyroblast, its shape asymmetry is used; the inclusion patterns are neglected (see figure 7c of Bozkurt, 2007 for similar interpretation). Photo in cross polarized light. Photo length: 2.0mm. Thin-section number: SJ29.

Fig. 3.8c Sheared porphyrblast of garnet. Grain boundary migration of the matrix quartzo-feldspathic minerals into the garnet has partially destroyed its shape. Had there been no grain boundary migration at its boundary, the shape of the deformed grain is shown with black lines. Elongated biotite grains in the matrix, pointed out with arrow, define the C-plane. Photo in plane polarized light. Photo length: 5.0mm. Thin-section number: SJ11.

Fig. 3.8d Extremely elongated garnet grain. Its long axis is parallel to the main foliation (the C-plane of the top-to-NE sense of shearing) indicating pronounced extension. Warping of the main foliation around this grain is marked with blue lines. Photo in plane polarized light. Photo length: 5.0mm. Thin-section number: SJ15.

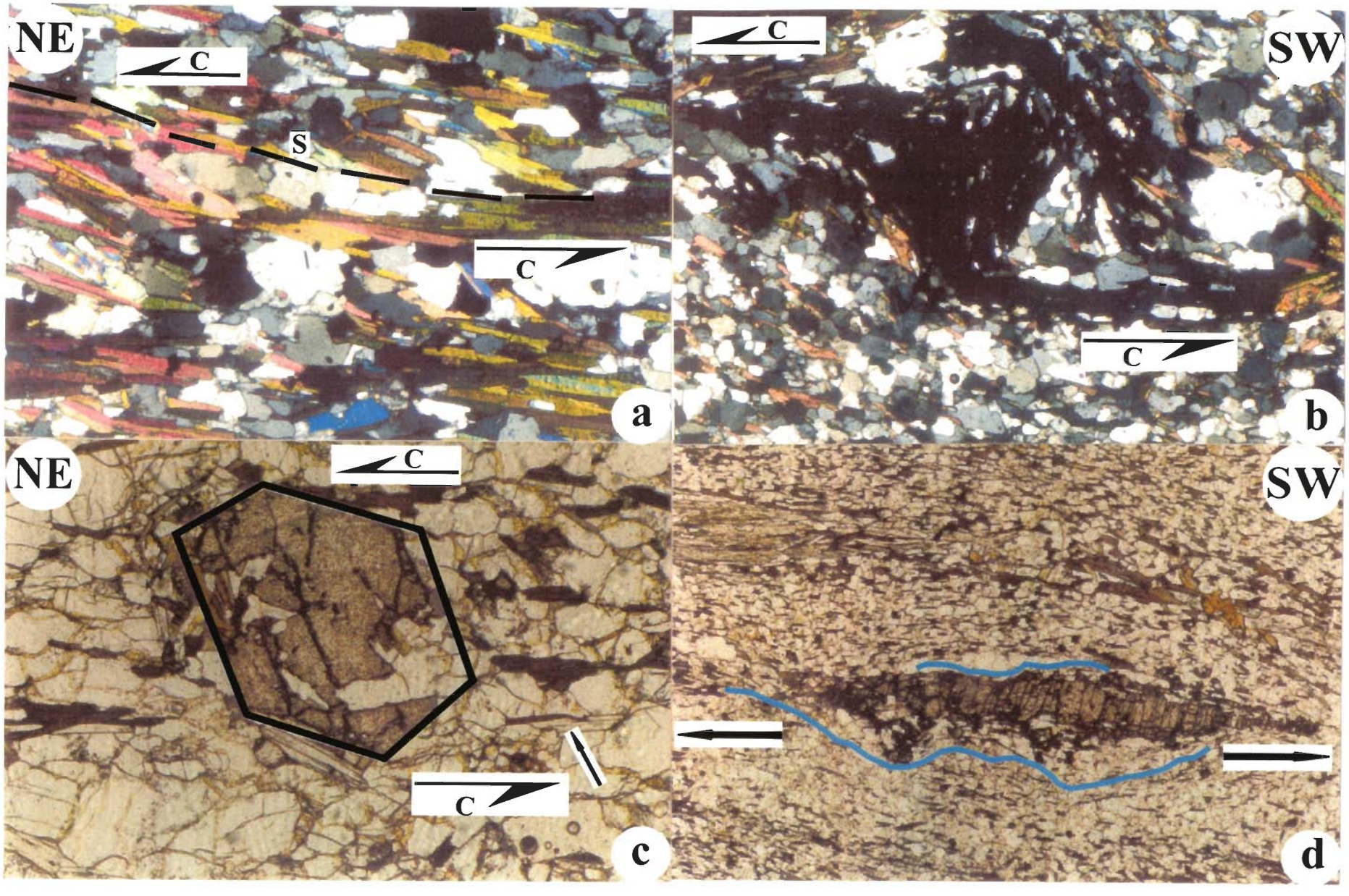

Fig. 3.8

Figure Captions

Fig. 3.9 XZ oriented thin section from the HD1 reveal reversal of ductile shear sense.

Fig. 3.9a Sigmoid muscovite fish giving top-to-NE extensional ductile shearing. The fish has been affected by extensive grain boundary recrystallisation at one of its tips. Photo in cross polarized light. Photo length: 4mm. Thin-section number: SJ34.

Fig. 3.9b Parallelogram-shaped biotite fish giving top-to-SW compressional ductile shearing. The C-plane is prominently marked by fish trail (marked by the arrow 'p'). Migration of boundary of the adjacent quartz grain has slightly destructed the fish outline (marked by the arrow 'q'). Photo in plane polarized light. Photo length: 1mm. Thin-section number: SJ17.

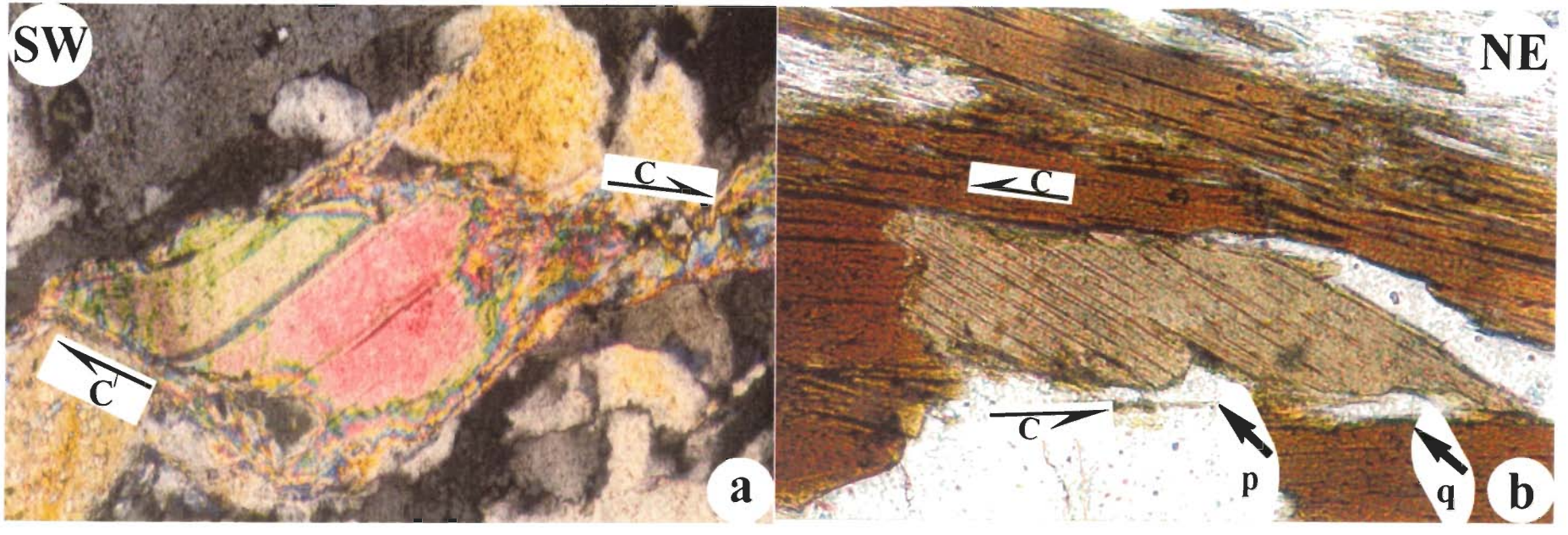

Fig. 3.9

(Fig. 3.9b). Some of the mica fishes demonstrating different shear senses possess a mouth (notch) at one of their corners and may be partially destroyed by dynamic recrystallization.

Top-to-SW sense of brittle shearing is deciphered from asymmetric duplexes defined by stacked minerals- usually micas (Figs. 3.10a, c). Some of these micro-duplexes are identified by their morphological resemblance with different well established geometries of duplexes on field-scales (e.g. McClay and Insley, 1986 and references therein). Micro-scale duplexes have also been reported from the HHSZ in the Zanskar section in the Chapter-2 of this thesis (Figs. 2.10a-d). To the knowledge of the author, this thesis is the first report of micro-scale duplexes. Some of the micro-duplexes are typically hat- or trapezium shaped and with straight grain boundaries. (Figs. 3.10a, -b). Such straight boundaries indicate that the hat shapes of these minerals are definitely not the results of grain boundary migration. It is interesting to note that duplexes with nearly trapezium-shapes have been reported from field and subsequently idealized (Figs. 6.93 and 6.96 of Davis and Reynolds, 1996). Thrust slices of mineral grains, usually micas, which are now surrounded by quartzo-feldspathic matrix (Fig. 3.10b), might be away from the underthrust counterpart grains possibly due to their longer distance of transport. Such grains are not used for shear sense determination. Nearly symmetric stacks of minerals do not reveal any sense of shearing (Fig. 3.10d). Similar symmetric duplexes on field-scales have been diagrammatically presented by Davis and Reynolds (1996).

Figure Captions

Fig. 3.10 Trapezium or hat shaped mineral grains observed in the XZ-oriented thin-sections although the HHSZ (including the HD1 and the HD2), at very high magnification. They have been interpreted in this work as overthrust grains. See text for more discussion. Photo lengths: 1mm.

Fig. 3.10a The longest arm of the hat shaped mica is northeasterly dipping. Top-to-SW sense of brittle searing is deciphered. Sharp primary brittle shear planes are pointed out with arrows. Location: HD2, Karcham. Photo in cross polarized light. Thin-section number: SJ18.

Fig. 3.10b Isolated biotite hat within quartzofeldspathic minerals. Such isolated hats are excluded from the determination of the brittle shear sense. Location: HD1, Between Kashang and Kharo. Photo in plane polarized light. Thin-section number: SJ21a.

Fig. 3.10c Hat of muscovite aggregate over another aggregate of muscovite. Top-to-SW sense of brittle searing is deciphered. Location: near and south to Shonghtongh; outside the HD1 and the HD2. Photo in cross polarized light. Thin-section number: SJ25.

Fig. 3.10d Longest grain boundary of one muscovite hat in contact with the cleavage plane of another muscovite. This grain boundary is sub-parallel to the main foliation (not seen in this photo. Location: at Jeori; outside the HD1 and the HD2. Photo in plane polarized light. Thin-section number: SJ27.

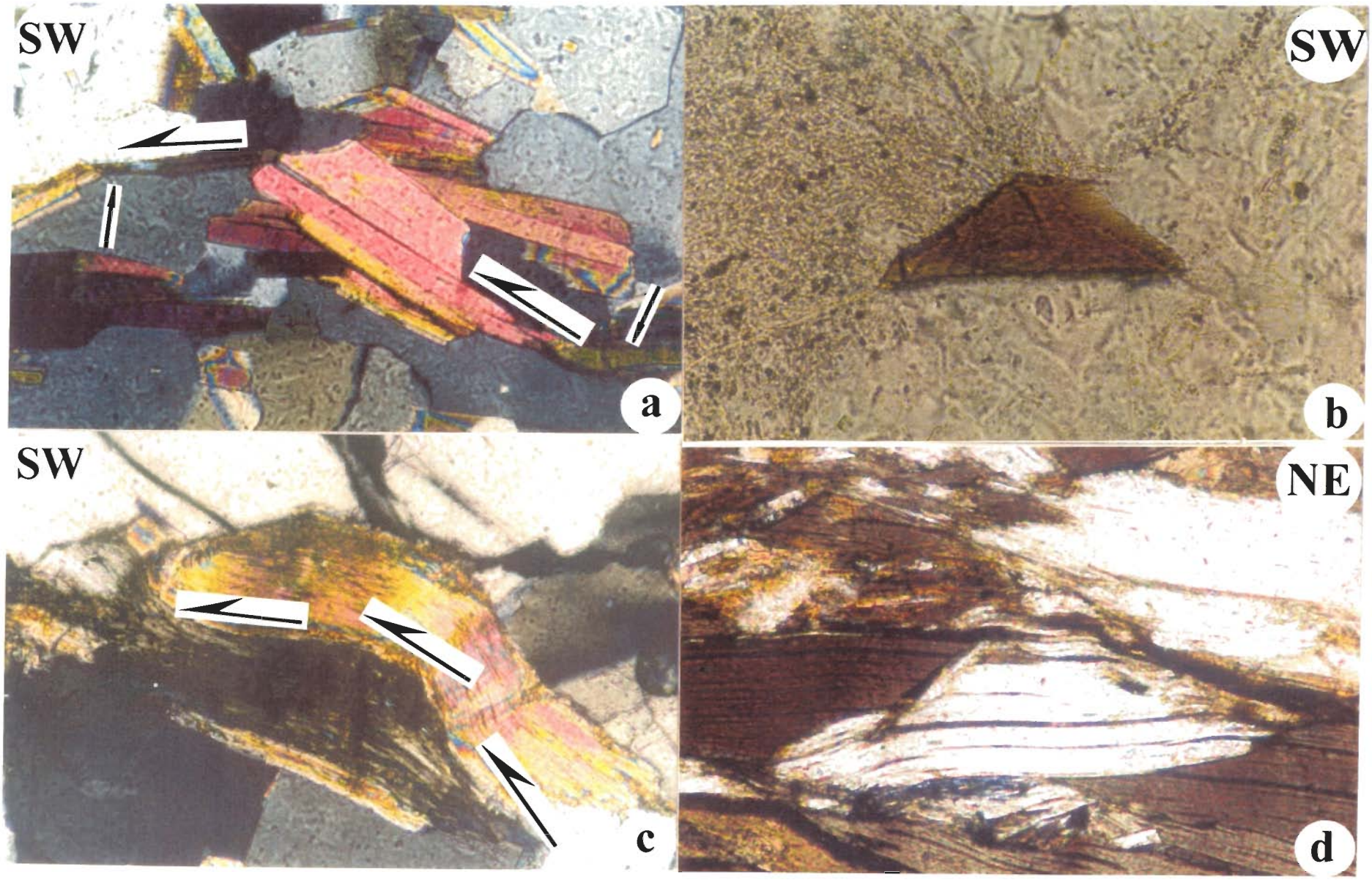

Fig. 3.10

3.5. STRUCTURAL COMPILATION

The structural geology of the HHSZ in the Sutlej section is summarized in a schematic NE-SW cross-section (Fig. 3.11). This cross-section is perpendicular to the main foliations and parallel to the stretching lineations. The ductile- and the brittle deformation phases, as presented as constraints (III) and -(V) of Section-3.7, are utilized to propose a model for exhumation of the HHSZ in the Sutlej section.

3.6. CONSTRAINTS OF THICKNESS

Considering the location of the MCT as given in Fig. 3.1 and the HD1 and the HD2 as delineated in Fig. 3.2, the ratio of orthogonal thicknesses amongst the HD1, the HD2 and the whole of the HHSZ, i.e. HD1:HD2:HHSZ, is calculated to be around 11:1:37. The geometric consideration of this calculation is given in Fig. 3.12. Both the HD1 and the HD2 are much thinner than the remainder of the HHSZ. Secondly, the HD2 is much thinner than the HD1.

3.7. FORMULATION OF THE MODEL

The geological constraints for modeling the exhumation of the HHSZ in the Sutlej section are framed as follows.

(I) Inverted metamorphism within the HHSZ.

(II) The top-to-SW sense of compressional ductile shearing persists throughout the HHSZ. This shearing is of early phase of Neo-Himalayan Period (~25 Ma).

(III) The presence of two zones, the HD1 and the HD2, with a top-to-NE extensional ductile shearing. The HD1 is located within the topmost part of the HHSZ. The HD2

Figure Captions

Fig. 3.11. The dominant structures within the HHSZ, Sutlej section, from the present macro- and micro-structural studies, are summarily presented in a NE-SW cross-section. The HHSZ is bounded by northeasterly dipping Main Central Thrust (MCT) and the Lesser Himalaya (LH) at the south, and the top of the Himalayan Detachment-2 (HD2) and the beginning of the Tethyan Sedimentary Zone (TSZ) at the north. The shearing, marked as '1', implies top-to-SW compressional ductile shearing. The shearing, marked as '2' represent top-to-NE extensional ductile shearing. The shearing, marked as '3', denotes secondary shearing synthetic to shearing '1'. Different shear sense indicators have been used to decipher '1', '2' and '3', but only the S-C fabrics are used in this sketch to represent them. The shearing, marked as $1'$, implies top-to-SW sense of brittle shearing (duplex movement). The number $2'$ implies boudinaging. Boudins of different types (lenticular-, pinch and swell and foliation varieties) are observed within the HHSZ, but are represented by only the lenticular variety in the sketch. HD1 and HD2 represent the two Himalayan detachments where the shearing '2' is confined. LVR and HVR stand for 'low viscosity rocks' and 'high viscosity rocks', respectively. The Diagram is neither to scale nor angle.

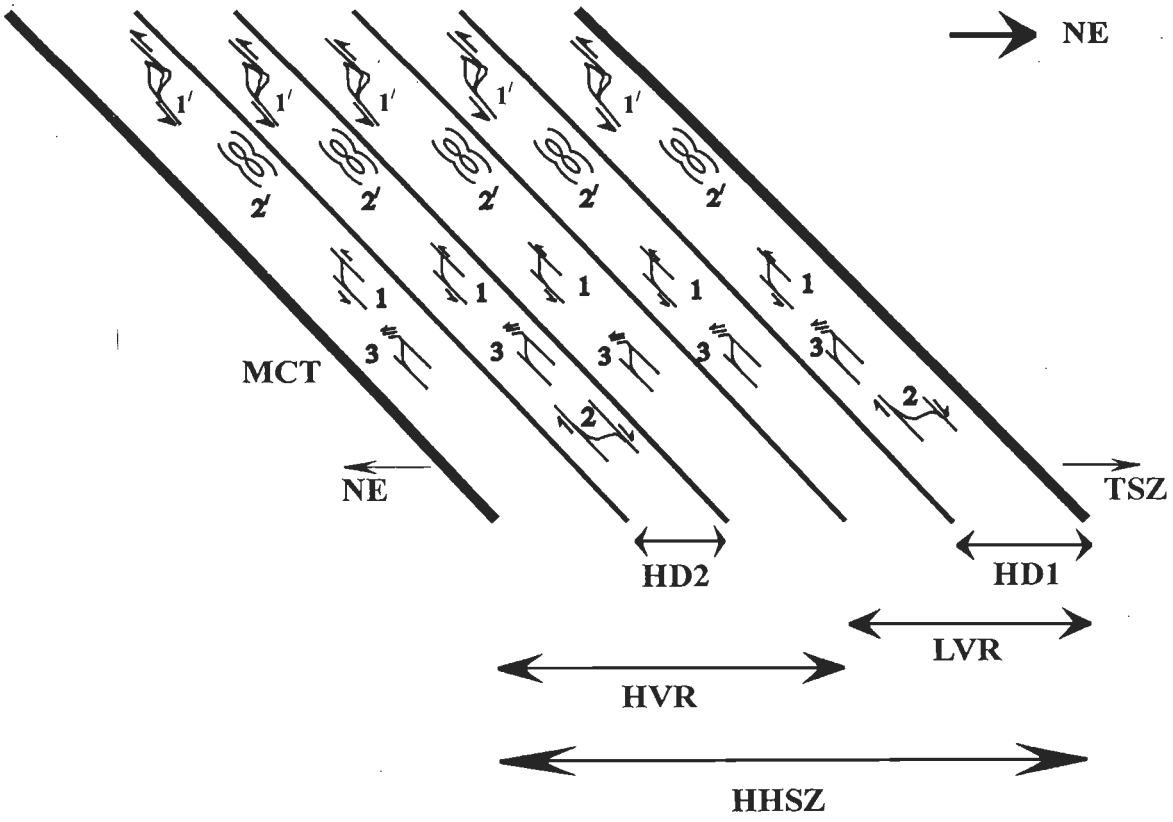

Fig. 3.11

Figure Captions

Fig. 3.12. The HHSZ is idealized as a shear zone (or a channel) with parallel walls dipping northeasterly. The thicknesses of the HD1, the HD2 and the HHSZ, measured on the ground surface, are 'a'', 'b''and 'c'', respectively. Their orthogonal thicknesses are represented by 'a', 'b' and 'c', respectively. From geometry, $a':b':c' = a:b:c$. This relation holds true for any angle of dip of the boundaries of the HHSZ. Using Figs. 3.1 and -3.2, the distances a', b' and c' are measured. These measurements are done along the line MM' as shown in Fig. 3.1. The ratio, a:b:c, comes out to be 11:1:37. Symbols: LH- Lesser Himalaya; MCT- Main Central Thrust; HD1- Himalayan Detachment-1; HD2- Himalayan Detachment-2; HHSZ- Higher Himalayan Shear Zone; and TSZ: Tethyan Sedimentary Zone.

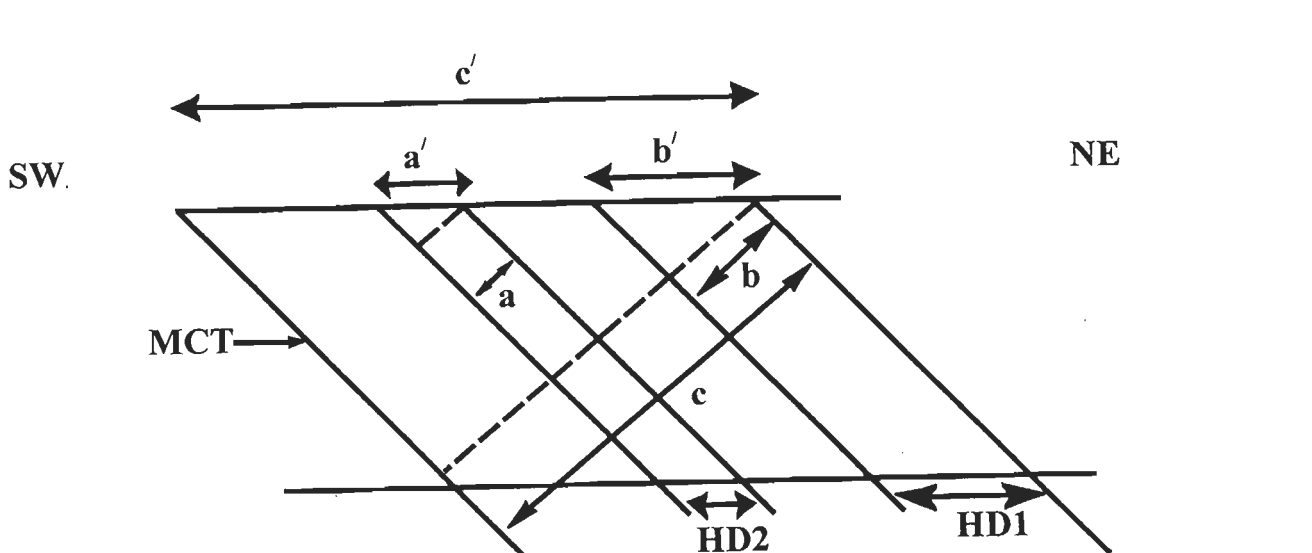

Fig. 3.12

occurs inside the HHSZ, and is thinner than the former. The HD1 and the HD2 lie within the rocks of lower- and higher viscosities, respectively. Both the HD1 and the HD2 are thinner than the whole of the HHSZ. Additionally, the HD2 is much thinner than the HD1. The top-to-NE sense of ductile shearing within the HD1 is ~18 Ma old and was simultaneous with the ongoing top-to-SW sense of shearing in the MCT. The absolute timing of the extensional ductile shearing within the HD2 is not known. Thus, the relative time relation of top-to-NE sense of ductile shearing within the HD1 and the HD2 remains indeterminate.

(IV) The HD2 is laterally discontinuous along the strike of the Himalaya.

(V) At least during part its exhumation, the HHSZ extruded like a fluid.

(VI) A late stage of brittle deformation involving top-to-SW sense of shearing is noted throughout the HHSZ.

3.8. EXISTING MODELS OF EXHUMATION

3.8.1 Summary

Four broad categories of models have been proposed for exhumation of the HHSZ in different sections of the Himalaya. These are (i) thermal models, (ii) coupled thermo-mechanical models, (iii) post-metamorphic deformation models, and (iv) syn-metamorphic deformation models (Yin, 2006). The drawbacks of these models are summarized by Hodges (2000). In the context of the HHSZ in the Sutlej section, one additional drawback of all these models is that none of them can explain the presence of the two detachments- the HD1 and the HD2. Only those models relevant to the present work are discussed below.

3.8.2. The ductile shear model

This model explains inverted metamorphism and exhumation of the HHSZ by considering top-to-SW sense of simple shearing along closely spaced shear planes (Jain and Manickavasagam, 1993) (Fig. 3.13). For a parallel wall infinitely long horizontal channel with thickness $2y_0$ units, full of incompressible Newtonian viscous fluid, and walls sheared with velocities U_1 and $-U_2$, the velocity profile is given by.

$$x = 0.5.(U_1 - U_2) + 0.5.y.\ y_0^{-1}.(U_1 + U_2) \quad \ldots\ \ldots\ \ldots\ (1)$$

(rewriting equation 3 in the Appendix of Chapter-2)

The velocity profile 1 in Fig. 3.14 is the mathematical representation of this model. The model takes care of the fluid flow behaviour of the HHSZ since the velocity profile is derived from fluid mechanics (constraint (V) of Section 3.7). The model cannot explain the occurrence of the zone(s) with a top-to-NE sense(s) of shearing, i.e. the detachment(s). Consequently, neither can it explain the constraints (III) nor -(IV) of Section 3.7.

3.8.3. The channel flow model

In this model, an incompressible Newtonian viscous fluid flows in a single direction through infinitely long parallel horizontal static channel walls. The fluid undergoes laminar flow driven by pressure gradient giving rise to a parabolic velocity profile (curve 2 of Fig. 3.14). For such a channel of thickness $2y_0$ units, the fluid of viscosity μ and the pressure gradient (dP/dx), the velocity profile is given by:

$$x = -0.5\mu.(dP/dx).(y_0^2 - y^2) \quad \ldots\ \ldots\ \ldots\ (2)$$

(see Pai, 1956 for derivation)

Figure Captions

Fig. 3.13 Idealized ductile shear model of inverted metamorphism of the Higher Himalayan Shear Zone (HHSZ) (Jain et al., 2002 and references therein). The HHSZ is bounded by the Lesser Himalaya in the south and the Tethyan Sedimentary Zone in the north. Displacement of isograd boundaries within the HHSZ by top-to-SW sense of simple shearing gives rise to inverted metamorphism and exhumation of the shear zone.

Figure Captions

Fig. 3.14 A channel with parallel, horizontal, infinitely long, NE-SW oriented walls, with thickness $2y_0$ units and full of Newtonian fluid with viscosity μ, is considered. The Y-axis is taken perpendicular to the walls. The X-axis is chosen parallel to, and equidistant from, the walls. Line 1 represents the velocity profile of the simple shear deformation (the E_1 phase of exhumation). The top and the bottom boundaries of the channel are sheared with velocities U_1 and $-U_2$, respectively in the top-to-SW sense and are shown by half arrows. In this case, $(dp/dx)=0$, and U_1 and/or $U_2 \neq 0$. Parabola-2 represents the channel flow, for which $U_1=U_2=0$ and $(dp/dx)\neq 0$. The flow direction is indicated by a solid arrow. Parabola-3 represents the combined simple shear and channel flow, when either or both U_1, $U_2\neq 0$, and $(dP/dx)\neq 0$. The vertex V' of this parabola is located within the upper part of the channel. The line 'Z' passing through V', and parallel to the walls of the channel, demarcates the lower boundary of the HD1. Note that this figure is same as Fig. 2.20 of the previous chapter, and that only the HD1 has been used in place of the ZSZ. Not to scale.

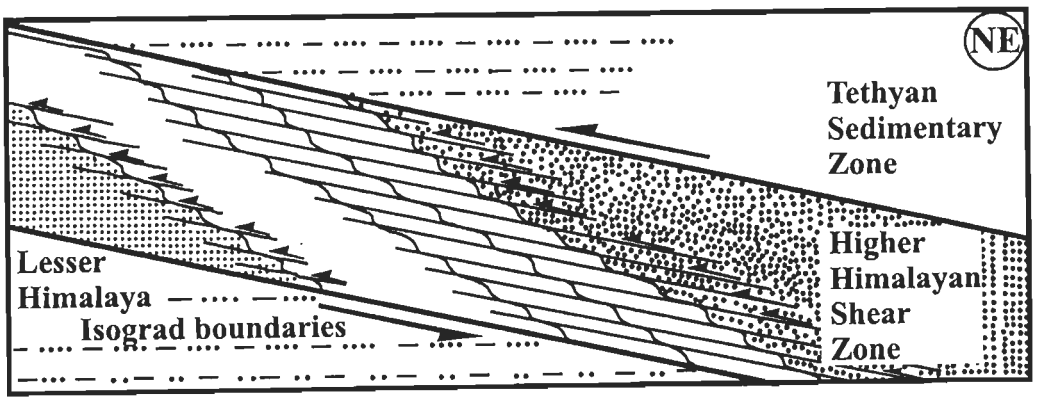

Fig. 3.13

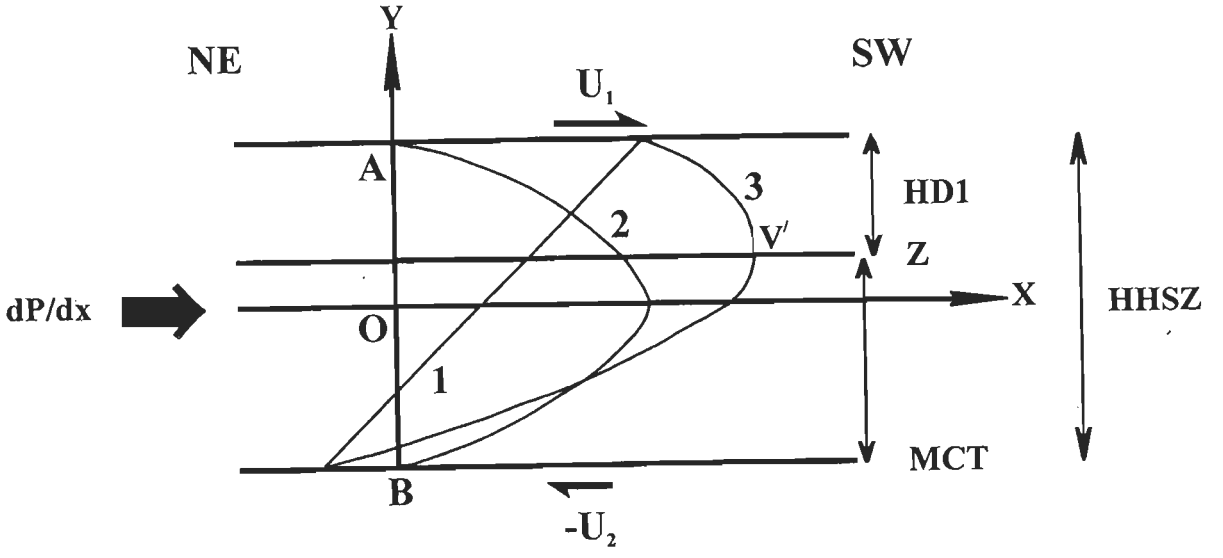

Fig. 3.14

The model takes care of the flow of the HHSZ like a fluid (constraint (V) of Section 3.7). With the geographic orientation of the channel as in Fig. 3.14 and its curve 2, the model can explain the presence of a single zone with a top-to-NE sense of shearing within the topmost part of the HHSZ. Since this zone is of the same thickness as that with a top-to-SW sense of shearing, it is not comparable with the HD1. One additional problem of this model in applying for the HHSZ in the Sutlej section is that it cannot explain the presence of two detachments (constraints (III) and -(IV) of Section 3.7).

3.8.4. The combined simple shear & channel flow model

Elaborating Grujic's (Grujic et al., 2002) conceptual velocity profiles for flow vectors of the Greater Himalayan Crystallines (or the 'HHSZ' of Jain and Anand, 1988) from the Nepal Himalaya, the exhumation of the HHSZ, Zanskar section is explained as a two-phase process. Along with micro-structural evidences from the Zanskar Shear Zone (a continuation of the STDS or the HD1) and mathematical analyses of velocity profiles, the model has been elaborated in Chapter-2. The first phase represents the top-to-SW sense of simple shearing within the HHSZ during the early phase of Neo-Himalayan Period. The velocity profile of the first phase is given by line 1 of Fig. 3.14.

During the second phase, prevalent in the Middle Miocene Period, upward plane Poiseuille flow took place in the HHSZ in combination with a top-to-SW sense of simple shearing. For the geometry-, orientation- and rheology of the channel same as that for the 'channel flow model' described above, the velocity profile for the second phase is given by writing equation 7 in the Appendix of Chapter-2:

$$x = 0.5[(U_1-U_2)+ (U_1+U_2)\, y_0^{-1}.y-\mu^{-1}.(dP/dx).(y_0^2-y^2)] \quad \ldots\ldots\ldots (3)$$

Here U_1 and $-U_2$ stand for the simple shear velocities for the top- and the bottom walls of the channel, respectively. The velocity profile of the second phase is represented by line 3 of Fig. 3.14.

The model takes care of the fluid flow behaviour of the HHSZ (constraint (V) of Section 3.7). The second phase of the model explains the presence of a single zone with a top-to-NE sense of shearing within the topmost part of the HHSZ, which is thinner than the remainder of the HHSZ. This shear zone is comparable with the HD1. However, the model cannot explain the presence of the HD2 (constraint (III) of Section 3.7). Consequently, constraint (IV) of Section 3.7 remains unexplained. Thus, the combined simple shear and channel flow model proposed for the exhumation of the HHSZ, Zanskar section cannot be applied directly that for the Sutlej section.

3.8.5. The general shear model

The "general shear model" involves a combination of pure shear and a top-to-SW sense of simple shear of the HHSZ as the mechanism of its exhumation/extrusion (Vannay and Grasemann, 2001). In this work, the velocity profiles of pure shear (Figs. 3.15a, -b) are deduced first (between equations 1 to 15 in the Appendix of this chapter). This has been followed by the deduction that for the general shear (between equations 16-18 in the Appendix of this chapter; Fig. 3.16). The velocity profile for general shear on a rectangle with length 'L', breadth '$2y_0$', simple shear on the top- and the bottom walls with velocities U_1 and $-U_2$, respectively, and pure shear with velocities U_3 and U_4, respectively, at instant 't' is given by:

Figure Captions

Fig. 3.15a. Pure shear deformation of the rectangle ABCD. A NE-SW geographic direction is assigned. One of its walls, AD, is pressed with velocity V_0. The bottom wall, BC, is maintained static. The coordinate axes are chosen in such a way that B is the origin (0,0) and AB coincides with the Y-axis. Let AD comes to $A'D'$ at instant t=t; V: vertex of the parabola P1; y_0= distance AB; l= distance BC; h_0: distance between AD and BC; P1, P2: parabolic velocity profiles; and h_t: distance between $A'D'$ and BC. Coordinates of A, B, C, D, A', D' and V are given in the diagram. Incompressible rheology of the rectangle has been assumed.

Fig. 3.15b. Pure Shear deformations of the rectangle ABCD. A NE-SW geographic direction is assigned. The top wall, AD, is compressed with velocity U_3. The bottom wall, BC, is compressed with velocity U_4. The Y-axis is chosen coincident with AB. The X axis is chosen parallel to, and equidistant from, AD and BC. Let the lengths of AB and BC are $2y_0$ and L units, respectively. On pure shear, parabolic velocity profiles, P1 and P2, are produced. Points A and B reach A' and B', respectively. Let V and V' are the vertices of P1 and P2, respectively. Incompressible rheology of the rectangle has been assumed in deducing the equation of the velocity profile P1 (equation 16 in the Appendix). Coordinate of V is deduced before equation 5 in the Appendix.

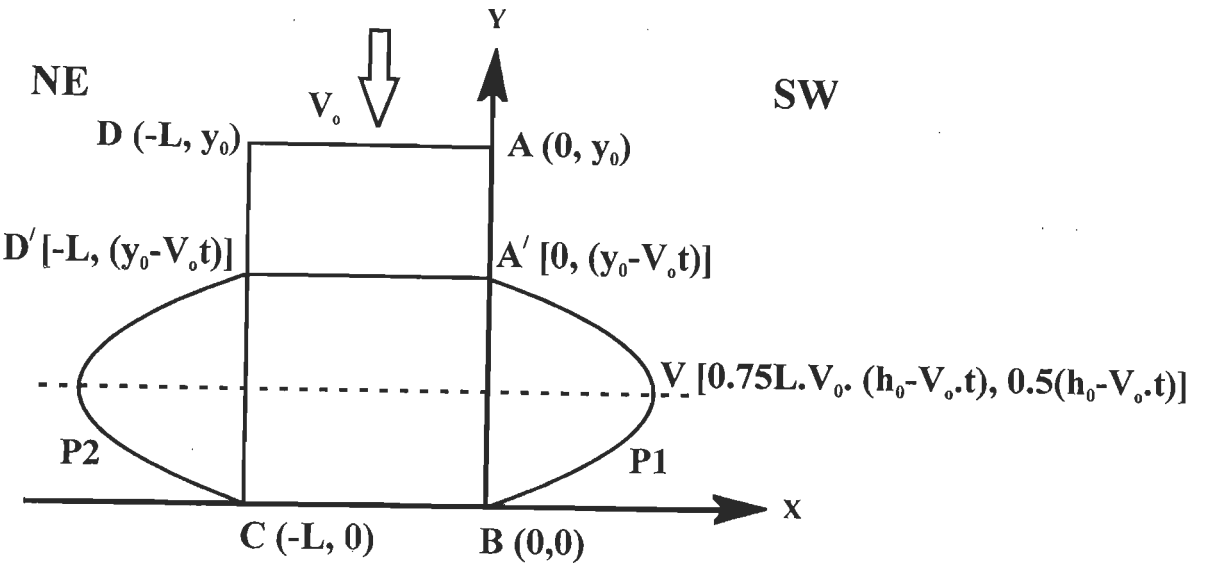

Fig. 3.15a

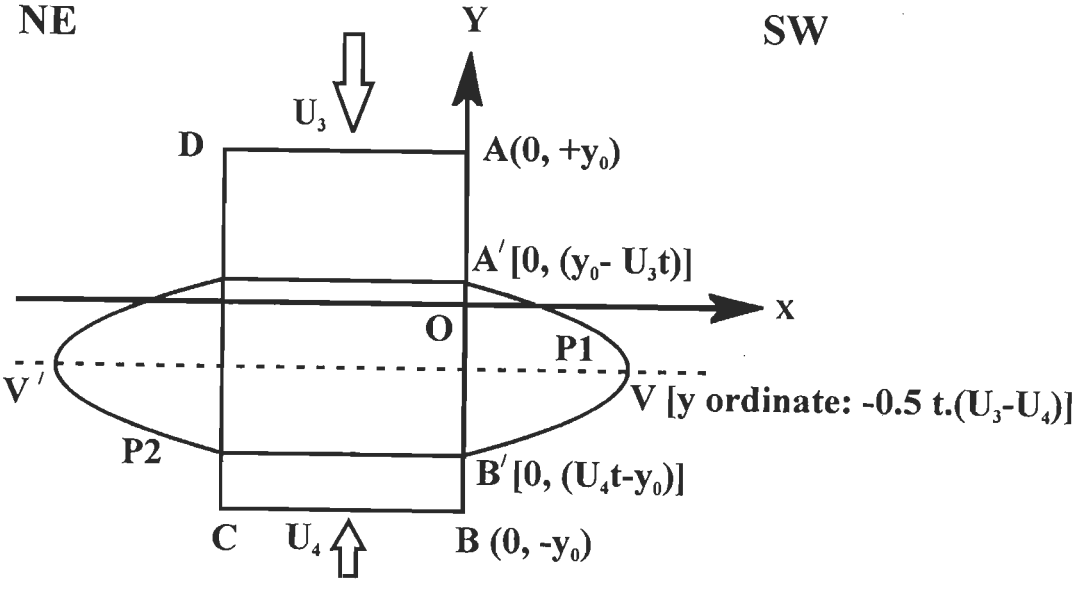

Fig. 3.15b

Figure Captions

Fig. 3.16. The General Shear Model. A rectangular block PQSR with incompressible Newtonian rheology and viscosity μ, and PQ and PR of lengths '$2y_0$' and 'L', respectively is considered. A NE-SW geographic direction is assigned. The Y-axis is chosen coincident with PQ. The X-axis is chosen parallel to, and equidistant from, PR and SQ. Wall PR undergoes simple shear and pure shear with velocities U_1 and U_3, respectively. Wall SQ undergoes these shears with velocities $-U_2$ and U_4, respectively. U_1 and $-U_2$ define top-to-SW sense of shear. In other words, the resultant velocities of the walls PR and SQ are: $R_1=(U_1^2+U_3^2)^{-2}$ and $R_2=(U_2^2+U_4^2)^{-2}$, respectively. The walls move with these velocities at angles $\tan^{-1}(U_3.U_1^{-1})$ and $\tan^{-1}(U_4.U_2^{-1})$, respectively to their lengths. PR and SQ move to $P'R'$ and $S'Q'$, respectively after time t=t. V and V' are the vertices of the velocity profiles of the deformed rectangle at the two boundaries $P'Q'$ and $R'S'$, respectively.

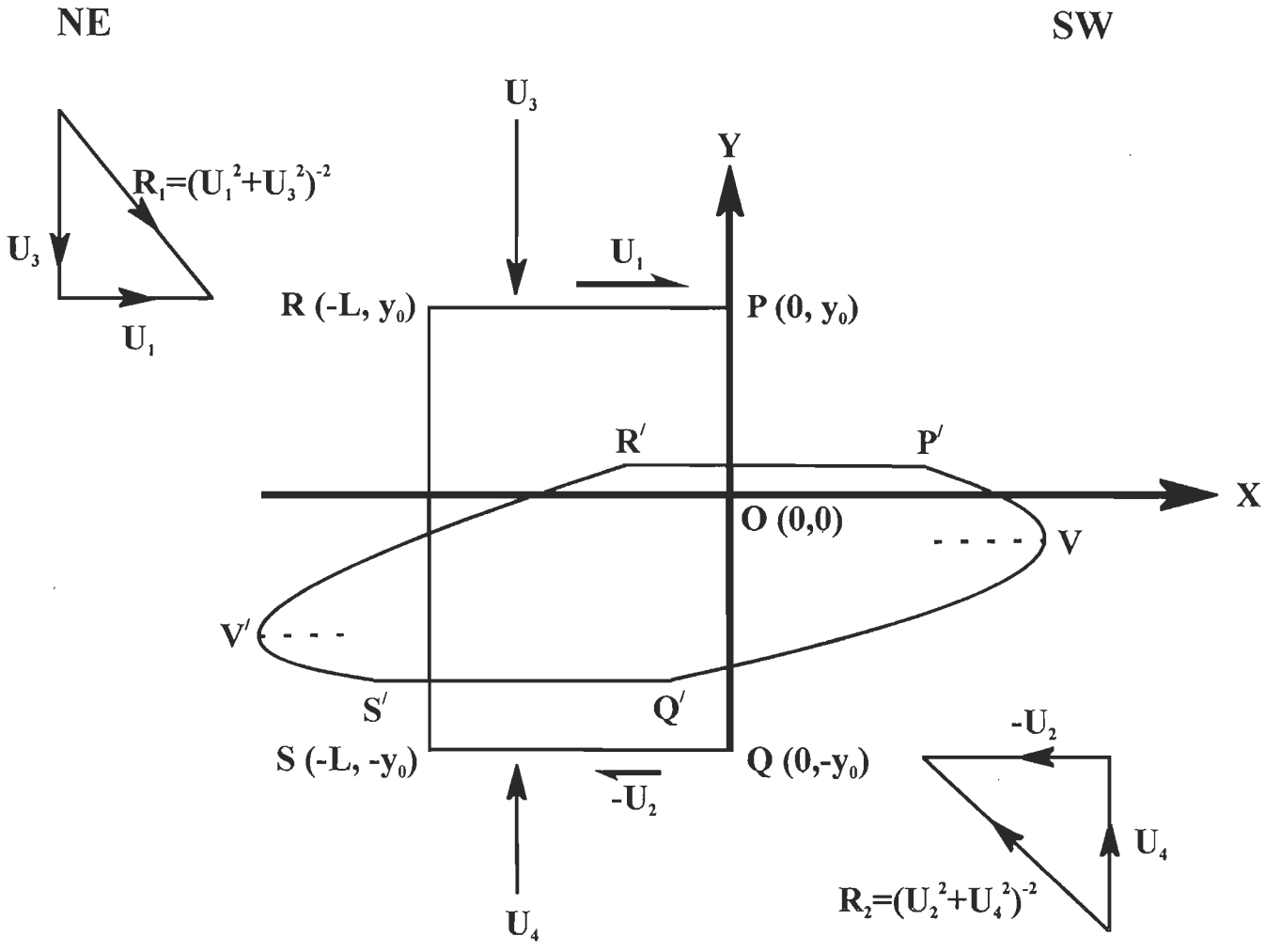
NE
SW
U3
Y
R1=(U1^2+U3^2)^-2
U3
U1
U1
R (-L, y0)
P (0, y0)
R′
P′
X
O (0,0)
V
V′
S′
Q′
S (-L, -y0)
Q (0,-y0)
-U2
-U2
U4
U4
R2=(U2^2+U4^2)^-2

Fig. 3.16

$x=(2y_0-U_3.t-U_4.t)^{-1}[(U_3+U_4).t\{4y_0-t.(U_3+U_4)\}-(2y_0)^2]^{-1}.3Lt.(U_3+U_4)[y^2+(U_3-U_4).y.t+(y_0-U_3.t).(U_4.t-y_0)]+0.5.(U_1-U_2)+0.5.y_0^{-1}(U_1+U_2)$ ... ... (4)

(equation 18 in the Appendix of this chapter)

The deduction assumes constant area deformation. The general shear model takes care of the significant component of pure shear that has been documented from a few sections of the HHSZ. From fold morphometry, Bhattacharya (1981) documented strong flattening near the MCT in the Kumaon Himalaya.

The 'general shear model' of exhumation of the HHSZ in the Sutlej section involves rotation with a vorticity of 0.86, post-metamorphic general shear of the hinterland dipping metamorphic isograds giving rise to gradual thinning and exhumation of the shear zone, inverted metamorphism and formation of the HD1. For the sake of simplicity, the model does not take into account the 'decelerating strain path' as documented from the HHSZ in the Sutlej section and the geothermal gradient (Grasemann and Vannay, 2001). The model, however, takes care of the fluid flow behaviour of the HHSZ (constraint (V) of Section 3.7), since it is derived from the fluid mechanical relations. For certain combination of the parameters U_1, U_2, U_3, U_4, L, y_0 and t,

$(y_0-U_3.t)-0.5*[(U_4-U_3).t-(U_1+U_2)\{(2y_0-U_3.t-U_4.t)\{(U_3+U_4).t.(4y_0-U_3.t-U_4.t)-4y_0^2\}\{1.5L.t.\ y_0^{-1}(U_3+U_4)\}^{-1}]$

is < or = 0 ... ... (5)

In these cases, the zone of shear sense reversal at the top of the shear zone, or the HD1, does not exist (from equations 20 and -21 in the Appendix of this chapter). Further, variation in magnitude of the mathematical expression 5 by varying its constituent parameters can explain the variable thickness of the HD1 in different sections of the

Himalaya. However, the model cannot explain (i) the preexisting top-to-SW sense of ductile shearing throughout the HHSZ including the HD1 and the HD2 (constraint (II) of Section 3.7); and (ii) the occurrence of the HD2 (constraint (IV) of Section 3.7).

3.9. PROPOSED EXHUMATION MECHANISM

To satisfy all the constraints in Section 3.7, the following model of exhumation of the HHSZ in the Sutlej section is proposed. The MCT and the top of HD1 are considered as the parallel walls of a very long channel. The exhumation phase 'E' is sub-divided into three phases: $E=E_1+E_2+E_3$. The first two phases, the E_1 and the E_2, represent exhumation in the ductile regime. The last E_3 phase stands for the exhumation in the brittle regime.

The E_1 phase (line 1 in Fig. 3.14): A top-to-SW sense of non-coaxial shearing of the HHSZ took place by shear movement of its walls during this phase, possibly during the early phase of the Neo-Himalayan Period. The velocity profile of this phase is given by:

$$x = 0.5.(U_1-U_2)+0.5.y.(U_1+U_2)y_0^{-1} \quad \ldots\ldots\ldots (6)$$

(equation 3 in the Appendix of Chapter-2)

Here $2y_0$ is the thickness of the infinitely long parallel wall horizontal channel full of Newtonian viscous fluid; U_1 and $-U_2$ are the velocity of shear of the top and the bottom walls; respectively; 'x' is the velocity of the fluid at distance 'y' from the origin along the Y-axis. The proposed E_1 phase is same as that proposed for the Zanskar section of the HHSZ as discussed in Chapter-2.

The E_2 phase (Fig. 3.17): In this work, this phase has also been referred as the 'shifting simple shear and channel flow', and abbreviated as the shifting 'combined flow'. During

this phase, rocks of the HHSZ underwent rheological weakening and subsequent reduction in viscosities to the extent that exhumation took place in the southwest direction by a combination of the upward flow induced by the pressure gradient (channel flow/plane Poiseuille flow) and ongoing top-to-SW simple shearing. The flow during this E_2-phase took place in two spatially restricted pulses. During the Middle Miocene Period, one of these pulses persisted throughout the HHSZ. The velocity profile is given by:

$$x_1=0.5.(U_{11}-U_{21})+0.5.\ y_0^{-1}\ (U_{11}+U_{21}).y-0.5\mu_1^{-1}.(dP_1/dx)(y_0^2-y^2) \quad \ldots\ \ldots\ \ldots\ (7)$$

(from equation 22 in the Appendix of this chapter)

where U_{11} and $-U_{12}$ are the velocities of shear of the walls of the very long paralle wall horizontal channel of thickness $2y_0$ units, and full of incompressible Newtonian fluid of viscosity 'μ_1'. (dP_1/dx) stands for the pressure gradient applied on the fluid. The pulse of this E_2-phase is same as the E_2 phase for the HHSZ, Zanskar section as discussed in Chapter-2.

The other pulse was restricted within the structurally lower part of the HHSZ- bounded by the MCT at the bottom- and the top of the HD2 as the upper boundary. Referring to Fig. 3.17, the line (y+t)=0 is considered as the upper boundary of the HD2. Let U_{21} and $-U_{22}$ stand for the velocities of shear on the top- and the bottom boundaries, and (dP_2/dx') as the pressure gradient. The velocity profile of this pulse, within the sub-channel, is given by:

$$x'=0.5.(U_{12}-U_{22})+(U_{12}+U_{22})(y_0-t)^{-1}.[y-0.5.(y_0+t)]-0.5\mu_2^{-1}.(dP_2/dx')[(y_0+t)-\{0.5.(y_0^2+t^2)\}-y^2]$$

$$\ldots\ \ldots\ \ldots\ (8)$$

(equation 24 in the Appendix of this chapter)

Figure Captions

Fig. 3.17. "The shifting combined flow". The combined simple shear and channel flow is assumed to have taken place in two pulses. With the same choice of the channel, its geographic orientation, the rheology of the fluid inside it, the coordinate axes and the marker as in Fig. 3.14, one of these pulses took place throughout the channel. This was guided by shear velocities of the walls U_{11} and $-U_{21}$, and the pressure gradient (dP_1/dx), which gave rise to the parabolic profile T_1. Another pulse took place between the lines $(y+y_0)=0$ and $(y+t)=0$. This was guided by shear velocities of the walls U_{12} and $-U_{22}$, and the pressure gradient (dP_2/dx'), which gave rise to the parabolic profile T_2. To deduce the velocity profile of this flow, the X axis is shifted to X' equidistant from the lines $(y+y_0)=0$ and $(y+t)=0$. A dashed lines passing through the vertices of the parabolic profiles T_1 and T_2 define the respective detachments- the HD1 and the HD2. See equations 22 to 30 in the Appendix for derivations.

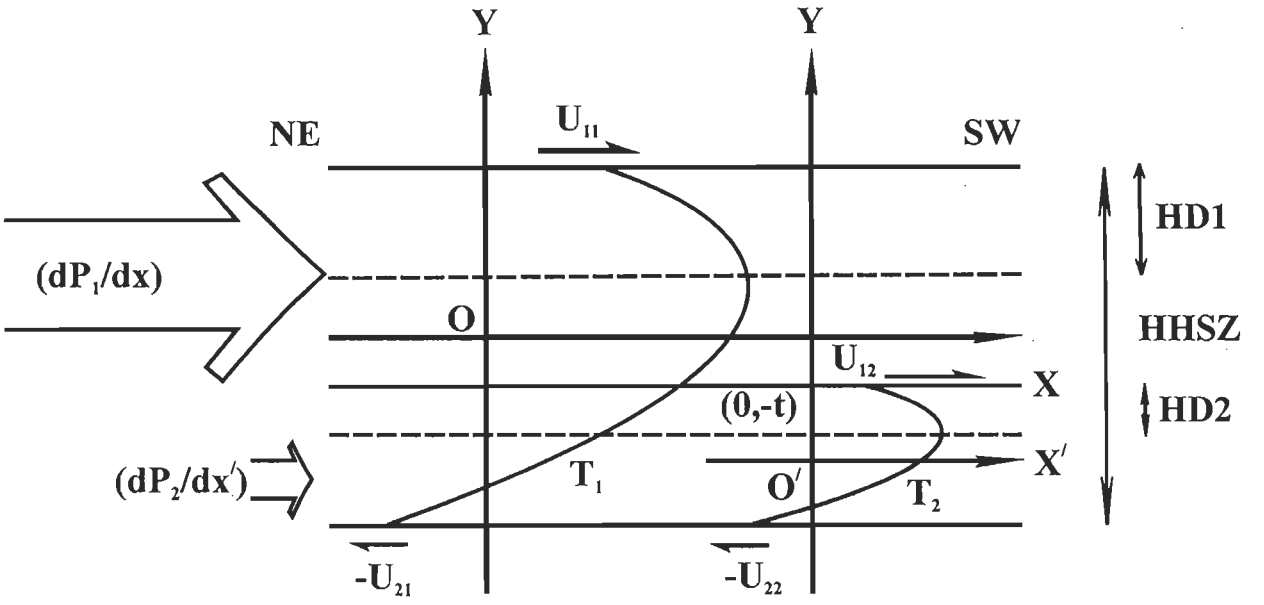

Fig. 3.17

The 'discussions and summary' of this mathematical analysis, given in the Appendix of this chapter, is briefly reproduced as follows. The spatial positions of the HD1 and the HD2 produced in this model matches with that observed in the HHSZ in the Sutlej section. The model HD1 and -HD2 are thinner than the remainder of the HHSZ. Taking the liberty of choosing the flow parameters, the geometry of the channel, and the rheology of the fluid, the lesser thickness of the HD2 than that of the HD1 can be explained. Even with the prevailing combined flow, the HD2 is expected to be discontinuous along the trend of the Himalaya. Both these pulses involve flow of the HHSZ. These satisfy all the constraints in Section-3.7. Further, the model predicts that: (i) The HD1 might be absent in certain sections of the Himalaya; and (ii) the bases of the HD1 and the HD2 exhumed at highest rates during the respective pulses.

The reason why the shifting 'combined flow', involving the development of the two detachments one after another, is chosen as the exhumation mechanism is as follows. Two shear zones with a top-to-NE sense of shearing with spatial positions of HD1 and the HD2 cannot be simulated simultaneously for the other possible cases of (i) two viscous layers of the HHSZ and the activation of the combined simple shear and channel flow (Fig. 3.18 equations 31-53 in the Appendix of this chapter and subsequent discussions); (ii) the flow of the HHSZ like a fluid restricted only to the top migmatite layer with low-viscosity (Fig. 3.19 equations 54-61 in the Appendix of this chapter and subsequent discussions); and (iii) analog modeling considering parallel-, gently- and strongly divergent walls of the inclined HHSZ Analog modeling has been discussed in Chapter-4.

Figure Captions.

Fig. 3.18. We choose the channel, its geographic orientation, the coordinate axes and the marker same as that of Fig. 3.14. The channel is assumed to be full of two Newtonian viscous fluids with viscosities μ_1 and μ_2 ($\mu_1<\mu_2$). Symbols: MCT: Main Central Thrust; A/M: upper boundary of the HHSZ passing between Akpa and Morang; Sh: Shongthong. Between the lines passing through 'Sh' and 'A/M', the fluid of lower viscosity (μ_1) is confined. Between the line passing through 'Sh' and the MCT, the fluid of higher viscosity (μ_2) is confined. The two media are subjected to the same pressure gradient (dP/dx). The topmost- and the bottommost walls are sheared with velocities U_1 and $-U_2$, respectively, in the top-to-SW sense. The possible parabolic velocity profiles, 1 to 10, are shown along with the different positions of their vertices. Profiles 1-5 and 6-10 are inside the fluid layers with lower- and higher viscosities, respectively. The dashed part of these velocity profiles remain outside the respective flow domains, and are drawn in order to show the locations of their vertices. Small black circles represent vertices of the parabolas 1 to 10. For the sake of representation in a single diagram, these parabolas have been drawn side by side. *They do not represent movement of the marker from one profile to another with time.* For northeasterly dipping channel, velocity profiles -1, -2, -4 and -5 do not give rise to the HD1. Only profile-3 gives rise to the HD1. The lower boundary of this HD1 is shown by a dashed line. In the lower fluid media of higher viscosity, profiles-6, -7, -9 and -10 do not give rise to the HD2. Only for profile-8, a detachment forms. The lower boundary of this detachment is marked by a dashed line. However, this is not comparable with the HD2 as observed in the Sutlej section. See Appendix for discussions and equations 31 to -53 for derivations of the velocity profiles.

Fig. 3.19. We choose the channel- its geographic orientation, the rheology of the fluid inside it, the coordinate axes and the marker same as that of Fig. 3.14. It is assumed that the pressure gradient (dP/dx) acts within a sub-channel defined by the lines y=t and $y=+y_0$. The master channel undergoes shear of its boundary walls with the velocities $+U_1$ and $-U_2$. Different possible positions of vertices of the parabolic velocity profiles in the top sub-channel are shown by the parabolic profiles -1, -2 and -3. Note that for the sake of representation in a single diagram, these parabolas have been drawn side by side. *They do not represent movement of the marker from one profile to another with time.* For northeasterly dipping channel walls and for profiles -2 and -3, the HD1 does not form. The HD2 is not simulated within the bottom sub-channel. Symbol- Sh: Shongthong. See equations 54 to 61 in the Appendix for relevant derivations.

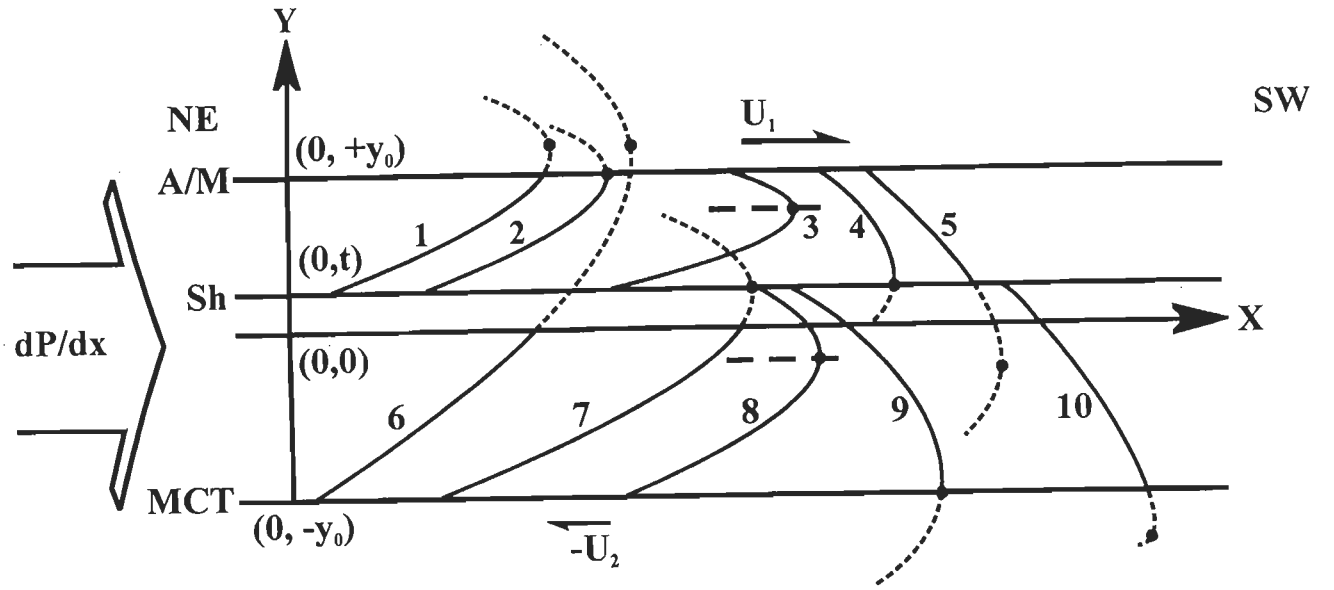

Fig. 3.18

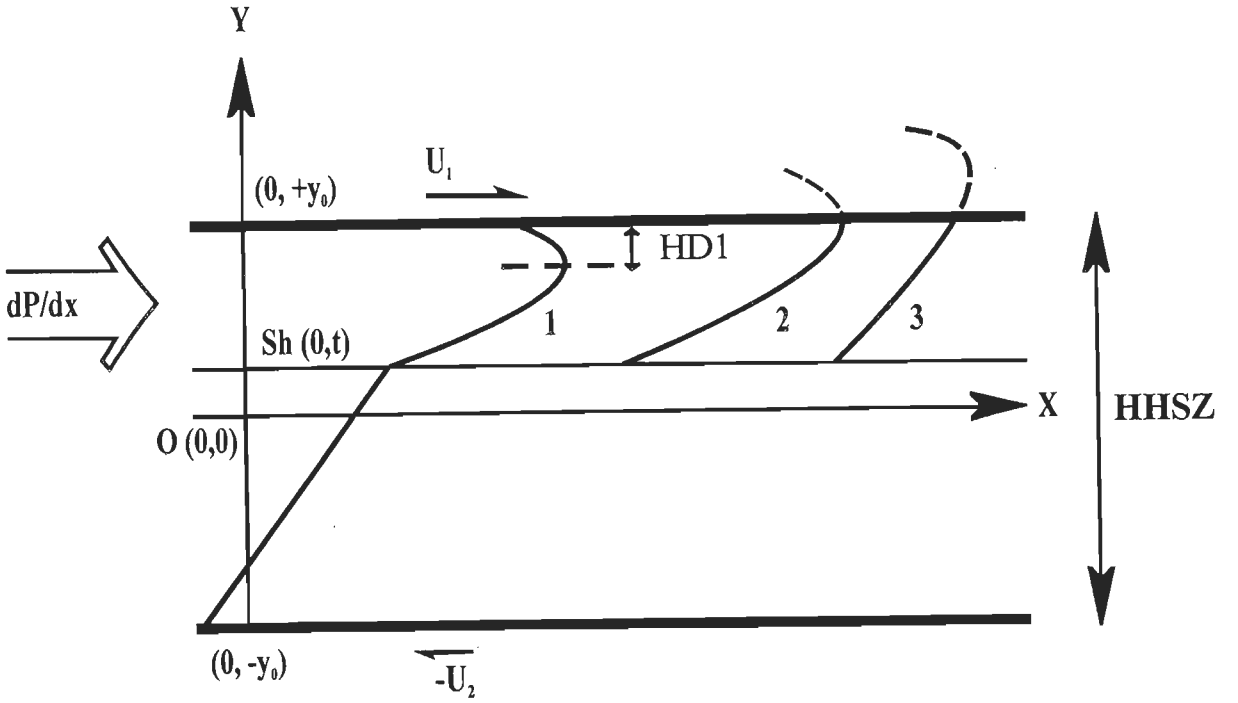

Fig. 3.19

The E_3 phase (Fig. 3.20): The consistent top-to-SW sense of brittle slip noted throughout the HHSZ in the Sutlej section has been documented along the pre-existing primary shear planes. This phase of exhumation is idealized and the velocity profile of the slipped markers are derived (equations 62 to -65 in the Appendix of this chapter) considering that the (i) HHSZ consists of brittle shear planes of even numbers (2n) and with equal spacing ($y_0.n^{-1}$), and (ii) the total amount of brittle slip (U_5+U_6) imparted by the movement of the boundary walls- the MCT and the top of HD1- is equally distributed into the amount of $0.5.n^{-1}(U_5+U_6)$ amongst the brittle slip planes inside the HHSZ. The velocity profile of this phase for the p-th layer from the origin is given by:

$x=0.5*[(U_5-U_6)+n^{-1}(p+1)(U_5+U_6)]$ ... ... (9)

which is defined within the range: $y=(n^{-1}\ y_0.p)$ to $y=[n^{-1}.y_0\ (p-1)]$.

(equation 65 in the Appendix of this chapter)

3.10. APPENDIX

(I) Derivation of velocity profile for general shearing:

(Ia) Velocity profile for pure shear will be derived first. It will be then be added up with that of simple shear to obtain the velocity profile for general shear.

With the choice of axes and symbols as of Fig. 3.15a, a rectangle ABCD is considered. Let the top wall AB is pressed with velocity V_0. The other length side of the rectangle, CD, is considered static. The velocity profile P1, at one side AB of the rectangle ABCD is given by:

$x=3.L.V_o.y.(1-y.h_t^{-1})h_t^{-2}$ (Spurk 1993) ... ... (1)

Figure Captions

Fig. 3.20 The E_3 phase of exhumation in the brittle regime. The HHSZ is considered as a channel of thickness of '$2y_0$' units consisting of '2n' number of brittle planes that are equidistant from each other. The Y-axis is chosen as the passive marker perpendicular to the walls. The X axis is taken equidistant from, and parallel to, the walls. The applied brittle shears on the walls are U_5 and $-U_6$. The marker is assumed to be broken across each brittle shear planes i.e. into '2n' parts. The distance between the subjacent and the superjacent broken marker are =s. Consistent top-to-SW sense of brittle shearing is allowed in this model. See equations 62 to 65 in the Appendix for derivation of the velocity profiles of the markers.

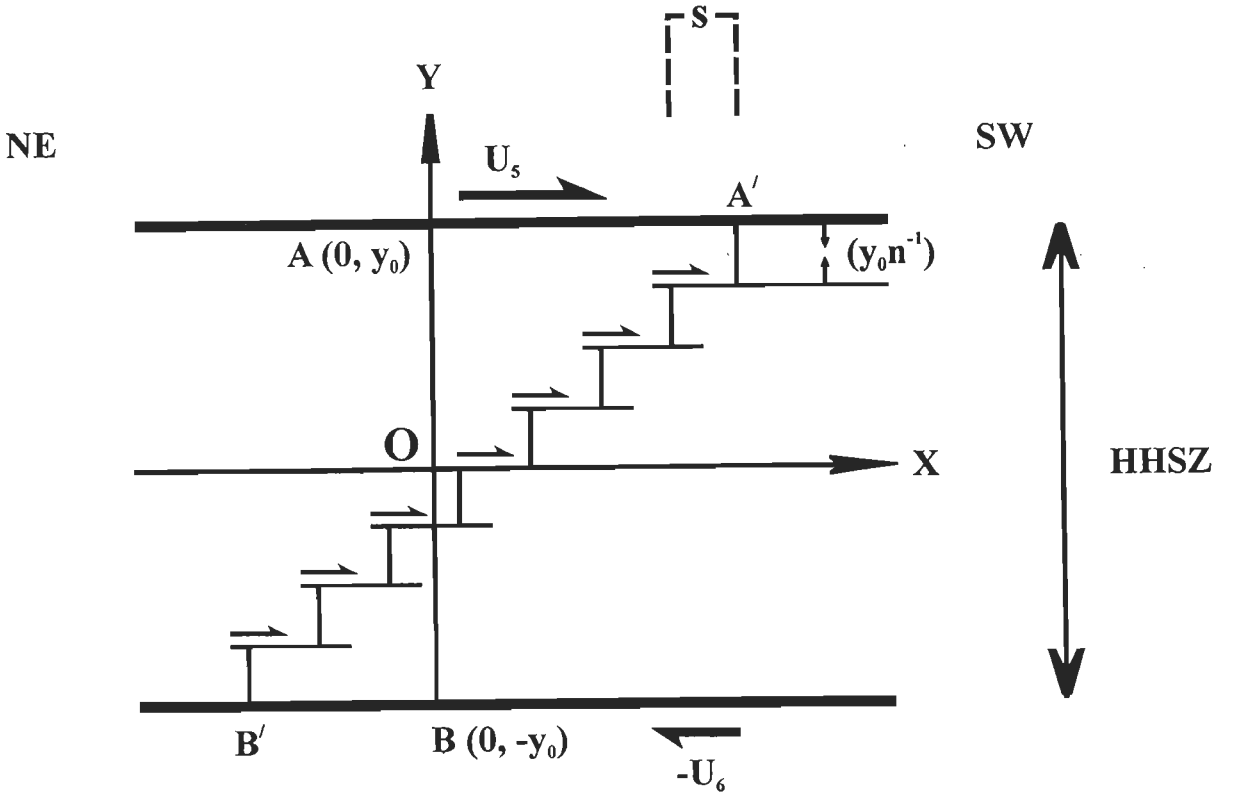

Fig. 3.20

where, L: length, BC or AB, of the rectangle; t: time instant starting from t=0; $V_o t$: distance traveled by AB between t=0 to t=t; h_0: the breadth of the rectangle ABCD, i.e. AB=BC; h_t : distance between the walls $A'B'$ and BC at t=t; x_{max}: maximum velocity on the velocity profile P1; $(h_0-V_o.t)= h_t$. Equation 1 is quadratic expression of 'y', hence represents a parabola. Area bounded between the parabola-1 and the line $A'B$ between the coordinates (0, 0) and (0, h_t) is given by:

$$A_1=3.L.V_o.h_t^{-2}\int_0^{h_t} y\,(1-y.h_t^{-1})\,dy \qquad \ldots\ldots\ldots (2)$$

This comes out to be

$$A_1=0.5.L.V_o \qquad \ldots\ldots\ldots (3)$$

Let the velocity profile at the left hand side of the line BC is P2. Similarly, the area bounded between P2 and BC between the coordinates (-L, 0) and (-L, $(h_0-V_o.t)$) is obtained as: $A_2=0.5.L.V_o$. So, $(A_1+A_2)=L.V_o$, which is same area of ABCD minus the area of $A'BCB'$ i.e. the area of the rectangle $AA'B'B$. Thus the pure shear, represented by equation 1, is a constant area deformation. Now equation 1 can be written in the following form:

$$(y-0.5.h_t)^2=-0.33.\,L^{-1}.V_0^{-1}.h_t\,(x-0.75L.V_0.h_t) \qquad \ldots\ldots\ldots (4)$$

Comparing equation 4 with the standard form of the parabola $(Y-P)^2=-4Q(X-R)$, coordinate of its vertex is obtained as: V $[0.75L.V_0.\,(h_0-V_o.t),\ 0.5(h_0-V_o.t)]$. The velocity

profile being a parabola, x-ordinate on the profile attains a maximum value at the vertex. The vertex is equidistant from the walls (as obtained by its y-ordinate- $(0.5.(h_0-V_o.t))$.

(Ib) Applying these constraints on pure shear in a generalized situation on a rectangle ABCD where a pair of opposite walls, AD and BC, move with unequal velocities U_3 and U_4, $(U_3>U_4)$, will be investigated (Fig. 3.15b). Let AD and AB are of lengths 'l' and '$2y_0$' units, respectively. Points A $(0, y_0)$ and B $(0, -y_0)$ on the two walls, after instant 't' come to A' and B'. The co ordinates of these points are given by $A'(0, y_0-U_3.t)$; and $B'(0, U_4.t-y_0)$.

The vertex of the parabola will be equidistant from these two points. Thus the Y-ordinate of vertex of the parabola is: $-0.5\ t.(U_3-U_4)$. Let the X-ordinate of the vertex is 'p'. Thus its co-ordinate $[p, -0.5.t.(U_3-U_4)]$. Let the equation of this parabola is:

$$y^2+D.x+E.y+F=0 \quad \ldots\ldots\ldots (5)$$

Putting the co-ordinate of A' and B' in this equation, E and F are solved as:

$$E=(U_3-U_4).t \quad \ldots\ldots\ldots (6)$$

$$F=(y_0-U_3.t).(U_4.t-y_0) \quad \ldots\ldots\ldots (7)$$

Putting 6 and -7 in equation 5:

$$y^2+D.x+(U_3-U_4).ty+ (y_0-U_3.t).(U_4.t-y_0)=0 \quad \ldots\ldots\ldots (8)$$

Area bounded by this parabola with the y-axis between coordinates $[0, (y_0-U_3.t)]$ and $[0, (U_4.t -y_0)]$ is given by:

$$A_1=\int_{(U_4.t-y_0)}^{(y_0-U_3.t)} x\,dy \qquad \ldots\ldots\ldots (9)$$

Putting 'x' in equation 9 from equation 8:

$$A_1=-D^{-1}\int_{(U_4.t-y_0)}^{(y_0-U_3.t)} [y^2+(U_3-U_4).ty+(y_0-U_3.t).(U_4.t-y_0)]dy \qquad \ldots\ldots\ldots (10)$$

or, $A_1=-0.17.D^{-1}.(2y_0-U_3.t-U_4.t).\{4(y_0-U_3.t)(U_4.t-y_0)-t^2.(U_3-U_4)^2\}$ $\ldots\ldots\ldots (11)$

Alternate expression of equation 11 is:

$A_1=-0.17D^{-1}[2y_0-t.(U_3+U_4)][\{(U_3+U_4).t\}.\{2.(2y_0)-(U_3+U_4).t\}-(2y_0)^2]$ $\ldots\ldots\ldots (12)$

It is assumed that the material in the rectangle is incompressible, i.e. it undergoes constant area deformation. The area bounded by the parabola P1 with the Y-axis is half to that of area lost from the original rectangle due to compression, i.e.

$A_1 = 0.5.(U_3+U_4).t.L$ $\ldots\ldots\ldots (13)$

Eliminating 'A_1' from equations 12 and -13,

$D=-0.33.t.^{-1}L^{-1}.(U_3+U_4)^{-1}.(2y_0-U_3t-U_4t)[t.(U_3+U_4)\{4y_0-(U_3+U_4).t\}-(2y_0)^2]$ $\ldots\ldots\ldots (14)$

From equations 6, -7, -14 and -5 the parabolic velocity profile for pure shear is given by:

$y^2-x.(2y_0-U_3.t-U_4.t)[(U_3+U_4)\{4y_0-t(U_3+U_4)\}-(2y_0)^2].0.33.t.^{-1}L^{-1}(U_3+U_4)^{-1}+t.y\,(U_3-U_4)$

$+(y_0-U_3.t).(U_4.t-y_0)=0$ $\ldots\ldots\ldots (15)$

Or,

$$x=(2y_0-U_3.t-U_4.t)^{-1}[(U_3+U_4).t\{4y_0-(U_3+U_4).t\}-(2y_0)^2]^{-1}.3L.t(U_3+U_4)[y^2+(U_3-U_4).t.y+(y_0-U_3t).(U_4.t-y_0)] \quad \ldots\ldots\ldots (16)$$

(Ic) Now a rectangular block full of incompressible Newtonian rheology and viscosity μ undergoing general shear is considered (Fig. 3.16). The velocity profile is represented by:

$$x_{general\ shear}=x_{pure\ shear}+x_{simple\ shear} \quad \ldots\ldots\ldots (17)$$

Putting the expressions for $x_{pure\ shear}$ and $x_{simple\ shear}$ from equation 16 in the Appendix of this chapter and equation 3 in the Appendix of Chapter-2, respectively, in equation 17 above:

$$x_{general\ shear}=(2y_0-U_3.t-U_4.t)^{-1}[(U_3+U_4).t\{4y_0-t.(U_3+U_4)\}-(2y_0)^2]^{-1}.3Lt.(U_3+U_4)[y^2+(U_3-U_4).y.t+(y_0-U_3.t).(U_4.t-y_0)]+0.5.(U_1-U_2)+\{0.5.y.\ y_0^{-1}.(U_1+U_2)\} \quad \ldots\ldots\ldots (18)$$

which is a quadratic equation of y, hence represents a parabola.

Representing '$x_{general\ shear}$' as 'x' and rearranging:

$$[y^2+y.t.(U_3-U_4)+(y_0-U_3.t).(U_4.t-y_0)]+[0.5.(U_1-U_2)+\{0.5y.y_0(U_1+U_2).y-x](2y_0-U_3t-U_4.t)[(U_3+U_4).t.\{4y_0-t.(U_3+U_4)\}-(2y_0)^2]\{3L.t(U_3+U_4)\}^{-1}=0 \quad \ldots\ldots\ldots (19)$$

Y-ordinate of the vertex of this parabola is given by:

$$Y\equiv 0.5*[(U_4-U_3).t-(U_1+U_2)\{(2y_0-U_3.t-U_4.t)\{(U_3+U_4).t.(4y_0-U_3.t-U_4.t)-4y_0^2\}\{1.5.L.t.(U_3+U_4)\}^{-1}y_0^{-1}] \quad \ldots\ldots\ldots (20)$$

Therefore, the thickness of the zone of shear sense reversal at the top of the shear zone is given by

$T'=(y_0-U_3.t)-Y$ ... ... (21)

Discussions:

(1) The lower length side of the rectangle is considered as the Main Central Thrust and the top length side as the top of the HHSZ. A NE-SW geographic direction is assigned along the length of the rectangle. Lines passing through the vertices of the parabolic velocity profiles of successive breadths of the deformed rectangle, for the cases of pure shear (Figs. 3.15a, -b) and the general shear model (Fig. 3.16), demarcate the lower boundaries of shear zones with a top-to-NE sense of ductile shearing in contrast to the subjacent shear zones with a top-to-SW sense of shearing. The top shear zone is comparable with the HD1, and the bottom one with the remainder of the HHSZ. Note that the second zone with a top-to-NE sense of shearing, defining the HD2, is not produced.

(2) The velocity profiles of pure shear (Figs. 3.15a, -b; equations 1 and -16 in the Appendix of this chapter) and general shear (Fig. 3.16; equation 18 in the Appendix of this chapter) involve the term of time (t) in them. This indicates that at every instant, the equation of the velocity profiles at the two boundaries of the rectangle will be different. They remain parabolas, for any value of 't', but the profile will be more and more constricted with time. In contrast, equations of the velocity profiles for simple shear (the ductile shear model; line-1 of Fig. 3.14), plane Poiseuille flow (the channel flow model; curve-2 of Fig. 3.14), and the combined simple shear and plane Poiseuille flow (or the 'combined flow' model; curve-3 of Fig. 3.14), equations 3, 6 and 7, respectively in the

Appendix of Chapter-2, do not possess the parameter of time, 't'. These profiles, therefore, are time independent.

(3) For the above mentioned reasons, the detachments simulated in pure shear- (Figs. 3.15a, -b) and in general shear (Fig. 3.16) models keep shifting spatially as time progresses and its wall(s) move(s). On the other hand, the detachment simulated in the channel flow- and the combined flow models remain spatially fixed.

(II) The Shifting "Combined Flow" (Fig. 3.17)

We assume an infinitely long channel, with parallel and horizontal walls, with thickness $2y_0$ units, and full of Newtonian viscous fluid with viscosity 'μ'. It is assumed that a combination of simple shearing and channel flow takes place, at time instant T_1 (~18 Ma back), throughout the channel under shear velocities of the walls U_{11} and $-U_{12}$ and a pressure gradient (dP_1/dx). Substituting $U_1=U_{11}$, $U_2=U_{12}$ and $(dP/dx)=(dP_1/dx)$ in equation 7 in the Appendix of Chapter-2, the velocity profile in this case is given by:

$$x=0.5.(U_{11}-U_{21})+0.5.y.y_0^{-1}\,(U_{11}+U_{21})-0.5.\mu^{-1}.(dP_1/dx)(y_0^2-y^2) \quad \ldots\ldots\ldots (22)$$

which is defined within the range $y=+y_0$ to $y=-y_0$.

For another combined flow taking place at the bottom of the channel between the 'y' ordinates y=-t; and $y=-y_0$ at some other instant T_2 due to shear velocities U_{12} and $-U_{22}$ on the two walls and pressure gradient (dP_2/dx'), the velocity profile has to be found out. The point O′ on the Y-axis is equidistant from (0,-t) and $(0,-y_0)$ and is given by $[0,-0.5.(y_0+t)]$. Transforming O′ as the new origin (0,0), the old coordinate (0,-t) becomes $[0,0.5.(y_0-t)]$,

and the old origin O (0,0) becomes [0,0.5.(y_0+t)]. Substituting y_0=0.5.(y_0-t), U_1=U_{12}, U_2=U_{22} and (dP/dx)=(dP_2/dx') in equation 7 in the Appendix of Chapter-2, the velocity profile of this combined flow, with reference to the new origin O′, is given by:

$$x'=0.5(U_{12}-U_{22})+0.5.(U_{12}+U_{22})(y_0-t)^{-1}.y-0.5.\mu^{-1}.(dP_2/dx')[\{0.5(y_0-t)\}^2-y^2] \quad \ldots\ldots\ldots (23)$$

which is defined within the range of 'y' ordinates between y=0.5(y_0-t) to y=0.5.(t-y_0), with reference to the new coordinate system.

Now we go back from new origin O′ (0,0) to the old origin O [0,0.5(y_0+t)] and rewrite equation 23. Substituting $x'=x'$, and y=[y-0.5(y_0+t)] in equation 23 and simplifying, the velocity profile is given by:

$$x'=0.5(U_{12}-U_{22})+(U_{12}+U_{22})(y_0-t)^{-1}.[y-0.5.(y_0+t)]-0.5.\mu^{-1}.(dP_2/dx')[(y_0+t)-\{0.5(y_0^2+t^2)\}-y^2] \quad \ldots\ldots\ldots (24)$$

which is defined within the range y=-t to y=-y_0, and is with reference to the old coordinate system.

The flow pulses given by equations 22 and -24 give rise to thinner zones of opposite ductile shearing at the top of the channel. These zones of opposite shearing are comparable with the HD1 and the HD2. The thicknesses of the model HD1 and the HD2 are given by:

$$T_1=y_0-0.5.y_0^{-1}(U_{11}+U_{21}).\mu_1.(dP_1/dx)^{-1} \quad \ldots\ldots\ldots (25)$$

and, $$T_2=0.5.(y_0-t)-(y_0-t)^{-1}(U_{12}+U_{22}).\mu_2.(dP_2/dx')^{-1} \quad \ldots\ldots\ldots (26)$$

respectively. Note that (i) equation 25 is written from equation 10a in the Appendix of Chapter-2, after replacing T_1, U_{11}, U_{21}, μ_1 and dP_1/dx in places of T, U_1, U_2, μ and dP/dx, respectively; and (ii) equation 26 is written from equation 10a in the Appendix of Chapter-2, after replacing T_2, y_0-t, U_{21}, U_{22}, μ_2 and $dP_2/dx^{/}$ in places of T, y_0, U_1, U_2, μ and dP/dx, respectively.

The thickness of the HHSZ outside the respective detachments, $T_1^{/}$ and $T_2^{/}$, are given by

$T_1^{/}=[y_0+0.5.y_0^{-1}(U_{11}+U_{21}).\mu_1.(dP_1/dx)^{-1}]$ ... ... (27)

(from equation 10b in the Appendix of Chapter-2, after replacing $T_1^{/}$, U_{11}, U_{21}, μ_1 and dP_1/dx in places of T_1, U_1, U_2, μ and dP/dx, respectively)

and, $T_2^{/}=[(y_0-t)+0.5.(y_0-t)^{-1}(U_{12}+U_{22}).\mu_2.(dP_2/dx^{/})^{-1}]$ ... ... (28)

(from equation 10b in the Appendix of Chapter-2, after replacing $T_2^{/}$, y_0-t, U_{12}, U_{22}, μ_1 and $dP_2/dx^{/}$ in places of T, y_0, U_1, U_2, μ and dP/dx, respectively)

From equations 25 and –27, it is noted that $T_1<T_1^{/}$

From equations 26 and -28, it is noted that $T_2<T_2^{/}$

Thus, it can be stated that the simulated HD1 and the HD2 are thinner than the remainder of the HHSZ in respective considerations.

From equation 27; and 'F' and 'G' in the Appendix of Chapter-2, it can be stated that for

$(U_{11}+U_{21}).(dP_1/dx)^{-1}$ = or >$(2.y_0^{2}.\mu_1^{-1})$; T_1become = or <0. ... ... (29)

the HD1 does not form. This is because for T_1=0, the vertex of the velocity profile of this pulse lies on the upper wall of the channel; for T_1<0, the vertex of the extrapolated

velocity profile locates outside the channel. Thus, this pulse of the model predicts that for certain combinations of the parameters U_{11}, U_{21}, dP_1/dx, y_0 and μ_1, the HD1 is absent in certain sections of the Himalaya.

From equation 28; and 'F' and 'G' in the Appendix of Chapter-2, it can be stated that for $(U_{12}+U_{22}).(dP_2/dx^{/})^{-1}$=or >$[2.(y_0-t)^2.\mu_2^{-1}]$; T_2 become = or <0. ... ... (30)

the HD2 does not form. This is because for T_2=0, the vertex of the velocity profile of this pulse lies on the upper wall of the sub-channel i.e. on the line y+t=0. For T_2<0, the vertex of the extrapolated velocity profile locates outside the sub-channel. Thus, this pulse of the model predicts that for certain combinations of the parameters U_{21}, U_{22}, $dP_2/dx^{/}$, y_0 and μ_2, the HD2 is absent in certain sections of the Himalaya. This satisfies constraint (III) of Section-3.7.

From equations 25 and -26, it can be stated that T_2 can be less that T_1 depending on the specific set of magnitudes of the parameters y_0, U_{11}, U_{21}, μ_1, dP_1/dx, U_{21}, U_{22}, μ_2 and $dP_2/dx^{/}$.

Discussions and summary:

The followings are the discussions and summary of the mathematical analyses from equations 22 to -30.

(1) Equating the line (y+t)=0 in this model with the top boundary of HD2 in field passing through Karcham, the model HD2 is produced at the same spatial position as that of HD2 in the field.

(2) The model HD1 and HD2 are thinner than the remainder of the HHSZ.

(3) The parameters involved in exhumation of the HHSZ show that the lesser thickness of HD2 than that of HD1 can also be explained with this mathematical analysis.

(4) The HD2 is expected to be laterally discontinuous along the Himalayan strike, even when the combined flow was active in the lower sub-channel.

(5) It is predicted that the HD1 might be absent in certain sections of the Himalaya, even when simple shear and channel flow were active.

(6) The maximum values of the x-ordinates on the parabolic profiles given by equations 22 and -23 are obtained at their vertices. The lines parallel to the X-axis, and passing through these vertices, define the bases of the respective detachments. Therefore, the model predicts that these bases were exhumed with highest rates during the respective pulses.

(III) Combined flow through a two-layer HHSZ (Fig. 3.18):

We consider an infinitely long horizontal channel, of thickness $2y_0$ units, and full with two immiscible fluids- the top layer with viscosity μ_1, and the bottom layer with viscosity μ_2 ($\mu_2>\mu_1$). The line y=t ($0<t< -y_0$) as taken as the fluid interface. This consideration is justified since fieldwork during this study has led to broad division of the rocks-of the HHSZ in the Sutlej section into higher- and lower viscosities (Fig. 3.2). Let the top wall be sheared with velocity $+U_1$, the bottom wall with $-U_2$, and $(dP/dx)<0$. Let the

distribution of velocities in the top- and the bottom layers of the fluid are x_1 and x_2 respectively.

From Navier-Stokes equation, for the top fluid layer:

$(dP/dx)=\mu_1.(d^2x_1/dy_2)$, ... (31)

And for the bottom fluid layer, $(dP/dx)=\mu_2.(d^2x_2/dy_2)$ ... ... (32)

At the fluid interface, i.e. at the line y=t, the momentum flux is continuous through fluid-fluid interface. In other words,

at y=t, $\mu_1.(dx_1/dy) =\mu_2.(dx_2/dy)$ ... ... (33)

Integrating equation 31:

$(dx_1/dy).\mu_1=y.(dP/dx)+C$ ... ... (34)

Integrating equation 32:

$(dx_2/dy).\mu_2=y.(dP/dx)+C'$ ... ... (35)

From equations 33, -34 and -35:

$C=C'$ ... ... (36)

Integrating equations 34 and -31, respectively:

$x_1=0.5y^2.\mu_1^{-1}(dP/dx)+C.y.\mu_1^{-1}+C_1$ ... ... (37)

$x_2=0.5.y^2.\mu_2^{-1}(dP/dx)+C.y.\mu_2^{-1}+C_2$ ... ... (38)

Now at y=t; $x_1=x_2$ ... ... (39)

at $y=+y_0$, $x_1=U_1$, ... (40)

and at $y=-y_0$, $x_2=-U_2$ ... ... (41)

From equations -39, -37 and -38:

$C_1=C_2$.

Applying condition 40 in equation 37:

$$U_1=0.5.y^2.\mu_1^{-1}(dP/dx)+C.y_0.\mu_1^{-1}+C_1 \quad \ldots\ldots\ldots (42)$$

Applying condition 41 in equation 38:

$$-U_2=0.5.y^2.\mu_2^{-1}(dP/dx)-C.y_0.\mu_2^{-1}+C_1 \quad \ldots\ldots\ldots (43)$$

Solving C and C_1 from equations 41 and -38:

$$C=[(U_1+U_2)y_0^{-1}(\mu_1^{-1}+\mu_2^{-1})^{-1}-0.5.y_0(dP/dx)(\mu_1^{-1}-\mu_2^{-1})\,(\mu_1^{-1}+\mu_2^{-1})^{-1}] \quad \ldots\ldots\ldots (44)$$

$$C_1=[\{(U_1\,\mu_1-U_2\,\mu_2)-y_0^2.(dP/dx)\}(\mu_1+\mu_2)^{-1}] \quad \ldots\ldots\ldots (45)$$

Putting equations 44 and -45 in equation 37 and -38, respectively, velocity profiles for the combined simple shear and channel flow at the top- and the bottom layers are obtained as follows:

$$x_1=0.5.\mu_1^{-1}y^2.(dP/dx)+y\mu_1^{-1}[(U_1+U_2)y_0^{-1}(\mu_1^{-1}+\mu_2^{-1})^{-1}-$$

$$0.5.y_0.(dP/dx)(\mu_1^{-1}-\mu_2^{-1})(\mu_1^{-1}+\mu_2^{-1})^{-1}]+[\{(U_1\,\mu_1-U_2\,\mu_2)-y_0^2.(dP/dx)\}(\mu_1+\mu_2)^{-1}]$$

$$\ldots\ldots\ldots (46)$$

and

$$x_2=0.5.y^2.\mu_2^{-1}.(dP/dx)+y\mu_2^{-1}[(U_1+U_2)y_0^{-1}(\mu_1^{-1}+\mu_2^{-1})^{-1}-$$

$$0.5.y_0.(dP/dx)(\mu_1^{-1}-\mu_2^{-1})(\mu_1^{-1}+\mu_2^{-1})^{-1}]+[\{(U_1\,\mu_1-U_2\,\mu_2)-y_0^2.(dP/dx)\}(\mu_1+\mu_2)^{-1}]$$

$$\ldots\ldots\ldots (47)$$

Equations 46 and -47 represent parabolas, since they are quadratic equations of 'y'.

Putting (dP/dx)=0 in equations 46 and -47 respectively, i.e. for simple shearing, the velocity profiles are:

$$x_1=y\mu_1^{-1}(U_1+U_2)y_0^{-1}(\mu_1^{-1}+\mu_2^{-1})^{-1}+(U_1\,\mu_1-U_1\,\mu_2)(\mu_1+\mu_2)^{-1} \quad \ldots\ldots\ldots (48)$$

$$x_2=y\mu_2^{-1}(U_1+U_2)y_0^{-1}(\mu_1^{-1}+\mu_2^{-1})^{-1}+(U_1\,\mu_1-U_2\,\mu_2)(\mu_1+\mu_2)^{-1} \quad \ldots\ldots\ldots (49)$$

Note that the parabolas represented by equations 46 and -48 are defined within the range of the y-ordinate between y=t to $y=+y_0$; and those represented by equations 47 and -49 are defined within the range of the y-ordinate between y=t to $y=-y_0$. Interestingly, equations 48 and -49 are independent of 't'. This means that the velocity profiles of simple shearing within the two-fluid media are independent of the absolute position of the fluid interface. Equations 48 and -49 represent straight lines, which mean that uniform sense of shear is displayed by bulk simple shearing of the two viscous layers.

The suitability of flows given by equations 46 and -47 as the model of exhumation of the HHSZ is studied as follows.

Expressing equations 46 and -47 as:

$$[y-\{-(U_1+U_2)y_0^{-1}(\mu_1^{-1}+\mu_2^{-1})^{-1}(dP/dx)^{-1}-0.5.y_0(\mu_1^{-1}-\mu_2^{-1})(\mu_1^{-1}+\mu_2^{-1})^{-1}\}]^2+(\text{remaining terms})=0 \quad \ldots\ldots\ldots (50)$$

and comparing with the standard form of parabola $(Y-P)^2=-4Q(X-R)$, the Y-ordinate of the vertex (the parameter 'P') of both the parabolas are found as follows:

$$\text{Y-ordinate: } -(U_1+U_2)y_0^{-1}(\mu_1^{-1}+\mu_2^{-1})^{-1}(dP/dx)^{-1}+0.5.y_0(\mu_1^{-1}-\mu_2^{-1})(\mu_1^{-1}+\mu_2^{-1})^{-1} \quad \ldots\ldots\ldots (51)$$

Putting y=t in equation 46, the x-ordinate of the intersection between the parabola in the upper fluid medium and the fluid interface at y=t, is given by:

$$x_1': 0.5.\mu_1^{-1}t^2.(dP/dx)+t\mu_1^{-1}[(U_1+U_2)y_0^{-1}(\mu_1^{-1}+\mu_2^{-1})^{-1}-0.5.y_0(dP/dx)(\mu_1^{-1}-\mu_2^{-1})(\mu_1^{-1}+\mu_2^{-1})^{-1}]+[\{(U_1.\mu_1-U_2.\mu_2)-y_0^2.(dP/dx)\}(\mu_1+\mu_2)^{-1}]$$

$$\ldots\ldots\ldots (52)$$

Similarly, putting y=t in equation 49, the x-ordinate of the intersection between the parabola in the lower fluid medium and the fluid interface at y=t, is given by:

x_2': $0.5.y^2.\mu_2^{-1}.(dP/dx)+y\mu_2^{-1}[(U_1+U_2)y_0^{-1}(\mu_1^{-1}+\mu_2^{-1})^{-1}-$

$0.5.y_0.(dP/dx)(\mu_1^{-1}-\mu_2^{-1})(\mu_1^{-1}+\mu_2^{-1})^{-1}]+[\{(U_1\,\mu_1-U_2\,\mu_2)-y_0^2.(dP/dx)\}(\mu_1+\mu_2)^{-1}]$

... ... (53)

Discussions:

(1) Except some special combinations of the parameters (dP/dx), t, μ_1, μ_2, U_1, U_2 and y_0, the ordinates of the vertices, x_1' and x_2', given by the expressions 52 and -53, respectively, are different. This fact is utilized in drawing the velocity profiles, 1 to 10, in Fig. 3.18.

(2) Referring to the expression 51, we note that both the parabolas have the same Y-ordinates. These parabolas are defined within the respective fluid media. Therefore, only one single point as the vertex occurs during the flow. The location of the vertex depends on the magnitudes of the parameters U_1, U_2, y_0, μ_1, μ_2 and (dP/dx).

(3) It is noted that the expression 51 is devoid of the term 'x'. This means that the locus of the vertices of the parabola, deformed from initially straight marker at every instant of the flow, lie on a line parallel to the X-axis.

(4) Within the upper layer of low viscosity, for the parabolic profile- 3, a shear zone equivalent to HD1 is produced with a top-to-NE sense of ductile shearing.

(5) A second shear zone with a top-to-NE sense of shearing is formed within the model flow/shear zone in the specific flow case (parabolic profile-8 in Fig. 3.18). The upper

boundary of this shear zone coincides with the fluid interface. This interface is equivalent to the contact between the rocks of lower- and the higher viscosity in the HHSZ in the Sutlej section, which is demarcated in this work at the locality Shongthong (Fig. 3.2). On the contrary, the HD2 has been demarcated in this work much south to, and spatially away from Shongthong. Thus, although a shear zone with a top-to-NE sense of ductile shearing is mathematically produced within this flow zone, it is spatially not comparable with the HD2 at Karcham.

(IV) Flow restricted within the rocks with low-viscosity (Fig. 3.19):

We consider a Newtonian fluid with viscosity 'μ' within an infinitely long channel, with parallel and horizontal walls, is undergoing simple shear in a top-to-SW sense with velocities of its walls as U_1 and $-U_2$. The lines $y=t$ and $y=y_0$, are taken as the bottom- and the top wall, respectively. An additional flow component imparted by the pressure gradient $(dP/dx)<0$ is also considered. The rationale of such idea is that only the top layer of the HHSZ channel acquired fluid character as indicated by protracted granitic melts and migmatization simultaneous with a top-to-NE sense of shearing ~18 Ma back. At the same time, a top-to-SW sense of shearing was taking place within the MCT. The velocity profile of flow for Fig. 3.18 of Chapter-2 is given by

$$x=0.5(U_1-U_2)+0.5.\ y_0^{-1}.y\ (U_1+U_2)(2y_0)^{-1}.y \qquad \ldots\ldots\ldots (54)$$

(rewriting equation 3 in the Appendix of Chapter-2)

In this situation, equation 47 stands for the velocity profile of the lower sub-channel defined within the range $y=-y_0$ to $y=t$.

Replacing 't' at 'y' in equation 47, the velocity along the x-direction at coordinate (0,t) is given by:

$x=0.5.(U_1-U_2)+0.5.\ y_0^{-1}\ t.(U_1+U_2)$ ... ... (55)

Thus, in the top sub-channel, velocities of its boundaries are:

$x=+U_1$, at $y=y_0$

and $x=0.5(U_1-U_2)+0.5.\ y_0^{-1}\ t.\ (U_1+U_2)$, at $y=t$

Using these boundary conditions and parameters in equation 7 in the Appendix of Chapter-2, the velocity profile for the top sub-channel is given by:

$x=0.5.\ \mu^{-1}.y^2\ (dP/dx)+C_1.y+C_2$ ... ... (56)

Putting the boundary conditions, the integration constants are solved as:

$C_1=0.5.y_0^{-1}(U_1+U_2)-0.5\mu^{-1}(dP/dx).(y_0+t)$ ... ... (57)

$C_2=0.5.(U_1-U_2)+0.5t.\mu^{-1}(dP/dx).y_0$ ... ... (58)

Putting them in equation 56:

$x=\ 0.5.\mu^{-1}y^2(dP/dx)+\{0.5y.y_0^{-1}(U_1+U_2)\}-0.5y.\mu^{-1}(dP/dx).(y_0+t)$

$+0.5.(U_1-U_2)+0.5.t.\mu^{1}.\ y_0\ (dP/dx).$ ... ... (59)

Following steps similar to equations 8 to -10 in the Appendix of Chapter-2, the Y-ordinate of the vertex of the parabola represented by equation 60 is given by:

$Y\equiv 0.5*[(y_0+t)-\mu(dP/dx)^{-1}.y_0^{-1}.(U_1+U_2)]$ ... ... (60)

The thickness of the zone of shear sense reversal produced at the top upper sub-channel, for $Y>y_0$, is given by:

$T=(y_0-Y)$ ... ... (61)

Discussions:

(1) Referring to equation 61, for $T>0$, a zone of shear sense reversal, equivalent to the HD1, forms within the topmost part of the channel (curve-1 of Fig. 3.19).

(2) For certain combination of the parameters y_0, t, μ, (dP/dx), U_1 and U_2, $T \leq 0$. For $T=0$, the vertex of the velocity profile lies on the top wall of the channel (curve-2 of Fig. 3.19). For $T<0$, the vertex of the extrapolated velocity profile, shown by dashed line, locates outside the channel (curve-3 of Fig. 3.19). In these cases, the zone of a top-to-NE sense of shearing is not produced even when combined simple shear and channel flow are active. The mathematical analysis, therefore, predicts that the HD1 may be absent in certain sections of the Himalaya.

(3) Since the lower sub-channel undergoes simple shear deformation (equation 54) in the top-to-SW sense, no zone of shear sense reversal is produced within it. The presence of HD2, therefore, cannot be explained with the concept of such flow mechanism. The constraint (III) of Section-3.7 remains unsatisfied.

(V) The E_3 phase (Fig. 3.20):

The HHSZ is considered as a channel with parallel and horizontal walls of finite length. The channel is assumed to be of thickness of '$2y_0$' units consisting of '2n' number of brittle shear planes. The spacing between these planes are taken as= $y_0.n^{-1}$. The Y-axis is taken as the passive marker before the deformation starts, which is perpendicular to the channel walls. The X axis is taken equidistant from, and parallel to, the walls. The

applied brittle shears on the walls are assumed to be U_5, and $-U_6$. The marker is assumed to be broken across each brittle shear planes i.e. into '2n' parts. Let the distance between the subjacent and the superjacent broken marker are =s. Velocity profiles for each broken part of the marker are different.

Total slip of the marker is (U_5+U_6), which is distributed amongst '2n' layers; therefore

$s=0.5.n^{-1}(U_5+U_6)$ ... ... (62)

Now the top boundary of 'p'th layer from origin is the same as the bottom of the '(n-p)'th layer from the top wall of the channel.

Over the top channel wall (i.e. within the top boundary of the '1st layer from top'), amount of slip is $D_1=+U_5$ units.

Along the top boundary of the '2nd layer from top', displacement is $D_2=(U_5-1.s)$.

Along the top boundary of the '3rd layer from top', displacement is $D_3=(U_5-2.s)$.

Therefore, by induction, along the top boundary of the '(n-p)th layer from top', the displacement is $D_{(n-p)}=[U_5-(n-p-1).s]$ ... ... (63)

Putting 's' from equation 62 in this expression and simplifying:

$D_{(n-p)}=0.5*[(U_5-U_6)+n^{-1}(p+1)(U_5+U_6)]$ ... ... (64)

which is the X-ordinate of all the points on the marker confined within the '(n-p-1)'th layer from the top', or 'p'th layer from origin. Equation of this marker is given by:

$x=0.5*[(U_5-U_6)+n^{-1}(p+1)(U_5+U_6)]$ ... ...(65)

Since the marker given by this equation is confined within the 'p'th layer from the origin, the equation is valid within the range $y=(y_0 n^{-1} p)$ to $y=[y_0 n^{-1}.(p-1)]$. For different values of p ($\leq n$), equations of different velocity profiles can be obtained.

Chapter 4

CHANNEL FLOW ANALOGUE MODELS

4.1. INTRODUCTION

The channel flow model (Fig. 4.1) has been a unifying and almost unanimously accepted theory of (i) exhumation, (ii) inverted metamorphism, (iii) ductile extensional shearing in a single detachment within the top activated coeval to ductile compressional shearing at the base 18 Ma ago, (iv) protracted granitic melting, anatexix and migmatization in the surface and (v) the presence of partially molten rocks at depth for the Higher Himalayan Shear Zone (HHSZ) in different sections of the Himalaya (Beaumont et al., 2001). The thermal-mechanical numerical model of channel flow involves oozing up of the partially molten mid-crustal rocks of the HHSZ in response to topography induced pressure gradient and augmented by surface denudation (Beaumont et al. 2001; Jamieson et al. 2004; Beaumont et al. 2004). The model demonstrates channel flow/Poiseuille flow of rheologically weakened crust starting from a sub-horizontal channel and entering into a linked inclined channel until it extrudes (also see Fig. 6 of Wu et al., 1998; Fig. 3a of Godin et al., 2006). The inclined channel (Fig. 4.2) represents the HHSZ. Its top- and bottom boundaries are equivalent with the South Tibetan Detachment System (STDS) and the Main Central Thrust (MCT), respectively. The sub-horizontal channel is equivalent to the feeder channel of partial melt for the HHSZ beneath the Eurasian plate, which in reality is extended at least till the latitude 32^0N. The base of the horizontal channel is defined by the Main Himalayan Thrust (MHT). Thus the HHSZ is defined as a ramp and the MHT as a flat (Hauck et al., 1998;

Figure Captions

Fig. 4.1. The channel flow/plane Poiseuille flow of a Newtonian viscous fluid through a channel with horizontal and parallel walls. Pressure gradient (dP/dx) guides this laminar flow. A marker initially perpendicular to the walls, take the shape of a parabola defining the velocity profile. The flow generates opposite senses of shear- while in the upper half of the channel the sense of shear is top-to-left, that in the bottom half is top-to-right. Assigning a NE-SW geographic sense and equating the channel with the Higher Himalayan Shear Zone (HHSZ), the model can explain some of its intriguing characters- most notably the presence of a single ductile extensional shear zone in the compressional regime of the Himalaya.

Fig. 4.2. Simplified and model compliant representation of the NE-SW cross-section of the Higher Himalayan Shear Zone (HHSZ) as an inclined channel. The lower boundary of the HHSZ is the Main Central Thrust (MCT). The upper boundary of it is the top of the South Tibetan Detachment System. The MCT merges at depth with the Main Himalayan Thrust (MHT). The linked horizontal channel feeds material for extrusion of the HHSZ. Over-thickened crust of the Tibetan plateau exerts pressure on the horizontal channel, squeezes rocks leading to extrusion of the HHSZ. The senses of shearing at the boundaries are given by half arrows. The pressure exerted by the Tibetan crust on the horizontal channel is shown by a thick arrow. Parameters 'A', 'B' and 'C' are the thickness of the horizontal channel, the thickness of the HHSZ, and the depth at which the upper boundary of the HHSZ meets the horizontal channel, respectively. The figure is a simplification of Fig. 2b of Jamieson et al. (2004). The figure is neither to scale nor to angle.

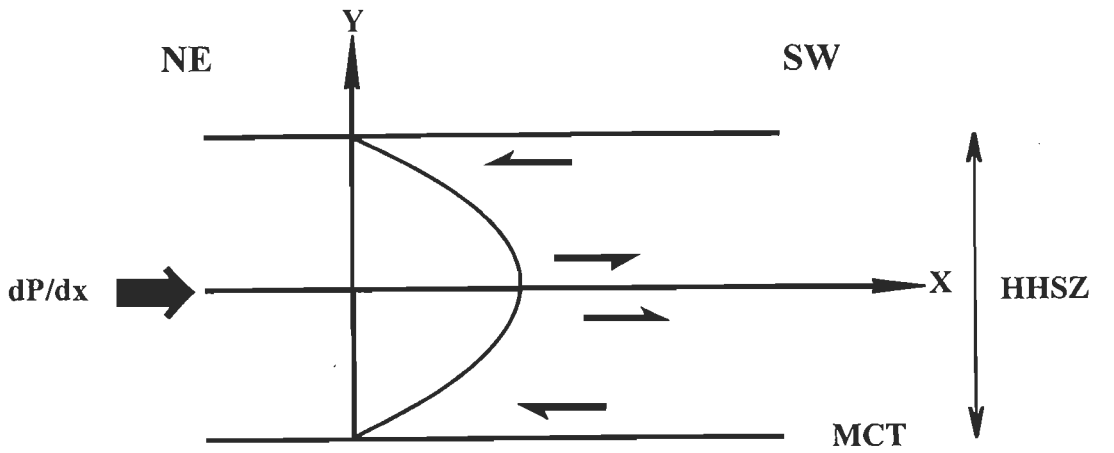

Fig. 4.1

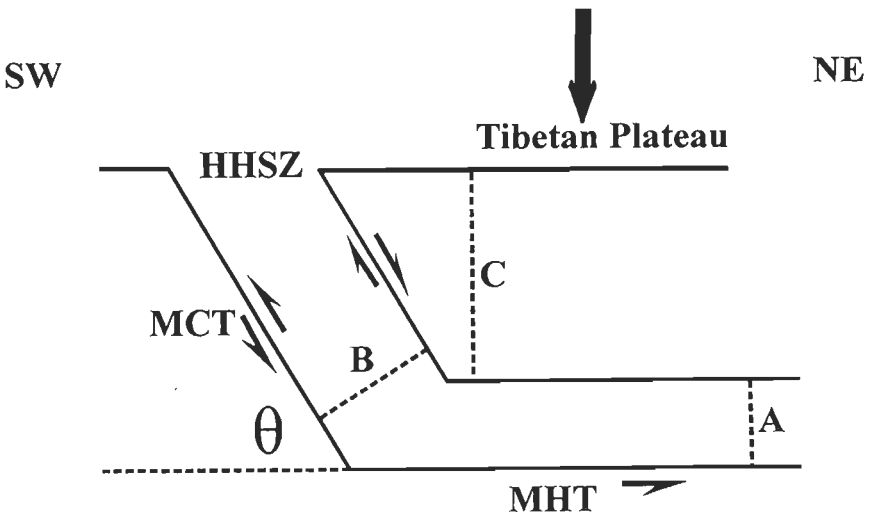

Fig. 4.2

and references therein; Wu et al., 1998 and references therein; Fig. 2a of Vannay and Grasemann, 2001). Jamieson et al. (2004) portray post collisional migration of both the channels towards the foreland side, deformation of their walls, and progressive reduction of slope of the inclined channel.

Interestingly, contrary to the single zone of ductile extensional shearing as reported from most of the sections of the Higher Himalayan Shear Zone (e.g. Burchfiel et al., 1992; Patel et al., 1993; Godin et al., 1999 to mention a few), two such zones, or the detachments, occur in the HHSZ at Gonto La (Edwards et al., 1996) and at the Everest Massif (Searle, 1999). One of these detachments occurs as the upper boundary of the HHSZ equivalent to the STDS, and the other is within it. Further, the Chapter-3 of this thesis reports the existence of two detachments from the Sutlej section of the HHSZ in the NW Indian Himalaya (Figs. 3.2; 3.11). These are named as the 'Himalayan Detachment-1' (HD1) and the 'Himalayan Detachment-2' (HD2). The HD1 is equivalent to the STDS in other sections. The HD2 occurs inside the HHSZ and is spatially much away from the HD1. The relative timing of extensional ductile shearing within these two spatially separated detachments has remained indeterminate. In Chapter-3, different mathematical analyses; were attempted to check whether ductile extensional shearing within the HD1 and the HD2 can be generated simultaneously. Considering the HHSZ to be bounded by parallel walls, the trials were (i) general shear (Fig.3.16); (ii) combined simple shear and channel flow through a two viscous media (Fig. 3.18); and (iii) preferential flow confined within the top sub-channel (Fig. 3.19). None of these trails could give simultaneous extensional shearing in two zones.

Interpreting the results of the INDEPTH seismic studies by Nelson et al. (1996), Grujic et al. (1996) and references therein, and Grujic et al. (2002) presented the HHSZ as a diverging-up crustal wedge (Fig. 2.17). Fluid flow through non-parallel walls has been described in fluid mechanics texts as 'Jeffery-Hamel flow' (e.g. Schlichting, 1968), which is fundamentally different from the Poiseuille flow. In this flow, the velocity profile might possess multiple inflection points (LeCureux and Burnett, 1975) (Fig. 4.3). If the two zones of extensional shearing are produced simultaneously within the wedge-shaped HHSZ, the expected profile, as per LeCureux and Burnett's (1975) terminology, should be of 'ND2' type (non-symmetric, diverging, two inflection points) (Fig. 4.4).

4.2. OBJECTIVES

This chapter aims at simulation of the exhumation of the HHSZ as fluid flow, induced by pressure gradient, with three possible geometries of the walls of the channel- inclined parallel wall, gently diverging-up and strongly diverging-up. The experiments attempt at (i) finding out whether the ND2 pattern forms within the divergent up inclined channels while maintaining the geologically realistic physically boundary conditions; and (ii) documenting the structures that are produced during channel flow/Jeffery Hamel flow. These experiments were performed in the 'Hans Ramberg Tectonic Laboratory', Uppsala University.

Figure Captions

Fig. 4.3 One of the many possible profiles in Jeffery Hamel flow through a channel with divergent walls. The circular arc is the inactive marker before the flow starts. The curve line that intersects the arc at two points is the velocity profile. Arrows represent radial flow vectors. Reproduced from Fig. 11c of Sykes and Reid (1984).

Fig. 4.4 The HHSZ is bounded by northeasterly dipping non-parallel divergent-up static walls. The circular arc SS_1 represents a marker before the flow starts. The curved line intersecting this marker at two points, I_1 and I_2, represent the velocity profile. Those two points are called the inflection points. The spatial position of the two ductile extensional shear zones or the detachments inside it, the HD1 and the HD2, are shown. S-C fabric represents the ductile sense of shearing in different sub-zones within the HHSZ. The HD1 is thinner than the HD2. To maintain this thickness constraint, the velocity profile has to asymmetric. Summarily therefore, the velocity profile is of 'ND2' type (non-symmetric profile, diverging flow, and two inflection points). Symbols: MCT- Main Central Thrust; LH- Lesser Himalaya; TSZ- Tethyan Sedimentary Zone. One of the aims of this chapter is to find out whether the extensional shearing in the HD1 and the HD2 were produced simultaneously under the chosen physical boundary condition as

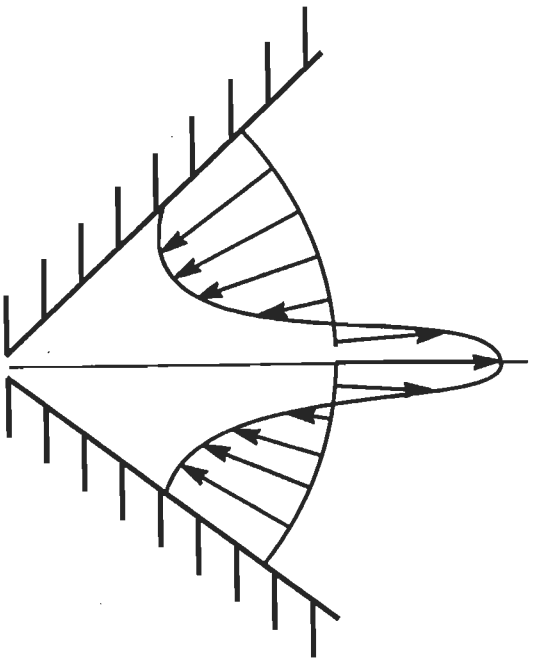

Fig. 4.3

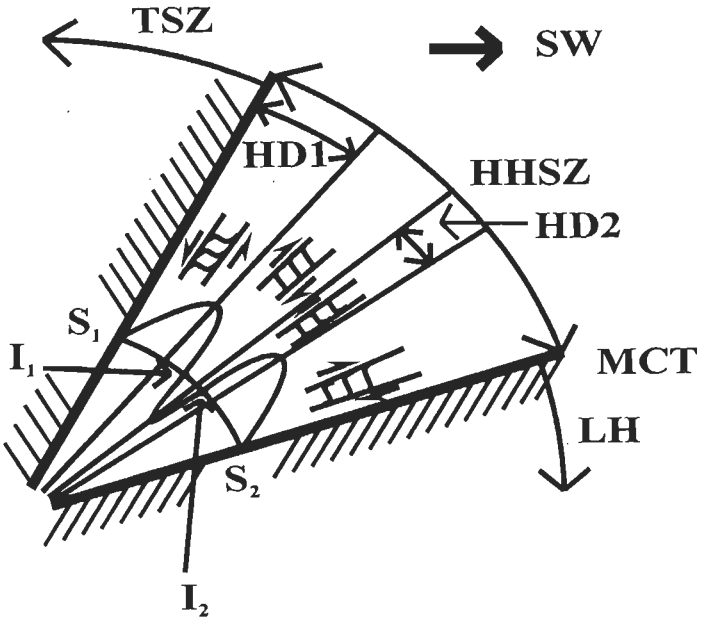

Fig. 4.4

4.3. THE JEFFERY HAMEL FLOW

The governing equation of this flow is given by:

$$F'''+2\alpha R_e FF'+4\alpha^2 F'=0 \quad \ldots\ldots\ldots (1)$$

with the boundary conditions: F(-1)=0; F(0)=+1; F(+1)=0. Symbols- Reynolds number $(R_e)=[\{x_{max}.r\alpha)/\nu]$, with conditions α, $x_{max}>0$; $[x(r,\varphi)/x_{max}(r)]=F(\alpha)$; x: fluid velocity for a particular (r,φ) polar coordinate; x_{max}: maximum fluid velocity; ν: kinematic viscosity; and 2α: acute angle between the channel walls. Equation 1 gives flow profiles with different geometry (cf. LeCureux and Burnett, 1975; Lu, 1977). The geometry of the velocity profile is dependent on 2α and R_e (Schlichting, 1968). Keeping 2α fixed, as R_e increases, multiple senses of shearing develop with the velocity profile getting a number of inflection points (Sykes and Reid, 1984). In the Himalayan context, the flow equivalent to the extrusion of the HHSZ is more complex as it takes place against gravity.

4.4. THE MODEL MATERIAL

Polydimethylsiloxane (PDMS 36), a transparent incompressible Newtonian viscous polymer with a density of 950 kg m^{-3} (or 0.95 cc) and a viscosity of 10^5 Pa s (or 10^6 Poise) (Talbot and Aftabi, 2004; and references therein) was used as the model material. Transparency of the PDMS helps to see through the imprinted deformed grids. The viscosity of the PDMS is such that, if kept on a horizontal free surface, it undergoes slow flow under its own weight. Thus, its slow deformation can be demonstrated in real time in the laboratory.

4.5. GEOLOGICAL PARAMETERS RELEVANT TO THE MODEL

The following geological parameters in Table-1 relevant to the exhumation of the HHSZ were collected from literature (there are more!). Some of these values were used in the Appendix in calculating the equivalent parameters for the model.

Table-1.

Sl No.	Parameters	References
1	Pressure gradient: 0.28±0.17 kbar.km^{-1}, Zanskar section	Searle et al. (1992)
2	Pressure gradient: 1.0-2.0 kb.km^{-1}, Nepal Himalaya	Grujic et al. (1996), as referred in Vannay and Grasemann (2001)
3	Crustal density: 2.70 gm cc^{-1}	As taken by Jamieson et al. (2004)
4	Viscosity of partially molten rock at 700^{0}C: 10^{20} Poise	
5	Viscosity of partially molten rock: 10^{17}-10^{19} Poise at 20-30 km depth	Unsworth et al. (2005)
	Rate of slip of the MCT	
6	Minimum amount of 10.0 mm yr^{-1}, central Nepal Himalaya	Catlos et al. (2001)
7	1.2 mm.yr^{-1}, central sector of the Himalaya	Valdiya (2001)
8	2.0 cm yr^{-1}	Vannay and Grasemann (2001)
9	2.2±0.7 cm.yr^{-1}, central Nepal Himalaya	Kohn et al. (2004)
10	Maximum 9.0 mm.yr^{-1}, central Nepal Himalaya	Whipp et al. (2005)
11	0.8 mm yr^{-1}, falls to 0.2 mm.yr^{-1} moving into the HHSZ, central Nepal Himalaya	Wobus et al. (2005)
11	40±20.0 mm.yr^{-1} between 10-0 Ma; 0.37±0.13 mm. yr^{-1} between 10-30 Ma in MCT zone in Nepal	Yin (2006) and references therein
12	3-5 mm.yr^{-1}, MCT zone, between 7-4 Ma, Nepal Himalaya	

Sl No	Parameters	References
Rate of slip of the STDS		
13	Average slip rate: 7 $mm.yr^{-1}$, between 23-12 Ma	Wu et al. (1998)
14	1.2-4.2 $cm.yr^{-1}$, Zanskar Himalaya	Dèzes et al. (1999)
15	35 km between 22-16 Ma, i.e. 5.83 $mm.yr^{-1}$, Nepal Himalaya	Vannay and Grasemann (2001) and references therein
16	2.25 $cm.yr^{-1}$ in average for extensional shear	Vannay and Grasemann (2001)
17	11:6 mm yr^{-1}, Zanskar Himalaya	Vannay and Grasemann (2001) and references therein
18	20 $mm.yr^{-1}$	Annen et al. (2006) and references therein
19	1.10±0.06 $mm.yr^{-1}$ between 0-10 Ma; 0.53±0.13 $mm.yr^{-1}$ between 10-30 Ma; Zanskar section	Yin (2006) and references therein
	Rate of slip of the MHT	
20	10-15 mm yr^{-1} in last 15-20 Ma	Wu et al. (1998) and references therein
21	5.0 cm yr^{-1}	As taken by Jamieson et al. (2004)
	Rate of exhumation of the HHSZ	
22	5.0- 8.8 mm yr^{-1} , Zanskar section	Dèzes (1999)
23	0.27 $mm.yr^{-1}$ mean rate, Kashmir Himalaya	Jain et al. (2002)
24	0.97±0.13 $mm.yr^{-1}$ between 0-20 Ma, Bhutan Himalaya	Yin (2006) and references therein
25	0.67±0.13 $mm.yr^{-1}$ between 0-20 Ma, Garhwal Himalaya	
26	0.30±0.20 $mm.yr^{-1}$, around rim of western Himalayan syntaxix	
27	1.10±0.06 $mm.yr^{-1}$, Zanskar region	
28	0.38±0.13 $mm.yr^{-1}$, Nepal Himalaya	
29	0.97±0.13 $mm.yr^{-1}$, Bhutan Himalaya	

Sl No.	Parameters	References
30	2-1 mm.yr^{-1}, Sikkim Himalaya	Yin (2006) and references therein
31	0.93-2.1 mm. yr^{-1}, core of eastern Himalayan syntaxis	
32	0.42±0.13 mm. yr^{-1}, between 57-31 Ma, eastern Himalaya	
Rate of erosion/denudation of the HHSZ		
33	3.5-5.0 mm.yr^{-1} in average, Central Nepal	Whipp et al. (2005)
34	1.0 km Ma^{-1} i.e. 1.0 mm.yr^{-1}	Vannay and Grasemann (2001) and references therein
35	0.67±0.13 mm.yr^{-1}, Garhwal Himalaya	Yin (2006) and references therein
36	0.53±0.13 mm.yr^{-1}, Zanskar region	Yin (2006) and references therein

4.6. ATTEMPTING SIMILARITY BETWEEN PROTOTYPE & MODEL

4.6.1. Geometric similarity

The thermo-mechanical model of channel flow by the Dalhousie group (Beaumont et al., 1996; Beaumont et al., 2001; Beaumont et al., 2004; Jamieson et al., 2004; Beaumont et al., 2006; Jamieson et al., 2006) is complicated. It involves deformation and southward propagation of the channel with progressive time. For the sake of simplicity, channels with temporally fixed walls are chosen in the analogue models (Fig. 4.2). Timing of the Neo-Himalayan M_2 metamorphism matches with the D_2 deformation episode in the Higher Himalayan Shear Zone (Jain et al., 2002) characterized by top-to-SW ductile shearing. According to Fig. 2 of Jamieson et al. (2004), during this time, the thickness of the horizontal channel was around 25 km, channel flow had initiated within it as early as 24 Ma ago, and the inclined channel had a maximum slope of around 60^0. The present

day dip amounts of the MCT and the foliation planes of the HHSZ are 30^0 (Fig. 2b of Vannay and Grasemann, 2001) and 40^0 (Fig. 6 of Yin, 2006). In analogue models, therefore, three different dip amounts of the HHSZ ('θ'in Fig. 4.2) were chosen- 30^0, 40^0 and 60^0 in defining the parallel- and the diverging-up walls of the HHSZ.

The thickness of the HHSZ ('B' in Fig. 4.2) is debatable since there is lack of consensus about the location of the lower boundary of the shear zone, i.e. the MCT (Thakur, 1993 and references therein). For example, in the Sutlej section, much north to the MCT of Jain and Anand (1988), the Vaikrita Thrust of Srikantia and Bhargava (1998) has been identified as the MCT by Vannay and Grasemann (2001), rendering reduction in thickness of the HHSZ. From Fig. 1 of Jain and Anand (1988), the thickness is calculated as 50 km; whereas the value obtained from Fig. 2b of Vannay and Grasemann (1998) is 30 km. Jain and Manickavasagam (1993) mentioned that the thickness of the HHSZ can vary from few up to 40 km. Stephenson et al. (2000) mentioned the width of the HHSZ to be between 30-50 km. Wu et al. (1998) referred this range for the eastern Nepal sector of the Himalaya to be 25-30 km. For the HHSZ bounded by parallel walls, thicknesses equivalent to 12.5 km, 25 km and 50 km were taken in different experiments. Out of these, a much lower value equivalent to 12.5 km was chosen to explore the velocity profile for the flow of fluid initiating from a thicker horizontal channel and entering into a thinner inclined HHSZ.

Figure 3 of Jamieson et al. (2006), in their numerical modeling of channel flow, shows the thicknesses of the horizontal channel ('A' in Fig. 4.2) to be 50 km, which was

prevalent 24 Ma ago. Figure 6 of Hauck et al. (1998), reproduced from Acharya and Ray (1977), on the Darjeeling corridor of Sikkim Himalaya shows this thickness to be around 15 km. A similar low amount is also obtained in partial palinspastic reconstruction of the cross-section of the central Himalaya ~12 Ma back, as given in Fig. 8b of Hauck et al. (1998). Since the two channels define a ramp-flat geometry, the thickness of the horizontal channel varies- a similar reconstruction of the present day central Himalayan cross-section reveals this thickness to be as high as 25 km near the north Himalayan gneissic domes (Fig. 8a of Hauck et al., 1998). The thicknesses of the horizontal channel in all the models are chosen as 25 km. The horizontal channel in the models is prepared sufficiently long (14.5 cm) so as to generate parabolic profiles in the PDMS inside it by pushing a piston.

The depth ('C' in Fig. 4.2) at which the inclined channel meets the horizontal channel is given as ~ 20 km (Fig. 5c of Wu et al., 1998), between 25 to 55 km in different parts of the ramp (Fig. 8b of Hauck et al., 1998); and 35 km before 15 Ma from the present (Fig. 3 of Jamieson et al., 2006). We choose the depth C= 35 km in all the experiments. The geometric similarity between the prototype and the model is achieved by dividing the 'A', 'B' and 'C' parametes by 10^6 and using the resultant magnitudes to define the dimensions of the channel flow box. For example, C is taken as 3.5 cm.

4.6.2. Kinematic similarity

The kinematic similarity between the prototype as depicted by Jamieson et al. (2004) and the analogue model is not achieved. During the channel flow, the prototype involves (i)

deformation of the walls of the channel through time; (ii) the slope of the inclined channel become gradually gentler; and (iii) the channels move towards the foreland side (Figs. 2a-d of Jamieson et al., 2004). In the analogue models, on the other hand, the channel flow box is spatially fixed, temporally maintains the same geometry as it remains undeformed. Further, for the sake of simplicity, the sub-horizontal channel in the prototype is considered to be perfectly horizontal in the model.

4.6.3. Dynamic similarity

To obtain dynamic similarity in the models, the following magnitudes of the parameters are to be generated in the model.

A. Velocity of shear of the lower wall of the horizontal channel, equivalent to the movement of the MHT, if no channel flow were active: $1.585*10^{-12}$ $mm.s^{-1}$ (calculated after equation 3 in the Appendix).

B. Pressure gradient within the horizontal channel, if only channel flow were active, without any basal shear: $0.23*10^{-6}$ $Dyne.cm^{-3}$ (calculated after equation 5 in the Appendix).

C. Maximum velocity generated in the combined simple shear and channel flow in the horizontal channel: $0.446*10^{-2}cm.s^{-1}$ (calculated after equation 7 in the Appendix).

To get similar geometric, kinematic and dynamic results as that of in the nature, the tectonic models must be tuned with the respective similarities (Ramberg, 1981). None of these flow parameters, as calculated above, can be achieved in the laboratory due to

instrumental limitations. For example, the pressure gradient generated on the PDMS in the horizontal channel using the slowest possible gear is 10^{12} times higher than the requirement. Therefore, the dynamic similarity could not be maintained in these experiments. All the experiments performed had the flow of the PDMS at a much higher speed. Therefore, strain and strain rate, if measured from these models, cannot be compared with those of the HHSZ. However, only the geometry of deformation can be compared since geometric similarity has been maintained in these experiments. Further, the very slow velocity of shear of the MHT, when translated to that for the lower wall of the horizontal channel, was found difficult to achieve in the laboratory. For this reason, a purely channel flow or a plane Poiseuille flow was simulated in the horizontal channel.

4.7. THE CHANNEL FLOW BOX

A "channel flow box" was designed, which consists of a piston, a base plate, a front plate, two side plates, two hanging-wall wedges, and two foot-wall wedges (Fig. 4.5). Wedges with different slopes (θ_1 and θ_2) were prepared. The box consists of a horizontal channel and a linked inclined channel. The box can be dismantled along the length of the channels into two halves of same shapes and sizes. PDMS was inserted within these halves and left undisturbed till the air bubbles go away. Grids, partially photocopied on transparencies, were imprinted at one of the halves at the place where '1 mm opening' is marked in Fig. 4.5, and the two halves were joined quickly and screwed. For experiments with parallel inclined walls, grids of equally spaced sets of orthogonal lines were chosen. For

Figure Captions.

Fig. 4.5. The channel flow box consisting of a horizontal channel and a linked inclined channel. Lengths shown in the instrument are not in proportion. The hanging wall- and the footwall wedges, at the right- and the left, respectively, of the channel are replacable. These wedges were made for various dip angles- θ_1 and θ_2, respectively. 'A' is the thickness of the horizontal channel. For divergent-up inclined channels (i.e. $\theta_1 > \theta_2$), the aperture angle is $\theta_3 = (\theta_1 - \theta_2)$. For inclined channels with parallel walls (i.e. $\theta_1 = \theta_2$ case), 'B' is its thickness. The 'C' parameter is the dimension of the hanging wall wedge. The values of 'A', 'B', 'θ_1' and 'θ_2'for different experiments are listed in Table-2. In all the experiments, C= 3.5 cm. A pair of thin, parallel and broken lines represents the 1 mm opening across which the whole box can be separated into two halves. A 'front plate' and a 'back plate' are screwed in the frontal- and the rear side of the channel flow box. The box is screwed on a 'base plate'. A 'glass plate' is used in some experiments. A rectangular parallelepiped piston is pushed from right towards left side within the PDMS filled horizontal channel. The piston push is represented by a dark arrow at the right hand side of the piston.

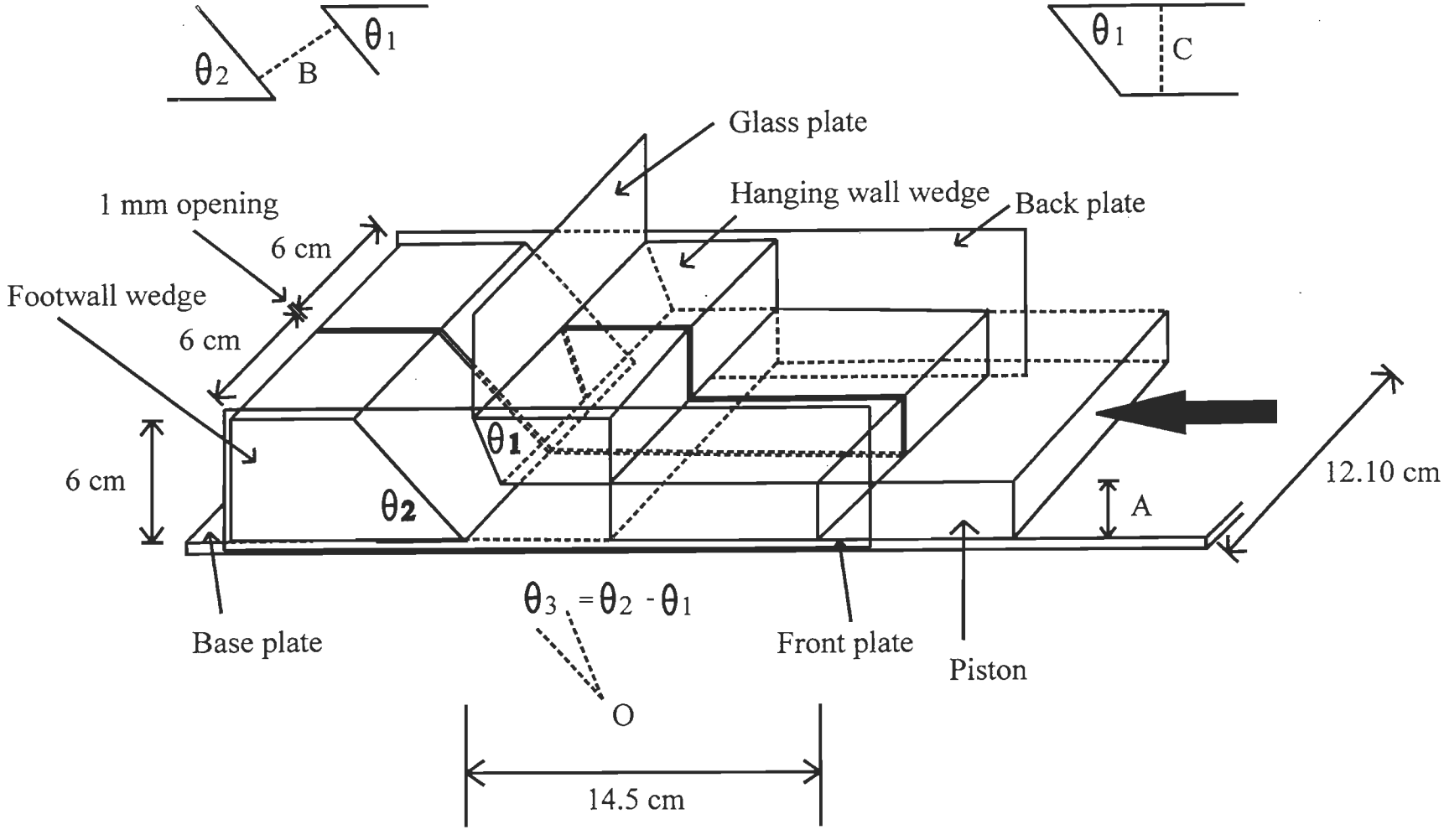
θ2
B
θ1
θ1
C
Glass plate
1 mm opening
Hanging wall wedge
Back plate
6 cm
Footwall wedge
6 cm
θ1
6 cm
θ2
A
12.10 cm
θ3 = θ2 - θ1
Base plate
Front plate
Piston
O
14.5 cm

Fig. 4.5

experiments with non-parallel inclined walls, grids of arcs and radial lines were used. The point 'O' in Fig. 4.5 was taken as the center of arcs of individual grids.

4.8. EXPERIMENTS & DISCUSSIONS

Using the channel flow box, 10 experiments were performed. The geometry of the channel flow box and the results of the individual experiments are presented in Table 2. The rectangular piston was pushed at the PDMS in the horizontal channel at a constant rate. In a few experiments (Exp no. 7, -8), a glass plate was fixed at the northeast boundary of the model HHSZ, which enables gravitational spreading of the PDMS preferentially towards southwest direction. The rationale for using the glass plate is that nappe movement of the HHSZ has been documented exclusively in the southwest direction (Thakur, 1993; Fig. 2b of Vannay and Grasemann, 2001).

It is important to mention that in the context of plate tectonics, no piston push exists in the (sub)horizontal channel. The over-thickened Tibetan plateau generated high temperature at depth and underwent partial melting. The molten material, due to buoyancy and overburden pressure, moved along the present HHSZ and gave rise to its extrusion in a channel flow mode (Fowler, 2005). High rate of erosion might have augmented this extrusion (Vannay et al., 2004). The exact replication of this complex process in experiment is difficult. Therefore, the experiments were aimed at generating parabolic velocity profile within the horizontal channel and let the fluid flow against gravity through inclined HHSZ channel of different geometries. The model material is PDMS, which is an incompressible fluid. Implicitly therefore, we neglect the possible

kinematic dilatancy effects due to partial melting (Grasemann et al., 2006) in these experiments.

Salient observations common in all these experiments are as follows.

(A) The distance traveled by the piston within the horizontal channel is a linear function of time (Figs. 4.6-4.15). This was found true even when, in some experiments, the PDMS touched the horizontal surface where it extrudes, which gives rise to the loss of mass from the channel flow box.

(B) Before the start of the piston push, Fig. 4.16a shows how the complete set up of the channel flow box looks like when the PDMS is inside it and grid are imprinted. Six flow domains in these experiments are visually deciphered in the two channels (Figs. 4.16b to 4.17a). From piston towards the inclined channel, these zones are as follows. (i) Zone-1: the complex flow behaviour near the piston within the horizontal channel; vertical markers in this domain get rounded and looks like a pitcher tilted at 90^0 (Fig. 4.16c). These profiles are related to piston push and are, therefore, not the orogenic case. (ii) Zone-2: congruent parabolic velocity profiles (Fig. 4.16c). (iii) Zone-3: the corner joining the horizontal- and the inclined channel (Fig. 4.16d). Here the velocity profile is of transition stage between that of a horizontal- and inclined channel. The deformed vertical markers demonstrate how the fluid enters from the horizontal- into the inclined channel. No documentation of Zone-2 and -3 are possible in fieldwork since these took place at depth. (iv) Zone-4: parabolic velocity profiles within the inclined channel with their vertices at the middle of the channel (Fig. 4.16d). (v) Zone-5: parabolic and somewhat

Table-2

Experiment Specifications											**Experiment Results for the horizontal channel**			
Exp No.	Channel flow box configuration						PDMS mass inside channel flow box (gm)	Exp continued till (minutes)	Pressure gradient measured till (minutes)	Gear	Piston velocity (mm per 10 minutes)	Pressure gradient versus time parameters of equation 13, in zone-2 in the horizontal channel		
	θ_1	θ_2	θ_3 (=θ_1-θ_2)	A (cm)	B (cm)	Glass plate at margin of upper inclined wall						a ($\times 10^6$)	b ($\times 10^6$)	Corr. Coeff. (r)
1	40	40	0 (P)	2.50	2.50	Not used	634	231(*1)	214	.3	3.13	0.44	-0.28	0.98
2	40	30	10 (GD)	2.50	D	Not used	728.4	202	104	.3	3.0	0.0007	0.021	0.998
3	60	30	30 (SD)	2.50	D	Not used	771.3	353	98	.3	0.25	0.0008	0.019	0.999
4	60	30	30 (SD)	2.50	D	Not used	771.3	250	54	.6	5.9	0.0016	0.185	0.99
5	40	40	0 (P)	2.50	2.50	Not used	634	252	42.5	.6	6.0	0.0014	0.152	0.983
6	40	30	10 (GD)	2.5	D	Used	728.4	471(*2)	126	.3	0.25	0.0006	0.198	0.976
7	30	30	0 (P)	2.5	5.0	Used	1032.7	484	38	.3	2.8	0.0008	0.456	0.967
8	30	30	0 (P)	2.5	5.0	Not used	1032.7	48	42	.6	5.6	0.002	0.281	0.996
9	30	30	0 (P)	2.5	1.25	Not used	519.7	55	49	.6	5.8	0.0018	0.2271	0.99
10	30	30	0 (P)	2.5	1.25	Not used	519.7	80	79	.3	3.51	0.0011	0.3677	0.997

Caption: Summary of specifications and results of analogue models. The parameters 'θ_1', 'θ_2', 'θ_3', 'A' and 'B' are defined in Fig (1). The parameters 'a' and 'b' are coefficients of equation 15 in the Appendix of this chapter. Symbols: D: divergent-up inclined channel, i.e. 'B' value increases in up-dip direction; GD: Gently divergent-up inclined channel; SD: Strongly divergent-up inclined channel; P: Parallel wall inclined channel; *1. Extruded PDMS was cut and removed after 1 hr 45 minutes; *2. Pulsed flow. Piston movement history- Piston run between: 0-62 minutes, 126-182 minutes, 243-303 minutes, and 363-423 minutes. Piston advance stopped between: 62-126 minutes, 182-243 minutes, 303-363 minutes, and 423-471 minutes.

Figure Captions.

Figs. 4.6-4.9 Rate of advance of the piston through the horizontal channel is represented by plotting time in seconds along the X-axis and displacement of the piston in mm along the Y-axis. From the best fit lines obtained, the average velocities of the piston for different experiments are calculated and are presented in Table-2. Figures corresponding to the experiments are as follows.

Fig. 4.6 → Exp-1
Fig. 4.7 → Exp-2
Fig. 4.8 → Exp-3
Fig. 4.9 → Exp-4

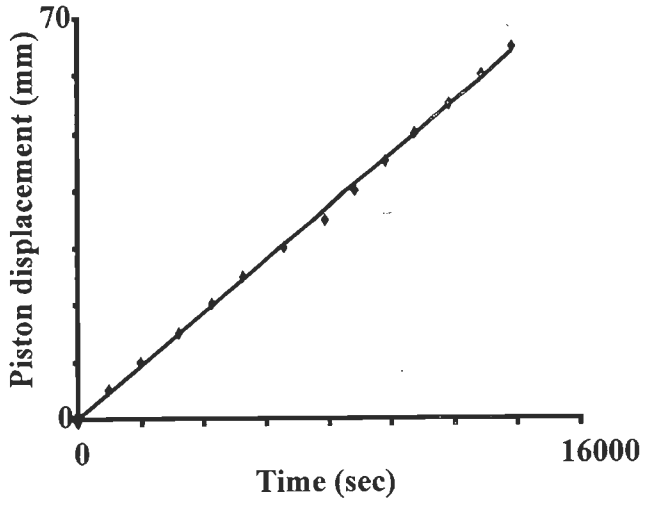

Fig. 4.6

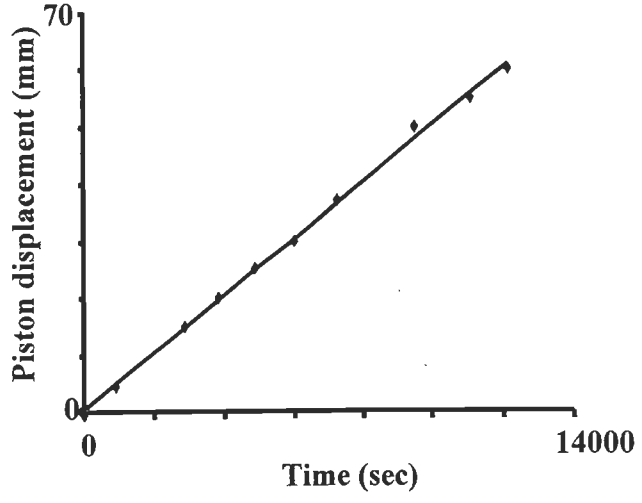

Fig. 4.7

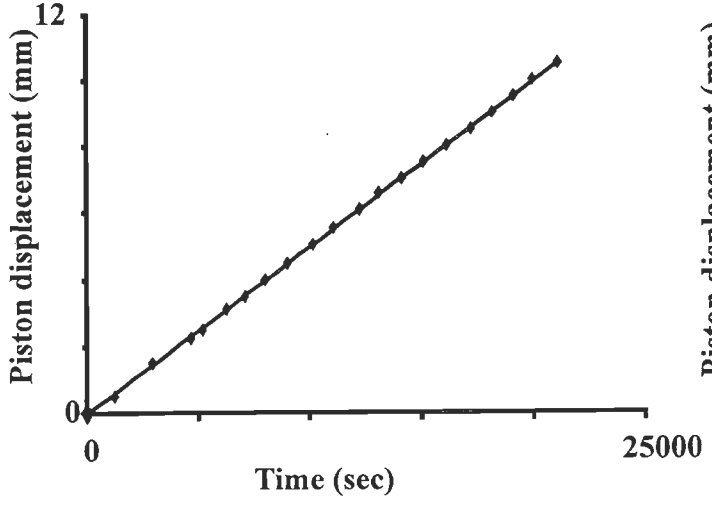

Fig. 4.8

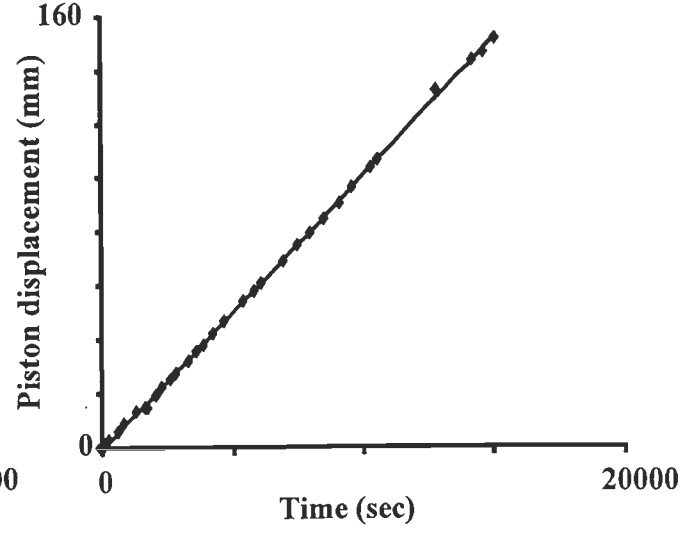

Fig. 4.9

Figure Captions.

Figs. 4.10-4.13 Rate of advance of the piston through the horizontal channel is represented by plotting time in seconds along the X-axis and displacement of the piston in mm along the Y-axis. From the best fit lines obtained, the average velocities of the piston for different experiments are calculated and are presented in Table-2. Figures corresponding to the experiments are as follows.

Fig. 4.10 → Exp-5
Fig. 4.11 → Exp-6
Fig. 4.12 → Exp-7
Fig. 4.13 → Exp-8

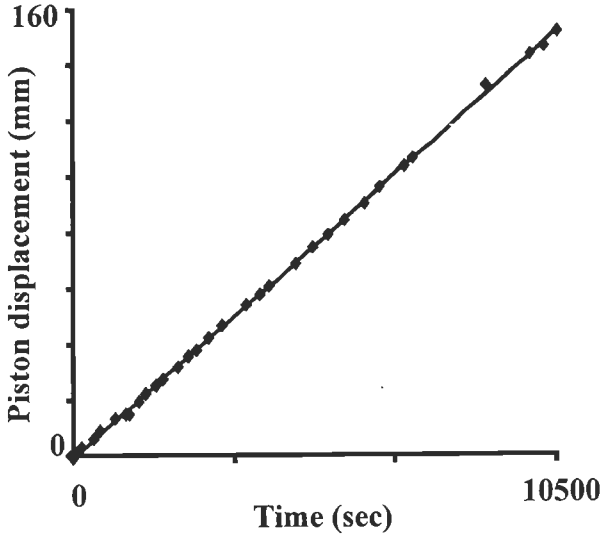

Fig. 4.10

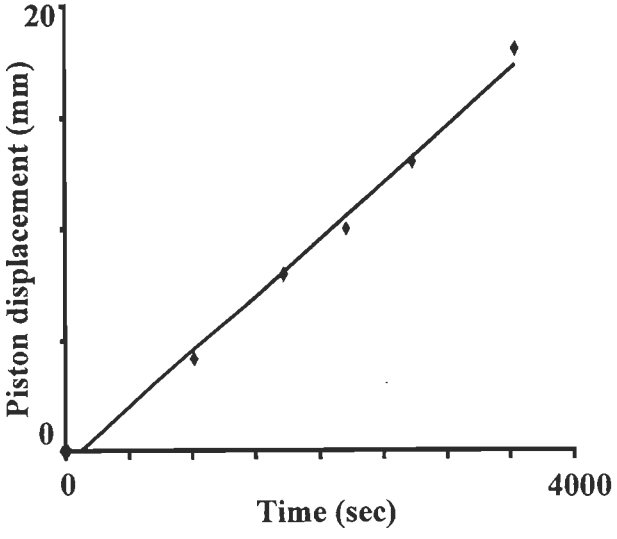

Fig. 4.11

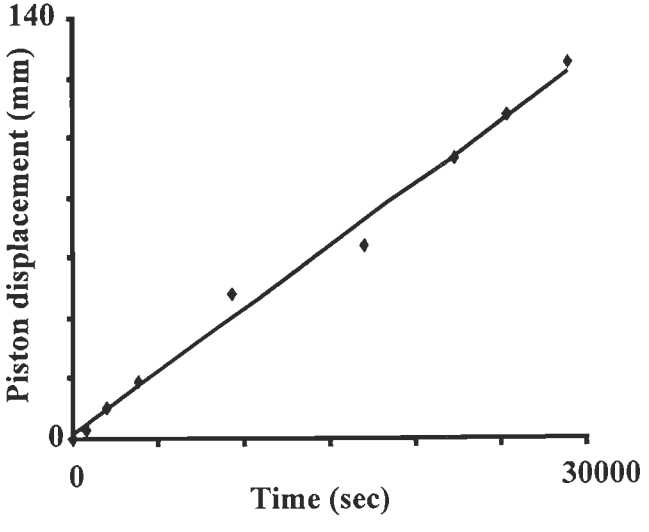

Fig. 4.12

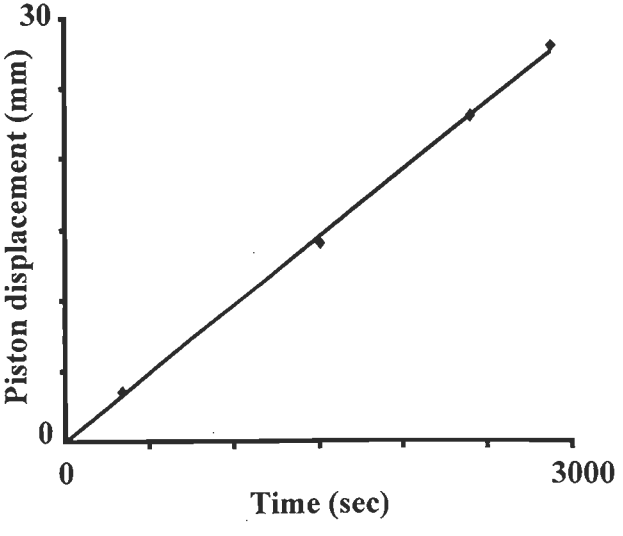

Fig. 4.13

Figure Captions.

Figs. 4.14-4.15 Rate of advance of the piston through the horizontal channel is represented by plotting time in seconds along the X-axis and displacement of the piston in mm along the Y-axis. From the best fit lines obtained, the average velocities of the piston for different experiments are calculated and are presented in Table-2. Figures corresponding to the experiments are as follows.

Fig. 4.14 → Exp-9

Fig. 4.15 → Exp-10

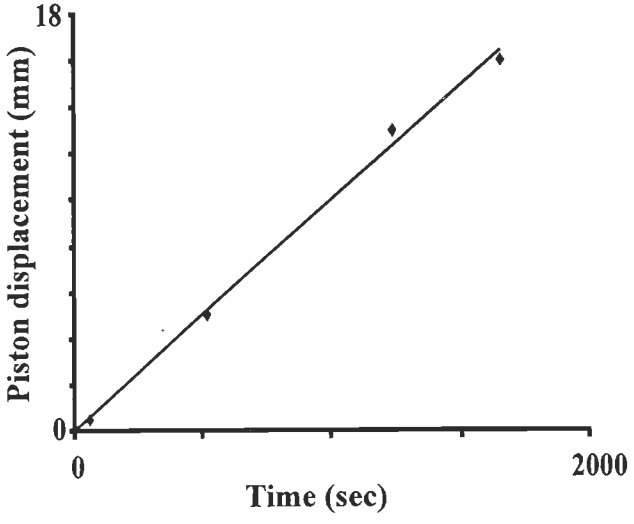

Fig. 4.14

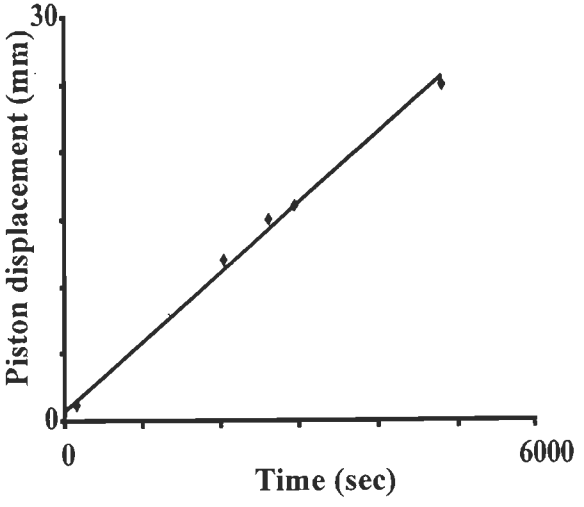

Fig. 4.15

Figure Captions.

Fig. 4.16a. The channel flow box full of PDMS, with grids imprinted at its middle, before the onset of deformation. Each smallest square in the grid are of 5mm×5mm dimension. The inclined channel, or the model HHSZ, dips northeasterly. The HHSZ is defined by the future MCT and the future STDS as the southwestern- and the northeastern boundaries, respectively. The dip direction and the symbols for the inclined channel boundaries are considered same in all the subsequent photographs. Circular markers have been used in the horizontal channel in this (but not in all) experiments. Experiment-1. Time 0 sec.

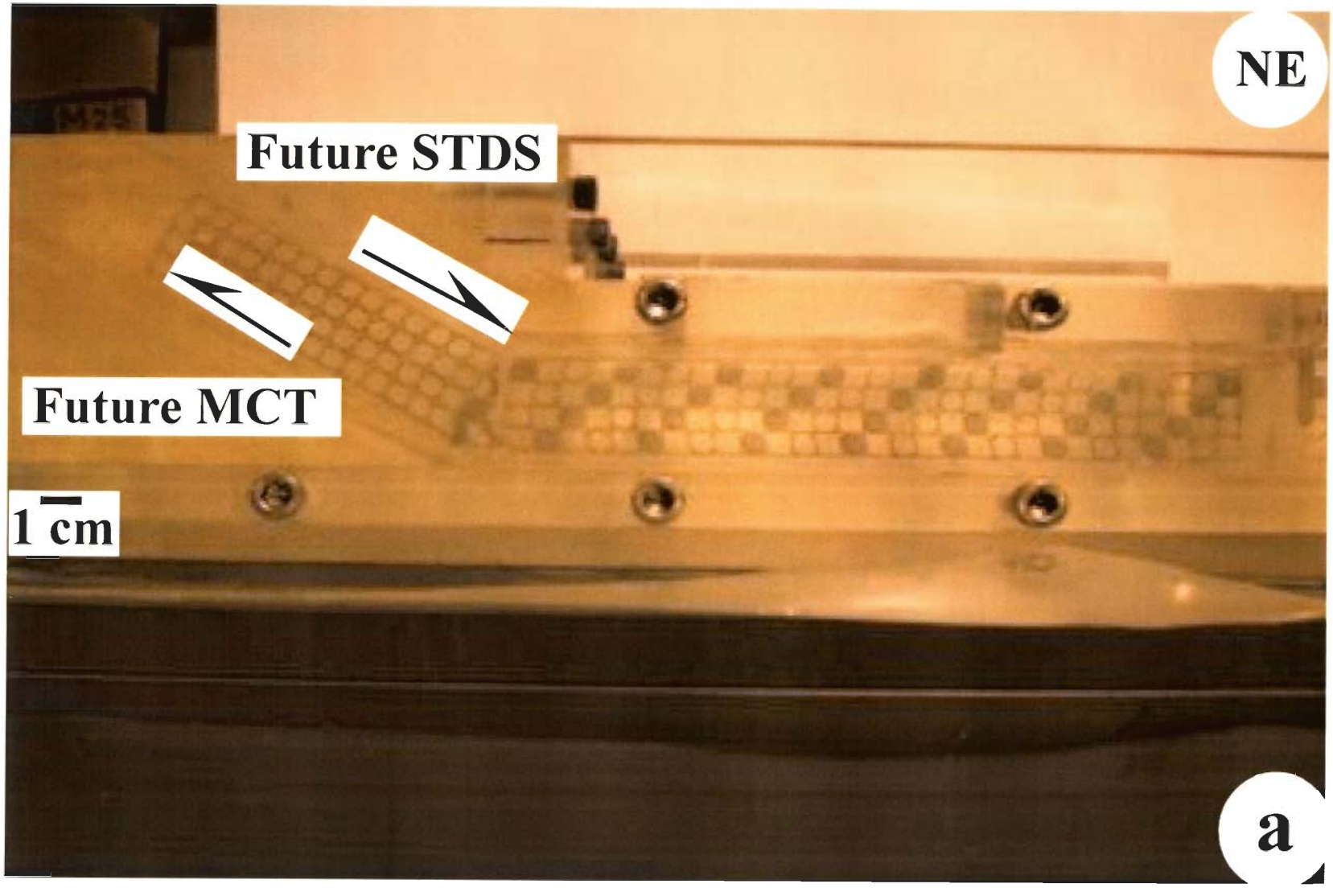

Fig. 4.16a

Figure Captions.

Fig. 4.16b. Pushing the piston towards the right hand side in the horizontal channel, the PDMS extrudes from the inclined channel. 6 decipherable flow zones are shown in the subsequent photographs. Experiment number-3. Photograph number-15. Time: 64 minutes.

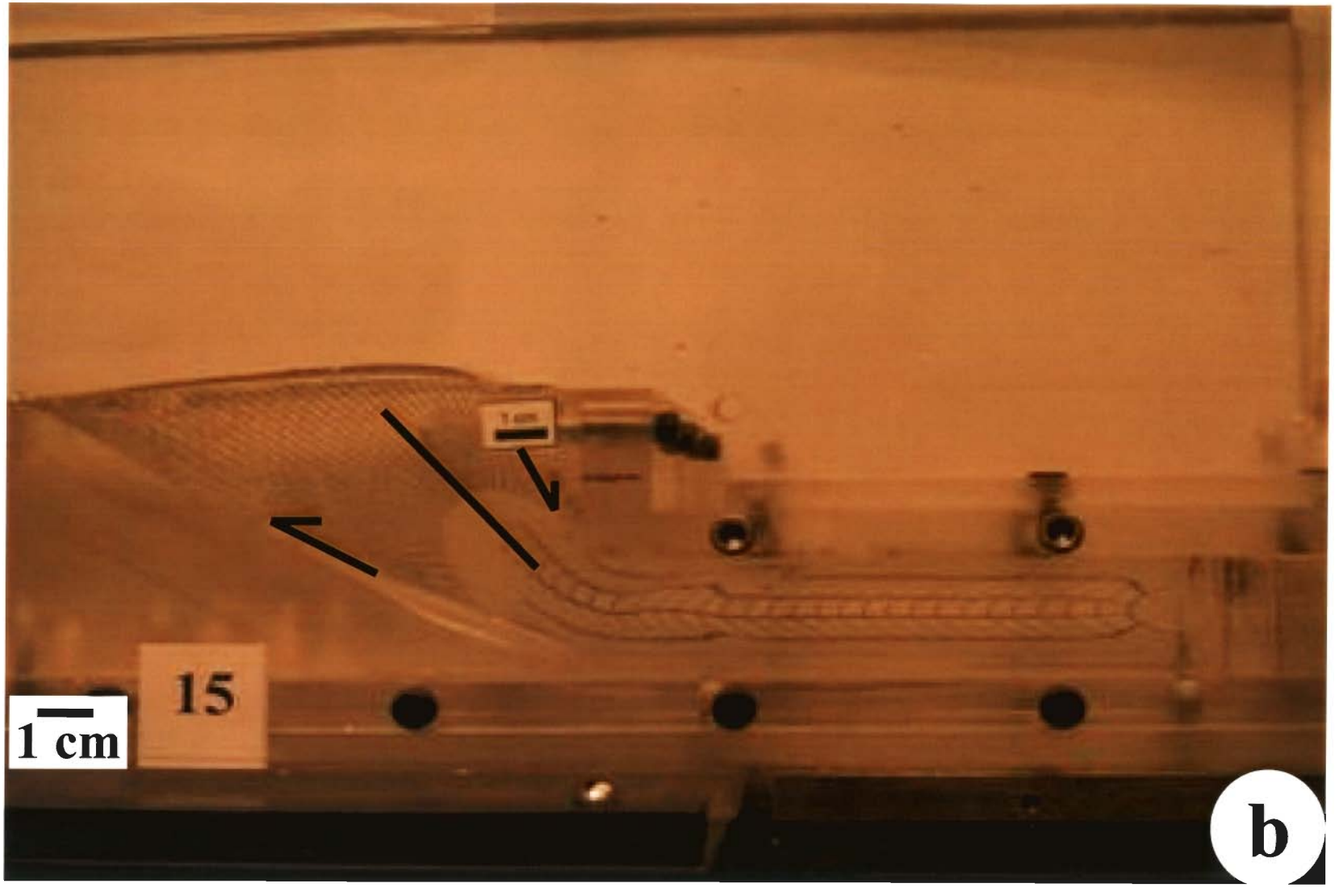

Fig. 4.16b

Figure Captions.

Fig. 4.16c Flow zones 1 and -2 within the horizontal channel are shown. In zone-1, horizontal lines of the grid are pinched at their contacts with the piston, pointed out by arrows. The vertical lines are pinched and resemble an inverted pitcher. In zone-2, the vertical markers are deformed into congruent parabolas. Experiment number-9. Photograph number-51. Time: 49 minutes.

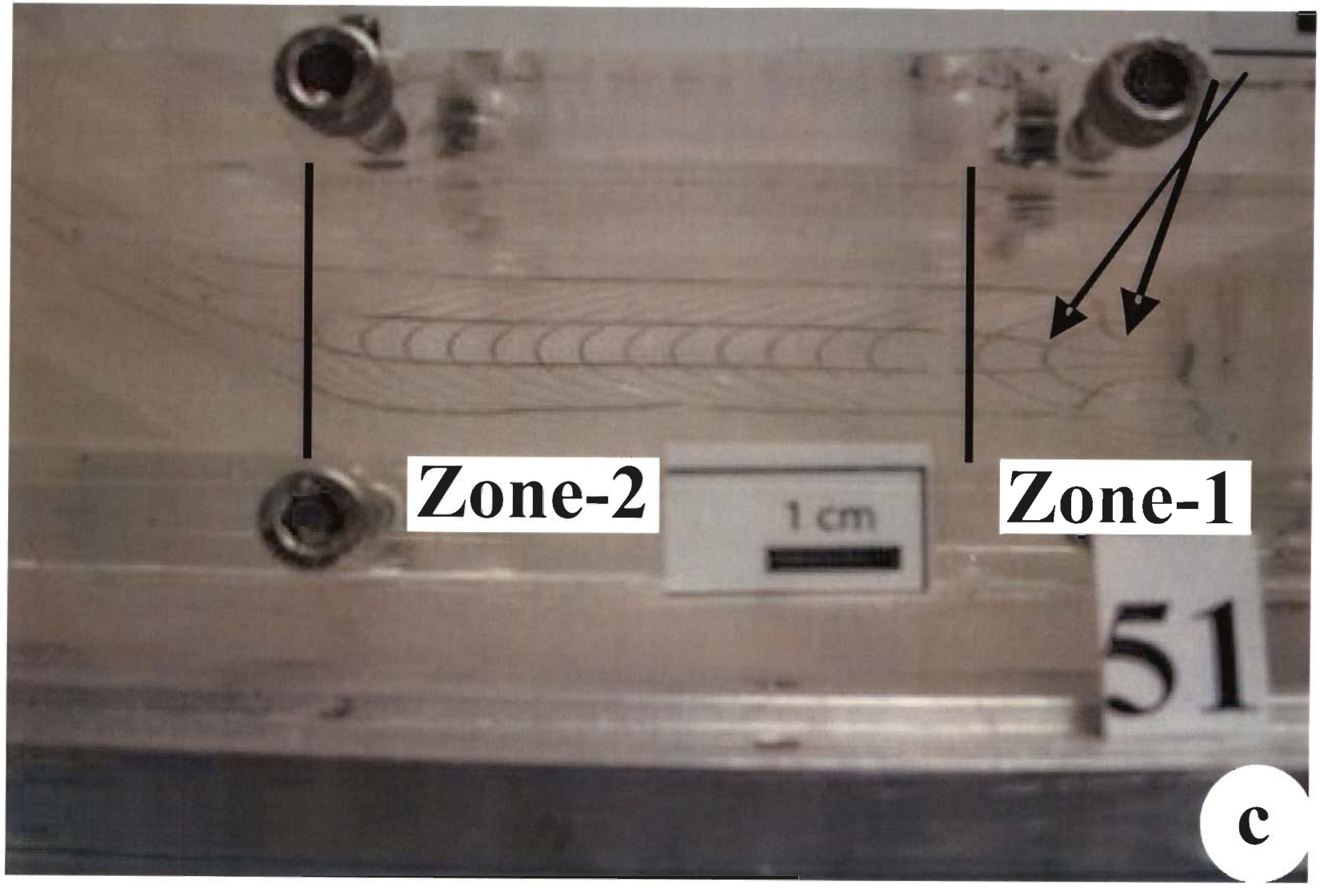

Fig. 4.16c

Figure Captions.

Fig. 4.16d. The flow zone-3 is defined at the corner where parabolic velocity profile in the horizontal channel enters the inclined channel. Lines in the grid that were initially horizontal become inclined as they enter the inclined channel, shown by arrow. The profiles show their vertices shifted towards the upper wall of the inclined channel. Experiment number-7. Photograph number-12. Time: 20 min 32 sec.

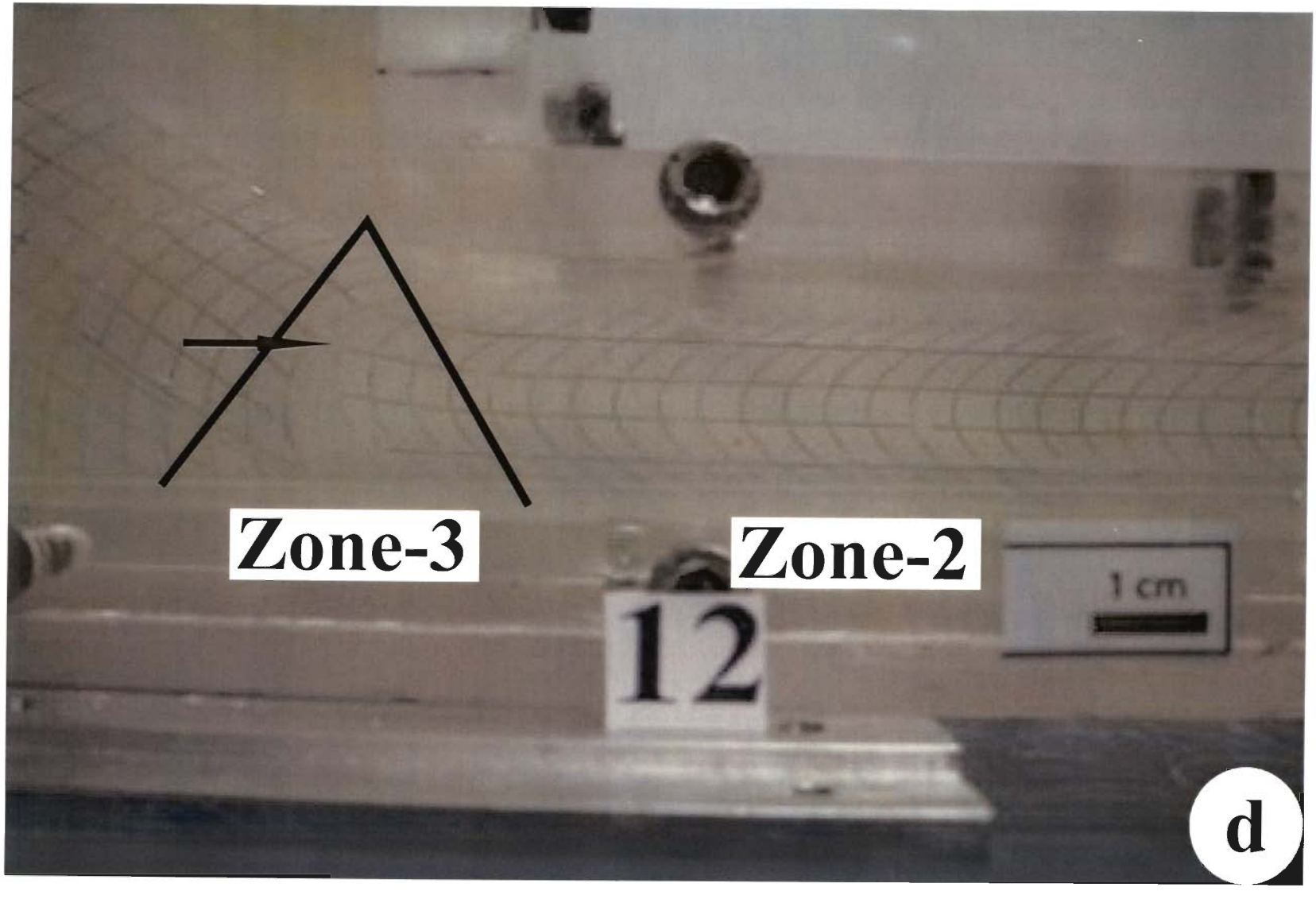

Fig. 4.16d

more rounded velocity profiles within the inclined channel with their vertices shifted at the upper wall of the inclined channel (Fig. 4.17a). Zones 4 and -5 are only important since they give the final sense of shear which is expected to be observed in the HHSZ. (vi) Zone-6: the extruded part of the PDMS. The extrusion profile is a parabola at the beginning with the vertex located closer to the upper wall of the inclined channel (Fig. 4.17b). Zone-6 can not be correlated with the topography of the HHSZ since exhumation related to top-to-SW intra-continental ductile shearing with the HHSZ (Jain and Manickavasagam, 1993) prior to channel flow might have already created a topography. The six flow zones are schematically represented in Fig. 4.18.

(C) Markers within the inclined channel, initially parallel to the walls, become diverging-up in zone-4 and -5 (Fig. 4.17b).

(D) In zone-6, markers initially (sub)parallel to the walls of the inclined channel become round-hinge folded, and are discordant to the parabolic profile of the extruded PDMS in zone-6 after the PDMS has undergone pronounced gravitational spreading (Figs. 4.17b, -c).

(E) In zone-4, an intrafolial fold forms near the contact between the grids that was initially in the horizontal channels and that initially in the inclined channel. The sense of shear given by this fold is same to that given by the extensional shear regime where it has formed (Fig. 4.17b). Intrafolial folds showing top-to-NE sense of shearing have been reported from field in the Sutlej section of the HHSZ in Chapter-3 (Fig. 3.5a) and in

micro-scales from that in the Zanskar section in Chapter-2 (Fig. 2.3c; 2.4a, -d; 2.6a). However, intrafolial folds are not exclusive within the detachments. Such folds have also been reported outside the Himalayan Detachment-1 and the Himalayan Detachment-2 in the Sutlej section of the HHSZ, showing top-to-SW sense of shearing of the Himalayan D2 deformation of Jain et al. (2002) (Fig. 3.3a).

(F) As time progresses, the extruded part of the PDMS in. zone-6 undergoes gravitational spreading. This spread is more efficient towards the lower wall of the inclined channel and shows neutral non-plunging cylindrical recumbent folds as revealed from markers that were initially perpendicular to the inclined channel walls. With prolonged gravitational spreading, the profile of the extruded mass looses its parabolic shape (Fig. 4.17c).

(G) The PDMS originally within the horizontal channel, on continuous push of the piston, starts moving up only through the upper part of the inclined channel. In effect, the boundary between the fluid initially within the horizontal channel, which moves up through the inclined channel, and that within the inclined channel itself, acts as a thrust plane. With progressive piston push, this northeast dipping blind thrust propagates upward, undergoes anticlockwise rotation and come closer to the lower wall of the inclined shear zone. The inclined shear zone gets divided into wedges when this thrust comes to the surface. From its formation till the surface appearance, the thrust remains within the ductile compressional shear regime. This holds true for (i) parallel-wall inclined channel with thickness same as that of the horizontal channel (Fig. 4.17d, 4.19a);

Figure Captions.

Fig. 4.17a. The Flow zone-4 is defined by parabolic velocity profiles with their vertices at the middle of the inclined channel. The Flow zone-5 is near the opening of the inclined channel. Here the velocity profiles are parabolic, somewhat rounded, with their vertices shifted near the upper inclined wall. The flow zone-6 is the extruded part of the PDMS. Experiment number-3. Photograph number-10. Time: 35 minutes.

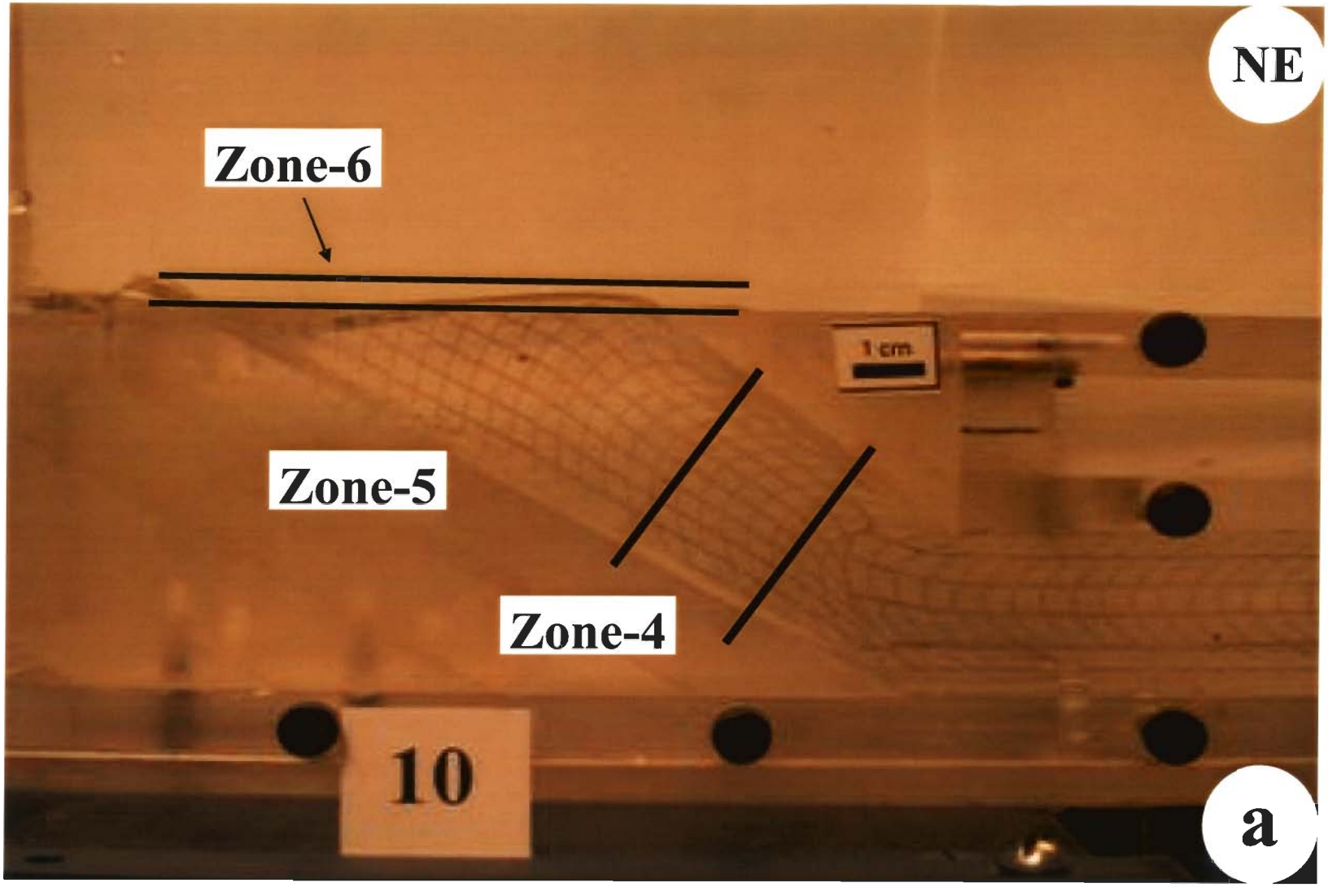

Fig. 4.17a

Figure Captions.

Fig. 4.17b. The vertical thickness of flow zone-6 keeps increasing as the piston moves inside the horizontal channel. The profile of the extruded PDMS is parabolic. Its vertex is pointed by an arrow within a white circular background. The glass plate 'gp' prevents gravitational spreading of the extruded PDMS towards right hand side (NE direction). The model inclined shear zone is divided into a compressional shear zone at the left, and a thicker extensional shear zone at the right. Half arrows indicate ductile extensional shearing as interpreted from intrafolial fold developed at the contact between grids that were initially within the inclined channel and that within the horizontal channel. The round-hinge folded markers in zone-6 are non-parallel to the parabolic profile of the extruded PDMS. The arrow within the white elliptical background points out diverging-up markers. Experiment number-3. Photograph number-28. Time: 111 minutes.

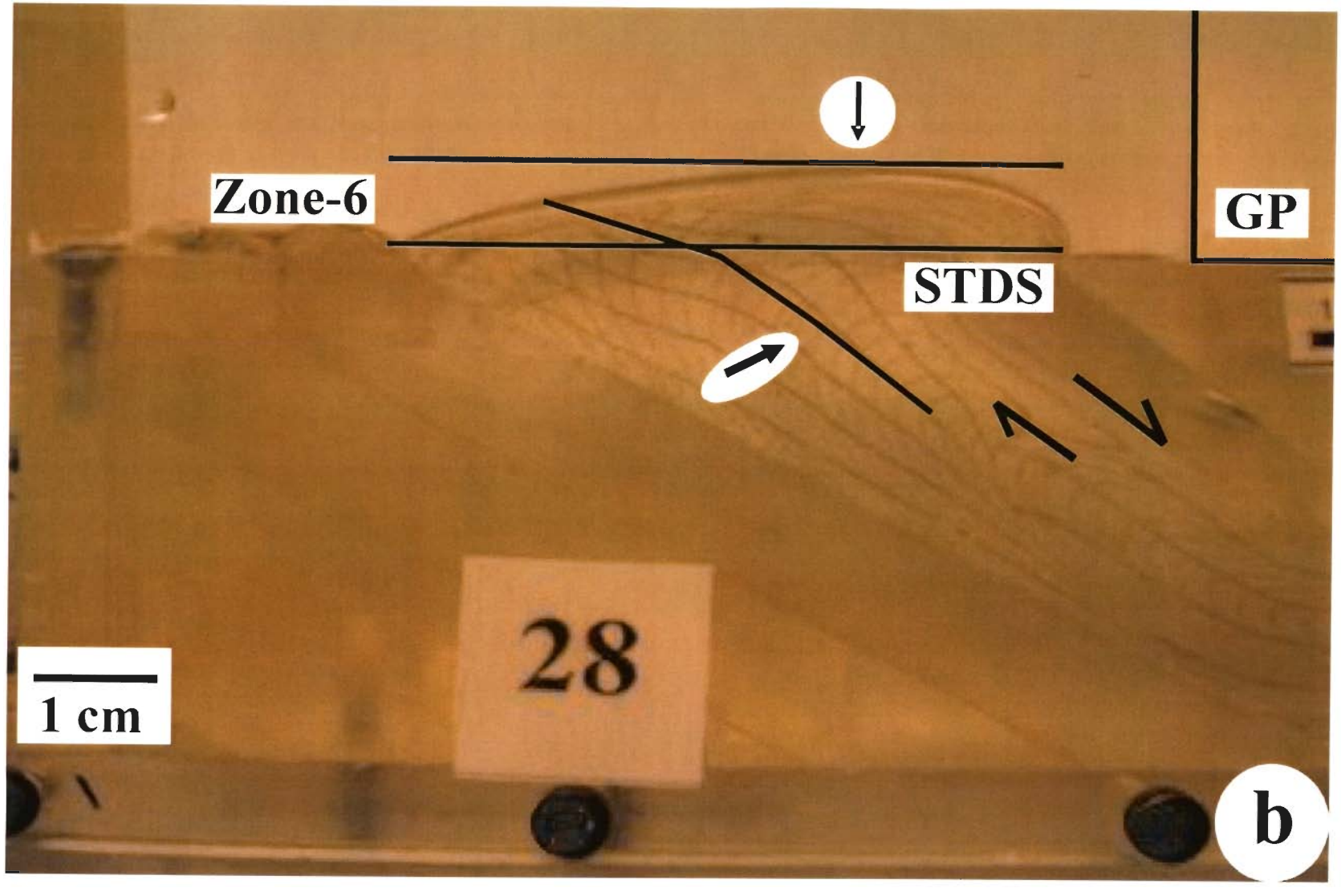

Fig. 4.17b

Figure Captions.

Fig. 4.17c. As the experiment is continued for a very long time, PDMS in zone-6 undergoes gravitational spreading preferentially towards the lower wall of the inclined channel. An arrow points at the recumbent folded marker within the gravitationally spread part of the PDMS. 's'=4.7 cm is the spread of the model nappe, measured from the lower wall of the inclined channel. A part of the extruded PDMS at the left side of the vertical line $AA^{/}$ rests on the horizontal surface, and therefore has its mass outside the channels. Experiment number-7. Photograph number-45. Time: 7hr 15 min.

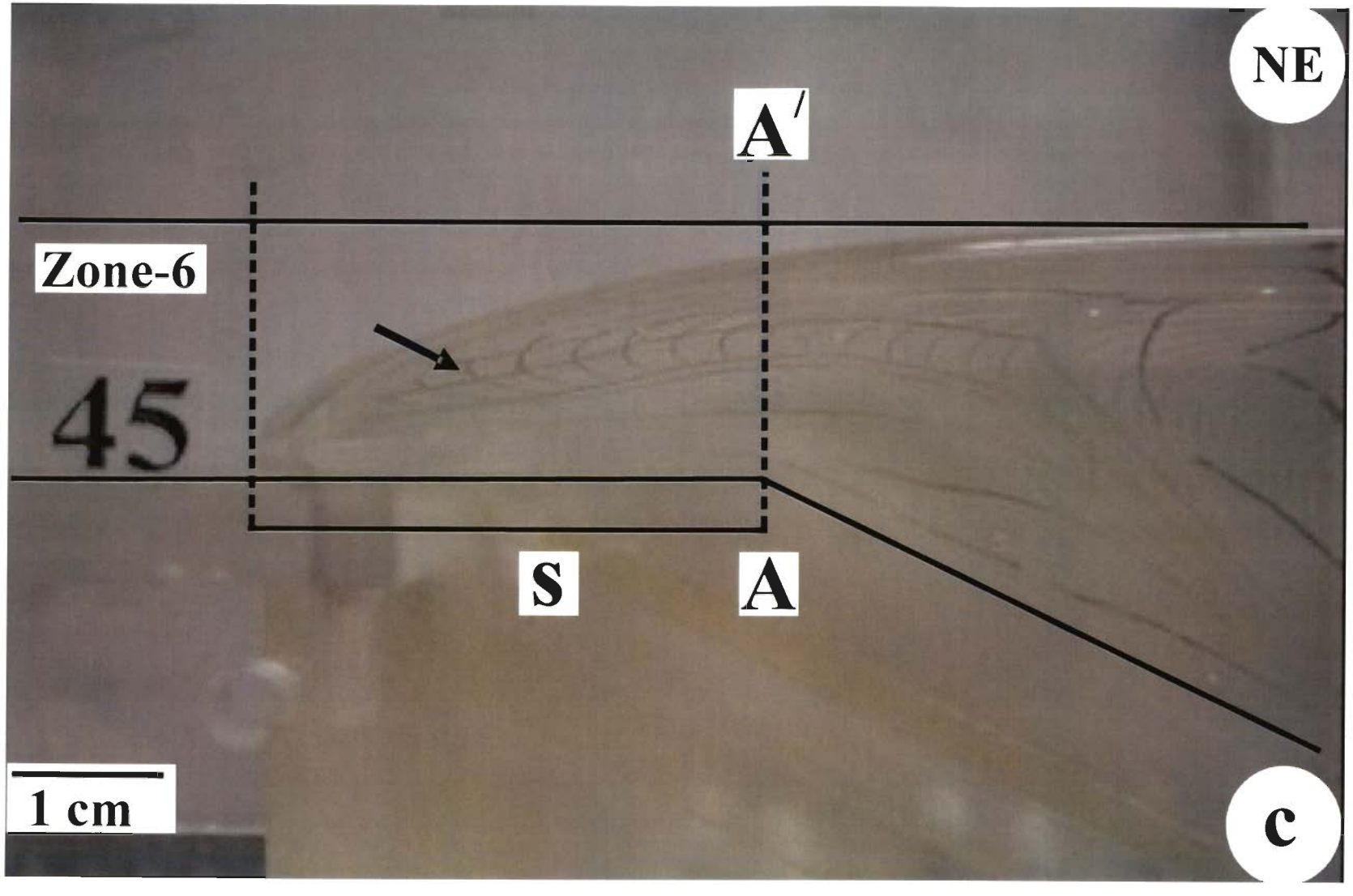

Fig. 4.17c

Figure Captions.

Fig. 4.17d. In this experiment, the inclined channel is defined by parallel walls and has its thickness equal to that of the horizontal channel. A ductile secondary blind thrust is produced within the inclined channel. The lower boundary of the grid, originally in the horizontal channel, defines this thrust. The curved dashed line separates the zone of ductile compressional shearing at its left from the zone of ductile extensional shear at its right. The blind thrust has formed within the zone of compressional shearing. This experiment is an example of free extrusion- no glass plate is used to dictate neither the extrusion nor the gravitational spreading. Experiment-1. Photo number: 12. Time: 90 minutes.

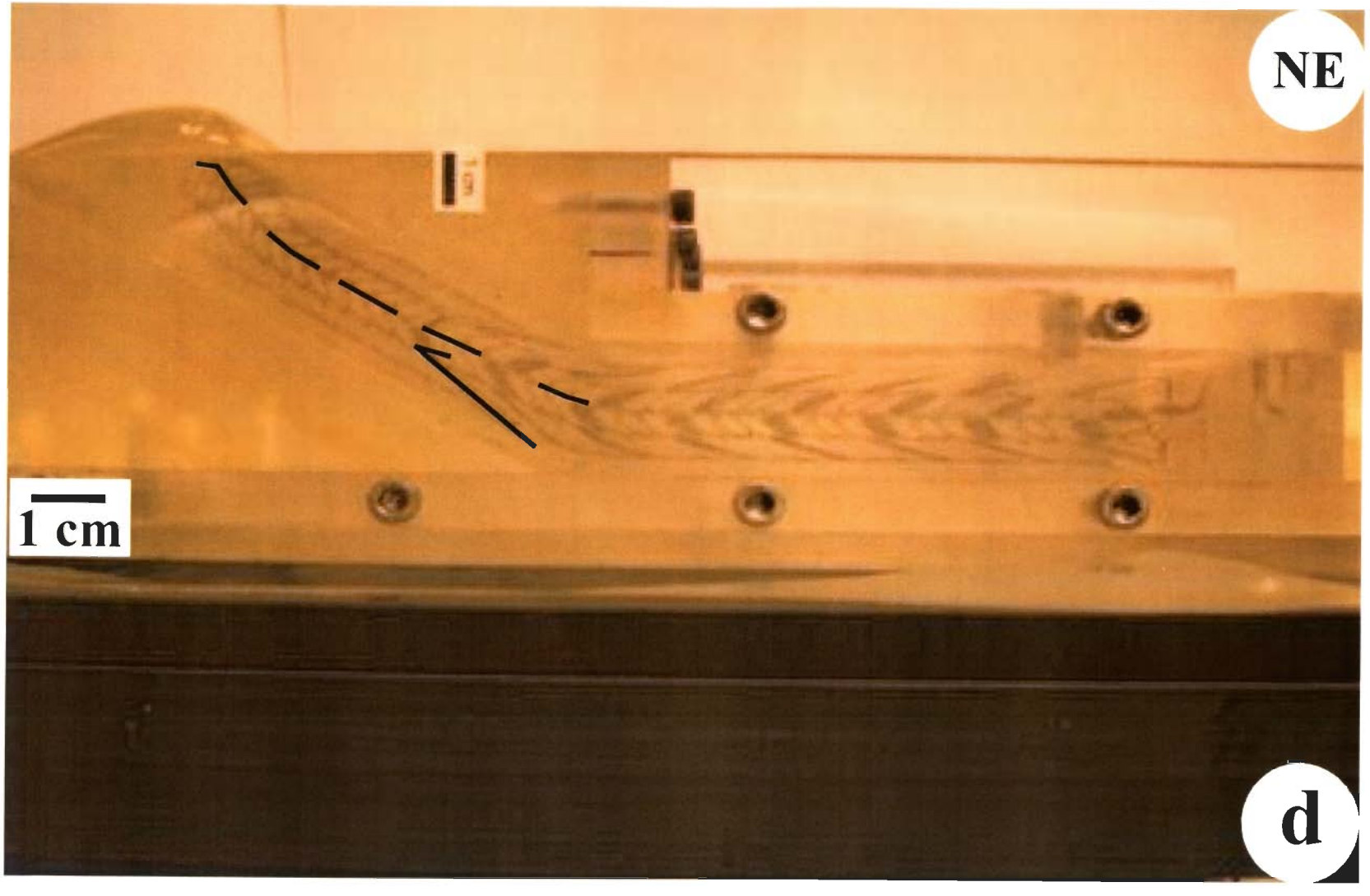

Fig. 4.17d

Figure Captions

Fig. 4.18. A schematic sketch of different flow profiles developed in all the experiments performed. These profiles are zone-1: formed at the contact with the piston, looks like an inverted pitcher; zone-2: parabolic profiles; zone-3: profile formed at the corner; zone-4: parabolic profiles; zone-5: rounded profile; and zone-6: profile of extrusion. The half arrow in the zone-3 indicates a blind ductile thrust. The solid arrow indicates the push of the piston.

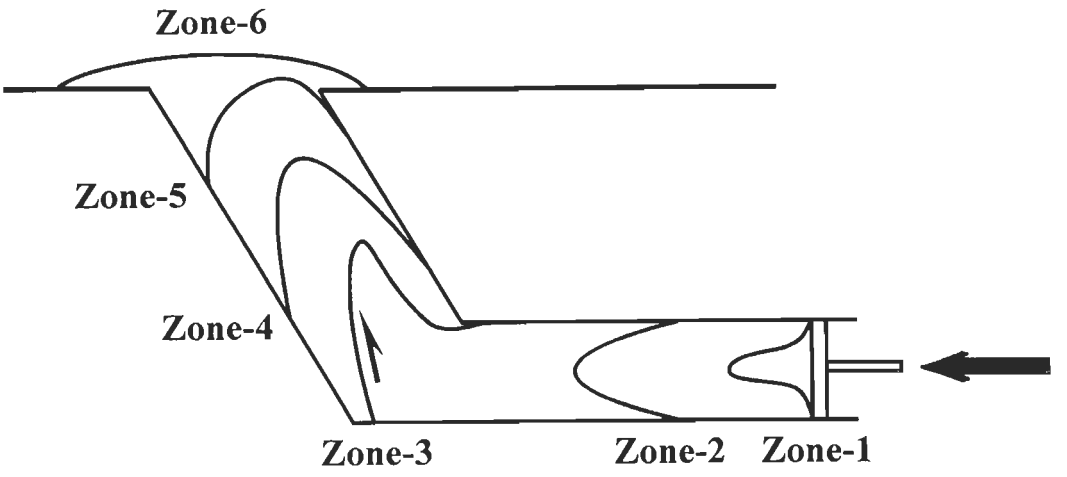

Fig. 4.18

Figure Captions.

Fig. 4.19a. The photograph is in the late stage of the experiment. In this experiment, the inclined channel is defined by parallel walls and has its thickness equal to that of the horizontal channel. The half arrow and the dashed line represent the ductile thrust and the boundary separating opposite senses of shearing, respectively. The thrust dips towards the upper wall of the inclined channel and defines a wedge with the lower wall. The thrust is within the ductile compressional shear regime. Experiment-1. Photo number: 22. Time: 215 minutes.

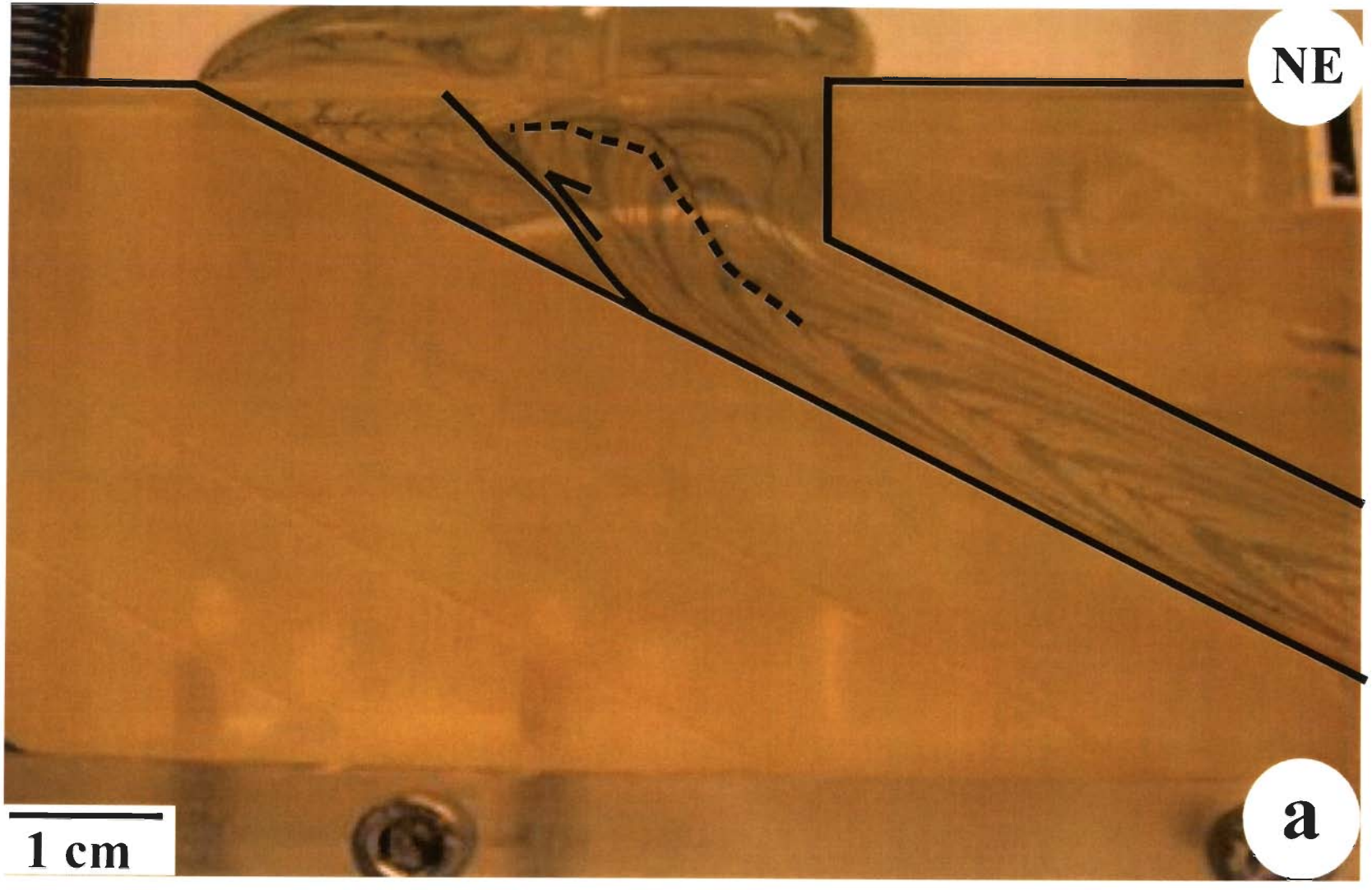

Fig. 4.19a

(ii) parallel-wall inclined channel with thickness more than that of the horizontal channel (Fig. 4.19b); (iii) gently diverging-up inclined channel (Fig. 4.19c); (iv) strongly diverging-up inclined channel (Fig. 4.19d).

The Chaura Thrust (Fig. 4.20) in the Sutlej section of the HHSZ (Singh and Jain, 1993; Jain et al., 2000) divides the shear zone into two parts. This thrust is south to the detachment equivalent to the STDS. In other words, it lies within the top-to SW of compressional ductile shear regime. The thrust was active 4.9-1.5 Ma ago within the HHSZ of the Sutlej section The Chaura Thrust has been visualized as a complex ductile shear zone, which continued to show displacement even in the brittle regime. This thrust is characterized by flattening type finite strain. The foot wall and the hanging wall of Chaura Thrust had differentially exhumed at rates of 0.61±0.10 $mm.yr^{-1}$ and 2.01±0.35 $mm.yr^{-1}$ from 4.9±0.2 Ma and 1.49±0.07 Ma to present, respectively; with a vertical displacement of 2.08±0.68 km between 4.9-1.5 Ma with an average of 0.6 $mm.yr^{-1}$ (Jain et al., 2000; Jain et al., 2002). This thrust movement is at least 13 Ma younger than the ongoing channel flow during Middle Miocene Period ~18 Ma ago. This means that the channel flow, which was going on during the Mid-Miocene Period by simultaneous ductile thrusting of the MCT and the ductile extensional shearing of the STDS, might be the reason of generating a younger subsidiary thrust within the HHSZ giving rise to localized faster exhumation rates.

(H) In all the experiments (Table-2) with different physical boundary conditions and flow rates, a single extensional shear zone, equivalent to the STDS in the HHSZ is produced.

A broad zone of ductile extensional shearing forms adjacent to the upper wall of the model inclined channel. This zone is comparable with the STDS in terms of the extensional shearing produced. In few of the models, the STDS is thicker than the remainder of the HHSZ (Fig. 4.17b). The ratio of thicknesses between the ductile extensional to -compressional shear zones within the inclined channel seems to be dependent on the minor variation of physical boundary conditions, such as free extrusion (Fig. 4.17d), extrusion only in the direction of the lower wall of the channel (Fig. 4.17b), and different outlet geometry of the inclined channel (Figs. 4.17a, -b, -d; 4.19a-d).

Simultaneous generation of two extensional shear zones (the ND2 pattern), as predicted in some of the analytical solutions of Jeffery-Hamel flow, does not arise in the present analogue models within inclined channels of different geometries realistic to that of the HHSZ. Therefore, under the chosen set of physical boundary conditions, the analogue models also indicate that simultaneous generation of two ductile extensional shear zones is not possible- hence they must be sequential. The only possible explanation for the occurrence of two distinct extensional shear zones within the HHSZ is that channel flow took place in two pulses- one of the pulses occurred throughout the shear zone, and the other was restricted in a lower sub-channel. The same conclusion was drawn in the previous chapter of this thesis from mathematical analyses of different situations of flow through parallel walls.

Figure Captions.

Fig. 4.19b The photograph is in the late stage of the experiment when pronounced gravitational spreading of the PDMS towards the left hand side of the horizontal surface has taken place. In this experiment, the inclined channel is defined by parallel walls and has its thickness half to that of the horizontal channel. The ductile thrust is marked with a half arrow. The broken line is the trace of the outer limit of the PDMS that was initially within the horizontal channel. Line 'mn' separates the zone of ductile compressional shearing at its left from the zone of ductile extensional shearing at its right. The thrust lies within the ductile compressional shear zone. The glass plate 'gp' prevents gravitational spreading of the extruded PDMS towards right hand side of the inclined model channel. A part of the extruded PDMS at the left side of the vertical line $AA^{/}$ rests on the horizontal surface, and therefore has its mass outside the channels. Experiment-7. Photo number: 42. Time: 6 hours 13 minutes.

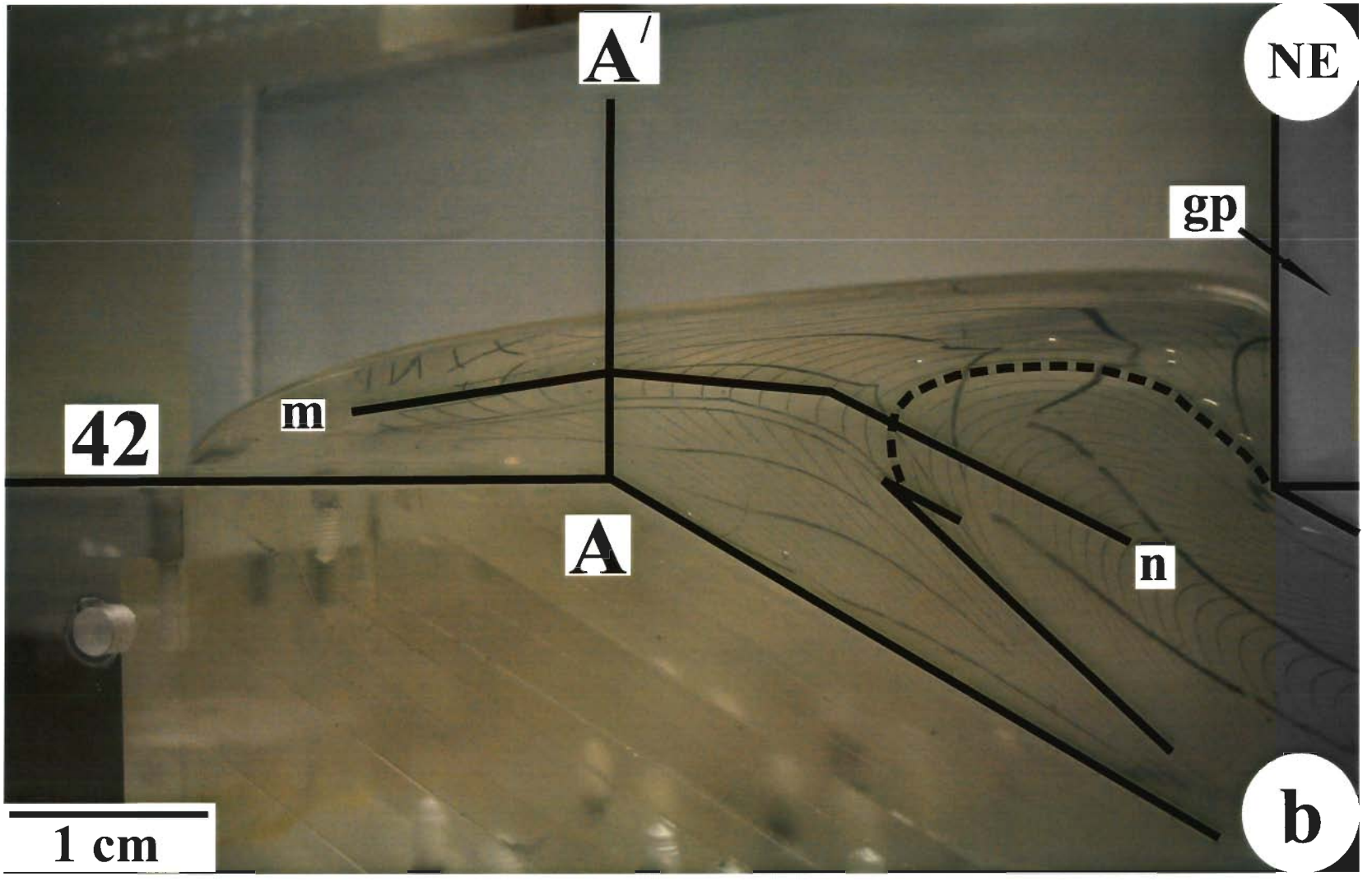

Fig. 4.19b

Figure Captions.

Fig. 4.19c In this experiment, the inclined channel is defined by parallel walls and has is gently divergent-up. The ductile thrust is marked with a half arrow. Line 'mn' separates the zone of ductile compressional shearing at its left from the zone of ductile extensional shearing at its right. The thrust lies within the ductile compressional shear zone. No 'glass plate' is used in this experiment. A part of the extruded PDMS at the right side of the vertical line AA' rests on the horizontal surface, and therefore has its mass outside the channels. Experiment-2. Photo number: 45. Time: 3 hours 5 minutes.

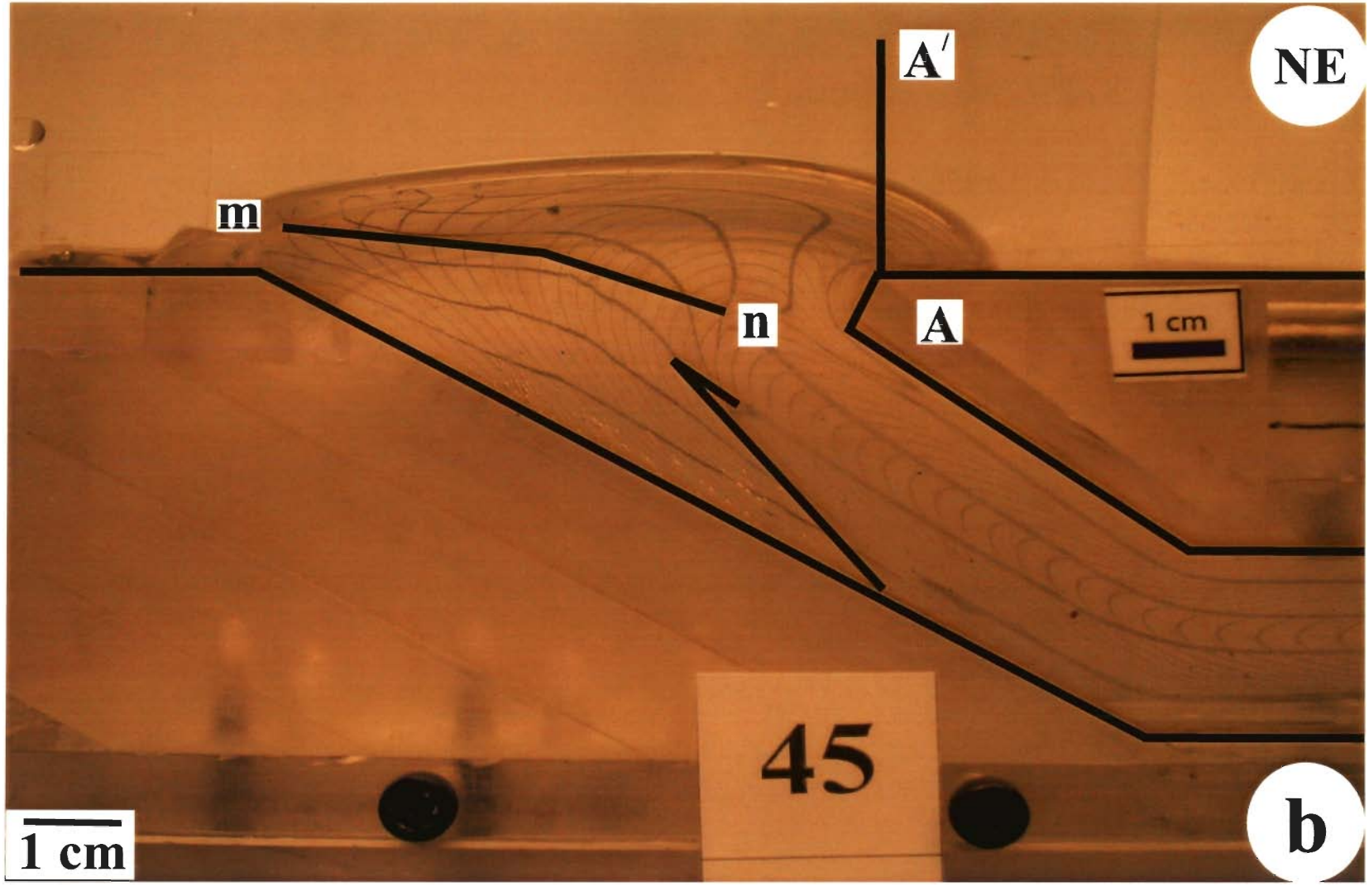

Fig. 4.19c

Figure Captions.

Fig. 4.19d. In this experiment, the inclined channel is defined by strongly divergent-up walls. The ductile thrust is marked with a half arrow. Line 'mn' separates the zone of ductile compressional shearing at its left from the zone of ductile extensional shearing at its right. The thrust lies within the ductile compressional shear zone. No 'glass plate' is used in this experiment. A part of the extruded PDMS at the right side of the vertical line $AA^{/}$ rests on the horizontal surface, and therefore has its mass outside the channels. Experiment-3. Photo number: 48. Time: 3 hours 40 minutes.

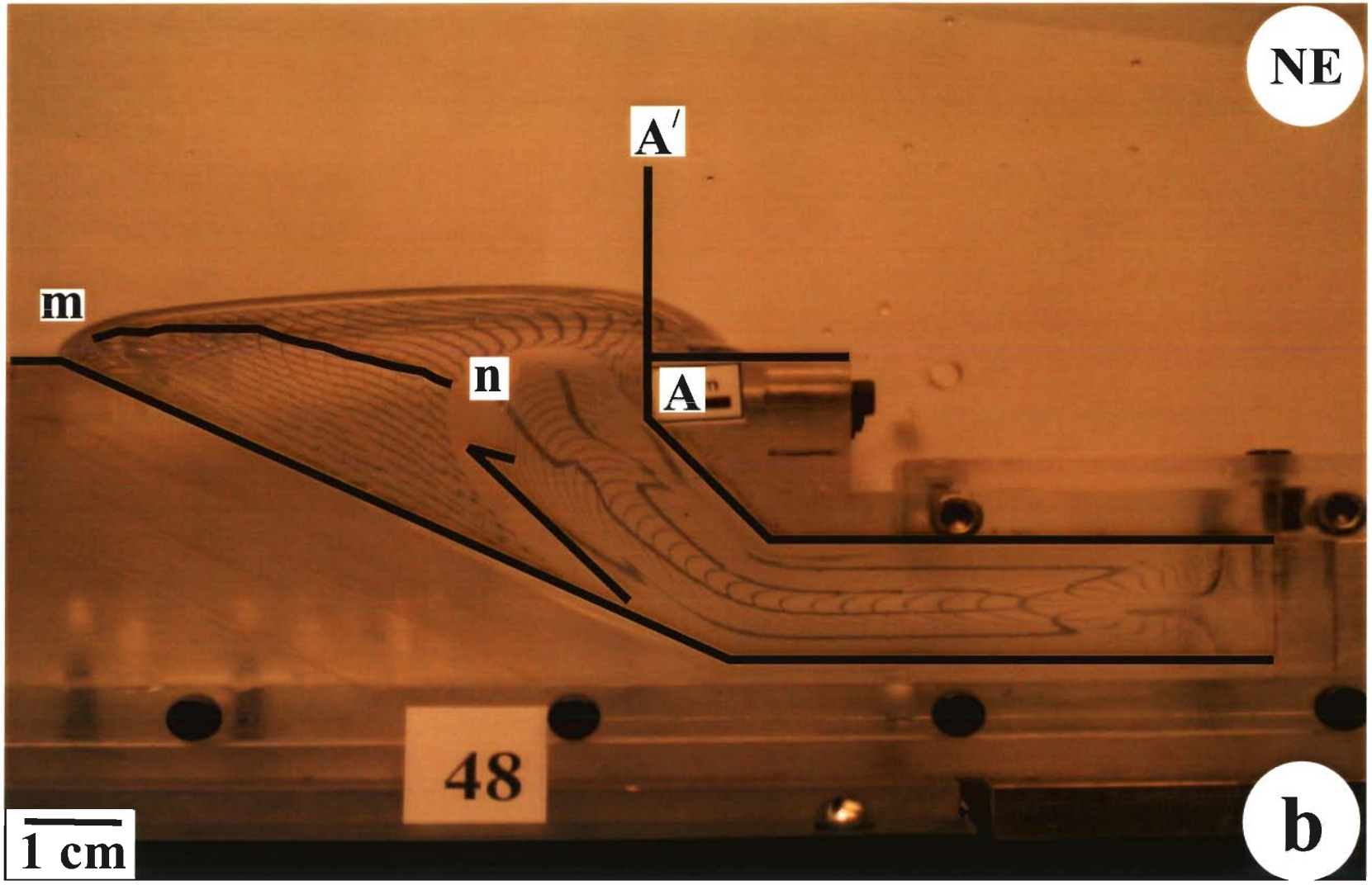

Fig. 4.19d

Figure Captions.

Fig. 4.20. Geological map of the Higher Himalayan Shear Zone (HHSZ) along the Sutlej-Baspa Valleys, Himachal Pradesh. Note that the Chaura Thrust is located between the MCT at southwest and the extension of the STDS at northeast, i.e. within the HHSZ and outside the STDS. 1: Lesser Himalayan (LH) Rampur Group: (a) Manikaran Quartzite; (b) Rampur Volcanics; (c) Carbonaceous phyllite. 2: Kulu Bajura Nappe-augen mylonite. 3. Higher Himalayan Shear Zone: (a) Jeori Group: staurolite/garnetiferous schist, banded biotite gneiss, augen gneiss (a1) amphibolite; (a2) quartz mica schist (a3) and Wangtu granite-gneiss/granite (a4), (b) Karcham Group: garnet/staurolite/kyanite/sillimanite schist/gneiss, calc-silicate, augen gneiss and migmatite (b1), Akpa leucogranite (b2). 4. Tethyan Sedimentary Zone (TSZ). Abbreviations: KT: Kulu Thrust, MCT: Main Central Thrust, VT: Vaikrita Thrust, STDS: extension of South Tibetan Detachment System in this section. R: Rampur, K: Karcham. Reproduced from Jain et al. (2000).

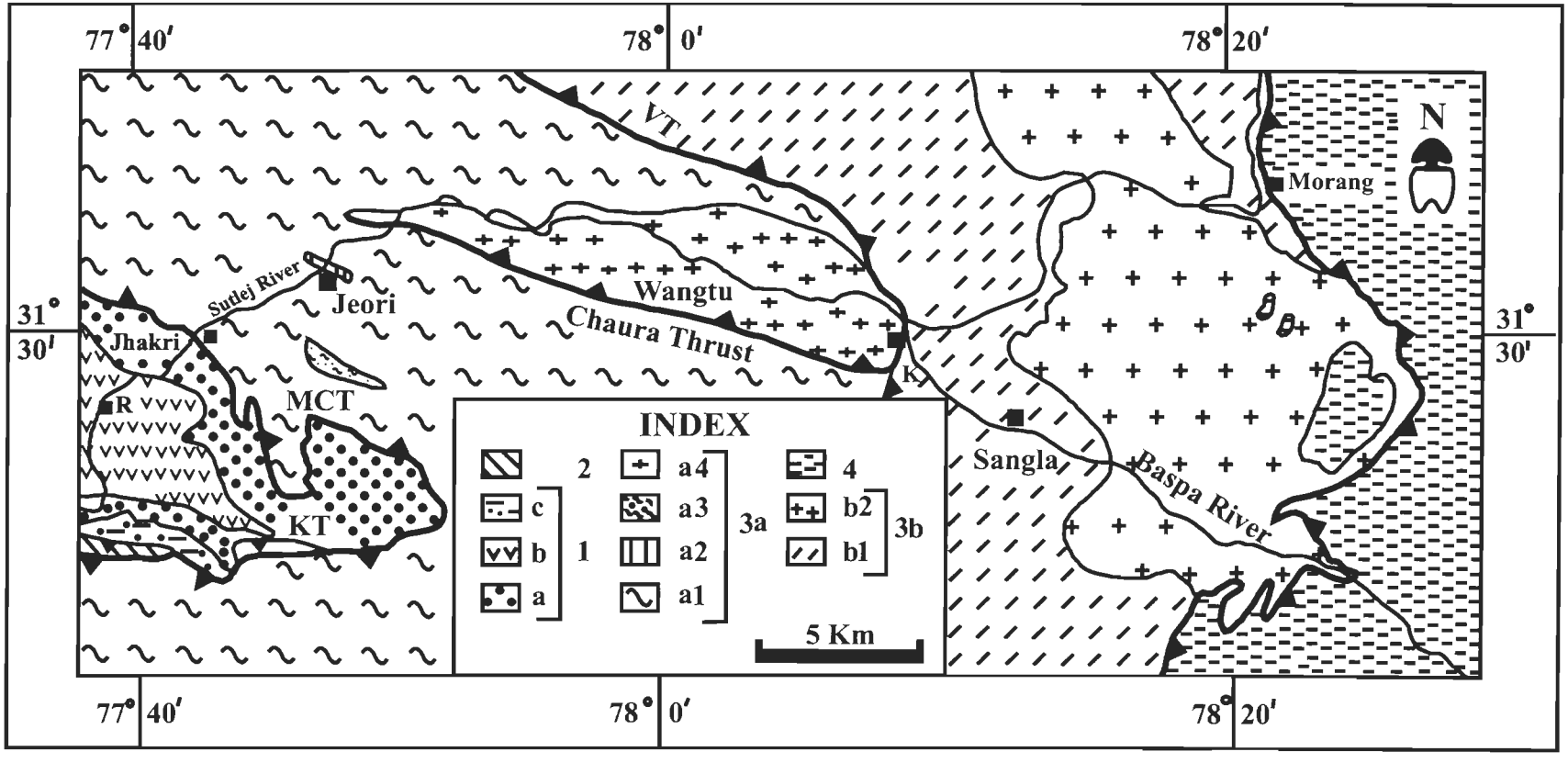
77° 40′
78° 0′
78° 20′
31° 30′
VT
Wangtu
Chaura Thrust
Sutlej River
Jeori
Jhakri
R
MCT
KT
K
Morang
N
Sangla
Baspa River
INDEX
2
a4
4
c
a3
3a
b2
3b
b
1
a2
b1
a
a1
5 Km

Fig. 4.20

(I) In zone 2, parabolic velocity profiles (Figs. 4.16c, -d) characteristic of plane Poiseuille flow is obtained, as is predicted from theory (Massey, 1975). With progressive time, even though the piston moves inside the channel with a constant rate (Figs. 4.6-4.15), the profiles gets more and more tapered. From this observation, the ductile flow is approximated as a channel flow/Plane Poiseuille flow with pressure gradient increasing with time (Figs. 4.21-4.30; equations 13, -15 in the Appendix). It is interesting to note that Pai (1956) mentioned a variety of a Poiseuille flow where the pressure gradient can be time dependent. The velocity of fluid at any point in zone-2 increases linearly with time (Equation 15 in the Appendix of this chapter).

Equation 16 in the Appendix shows that the pressure gradient in zone-4, in case of parallel inclined walls, also increases linearly with time. Further, the temporal increase of shear strain at any point within the zone-2 in the horizontal channel and zone-4 in case of parallel inclined walls are also linear, as are deduced in equations 21 and 23, respectively, in the Appendix. The temporally increasing pressure gradient and shear strain within the two zones in the channels are due to the intrinsic flow behaviour of the Newtonian viscous fluid (here the PDMS) even if the piston is pushed with constant rates. As stated earlier, the piston push does not exist in the orogenic situation. Therefore, the temporal variations of shear strain and pressure gradient are merely instrument-specific information and cannot be correlated with the kinematics of the HHSZ. As a matter of fact, Grasemann e al. (1999) has demonstrated that the HHSZ in Sutlej section underwent a decelerating strain path during its extrusion.

Figure Captions.

Figs. 4..21-4.24. Plots of pressure gradient in 10^6 dynes.cm^{-3} along the Y-axis versus time in seconds along the X-axis, calculated for the zone-2 in the horizontal channel for different experiments. The plot is linear with high correlation coefficient (r) >0.9 in all the cases. Values of 'r for different experiments are listed in Table-2'. The parameters, 'a' and 'b', for the best fit lines are defined in equation 13 in the Appendix of this chapter, and are also given in Table-2. Figure numbers corresponding to experiment numbers are as follows:

Fig. 4.21→Experiment-1
Fig. 4.22→Experiment-2
Fig. 4.23→Experiment-3
Fig. 4.24→Experiment-4

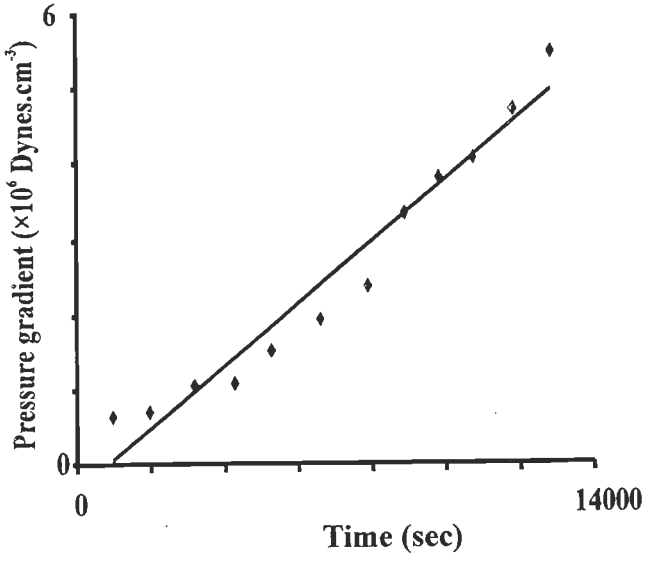

Fig. 4.21

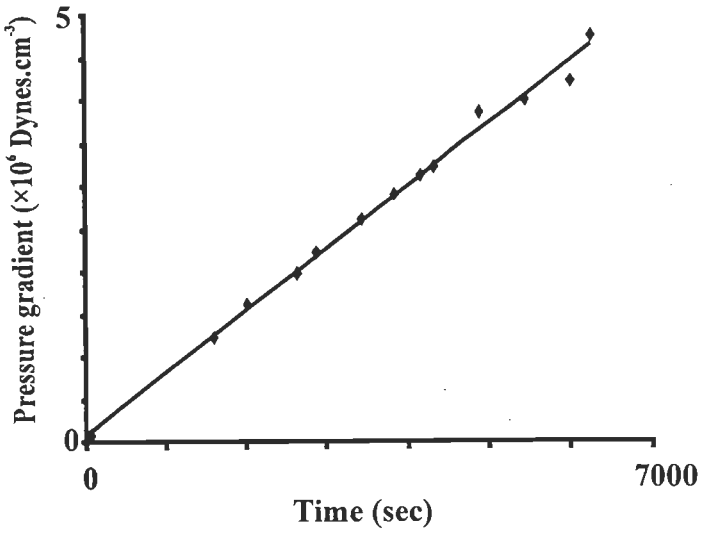

Fig. 4.22

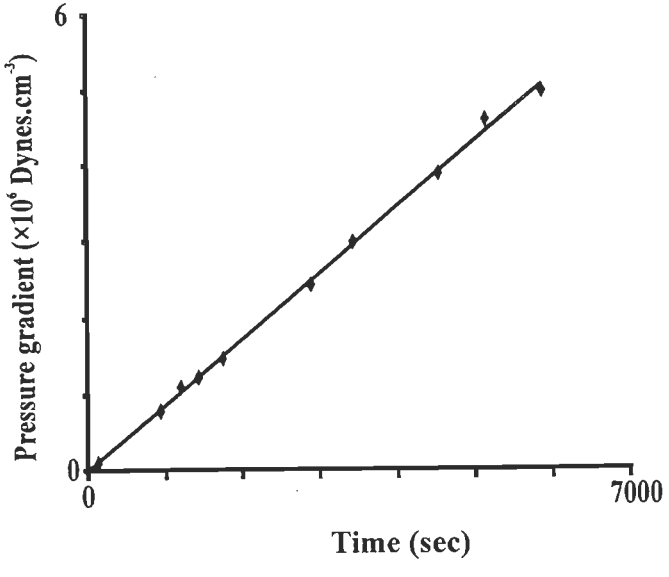

Fig. 4.23

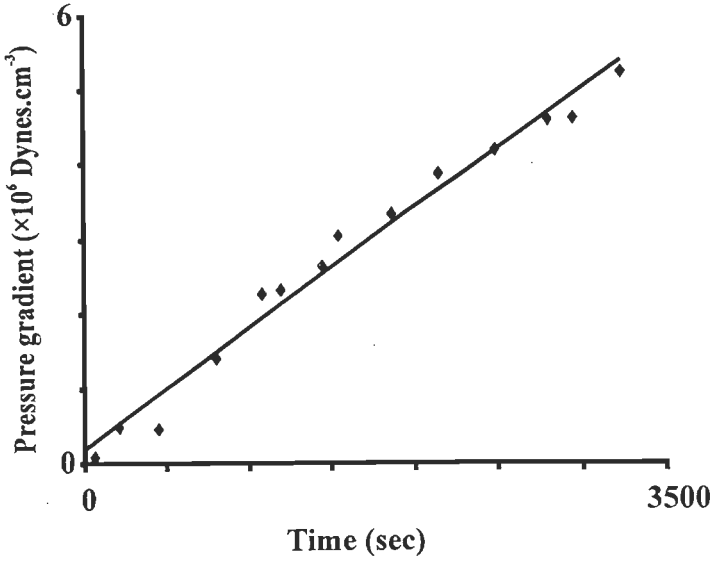

Fig. 4.24

Figure Captions.

Figs. 4.25-4.28. Plots of pressure gradient in 10^6 dynes.cm^{-3} along the Y-axis versus time in seconds along the X-axis as calculated for the zone-2 in the horizontal channel for different experiments. The plot is linear with high correlation coefficient (r) >0.9 in all the cases. Values of 'r for different experiments are listed in Table-2'. The parameters, 'a' and 'b', for the best fit lines are defined in equation 13 in the Appendix of this chapter, and are also given in Table-2. Figure numbers corresponding to experiment numbers are as follows:

Fig. 4.25→Experiment-5
Fig. 4.26→Experiment-6
Fig. 4.27→Experiment-7
Fig. 4.28→Experiment-8

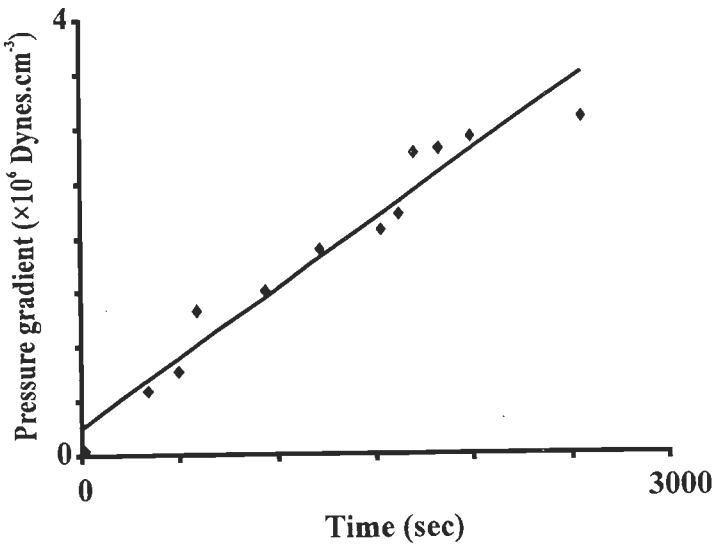

Fig. 4.25

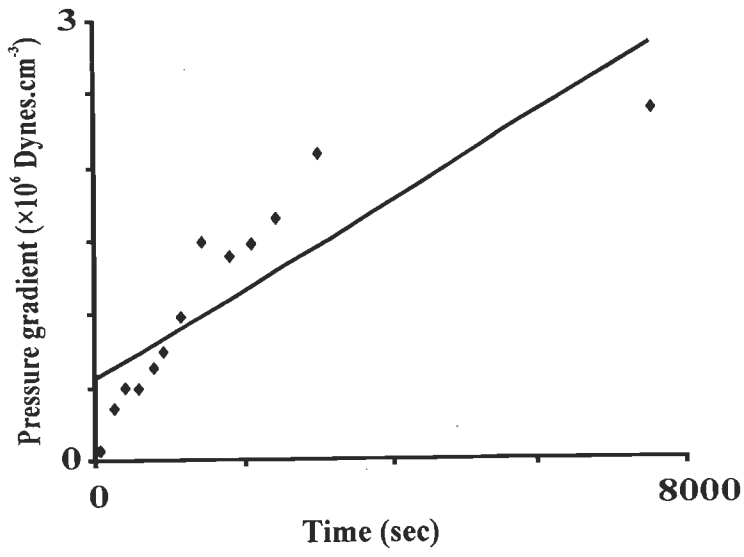

Fig. 4.26

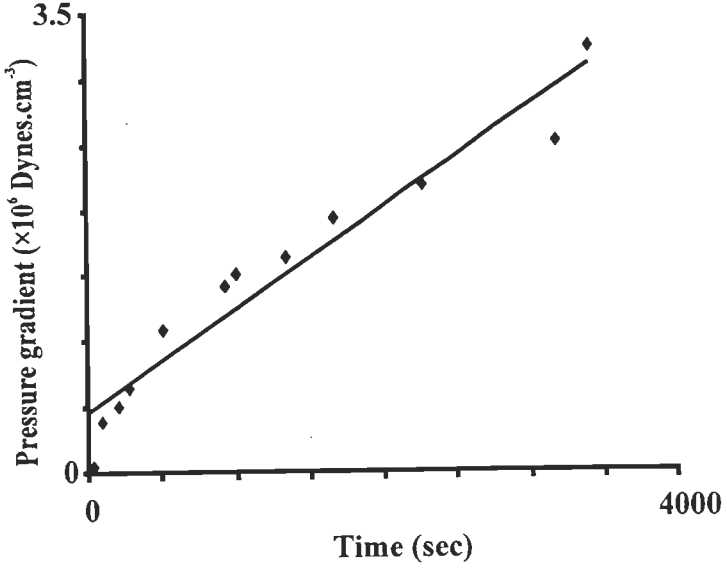

Fig. 4.27

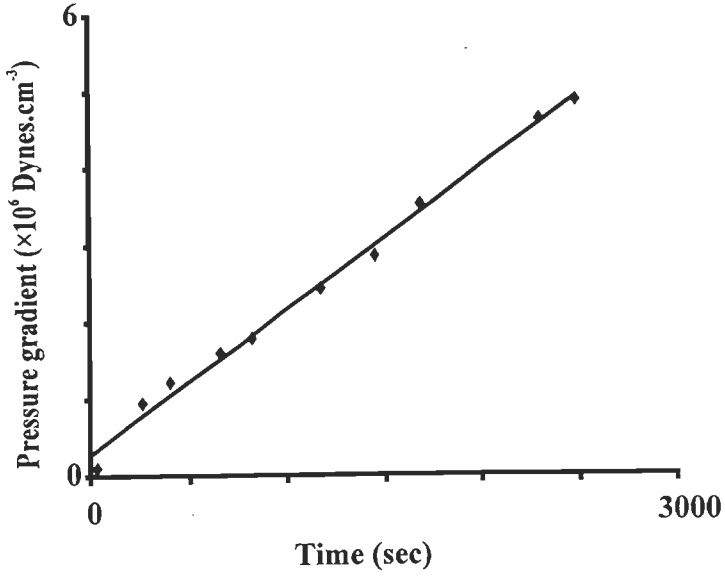

Fig. 4.28

Figure Captions.

Figs. 4.29-4.30. Plots of pressure gradient in 10^6 dynes.cm^{-3} along the Y-axis versus time in seconds along the X-axis as calculated for the zone-2 in the horizontal channel for different experiments. The plot is linear with high correlation coefficient (r) >0.9 in all the cases. Values of 'r for different experiments are listed in Table-2'. The parameters, 'a' and 'b', for the best fit lines are defined in equation 13 in the Appendix of this chapter, and are also given in Table-2. Figure numbers corresponding to experiment numbers are as follows:

Fig. 4.29→Experiment-9

Fig. 4.30→Experiment-10

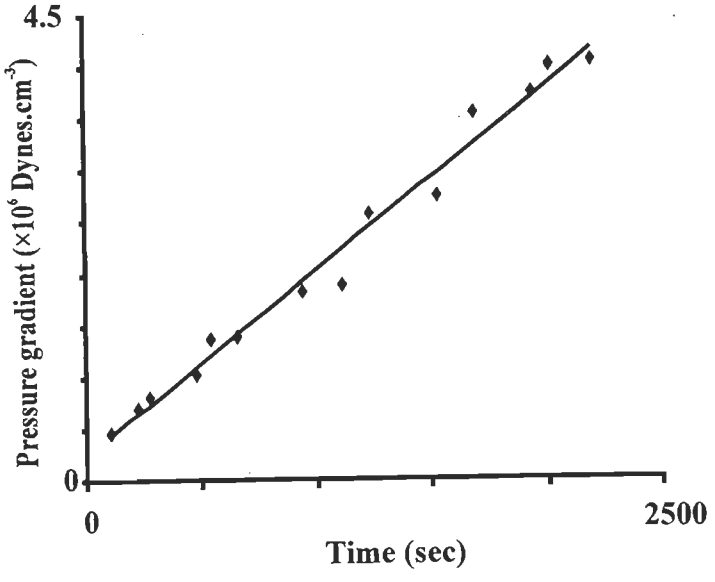

Fig. 4.29

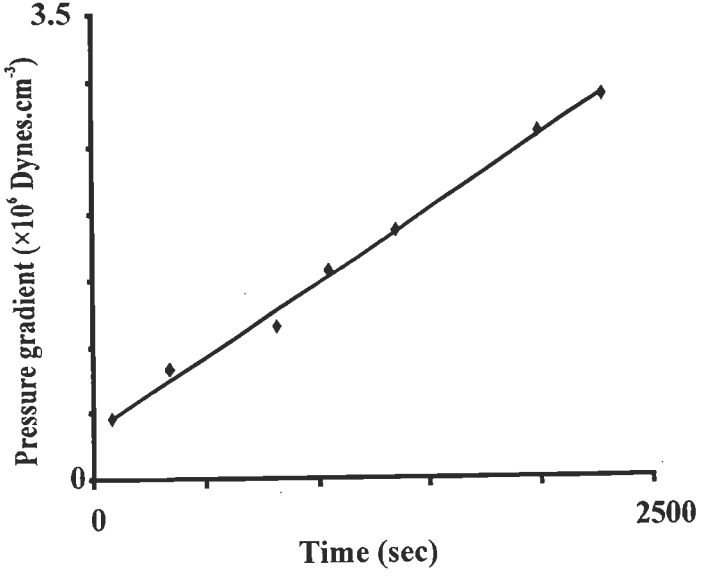

Fig. 4.30

4.9. APPENDIX

(I) The dynamically similar parameters for the model horizontal channels is calculated by answering the following questions.

Q 1. What should be the velocity of the lower wall of the model horizontal channel to produce a geometrically similar flow (velocity profile)? Assume that only the basal shear of the MHT was active but no channel flow.

Ans. For Couette flow in a horizontal parallel wall channel, the velocity profile of an incompressible Newtonian fluid is given by

$$x_s = 0.5*(U_1 - U_2) + 0.5*y\,.y_0^{-1}(U_1 + U_2) \quad \ldots\ldots\ldots (1)$$

(as in equation 3 in Appendix of Chapter-2)

Here '$2y_0$' is the perpendicular distance between the walls; and 'U_1' and 'U_2' are the velocities of the upper and the lower walls, respectively. In this situation, $U_1=0$ and $U_2 \neq 0$, i.e.

$$x_s = -0.5*U_2(1 - yy_0^{-1}) \quad \ldots\ldots\ldots (2)$$

The Reynolds Number is defined as

$$R_e = \rho.v.d.\mu^{-1} \quad \ldots\ldots\ldots (3)$$

where 'ρ', 'μ' and 'v' stand for the density and dynamic viscosity of the fluid, and the velocity of flow, respectively. Since 'ρ' and 'μ' are not involved in equation 2, matching 'Re' for the prototye and the model to achieve dynamic similarity is not required. Instead, the angle between the Y-axis and the velocity profile has to be maintained constant.

In the prototype, the MHT is sheared at a rate of 5 $cm.yr^{-1}$ (from Sl No. 21 of Table-1). The thickness of the horizontal channel is 25 km = $25*10^5$ cm in one of the

considerations. In the model, the channel thickness is 2.5 cm. The shear velocity of the wall X_1 is calculated from equation $25*10^5/5 = 2.5/X_1$. X_1 is obtained as $=0.5*10^{-5}$cm.yr^{-1} $= 1.585*10^{-12}$ mm.s^{-1}. This velocity cannot be generated in the laboratory.

Q 2. What should be the pressure gradient within the model horizontal channel to produce a geometrically similar channel flow as that of the prototype channel? Assume that only channel flow is active in the prototype but no basal shear.

Ans. The velocity profile of the channel flow is given by the parabola

$$x_p=-0.5*.\mu^{-1}.(dP/dx)(y_0^2-y^2) \quad \ldots\ldots\ldots (4)$$

(as in many fluid mechanics texts such as Pai, 1956)

Here (dP/dx) stands for the pressure gradient. The absolute value of the maximum velocity on this velocity profile is given by the X-ordinate of the vertex of this parabola:

$$V_{max}=0.5*\mu^{-1}y_0^2\,(dP/dx) \quad \ldots\ldots\ldots (5)$$

For the prototype, $\mu^-= 10^{20}$ Poise (from Sl No. 4 in Table-1); $y_0= 25*10^5$cm in one of the considerations; (dP/dx) = 1 to 2 Kb km^{-1} (from Sl No. 2 in Table-1). (dP/dx) =2 Kb km^{-1} $= 2*10^4$ Dyne.cm^{-3} is chosen for calculation. Putting these in equation 5, V_{max} is obtained as $= 0.625*10^{-3}$ cm.s^{-1}.

Putting the calculated $V_{max}=0.625*10^{-3}$ cm.s^{-1}, $\mu^-= 10^{20}$ Poise and $\rho=2.70$gm cc^{-1} in equation 3, the Reynolds Number is calculated as

$R_e=0.422*10^{-16}$

For the sake of "dynamic similarity", the calculated R_e for the prototype and the model must be the same (Ramberg, 1981). Therefore, putting $R_e=0.422*10^{-16}$, density and

viscosity of the PDMS $\rho = 0.95$ gm.cm^{-3} and $\mu=10^6$ Poise, respectively, and the thickness ($2y_0$) of the model horizontal channel = 2.50 cm in equation 3, the maximum velocity, V_{max}, for flow in the model is obtained as $V_{max}=0.18*10^{-12}$ cm.s^{-1}.

Putting this value of V_{max}, $\rho=0.95$ gm.cm^{-3}, and $\mu=10^6$ Poise in equation 5, the pressure gradient for the model is calculated as, $(dP/dx) = 0.23*10^{-6}$ Dyne.cm^{-3}. This pressure gradient cannot be generated in the laboratory. The lowest possible pressure gradient possiblel to generate is in the order of 10^6 Dyne.cm^{-3}.

Q3. What should be the pressure gradient within the model horizontal channel to produce a dynamically similar flow in the model? Assume that both Couette- and channel flow are active.

Ans. The X-ordinate of the vertex of the parabolic velocity profile for combined simple shear and channel flow of an incompressible Newtonian viscous fluid in a parallel-wall infinitely long horizontal channel is given by

$$X\equiv 0.5\,(U_1-U_2)- 0.125\,(U_1+U_2)^2\mu.(dP/dx)^{-1}.y_0^{-2}-0.5.\mu^{-1}.y_0^{2}.(dP/dx) \quad \ldots\ldots\ldots (6)$$

(deduced after equation 9 in Appendix of Chapter-2)

This represents the maximum velocity of flow within the channel. Since only the basal wall of the channel undergoes shear, $U_1=0$, and $U_2\neq 0$. Therefore,

$$X\equiv -0.5U_2-0.125\,\mu\,U_2^{2}\,(dP/dx)^{-1}.y_0^{-2}-0.5.(dP/dx).y_0^{2}\mu^{-1} \quad \ldots\ldots\ldots (7)$$

Since the flow is along the positive direction of X-axis as per the choice of axes and the flow direction, the absolute value of pressure gradient has to be negative. Hence (dP/dx)

=-2Kbar (from Sl No. 2 in Table-1) = $2*10^5$ gm.cm^{-2}.s^{-2} is taken. U_2 is 5 cm.yr^{-1} (from Sl No. 21 in Table-1) = $1.58548*10^{-7}$ cm.s^{-1}, 'y_0' is half of the channel thickness=12.5 km in one of the considerations=$12.5*10^5$ cm. Putting these values in equation 7 and neglecting terms of the order of 10^{-10} and those which are still smaller, X is obtained as $1.57*10^{-5}$ cm.s^{-1}.

Taking density ρ =2.70 gm cc^{-1} (from Sl No. 3 in Table-1); maximum velocity V_{max}=X= $1.57*10^{-5}$ cm.s^{-1}; the thickness of the channel = $2.y_0 = 25*10^5$ cm; viscosity μ= 10^{20} Poise (from Sl No. 4 in Table-1); the 'R_e' is calculated as = $1.06*10^{-8}$.

For the sake of "dynamic similarity", the calculated R_e for the prototype and the model must be the same (Ramberg, 1981). Therefore, putting R_e=$1.06*10^{-8}$, density and viscosity of the PDMS ρ = 0.95, and μ=10^6 Poise, respectively; and the thickness ($2y_0$) of the model horizontal channel = 2.50 cm, the maximum velocity (v) for flow in the model is obtained from equation 7 as V_{max}= $0.446*10^{-2}$cm.s^{-1}. Such a very slow flow of fluid cannot be generated in the laboratory inside the horizontal channel.

(II) Velocity profiles in 'zone-4' and 'zone-2':

The 'Poisson equation' of rectilinear flow of an incompressible Newtonian viscous fluid upwards in the x-direction, in an infinitely long parallel-wall inclined channel, is given by: $(\partial^2 U_x/\partial y^2)=\mu^{-1}[(\partial P/\partial x)-d.g.Sin\theta]$ ... ... (8)

This equation is the same as equation 6.190 of Papanastasiou et al. (2000) but is with different symbols. Here 'x' and 'y' are the mutually perpendicular axes, which lie along

the length of the inclined channel. 'U_x' is the velocity of the fluid in the 'x' direction; 'μ' is the dynamic viscosity of the fluid; $(\partial P/\partial x)$ is the pressure gradient acting on the fluid along the x-direction; 'd' is the density of the fluid. 'g' is the acceleration due to gravity; and 'θ' is the inclination of the channel.

Integrating twice and applying no slip boundary conditions, equation 8 becomes

$$U_x=-0.5\mu^{-1}.(\partial P/\partial x- d.g.Sin\theta)(y_0^2-y^2) \quad \ldots\ldots\ldots (9)$$

where '$2y_0$' is the thickness of the inclined channel. The pressure gradient $(\partial P_1/\partial x_1)$ generated inside the horizontal channel is linked to that of the inclined channel by:

$$(\partial P/\partial x)=(\partial P_1/\partial x_1)Cos\theta \quad \ldots\ldots\ldots (10)$$

Putting this in equation (9),

$$U_x=-0.5\mu^{-1}.(\partial P_1/\partial x_1.Cos\theta - d.g.Sin\theta)(y_0^2-y^2) \; . \quad \ldots\ldots\ldots (11)$$

The Plane Poiseuille flow of velocity profile in 'zone-2' is given by:

$$U_{x1}=-0.5\mu^{-1}.(\partial P_1/\partial x_1).(y_1^2-y^2) \quad \ldots\ldots\ldots (12)$$

where 'U_{x1}' is the velocity of the fluid at y=y; '$2y_1$' is the thickness of the channel; 'μ' is the viscosity of the fluid, and $(\partial P_1/\partial x_1)$ is the pressure gradient in the x_1 direction. Considering the absolute value of $(\partial P/\partial x)$, the vertex of the parabolic velocity profile is given by $[0.5\mu^{-1}(\partial P_1/\partial x_1).y_1^2,0]$. The thickness of the channel $(2y_1)$ and the viscosity of the fluid (μ) being known, measuring the co-ordinate of the vertex of the parabola in time intervals from photographs, temporal increase of pressure gradient in the horizontal channel are obtained and plotted against time for experiments with both the cases of non-

parallel- and parallel-wall inclined channels. These plots are fitted with the straight line equation:

$$(\partial P_1/\partial x_1)=(a.t+b) \quad \ldots\ldots\ldots (13)$$

where $(\partial P_1/\partial x_1)$ is in dyne per cm cube and 't' is time in second. The correlation coefficient in all the cases are >0.9. For different experiments, the set of 'a' and 'b' values in equation 13 are presented in Table 2.

From equations 13 and -10, in zone-4 within the inclined channel with parallel walls,

$$(\partial P/\partial x)=(a.t+b).Cos\theta \quad \ldots\ldots\ldots (14)$$

This means that the pressure gradient within the zone-4 in the inclined channel increases linearly with time.

From equations 12 and -13, an empirical relation between time and velocity profile for the plane Poiseuille flow in the horizontal channel in 'zone-2' is obtained as follows

$$U_{x1}=-0.5\mu^{-1}(a.t+b).(y_1^2-y^2) \quad \ldots\ldots\ldots (15)$$

From equations 11 and -15, an empirical relation between time and velocity profile for the plane Poiseuille flow in the inclined channel with parallel walls, in 'zone-4', is given by:

$$U_x=-0.5\mu^{-1}[(a.t+b).Cos\theta-d.g.Sin\theta].(y_0^2-y^2) \quad \ldots\ldots\ldots (16)$$

(III) Temporal variation of shear strain in 'zone-2' and 'zone-4':

Rewriting equation 12, the velocity profile for plane Poiseuille flow through 'zone-2' is given by:

$U_{x1}= -0.5\mu^{-1}.(dP_1/dx_1).(y_1^2-y^2)$ ... ... (17)

The shear strain at the point $(0,y_2)$ on this profile is given by

$(dU_{x1}/dy)_{at\ (0,\ y2)} = \mu^{-1}.y_2.(dP_1/dx_1)$ ... ... (18)

The absolute value of (dP_1/dx_1) being <1, the absolute value of shear strain, 's', at $(0,y_2)$ is:

$s=- \mu^{-1}.y_2.(dP_1/dx_1)$ ... ... (19)

This means that the shear strain at any point on the parabolic velocity profile of zone-2 is fundamentally dependent on the pressure gradient.

Further, from equations 19 and –13,

$s=-\mu^{-1}.y_2.(a.t+b)$ ... ... (20)

This means that shear strain at any point in zone-2 increases linearly with time.

Rewriting equation 11, the velocity profile for Poiseuille flow through the parallel wall inclined channel, in 'zone-4', is given by:

$U_x=-0.5\mu^{-1}.(\partial P_1/\partial x_1.Cos\theta - d.g.Sin\theta)(y_0^2-y^2)$ . ... (21)

The shear strain, 's', at the point $(0,y_3)$ is given by $(dU_{x1}/dy)_{at\ (0,y3)}$, which is

$s= \mu^{-1}. y_3.(\partial P_1/\partial x_1.Cos\theta - d.g.Sin\theta)$ ... ... (22)

This means that the shear strain at any point on the parabolic velocity profile in 'zone-4', in the inclined channel with parallel walls, is fundamentally dependent on the pressure gradient in 'zone-2'.

From equations (22) and -(13),

$s = \mu^{-1}. y_3. [(a.t+b)Cos\theta - d.g.Sin\theta]$ ... ... (23)

This means that shear strain at any point on the velocity profile in 'zone-4', in the inclined channel with parallel walls, increases linearly with time.

Chapter 5

MICROFLANKING STRUCTURES

5.1. INTRODUCTION & OBJECTIVES

"Flanking structures" are "deflection of planar or linear fabric elements in a rock alongside a cross-cutting object" (Passchier, 2001). The structural element which crosscuts earlier rock fabric is called the 'crosscutting element' (CE). The rock fabric, which is crosscut by the CE, is called the 'host fabric element' (HE). Part of the HE that is curved near its contact to the CE is called the 'internal HE'. The undeflected part of the HE, which is away from the CE, is called the 'external HE' (Passchier, 2001). The domain within which the internal HE is confined around the CE is called the 'internal HE zone' in this work (Fig. 5.1a). The internal HE showing reverse faulting, normal faulting, or no fault movement across the CE define 's-', 'a-', or 'n-type' flanking structures, respectively (Grasemann et al., 2003). If the HE is convex (or concave) towards the direction of slip along the CE, the drag of the HE is called 'normal' (or 'reverse') (Grasemann et al., 2003) (Fig. 5.1b). Any combination of drag and slip are possible in flanking structures (Passchier and Trouw, 2005). A fuller review of the morphologies and classifications of flanking structures have been presented by Mulchrone (2007).

Flanking structures have been reported from macro-scale in different geological contexts and rock types, but more commonly from mylonites (Passchier and Trouw, 2005). While

Figure Captions

Fig. 5.1a-b Terminologies of flanking structure used in this work.

Fig. 5.1.a Diagrammatic representation of flanking structure. The dragged part of the host fabric element (HE), near the crosscutting element (CE), is called the 'internal HE'. Away from the internal HE is the straight and undisturbed 'external HE' Reproduced from Fig. 1 of Passchier (2001). The region within which the internal HE is confined, the dotted region in the diagram, is defined in this work as the 'internal HE zone'.

Fig. 5.1.b Different senses of slip and -drag of the HE for flanking structures. For this purpose, identification of marker HE (shown by thick line) would be a prerequisite. Any combinations of senses of slip and -drag are possible in flanking structures Reproduced from Fig. 1 of Grasemann et al. (2003).

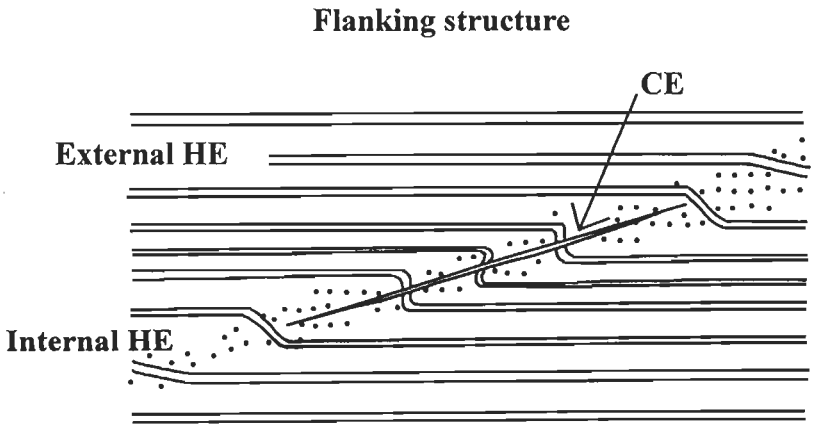

Fig. 5.1a

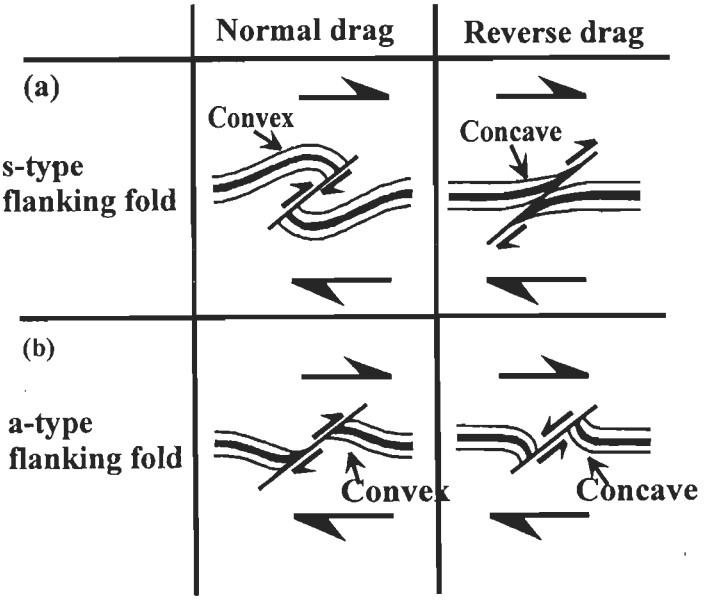

Fig. 5.1b

the CE can be dykes, fractures, joints, faults, secondary shear planes/zones, veins, burrows, inclusions, minerals, boudins, or melt such as leucosomes; the HE can be bedding planes, foliations, or lineations (Passchier, 2001; Grasemann et al., 2003 and references therein; Coelho et al., 2005; Exner, 2005; Mulchrone, 2007). Documentation of flanking structures from micro-scales has so far been scanty (photo 31 of Gansser, 1983; Fig. 3 of Augustithis, 1990; Shelley, 1994; Fig. 6d of Grasemann and Stüwe, 2001; Fig. 12b of Mulchrone, 2007). No restriction of rigidity and thickness in defining the CE was indicated in Passchier's (2001) original definition of 'flanking structures', and this was followed by all subsequent workers, most notably Coelho et al. (2005). Curvature of markers around mineral grains of different rigidities within ductile matrices and subjected to different shear regimes were simulated in analog- (Ildefonse et al., 1992 for rigid grains; Odonne et al., 1994 for non-rigid grains) and numerical models (Ghosh and Sengupta, 1973, Mulchrone, 2007) but as byproducts of other kinematic studies. Incidentally, while flanking structures with dominantly opposite senses of drag of the internal HEs across the CEs (Figs. 8 I-V of Passchier, 2001) received more interest (Grasemann and Stüwe, 2001; Grasemann et al., 2003; Exner et al., 2004; Kocher and Mancktelow, 2005; Wiesmayr and Grasemann, 2005; Kocher and Mancktelow, 2006), those with same senses of drag, though idealized (Fig. 8V$^{/}$ of Passchier, 2001), received no further attention.

This chapter aims at (i) documentation and morphologic description of flanking structures from thin-sections of the rocks of the Higher Himalayan Shear Zone from the Sutlej section and their classification; (ii) discussion on their validity and use as shear sense indicators; and (iii) presentation of the observed rheological variations of the HE

and the CE. Additionally, by comparing morphology between these flanking structures on micro-scale with those previously reported from macro-scale and simulated in models, the genesis of the former has been selectively commented.

5.2. MICROFLANKING STRUCTURES

5.2.1. Sample location & definition

The studied thin-sections are XZ-oriented, and are from the Higher Himalayan Shear Zone (HHSZ) from the Sutlej section, NW Indian Himalaya (Fig. 5.1c). The HHSZ is the central core of the Himalaya, an intra-continental ductile shear zone, and is bounded by the Main Central Thrust (MCT) at the base and the Himalayan Detachment-1 (HD1) at the top (Figs. 3.2; 3.11). The HHSZ is characterized by: *(i)* medium- to high-grade metamorphosed greenschist- to amphibolite facies sequence of pelitic- and psamitic rocks of Precambrian age; *(ii)* inverted metamorphism; *(iii)* NE-dipping main foliation (the C-planes) and the stretching lineation; and top-to-SW sense of compressional ductile shearing. This sense of shearing was produced during the crustal shortening at the early phase of the Neo-Himalayan period, and are deciphered mainly from the S-C fabric (Jain et al., 2005 and references therein), mineral fishes and also from flanking structures in macro-scales (Grasemann et al., 1999); and *(iv)* heterogeneous shear regime with pure- and simple shear dominated flow towards its middle and at the boundaries, respectively (Exner, 2005 and references therein). In Chapter-3, it is proposed that the major ductile deformation within the HHSZ in the Sutlej section was produced by a uniform simple shearing (line 1 in Fig. 3.14), which was followed by combined simple shear and channel flow in two spatially and temporally separated pulses (Fig. 3.17).

Figure Captions

Fig. 5.1c. The Higher Himalayan Shear Zone in the Sutlej section. The sample locations 1-10 are shown. The rock samples for thin-sections are chosen excluding the two detachments (the HD1 and the HD2). The map is compiled and simplified from Singh (1993), Srikantia and Bhargava (1998) and Vannay and Grasemann (1998).

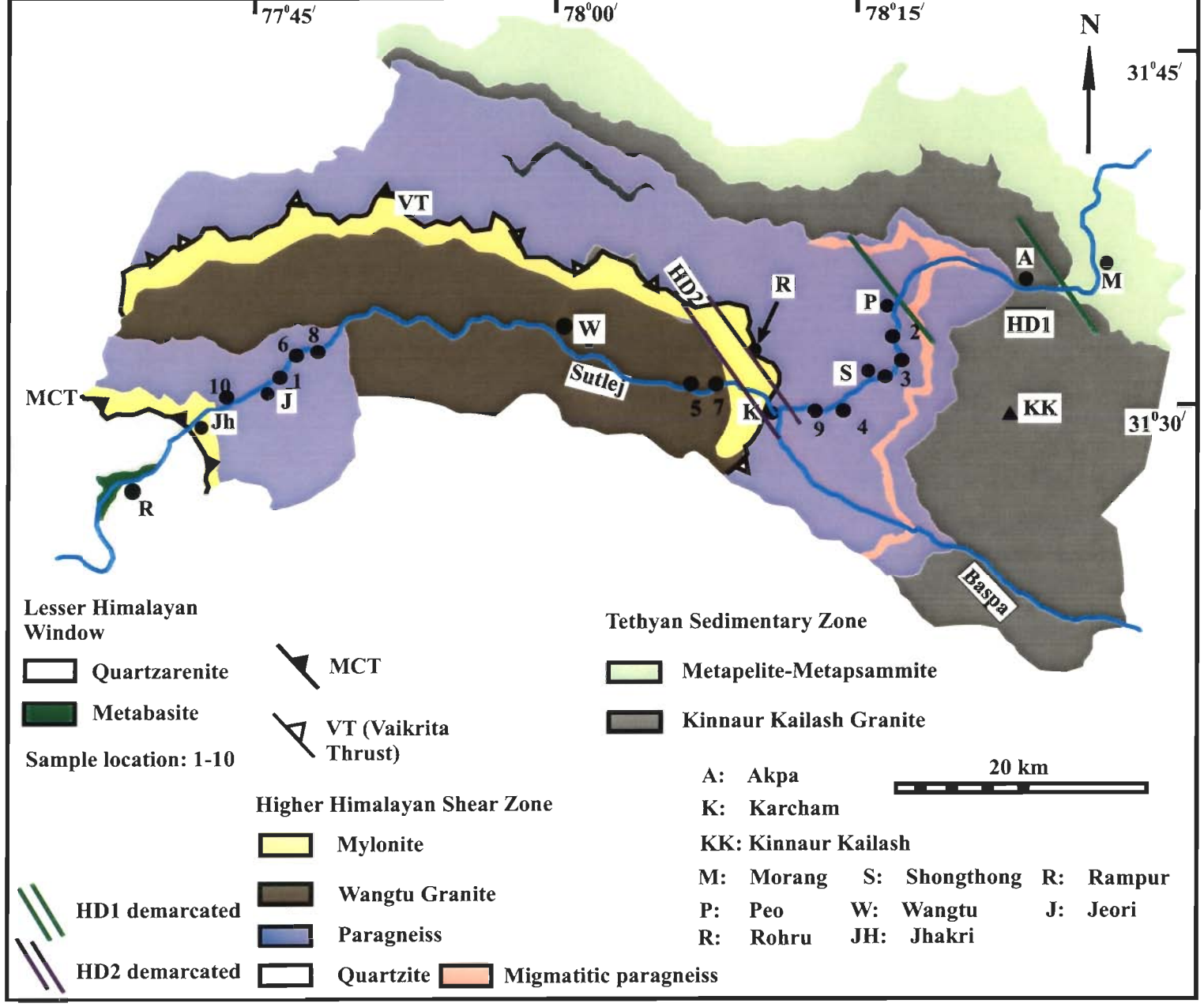
77°45′
78°00′
78°15′
N
31°45′
31°30′
VT
HD2
HD1
MCT
Sutlej
Baspa
R
W
P
A
M
S
K
KK
J
Jh
1
2
3
4
5
6
7
8
9
10
Lesser Himalayan Window
Quartzarenite
Metabasite
Sample location: 1-10
MCT
VT (Vaikrita Thrust)
Higher Himalayan Shear Zone
Mylonite
Wangtu Granite
Paragneiss
Quartzite
Migmatitic paragneiss
HD1 demarcated
HD2 demarcated
Tethyan Sedimentary Zone
Metapelite-Metapsammite
Kinnaur Kailash Granite
20 km
A: Akpa
K: Karcham
KK: Kinnaur Kailash
M: Morang
S: Shongthong
R: Rampur
P: Peo
W: Wangtu
J: Jeori
R: Rohru
JH: Jhakri

Fig. 5.1c

The studied thin-sections, under microscope usually at high magnification, reveal that some of the nucleated mineral grains cut and characteristically deflect cleavages (if any) and/or grain boundaries of the host grains. Such nucleated minerals are designated as the CE, the deflected cleavages and grain boundaries as the HE, and the CE-HE composite as the microflanking structures (MFS) (Figs. 5.2a, -b, 5.3a-d, 5.4a, -b, -d). Keeping in mind the definition of flanking structure of Passchier (2001), where the 'deflection' (or the 'drag' of Grasemann et al., 2003) of the HE has been considered essential, it is state that the nucleated minerals that have only cut (Fig. 5.2c), or cut and faulted the cleavages/grain margins (Fig. 5.2d) without any drag, will *not* be considered as the MFS.

5.2.2. Morphological descriptions

Amongst the observed varieties of the MFS, micas most commonly define the CE, and the also the host mineral(s) over which the CE nucleated (Figs. 5.2a, -b, 5.3a, -d). The HE are curved near their contacts to the CE minerals, thereby defining the internal HE. Compared to the flanking structures reported from macro-scale, the CE of the observed MFS is usually thicker than the internal HE zone.

Classification of flanking structures into 's-', and 'a-' (or 'n-') type is done on the basis of the sense of slip (or no slip) of the marker HE across the CE (Passchier, 2001; Grasemann et al., 2003). However, this exercise is untenable for the MFS since cleavages or grain boundaries defining the HEs usually cannot be distinguished as markers. This hinders to categorize the sense of drag of the internal HE into the normal- or the reverse type (see Grasemann and Stüwe, 2001, Exner, 2005 for similar problem arising in the

Figure Captions

Fig. 5.2a Type-(i) MFS defined by nucleated biotite CE, and swerved cleavages of the host grain as the HE. Concave-up (and slightly convex-up) HEs at the right (and at the left) margin of the CE characterizes the internal HE zone. The parallelogram shape of the CE indicates top-to-right (top-to-SW regional) shearing. This, and all the subsequent examples of the Type-(i) MFS (Figs. 2a, 2b, 3c, 3d, 4a, 4b, 4d), characteristically lack 'marker HE'. The HEs, bounding the CE, act as the primary shear plain (C-plain) along which ductile shear took place in the grain scale, and the CE mineral underwent crystal-plastic deformation. Sample number: 3. Photographed in plane-polarized light. Photomicrograph length: 2mm.

Fig. 5.2b Type-(i) MFS defined by two adjacent parallelogram-shaped biotite CEs (marked by '1' & '2'), and dragged cleavages HEs of the host biotite. The CEs '1' and '2' indicate top-to-left (top-to-SW regional) shearing. Note that (i) the right margin of the CE '2' displays both concave-up and convex-up senses of drag; and (ii) the left margin of the CE '1' displays a thin hazy zone and almost straight HE. Sample number: 8. Photographed in plane-polarized light. Photomicrograph length: 1mm.

Fig. 5.2c A muscovite grain has nucleated and cut-across cleavages of the host muscovite grain. A thin but prominent hazy zone is present at the left margin of the cross–cutting muscovite. The right margin of this muscovite is sharp. The crosscut cleavages at both the margins of the nucleated grain are straight. In this case, cleavages of the host grain and the nucleated grain together will *not* be designated as the MFS. See text for discussion. Sample number: 9. Photographed in plane-polarized light. Photomicrograph length: 0.5mm.

Fig. 5.2d A nearly parallelogram-shaped muscovite grain, nucleated within an aggregate of muscovite host, shows top-to-left (top-to-SW regional) shearing. A grain boundary of the muscovite host is identified as 'marker' based on the observation that, with respect to the particular orientation of the crosscutting grain, as in the photograph, the cleavage plains above (and below) the 'marker boundary' is parallel (and make an angle) to it. Some of these cleavage plains, at the top (and bottom) of the 'marker boundary', are shown by horizontal (and inclined) short thin lines. The marker boundary is not dragged although it got normal faulted along the margins of the crosscutting mineral. The crosscutting mineral and the cleavages of the host grain, considered together, cannot be designated as the MFS. See text for discussion. The grain margins of the crosscutting mineral are very sharp and no hazy zones exist. Sample number: 1. Photographed in cross-polarized light. Photomicrograph length: 1mm.

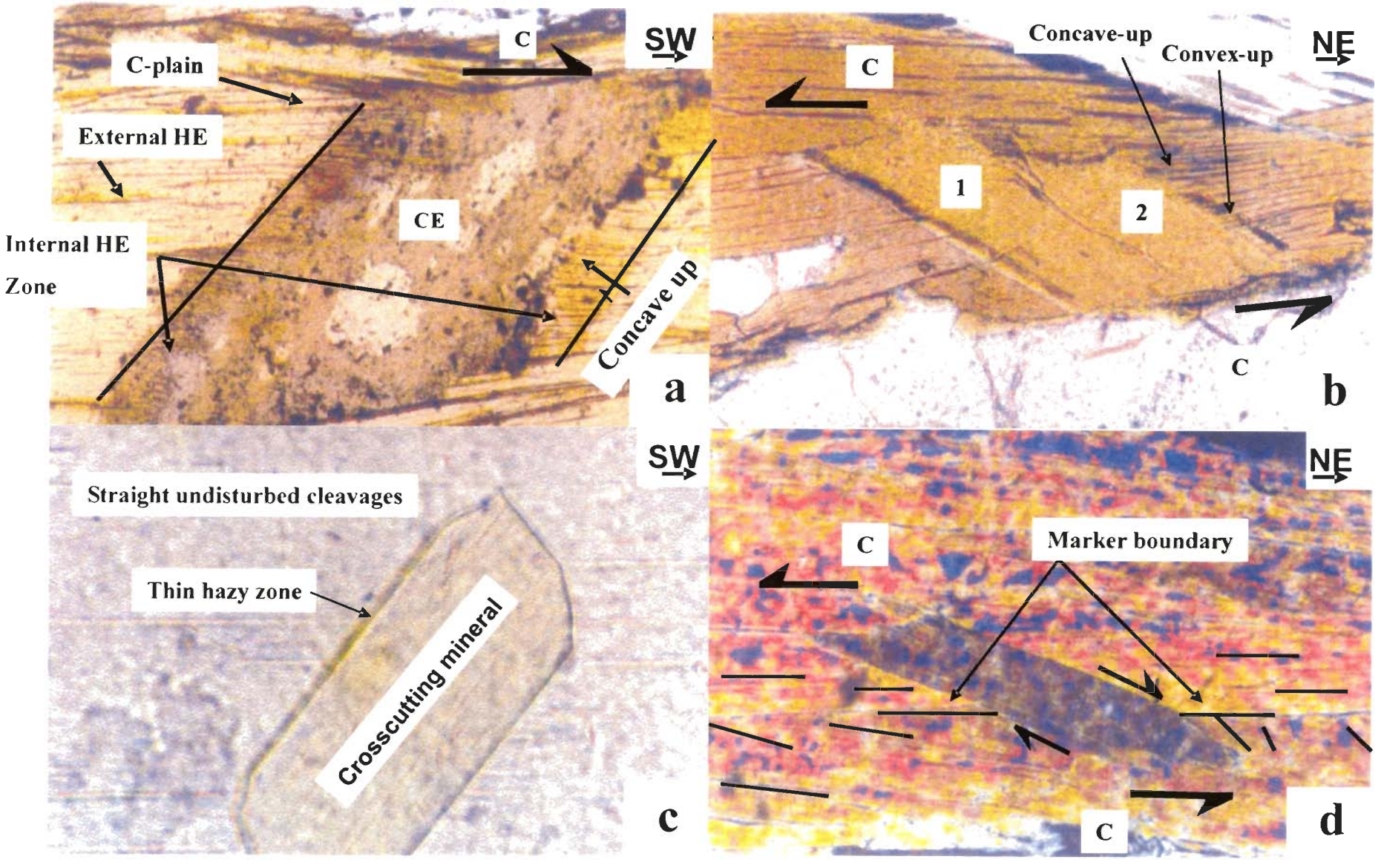
C-plain
External HE
Internal HE
Zone
CE
C
SW
Concave up
a
C
Concave-up
Convex-up
NE
1
2
C
b
SW
Straight undisturbed cleavages
Thin hazy zone
Crosscutting mineral
c
NE
C
Marker boundary
C
d

Fig. 5.2

Figure Captions

Fig. 5.3a Type-(ii) MFS defined by biotite CE (marked by '1'), and dragged HE cleavages of a biotite host grain (marked by '2'). The external HEs are sub-parallel to the main foliation (outside the photograph). With respect to the particular orientation of grain '1', as that in the photograph, the HEs are strongly concave-up at both the sides of the CE. The inferred preferred direction of growth of the biotite CE is almost perpendicular to the external HE cleavages/main foliation. The direction is shown by a thick arrow inside the CE grain. The CE grain is markedly elongated along its inferred direction of growth. Thin hazy zones exist at the HE-CE contact. The HE tends to penetrate the CE within this zone, shown by an arrow. Muscovite grains, marked by '3', '4' and '5', cut grain '1'. Amongst them, grain '5' is concave-up with the same intensity of curvature as that of the HE. It is interpreted that grain '5' was affected by the preferential directional growth of the CE presumably indicating its nucleation either prior or simultaneous with the CE's directional growth. Straight grain boundaries and cleavages of grains '3' and '4' indicate that these grains nucleated after grain '1' stopped growing. Sample number: 1. Photographed in cross-polarized light. Photomicrograph length: 0.5 mm.

Fig. 5.3b Type-(ii) MFS defined by a garnet grain as the CE; and gently dragged concave-up margins of the biotite host grains, as the HE. The HEs are variably dragged at the CE margin, and are marked by thin arrows. Inferred preferred direction of growth of the CE is shown by a bold arrow (inside the garnet grain). The CE is slightly elongated along its preferred direction of growth. The HE-CE contact is sharp. Sample number: 4. Photographed in plane-polarized light. Photomicrograph length: 0.5 mm.

Fig. 5.3c Type-(i) MFS defined by sheared sigmoid-shaped alkali feldspar as the CE and dragged cleavages of the muscovite host grains as the HE. MFS type is inferred not from the senses of drag of the HE, but from the shape of the CE. CE shape indicates top-to-left down (top-to-SW regional) shearing. The feldspar grain CE is in extinction position. Straight and undisturbed HE cleavages, bounding the CE, act as the C-plains. The HEs are intensely dragged into both convex-up and concave-up senses at the same margin of the CE, and are shown by the arrows 'p' and 'q' respectively. One of the margins of the feldspar grain is inclined to the C-plane in the direction of shear at 134^0. One possible explanation for the two senses of drag at the same margin of the CE can be that the CE underwent simple shearing initiating from $x<20^0$ to the present angle $x=46^0$. See text for discussion. At one side of the CE, from the arrow 'q' towards the arrow 'r', the convexity of the internal HEs are gradually reduced. At the other margin of the CE, the HEs are gently convex-up. Sample number: 8. Photographed in cross-polarized light. Photomicrograph length: 1 mm.

Fig. 5.3d Type-(i) MFS defined by a parallelogram-shaped muscovite CE and gently swerved HE cleavages of a host grain of muscovite. CE shape indicates top-to-right (top-to-SW regional) shearing. The HEs are variably dragged into gently convex-up at one side of the CE, shown by the arrow 'p'; and are nearly straight therefore not dragged at the other margin, and are shown by the arrows 'q'. Sample number: 3. Photographed in plane-polarized light. Photomicrograph length: 1 mm.

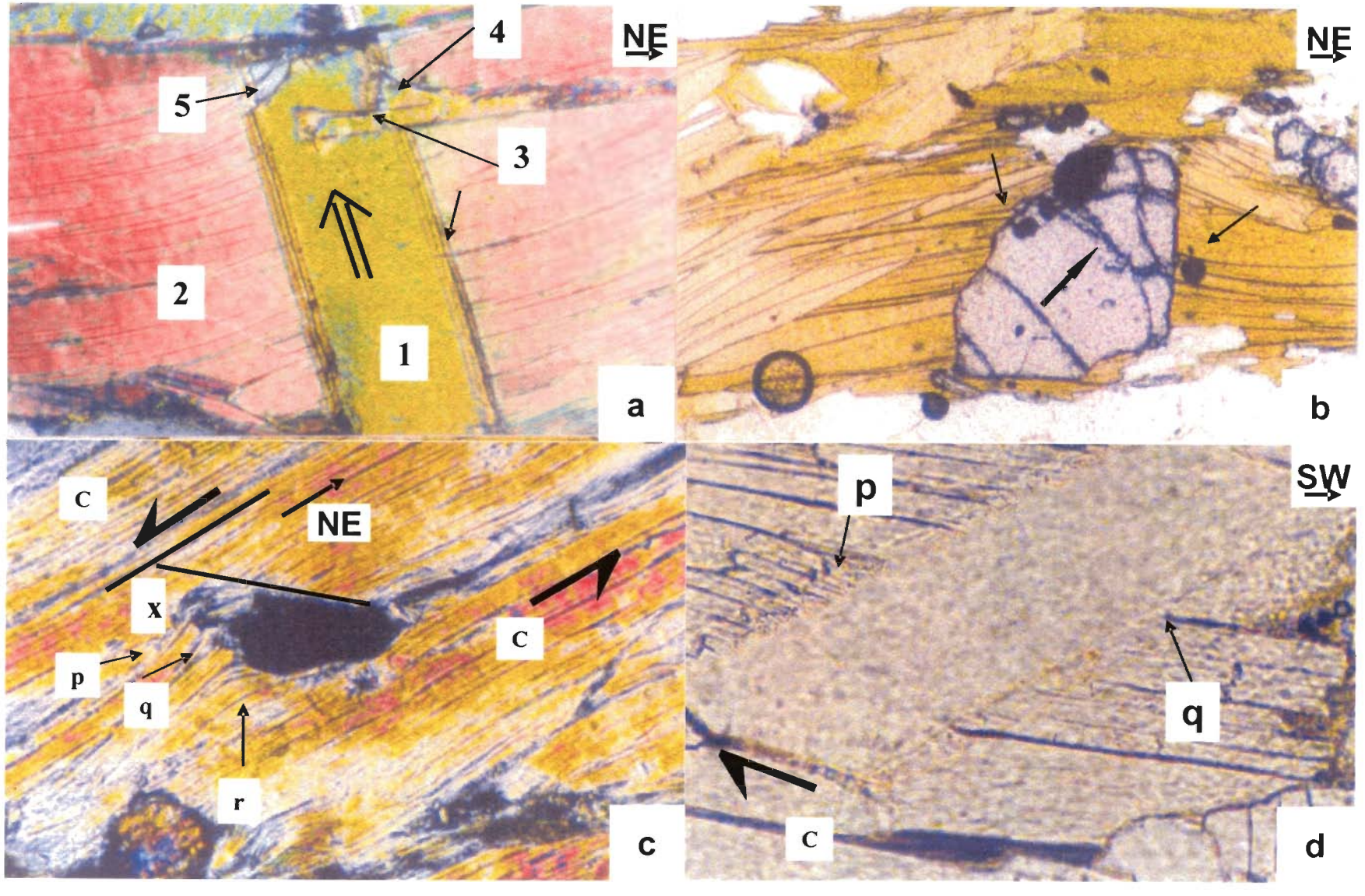

Fig. 5.3

Figure Captions

Fig. 5.4a Type-(i) MFS defined by a nucleated muscovite (mus) CE, and swerved HE cleavages of the biotite (bt) host grain at the single side of the CE. Quartz (qz) is the other host mineral for the CE. The arrow points at the prominent concave-up HE. HEs are defined only at one side of the CE, by differentially concave-up cleavages of biotite. The curve line drawn demarcates the contact between muscovite and quartz. Migration of this contact towards muscovite has partly eaten the grain. Had there been no migration, the muscovite would have been parallelogram-shaped. This is inferred from the non-orthogonal angular relation (shown by two short lines and 'x'=61^0) between the adjacent straight therefore original margins of the CE unaffected by grain boundary migration. Two long thin straight lines show the inferred grain boundaries of the CE before grain boundary migration took place. Reconstructed parallelogram shape of the CE indicates a top-to-right (top-to-SW regional) sense of shearing. Note that the C-plains are parallel to the HE. Sample number: 5. Photographed in plane-polarized light. Photomicrograph length: 1 mm.

Fig. 5.4b Type-(i) MFS defined by a nearly parallelogram-shaped muscovite CE and HEs of deflected cleavages, and grain boundaries of the host aggregate of biotite grains. CE shape indicates top-to-right (top-to-SW regional) shearing. Note that the C-plains are parallel to the HE. Thin hazy zones, marked by 'p' and 'q', occur the contacts between the HE and the CE. These diffuse zones cannot be resolved with the present magnification (photomicrograph length: 2mm). Interestingly, at ten times higher magnification, as in **Fig. 5.4c** (photo length: 0.2mm), the diffuse zone 'p', demarcated by two parallel lines, reveals internal HE to be strongly convex-up. Better visibility at this very high magnification is achieved by focusing (yellow) light on the thin-section from an external source (in addition to what is available from the microscope), but at the cost of slightly changed observed colour of the minerals! Sample number: 2. Both photographed in plane-polarized light.

Fig. 5.4d Type-(ii) MFS within Type-(i) MFS. Type-(i) MFS is defined by nearly parallelogram-shaped muscovite (mus) nucleated within an aggregate of biotite (bt). The CE shape indicates top-to-right (top-to-SW regional) shearing. Gently concave-up cleavages of the biotite host, shown by the arrow 'p', define the HE. The curve line drawn demarcates the contact between the muscovite- and the quartz (qz) grains. Grain boundary migration of quartz towards muscovite has partially destructed the later mineral. Had there been no such migration, the possible parallelogram shape is reconstructed by extrapolating adjacent sides of the muscovite by straight lines, which have an angle 'x'=45^0. The pair of HEs bounding the CE defines the C-plains. Interestingly, the muscovite CE for the Type-(i) MFS has hosted an opaque mineral to nucleate. A Type-(ii) MFS is defined by this opaque as the CE, and the leftward convex-up dragged cleavages at its both sides (shown by arrows 'q' and 'r') as the HE. The arrow within the white box shows the preferential direction of growth of the opaque. 10. Photographed in plane-polarized light. Photomicrograph length: 0.5mm.

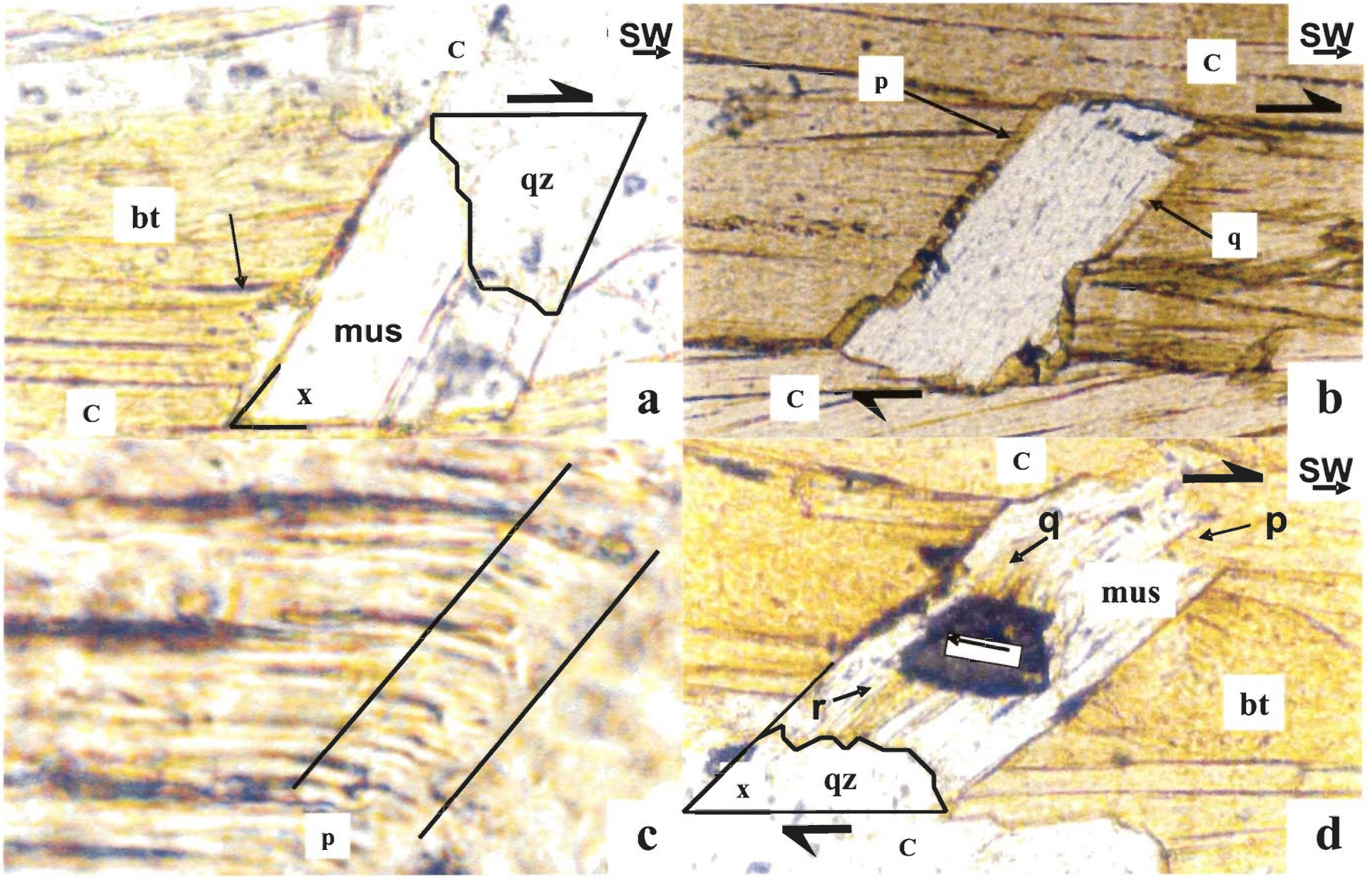

Fig. 5.4

the Type-(ii) (micro)flanking structures.

In his Fig. 8V′, Passchier (2001) recognized intrusions and burrows as the CEs and the adjacent bedding planes displaying the same sense of drag as the HEs. These HE-CE couples are designated as the Type-(ii) varieties of flanking structures in this work. An intrusion, whether magma (Fig. 3.22A of Montgomery, 1987), diapiric salt (Chapman, 1973) or a burrow of trace fossil (Fig. 2.1b of Bromley, 1990) make the adjacent bedding/foliation plains concave-up towards its movement direction. Similarly, the unidirectional preferred growth of the CE minerals of the Type-(ii) MFS are deciphered to be from the convex towards the concave side of the internal HEs. The CEs are defined by both low- (Fig. 5.3a) and high-grade minerals (Fig. 5.3b). They grow in a preferential direction, usually at high-angle to the main foliation, and are variably elongated along the direction of growth. Grain boundary HEs, defining the main foliations (or the C-plains for the D_2 deformation), are sometimes cut by the CEs (Fig. 5.3b), which indicates that those CEs are post-D_2 nucleations. Thus, the deformation that make the HEs curved, for the Type-(ii) MFS, is exclusively micro-tectonic phenomenon, and is unrelated to the regional deformation events of the HHSZ. Amongst the studied thin-sections, the Type-(ii) MFS are rather rare compared to the Type-(i) varieties. A CE mineral with two preferred growth directions, 180^0 apart from each other, do exist (Fig. 2.9a; Fig. 3 of Augustithis, 1990). An upward propagating blind thrust, which cuts across and make brittle fractures concave-up at its superjacent country rocks (p-157 of Mandl, 2005), thereby defining the thrust as the CE and the fractures as the HE, is a macro-scale example of the Type-(ii) flanking structure.

Most of the natural examples of flanking structures described from macro-scale (Grasemann et al., 1999; Grasemann and Stüwe, 2001; Passchier, 2001; Grasemann et al., 2003; Coelho et al., 2005; Exner, 2005; Grasemann et al., 2005; Kocher and Mancktelow, 2005; Wiesmayr and Grasemann, 2005; Exner et al., 2006; Færseth, 2006; Kocher and Mancktelow, 2006; Patel and Kumar, 2006) and most of the MFS encountered in the present study belong to the Type-(i) variety. Since the opposite sense of drag across the CE, as observed in the Type-(i) MFS, has been simulated in a number of analogue- (Exner et al., 2004 and references therein; Exner, 2005; Exner et al., 2006) and numerical models (Grasemann and Stüwe, 2001; Grasemann et al., 2003; Kocher and Mancktelow, 2005; Wiesmayr and Grasemann, 2005) in various ductile shear regimes in relation to 'flanking structures', and in other contexts too (Ghosh and Sengupta, 1973; Ildefonse et al., 1992; Odonne, 1994), the Type-(i) MFS are inferred to be the product of ductile shearing of the rock which contains them. The inclination of the CEs of the Type-(i) MFS are synthetic to the primary shear direction within the spatially heterogeneous shear regime of the studied HHSZ rocks. This indicates that irrespective to the specific regime of ductile shear, the CE of the Type-(i) MFS, in the grain-scale, undergoes dominantly non-coaxial shearing.

The Type-(i) MFS are characterized by usually parallelogram- (Figs. 5.2a, -b, 5.3d, 5.4a, -b) and less often sigmoid shaped CEs (Fig. 5.3c). In case of variable sense and degree of curvature of few of the internal HEs along the same and/or the different margins of the CE, the shape constraint of the CE can, therefore, be used as an alternative criteria to identify the Type-(i) MFS. These situations are described in points (1) and -(3) mentioned

later. For parallelogram-shaped CEs, a pair of their parallel grain boundaries are bounded by a pair of external HEs (Figs. 5.2a, -b, 5.3c, -d, 5.4a, -b, -d). The external HEs in such cases are parallel to the C-plains. Thus, in addition to imposing possible mechanical anisotropy (Kocher and Mancktelow, 2006) in the shear regime, the grain boundaries and the brittle cleavage plains of the host mineral(s) efficiently act as ductile primary shear plains leading to the crystal-plastic deformation of the CE.

Important morphological observations of the MFS, observed mainly amongst the Type-(i) variety, are as follows. (1A) At one particular margin of the CE, intensity and sense of drag of different internal HEs can vary. This can arise in the following two situations. (1A1) The internal HEs may display visually decipherable progressively reducing curvature (Fig. 5.3c), similar to what has been observed in the macro-scale by Passchier and Trouw (2005). (1A2) The drag of few of the HE may be opposite to the rest of them (Fig. 5.3c). Similar natural examples have also been reported in macro-scale (Grasemann et al. 2003; Wiesmayr et al., 2004; Fig. 11a of Coelho et al., 2004; Grasemann et al., 2005 and references therein; Wiesmayr and Grasemann, 2005). Non-coaxial rotation of the CE, initiating from low-angle to the shear zone boundary ($<20^0$) reaching at higher angle (between 20^0 and 160^0), or starting from a higher angle and ending at still higher value ($>160^0$), switch the sense of drag from normal- to reverse-, or reverse- to normal, respectively. (Fig. 1.5; Exner et al., 2004; Exner, 2005, Mulchrone, 2007). Similarly, in micro-scales, prolonged rotation of the CE might give rise to variable sense of drag of the HE whereby the previous senses remain as relic. Alternately, the same result could be reached due either to (temporally?) heterogeneous displacement field along the CE

(Grasemann et al., 2005), or mechanical anisotropy in the ductile shear regime (Kocher and Mancktelow, 2006) imparted by the grain margin/brittle cleavage plain HEs.

(1B) The HE may be curved only at one the margins of the CE mineral (Fig. 5.3d). In macro-scale, similar situations have been encountered in terms of (i) dykes as CEs and meta-sedimentary layers as HEs (Fig. 3B of Rice, 1986); and (ii) elongated clast as CE and foliations as HEs (Fig. 10c of Rajesh and Chetty, 2006), respectively.

(2) When the CE mineral nucleates over two minerals, with only one of the host minerals having cleavages, the internal HE may be defined, and hence the MFS, by dragged cleavages at a single margin of the CE (Fig. 5.4a).

(3) Sometimes, the CE mineral margins in contact with the internal HEs are found to be thin zones of haziness (Figs. 5.2b, 5.3a, 5.4b). Focusing the microscope lens at one of these zones of a particular CE renders the other zone defocused. Usually at higher magnification, these zones reveal strongly curved HEs, which tend to penetrate the CE (Figs. 5.3a, 5.4b). In macro-scale, diffuse boundaries at the contact between the migmatite wall rocks and the vein CEs (Passchier, 2001) are visually comparable with these hazy zones in the MFS. However, their occurrence is not exclusive for the MFS. For example, it has also been noted around a mineral that has merely cut but not dragged the cleavages of the host mineral (Fig. 5.2c).

Besides, two rare observations are: (4A) The host mineral, over which the MFS of one

type has developed, can act as the CE for a different type of MFS (Fig. 5.4d); and (4B) the MFS can be disturbed by other grain-scale phenomena such as: (4B1) migration of the boundary of an adjacent grain (Fig. 5.4a) or the host grain itself (Fig. 5.4d) leading to partial destruction of the CE mineral; and (4B2) both the HE and the CE may be cut by mineral(s) that formed prior, simultaneous, or late to the deformation event represented by the MFS (Fig. 5.3a).

The drag- and the slip of the HE, along the CE margins, are facilitated usually by the presence of a lubricating phase at the HE-CE contact, e.g. partial melt (Passchier, 2001), infiltrating fluids (Passchier and Trouw, 2005) or incompetent rock such as shale (Færseth, 2006) for some natural examples of flanking structures in macro-scale; and transparent silicon oil as performed in analog models (Exner, 2005, Exner et al., 2006). In contrary, none of the MFS encountered (Figs. 5.2a, -b, 5.3a-d, 5.4a-d) reveals neither a melt phase nor any recrystallization at the HE-CE contacts. This indicates that, *(a)* for the MFS, rheological weakening at these contacts is not an essential criterion for the HE to get dragged (and probably slipped) along the CE margin; and *(b)* to account for the additional fact that the CE mineral of the Type-(i) MFS reported here are 'non-rigid' (Fig. 5.2a and its caption), a high degree of bonding between the nucleated CE- with the host mineral might exist (cf. Odonne, 1994). For some of the Type-(ii) MFS, significant dragging of the HE cleavages/grain margins may be the result of such strong CE to host grain bonding and/or intense directional growth of the CE (Fig. 5.3a).

5.2.3. Type-(i) 'MFS' as shear sense indicator

Depending on the initial angle between the HE (acting as the C-plain) and the CE, the Type-(i) flanking structures can form not only in simple shear regime (Grasemann and Stüwe, 2001), but also for different ratios of pure- to simple shear within thinning- (Grasemann et al., 2003) and thickening general shear regimes (Wiesmayr and Grasemann, 2005), whereby the CE may undergo rigid body rotation (Figs. 1, -2, -6 and -7 of Grasemann and Stüwe, 2001; Figs. 3-, 5- and 8 of Wiesmayr and Grasemann, 2005; Fig. 5.47 of Passchier and Trouw, 2005), or ductile deformation (Fig. 6b of numerically modeled flanking structure of Passchier et al., 2005; all the Type-(i) MFS described here). Deciphering the sense of non-coaxial shearing from the flanking structures in macro-scale is further complicated by the fact that reverse a-type flanking structures and reverse shear bands are geometric mirror images to each other (Grasemann et al., 2003), and contractional a-type and s-type flanking structures bear morphologic resemblance (Wiesmayr and Grasemann, 2005) rendering limited application of macro-scale flanking structures in shear sense determination (Passchier and Coelho, 2006). However, these problems do not arise for the Type-(i) MFS since, its shear sense can be deduced based solely from the shape and the inclination of the CEs. The Type-(i) MFS, in oriented thin-sections from the HHSZ rocks outside the detachments, give top-to-SW shear sense (Fig. 5.2a, -b, 5.3c, -d, 5.4a, -b, d), which matches with that previously deciphered mainly from the S-C fabric in the macro-and in the micro-scales. Structural summary of the observed MFS within the HHSz, outside the detachments, is presented in Fig. 5.5.

The three-phase model of exhumation proposed for the HHSZ, Sutlej section (Chapter-3)

predicts that uniform top-to-SW sense of ductile shearing will be obtained outside the two detachments (the HD1 and the HD2). The Type-(i) MFS also shows uniform top-to-SW sense of shearing. Thus, this study on MFS supports the proposed model of shifting channel flow mode of exhumation of the HHSZ, Sutlej section.

5.2.4. Constitutive equation

Assuming Newtonian viscous rheology of the HE-CE composite and neglecting the anisotropic effect that may be imparted by the HE, the constitutive relationship of the Type-(i) MFS, under general shear regime, is given by

$$\tau_{ij} = B.\dot{\varepsilon}_{ij} \qquad \ldots\ \ldots\ \ldots\ (1)$$

(Simplified from Grasemann and Stüwe, 2001)

where τ_{ij} – deviatoric components of stress tensor

B- a unitless number denoting the ratio of viscosity between the HE and the CE

$\dot{\varepsilon}_{ij}$ – components of strain rate tensor, and is given by

$$\dot{\varepsilon}_{ij} = \tfrac{1}{2} \left[\partial u_i / \partial x_j + \partial u_j / \partial x_i \right] \qquad \ldots\ \ldots\ \ldots\ (2)$$

Figure Caption

Fig. 5.5. The observed MFS within the HHSZ, Sutlej section, outside the two detachments, is represented in an XZ-section of the HHSZ, which is also its NE-SW geographic section. The HHSZ is bounded by northeasterly dipping Main Central Thrust (MCT) at the south and the South Tibetan Detachment System (STDS) at the north. The half arrows, marked by '1' at the HHSZ boundaries, imply top-to-SW compressional ductile shearing as revealed mainly from S-C fabric and mineral fishes (examples 'a' and 'b' respectively) (summarized from Jain et al., 2005). CE of the Type-(i) MFS demonstrating top-to-SW sense of regional shearing, as observed in micro-scale in the HHSZ rocks from different valleys, are shown (examples 'c', 'd' and 'e'). The CEs for the Type-(i) MFS are either sigmoid- (example 'c'; natural example is Fig. 5.3c) or parallelogram shaped (examples 'd' and 'e'; natural examples are Figs. 5.2a, -b, 5.3d, and 5.4a, -b, -d). The external HEs of the Type-(i) MFS are parallel to the C-plains. Cases of Type-(ii) MFS showing preferential directional grain growth (example 'f'; natural examples are Figs. 5.3a, -b), and a grain merely cutting cleavages of the host grain (example 'g'; natural examples are Figs. 5.2c, -d) are also shown. Note that (I) the sketch is not to scale; (II) true location of examples ' a', 'b'....'g' in the HHSZ are not maintained; and (III) not all morphological variations of the MFS are shown in this diagram.

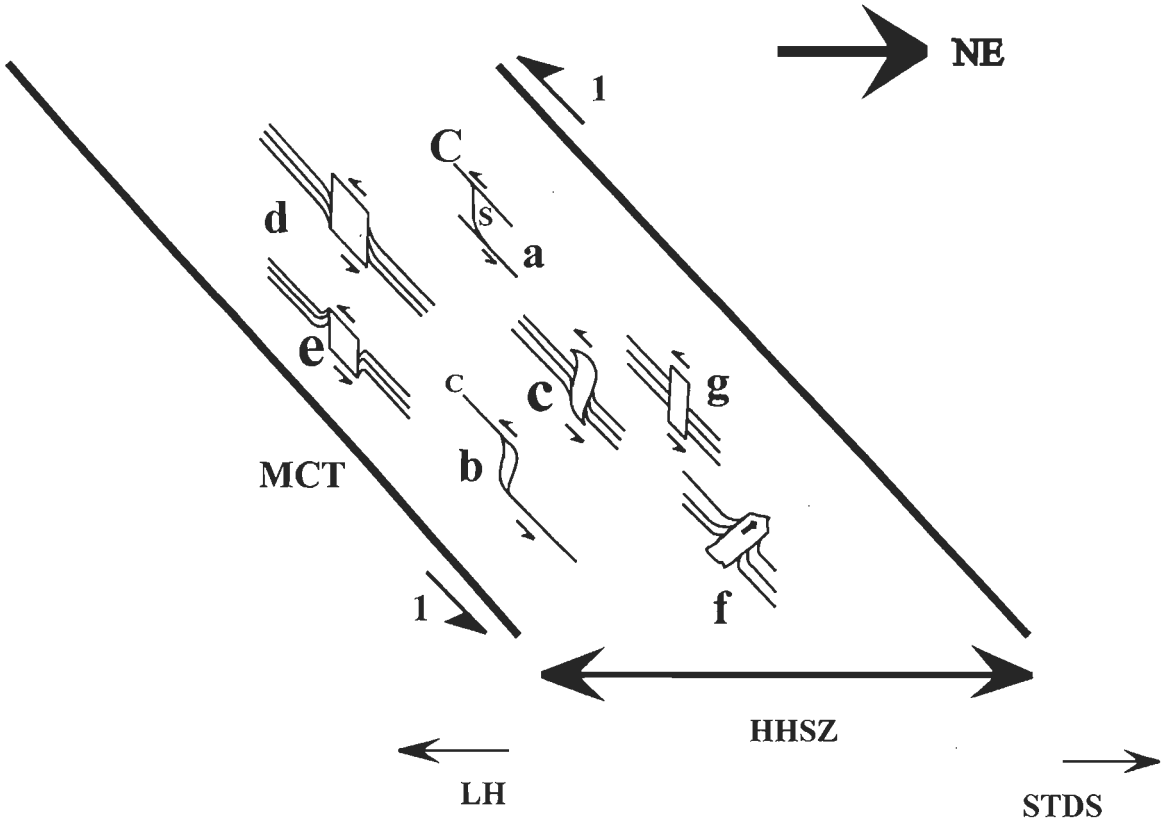

Fig. 5.5

Strain rate is defined in equation 2 in terms of velocity 'u' in the two Cartesian directions 'i' and 'j'. Note that equation 1 is valid for the MFS with the CE nucleated over a single mineral.

Although absolute values of viscosities of minerals are not available, few comments can be made from equation 1 and the present micro-scale observations. For the Type-(i) MFS with a rigid CE within a weaker host mineral (Fig. 5.3c), e.g. a feldspar or apatite grain within muscovite, B is < 1. In this situation, a-type flanking structure is expected (Grasemann and Stüwe, 2001), but cannot be checked for the studied MFS due to the unavailability of the HE as marker. When both the host- and the nucleating mineral are of same viscosity, i.e. they are of the same mineral species, e.g. a biotite grain nucleating within a biotite host grain, B should be ideally equal to 1 and the deformation simplifies to deformation of a single object (Grasemann and Stüwe, 2001), where drag and slip of the HE are not expected. However, in the present study, drag of cleavages of the host grain has been noted under microscope even if the MFS is defined by the CE and the HE belonging to the same mineral species (Figs. 5.2a, -b, 5.3d). Range of B for such cases should, therefore, be close (but not equal) to 1. The third possibility, i.e. the MFS defined by weak CE and a more viscous HE, i.e. $B > 1$, numerically simulated for a simple shear heterogeneous deformation regime with flow perturbation (Passchier et al., 20005), and for which n-type flanking structure is expected for $B >> 1$ (Grasemann and Stüwe, 2001), has not been encountered in the present study. The observed rheological ranges of the MFS encountered in this work are shown in deviatoric stress versus strain-rate graph (Fig. 5.6).

Figure Caption

Fig. 5.6. Tentative domains of the observed Type-(i) MFS within the 'deviatoric component of stress tensor (τ_{ij})' vs. the 'component of strain rate tensor ($\dot{\in}_{ij}$)' graph. Linear viscous rheology for such MFS types is assumed. 'B' is the ratio between the viscosity of the HE and that of the CE. Lines B=b and B=c are boundaries differentiating the P- (b>B>0), Q- (c>B>b), and R- (B>c) domains. The numerical values of 'b' and 'c' are close to 1 with b<1<c, though their exact values are not known. A Type-(i) MFS, with more viscous CE nucleating within a less viscous host, comes within the P-domain; that defined by the CE and the host of the same mineral, plots within the Q-domain. A Type-(i) MFS, with less viscous CE and more viscous host, i.e., that falling within the R-domain, has not been encountered in the present study.

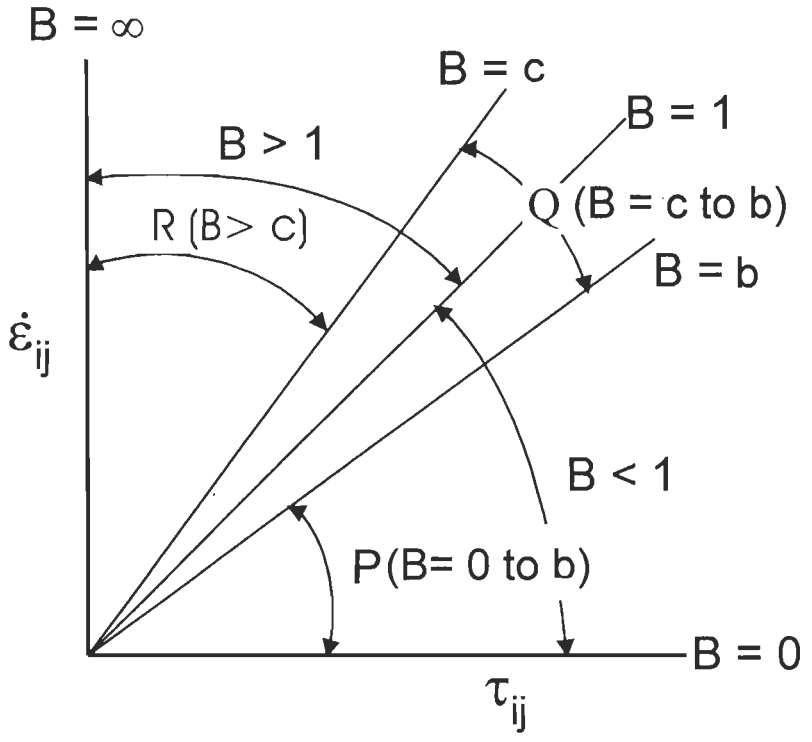

Fig. 5. 6

CHAPTER-6

CONCLUSIONS

The Zanskar Shear Zone (ZSZ) in the Suru and Doda valleys of the NW Indian Himalaya demarcates the northern boundary of the Higher Himalayan Shear Zone (HHSZ), and is characterized by a top-to-NE sense of ductile shearing. The deformation phases of the rocks of the ZSZ, identified under a microscope, are: (i) 'shearing-1'- initial top-to-SW sense of ductile shearing, survived as remnants, along the northeasterly dipping C-planes (the main foliation); (ii) 'shearing-2'- subsequent top-to-NE sense of ductile shearing along the main foliation; (iii) 'shearing-3'- strong extensional ductile shearing along northeasterly steeply dipping shear planes at an angle to the previous shear fabrics; (iv) brittle-ductile extension parallel to the main foliation, indicated by boudins of different varieties; (v) top-to-SW sense of brittle shearing along the main foliation, deciphered from asymmetric duplexes of a number of minerals and V-pull aparts of originally single mineral grains; (vi) northeasterly steeply dipping brittle faulting that cuts and displaces individual minerals; and (vii) brittle extension parallel to the main foliation, given by parallel pull apart of minerals. Different phases of ductile deformation are deciphered using S-C fabric, mineral fishes of different morphological types, intrafolial folds, Type-1 microflanking structures and preferred orientation of grains.

Within the ZSZ, reversal of ductile sense of shearing from a top-to-SW into a top-to-NE sense is confirmed with the documentation of rare hook shaped minerals. 'Shearing-2' and hook-shaped minerals are new findings from this study from the ZSZ, hitherto not

reported from macro-scales. 'Shearing-3' is interpreted as secondary and synthetic to 'shearing-2'. Duplexes in grain-scales are also new observations. It seems that the thrust-up mineral grains, in micro-scales, acquire the characteristic shape of a trapezium or a hat. Hat-shaped grains that are (i) isolated from the underthrust grain, and (ii) produced due to migration of boundaries of the adjacent grains were not used to determine the brittle shear sense.

The deformation phases deciphered from the ZSZ, and those previously reported from the HHSZ are summarized in a schematic cross-section. The top-to-SW sense of ductile shearing within the Higher Himalayan Shear Zone was initiated during the early Neo-Himalayan Period and continued during the Middle Miocene Period when the top-to-NE sense of ductile shearing of the ZSZ was also active. Existing models of exhumation of the HHSZ do not take into account of these constraints. A two-phase exhumation model $E=(E_1+E_2)$ is, therefore, proposed. Velocity profiles of these phases are derived assuming incompressible Newtonian viscous rheology of the rocks of the HHSZ. The E_1 phase, same as the 'ductile shear model', is represented by a top-to-SW sense of simple shearing of the parallel walls of the HHSZ. This Neo-Himalayan event can take into account the top-to-SW sense of ductile shearing throughout the HHSZ. The E_2 phase, during the middle-Miocene Period, represented the flow of the HHSZ like a fluid by a combination of top-to-SW simple shear of the walls of the shear zone and a component of channel flow guided by the pressure gradient. This combined flow gave rise to a thin ZSZ at the upper part of the HHSZ and was characterized by apparent top-to-NE ductile shearing in a bulk southwestward flow. Metamorphic isograds within the HHSZ were deformed into

the same geometries as of the velocity profiles of the respective phases, and gave rise to inverted metamorphism within the shear zone. The spatially variable thickness of the ZSZ along the Himalayan trend is explained by varying the ratio of the relative velocity of the walls of the HHSZ to the pressure gradient driving the channel flow. The E_2 phase predicts that (i) the base of the ZSZ underwent the highest rate of exhumation; and (ii) the top-to-NE sense of ductile shearing might be absent in some sections of the HHSZ even with the presence of a component of channel flow.

Modeling the exhumation of the HHSZ in the Sutlej section is attempted as follows. The HHSZ rocks that underwent post-collisional deformation are grouped into two types: rocks of higher viscosities consisting mainly of granites, schists and quartzites- all in solid states, and that of lower viscosities comprising of migmatites, gneisses, (leuco)granites and pegmatites with the presence of granitic material in a (partially)molten stage. Field- and micro-structural studies of the HHSZ reveal (i) initial top-to-SW sense of ductile compressional shearing throughout the shear zone; (ii) top-to-NE sense of extensional ductile shearing dominantly present in two distinct zones named as- the 'Himalayan Detachment-1' (HD1) and the 'Himalayan Detachment-2' (HD2); (iii) uniform top-to-SW sense of brittle shearing along the pre-existing ductile primary shear planes; and (iv) brittle-ductile extension parallel to the main foliation. The first two senses of ductile shearing are deciphered mainly from S-C fabrics, mineral fishes and intrafolial folds. The S-planes are defined by discrete mineral grains, leucosomes and melanosomes of different thicknesses, and bulges of sigmoid shaped leucosomes and quartz veins. The brittle sense of shearing is deciphered in the field from duplexes of

different dimensions. On micro-scales, hat-shaped minerals with their longest grain boundaries dipping northeasterly are examples of such duplexes. Brittle-ductile extension is represented by boudins of different morphologies in the field. The HD1 occurs at the top of the HHSZ and is the continuation of the South Tibetan Detachment System. The HD2 occurs inside the HHSZ. Both the HD1 and HD2 are thinner than the remainder of the HHSZ, and are absent in some Himalayan sections. Extensional shearing within the HD1 was contemporaneous with the compressional shearing of the MCT during the Middle Miocene Period. The absolute timing of ductile extensional shearing within the HD2 is indeterminate.

None of the recent models of the exhumation of the HHSZ, viz. (i) 'ductile shear model', (ii) channel flow model, (iii) 'combined flow model', and (iv) 'general shear model' can explain the presence of the two detachments within it. Therefore, a three-phase model of exhumation, $E=E_1+E_2+E_3$, is proposed for the study area. The velocity profiles of the first two phases are derived assuming the HHSZ to be of incompressible Newtonian rheology and bonded by very long parallel walls. The E_1 phase stands for the uniform top-to-SW sense of non-coaxial shearing within the HHSZ.

The E_2 phase is represented by a combined top-to-SW sense of simple shearing and upward channel flow mode of exhumation in two pulses. One of these pulses occupied the whole of the HHSZ, i.e. from the MCT to the top of HD1, during the Middle Miocene Period. The other pulse was restricted within the lower part of the HHSZ -from the MCT to the top of HD2. During the respective pulses, thin HD1 and HD2 were produced

characterized by a top-to-NE sense of ductile extensional shearing in bulk southwestward flow within them. The relative time relation between these two pulses is unconstrained. The HD2 might be absent in some sections of the Himalaya even with the presence of a component of channel flow. Further, mathematical analyses of the two pulses predict that (i) the bases of HD1 and the HD2 underwent the highest rates of exhumations in respective flows; and (ii) the HD1 might also be absent in particular sections of the Himalaya even when simple shear and channel flow were active. In the two mathematical analyses- one incorporating the constraints of viscosity, and the other with a possible flow partitioning, it is shown that the extensional ductile shearing can never be produced simultaneously within the two detachments. The development of extensional shearing in the two detachments is therefore sequential, and not simultaneous. The E_3 phase represents consistent top-to-SW sense of brittle shearing, and is idealized in terms of markers disrupted into a top-to-SW sense in the shear zone/channel of the same geometry. The brittle-ductile extensional phase parallel to the main foliation planes is not brought into the tectonic modeling.

The channel flow model takes into account exhumation, inverted metamorphism, and ductile extensional shearing coeval to ductile compressional shearing at the base of the Higher Himalayan Shear Zone. However, a pure channel flow mode of exhumation cannot explain the presence of two detachments that has recently been reported from a few sections of the HHSZ. The classical channel flow model assumes parallel wall geometry of the HHSZ. On the other hand, seismic studies reveal that the geometry of the walls might also be diverging-up. To explore the geometry of flow within non-parallel

walls, ten analogue models of channel flow were performed. The considered situations are a horizontal channel and linked with it an inclined channel with parallel, gently divergent-up and strongly divergent-up geometries of the walls of the later in different considerations. The inclined channel is the model HHSZ. Very slow flow parameters of the exhumation of the HHSZ in one hand, and the limitations of the instruments in the laboatory on the other, did not allow dynamic- and kinematic similarities to achieve between the prototype and the model. However, only the geometric similarity was maintained.

In these experiments, the flow within the horizontal channel was initiated by pushing polydimethylsiloxane (PDMS), a transparent incompressible Newtonian viscous polymer model material, by a piston with a constant rate. The induced flow in the inclined channel gave rise to extrusion of the PDMS on the free surface. Six flow domains were visually deciphered from all these experiments. Gradually away from the piston, these zones are as follows. Zone-1: velocity profile of inverted pitcher shape. Zone-2: plane Poiseuille flow given by parabolic velocity profiles. Zone-3: the profile at the contact between the horizontal and the inclined channel. In the inclined channel the following zones are produced sequentially away from the corner. Zone-4: parabolic profiles. Zone-5: rounded profiles. The extruded PDMS define parabola-shaped zone-6. Pressure gradients in zone-2 and -4 linearly increase with time. The shear strain at any moment at a fixed point is linearly related with the pressure gradient in these zones. Therefore, shear strain at any point in zone-2 and -4 also increase linearly with time. However these relations are instrument-specific and are not related with the extrusion of the HHSZ. Intrafolial folds

showing top-to-NE sense of ductile shearing is formed inside the inclined channel at the later stages of all the experiments. Similar intrafolial folds have also been documented in this work from the Himalayan Detachments.

The PDMS in the horizontal channel enters the inclined channel and moves at a faster rate than the part of the PDMS that is already in the inclined channel. This in effect defines a blind secondary ductile thrust inside the inclined channel. The thrust rotates while moving up and finally comes to the surface. This thrust may be correlated with the Chaura Thrust in the Sutlej section of the HHSZ that was active at least 13 Ma after the ongoing channel flow event ~18 Ma ago. In all the analog models a single broad zone of top-to-NE sense of shear sense is produced equivalent to that in the South Tibetan Detachment System (or the HD1). This confirms that a single pulse of channel flow throughout the HHSZ cannot give rise to two ductile extensional shear zones even when extrusion takes place through diverging-up walls. These two shear zones, therefore, must be sequentially produced by channel flow in two distinct pulses.

XZ oriented thin-sections from the Sutlej section of the HHSZ reveal that nucleated minerals (the cross-cutting elements-CEs) cut and drag cleavages and grain-margins (the host fabric elements-HEs) of the host mineral(s). The HE-CE composite is designated as the 'microflanking structure' (MFS). Unavailability of HE as marker in most cases precludes deciphering its sense of slip across the CE. Depending on whether the sense of drag of the HE at the two sides of the CE is different or same, the MFS are grouped into the Type-(i) and the Type-(ii) varieties, respectively. The later type indicates preferential

growth of the CE from the convex- towards the concave direction of the internal HE. The former types are a product of ductile shearing. Their CEs are parallelogram or sigmoid shaped, non-coaxially sheared; and are bounded by HEs that act as the C-plains. The shape of the CE is an alternative criterion to identify the Type-(i) MFS.

Variation in the intensity- and sense of drag of internal HEs has been noted, and may be due to *(a)* considerable rotation of the CE in simple shearing; *(b)* heterogeneous displacement field around the CE; or *(c)* mechanical anisotropy imposed by the HEs. The internal HE may be defined only at one side of the CE when one of the host minerals lacks cleavages. A thin hazy zone may mark the HE-CE contact, with the internal HEs strongly swerved and penetrating the CE within it. Lack of rheological weakening at the HE-CE contacts for the studied MFS indicates that it is not to an essential criterion for the drag (and slip) of the HE. This, along with the fact that the reported CEs are non-rigid, indicates that the CEs are strongly coupled with the host minerals. Top-to-SW ductile shear sense is deduced from the inclination of the CE of the Type-(i) MFS, which matches with that given by other shear sense indicators. This supports the channel flow mode of exhumation of the HHSZ. The Type-(i) MFS with (I) rigid CE and a weaker host mineral, and (II) CE and the host of the same minerals, have been observed. The second observation indicates that little variation in viscosities between the CE- and the host mineral must exist even if they belong to the same species.

REFERENCES

Acharya, S.K., Ray, K.K., 1977. Geology of the Darjeeling-Sikkim Himalaya. In: Guide to Excursion No. 4 Fourth International Gondwana Symposium, India, report. 25 pp, Calcutta, India, 1977.

Annen, C., Scaillet, B., Sparks, R.S.J., 2006. Thermal constraints on the Emplacement Rate of a Large Intrusive Complex: The Manaslu Leucogranite, Nepal Himalaya. Journal of Petrology 47, 71-95. doi: 10.1093/petrology/egi068.

Argles, T.W., Edwards, M.A., 2002. First evidence for high-grade, Himalayan age synconvergent extension recognized within the western syntaxis-Nanga Parbat, Pakistan. Journal of Structural Geology 24, 1327-1344.

Augustithis, A.A., 1990. Atlas of Metamorphic-Metasomatic Textures and Processes. Elsevier. Amsterdam.

Batchelor, G.K., 1967. An Introduction to Fluid Dynamics. Cambridge University Press. New York. pp. 180.

Beaumont, C., Jamieson, R. A., Nguyen, M.H., Medvedev S., 2004. Crustal Channel Flows: 1. Numerical models with application to the tectonics of the Himalayan-Tibetan Orogen. Journal of Geophysical Research 109 B06406, doi:10.1029/2003JB002809.

Beaumont, C., Jamieson, R.A., Nguyen, M.H., Lee, B., 2001. Himalayan tectonics explaneed by extrusion of a low-viscosity crustal channel coupled to focused surface denudation. Nature 414, 738-742.

Beaumont, C., Nguyen, M.H., Jamieson, R., Ellis, S., 2006. Crustal Flow Model in Large Hot Orogen. In: Law, R.D., Searle, M.P., Godin, L. (Eds) Channel Flow, Ductile Extrusion and Exhumation in Continental Collisional Zones. Geological Society, London, Special Publications. 268, pp. 91-145.

Berthe, D., Choukroune, P., Jegouzo, P., 1979. orthogneiss, mylonite and non-coaxial deformation of granite: the example of the south Armorican shear zone. Journal of Structural Geology 1, 31-42.

Bhattacharya, A.R., 1981. Stratigraphy and correlation of the Inner Kumaun Lesser Himalaya: Implications of A Mathematical Study. In: Sinha, A.K. (Ed). Contemporary Geoscientific Research in Himalaya. Vol. 1. pp. 137-150. Siva Printers. Dehradun.

Bozkurt, E., 2007. Extensional v. contractional origin for the southern Menderes shear zone, SW Turkey: tectonic and metamorphic implications. Geological magazine 144, 191-210.

Broadkey, R.S., 1967. The Phenomenon of Fluid Motion. Addison-Wesley Publishing Company. Reading-Massachusetts. Chapter 7.

Bromley, R.G., 1990. Special Topics in Palaeontology. Trace Fossils. Biology and Taphonomy. Unwin Hyman. London.

Brown, M., 2001. Orogeny, migmatites and leucogranites: A review. Proceedings of the Indian Academy of Sciences: Earth and Planetary Sciences 110, 313-336.

Burchfiel, B.C., Chen, Z., Hodges, K.V., Liu, Y., Royden, L.H., Deng, C., Xu, J., 1992. The South Tibetan Detachment System, Himalayan orogen: Extension contemporaneous with and parallel to shortening in a collisional mountain belt. Geological Society of America Special Paper 269, 1-41.

Burchfiel, B.C., Royden, L.H., 1985. North-south extension within the convergent Himalayan region. Geology 13, 679-682.

Burg, J.P., Chen, G.M., 1984. Tectonics and structural formation of southern Tibet, China. Nature 311, 219-223.

Caby, R., Pecher, A., Le Fort, P., 1983. Le M.C.T. Himalayan: Nouvelles donnees sur le metamorphisme inverse a la base de la Dalle du Tibet, Revue de Geographie Physique et de Geologic Dynamigue 24, 89-100.

Catlos, E.J., Harrison, T.M., Kohn, M.J., Grove, M., Reyerson, F.J., Manning, C.E., Upreti, B.N., 2001. Geochronologic and Thermobarometric Constraints on the Evolution of the Main Central Thrust, central Nepal Himalaya. Journal of Geophysical Research. Solid Earth. 106, 16177-16204. doi:10.102912000JB900375.

Chapman, R.E., 1973. Petroleum Geology A Concise Study. Elsevier Scientific Publishing Company, Amsterdam, pp. 105.

Coelho, S., Passchier, C., Grasemann, B., 2005. Geometric description of flanking structures. Journal of Structural Geology 27, 597-606.

Davis, G.H., Reynolds, S.J., 1996. Structural Geology of Rocks and Regions. Second Edition. Wiley, Newyork.

Dèzes, P.J, Vannay, J.C., Steck, A., Bussy, F., Cosca, M., 1999. Synorogenic extension: Quantitative constraints on the age and displacement of the Zanskar shear Zone. Geological Society of America Bulletin 111, 364-374.

Druguet, E., Carreras, J., 2006. Analog modeling of syntectonic leucosomes in mylonitic schists. Journal of Structural Geology 28, 1734-1747.

Eagles, P.M., 1966. The stability of a family of Jeffery-Hamel solutions for divergent channel flow. Journal of Fluid Mechanics 24, 191-207.

Edwards, M.A., Kidd, W.S.F., Li, J., Yue, Y., Clark, M., 1996. Multi-stage development of the southern Tibet detachment system near Khula Kangri: new data from Gonto La. Tectonophysics 260, 1-19.

Exner, U. 2005. Analog Modelling of Flanking Structures. Unpublished Ph.D. Thesis. ETH. pp. 65-78.

Exner, U., Grasemann, B., Mancktelow, N.S., 2006. Multiple faults in ductile simple shear: analog modeling of flanking structure systems. In: Buiter, S.J.H., Schreurs, G., (Eds). Analogue and Numerical Modeling of Crustal-Scale Processes. Geological Society, London, Special Publication 253, 381-395.

Exner, U., Mancktelow, N.S., Grasemann, B., 2004. Progressive development of s-type flanking folds in simple shear. Journal of Structural Geology 26, 2191-2201.

Færseth, R.B., 2006. Shale smear along large faults: continuity of smear and the fault seal capacity. Journal of the Geological Society 163, 741 – 751.

Fowler, C.M.R., 2005. The Solid Earth an Introduction to Global Geophysics. Cambridge University Press.

Gansser. A. 1983. Geology of the Bhutan Himalaya.. Birkhäuser Verlag. Basel.

Ghosh, S.K., 1993. Structural Geology Fundamental and Modern Development. Pergamon Press.

Ghosh, S.K., Sengupta, S., 1973. Compression and simple shear of test models with rigid and deformable inclusions . Tectonophysics 17, 133-175.

Godin, L., Brown, R.L., Hanmer, S., 1999. High strain zone in the hanging wall of the Annapurna detachment, central Nepal Himalaya. In: Macfarlane, A., Sorkhabi, R.B., Quade, J. (Eds.) Himalaya and Tibet: Mountain Roots to Mountain Tops. Geological Society of America Special Publication 328, 199-210.

Grasemann, B., Edwards, M.A., Wiesmayr, G., 2006. Kinematic dilatancy effects on orogenic extrusion. In: Law, R.D., Searle, M.P., Godin, L. (Eds) Channel Flow, Ductile Extrusion and Exhumation in Continental Collisional Zones. Geological Society, London, Special Publications. 268, pp. 183-199.

Grasemann, B., Fritz, H., Vannay, J.C., 1999. Quantitative kinematic flow analysis from the Main Central Thrust Zone (NW-Himalaya, India): implications for a decelerating strain path and extrusion of orogenic wedges. Journal of Structural Geology 21, 837-853.

Grasemann, B., Martel, S., Passchier, C., 2005. Reverse and normal drag along a fault. Journal of Structural Geology 27, 999-1010.

Grasemann, B., Stüwe, K., 2001. The development of flanking folds during simple shear and their use as kinematic indicators. Journal of Structural Geology 23, 715-724.

Grasemann, B., Stüwe, K., Vannay, J.-C., 2003. Sense and non-sense of shear in flanking structures. Journal of Structural Geology 25, 19-34.

Grujic, D., Casey, M., Davidson, C., Hollister, L.S., Kündig, R., Pavlis, T., Schmid, S., 1996. Ductile extrusion of the Higher Himalayan Crystalline in Bhutan: evidence from quartz microfabrics. Tectonophysics 260, 21-43.

Grujic, D., Hollister, L.S., Parrish, R.R., 2002. Himalayan metamorphic sequence as an orogenic channel: insight from Bhutan. Earth and Planetary science Letters 198, 177-191.

Hauck, M.L., Nelson, K.D., Brown, L..D., Zhao, W., Ross, A.R., 1998. Crustal structure of the Himalayan orogen at ~90^0 east longitude from project INDEPTH deep seismic reflection profiles. Tectonics 17, 481-500.

Hipperitt, J.F.M., 1993. 'V' pull-apart microstructures: a new shear sense indicator. Journal of Structural Geology 15, 1394-1403.

Hodges, K.V., 1998. The thermodynamics of Himalayan orogenesis. In: Treloar, P.J., O'Brien, P.J. (Eds). What Drives Metamorphism and Metamorphic Reactions? Geological Society, London, Special Publication, 138, 7-22.

Hodges, K.V., 2000. Tectonics of the Himalaya and southern Tibet from two decades perspectives. Geological Society of America Bulletin 112, 324-350.

Hodges, K.V., Hurtado, J.M., Whippe, K.X., 2001. Southward extrusion of Tibetan crust and its effect on Himalayan tectonics. Tectonics 20, 799-809.

Ildefonse, B., Sokoutis, D., Mancktelow, N.S., 2002. Mechanical interactions between rigid particles in a deforming ductile matrix: Analogue experiments in simple shear flow. Journal of Structural Geology 14, 1253-1266.

Jain, A.K., Anand, A., 1988. Deformational and strain patterns of an intracontinental ductile shear zone- an example from the Higher Garhwal Himalaya. Journal of Structural Geology 10, 717-734.

Jain, A.K., Kumar, D., Singh, S., Kumar, A., Lal, N., 2000. Timing, quantification and tectonic modelling of Pliocene-Quaternary movements in the NW Himalaya: evidences from fission track dating. Earth Planetary Science Letters 179, 437-451.

Jain, A.K., Manickavasagam, R.M., 1993. Inverted metamorphism in the intracontinental ductile shear zone during Himalayan collision tectonics. Geology 21, 407-410.

Jain, A.K., Manickavasagam, R.M., Singh, S. 1999. Collision tectonics in the NW Himalaya: deformation, metamorphism and emplacement of leucogranite along Beas-Parbati Valleys, Himachal Pradesh. In: Jain, A.K., Manickavasagam, R.M. (Eds.), Geodynamics of the NW Himalaya. Gondwana Research Group Memoir 6, Field Science Publishers, Osaka. 3-37.

Jain, A.K., Manickavasagam, R.M., Singh, S., Mukherjee, S., 2005. Himalayan collision zone: new perspectives- its tectonic evolution in a combined ductile shear and channel flow model. In: Arora, B.R., Dubey, A.K. (Eds) Himalayan Geology. Special Issue. 26 (1), 1-18.

Jain, A.K., Patel, R.C., 1999. Structure of the Higher Himalayan Crystallines along the Suru-Doda Valleys (Zanskar), NW-Himalaya. In: Jain, A.K., Manickavasagam, R.M. (Eds.), Geodynamics of the NW Himalaya. Gondwana Research Group Memoir 6, Field Science Publishers, Osaka. 91-110.

Jain, A.K., Singh, S., Manickavasagam, R.M., 2002. Himalayan Collisional Tectonics. Gondwana Research Group. Memoir No. 7, Field Science Publishers. Hashimoto. p. 4.

Jamieson, R. A., Beaumont, C., Medvedev, S. & Nguyen, M. H., 2004. Crustal Channel Flows: 2. Numerical models with implications for metamorphism in the Himalayan-Tibetan Orogen. Journal of Geophysical Research, 109, B06407, doi:10.1029/2003JB002811.

Jamieson, R. A., Beaumont, C., Nguyen, M.H., Grujic, D., 2006. Provenance of the Greater Himalayan Sequence and associated rocks: Predictions of channel flow models. In: Law, R.D., Searle, M.P., Godin, L. (Eds) Channel Flow, Ductile Extrusion and Exhumation in Continental Collisional Zones. Geological Society, London, Special Publications. 268, pp. 165-182.

Jamieson, R.A., Beaumont, C., Nguyen, M.H., Lee, B., 2002. Interaction of metamorphism, deformation and exhumation in large convergent orogens. Journal of Metamorphic Geology 20, 9-24.

John, J.A.E., Haberman, W., 1971. Introduction to Fluid Mechanics. Prentice-Hall. London. pp. 101, 209.

Kocher, T., Mancktelow, N.S., 2005. Dynamic reverse modeling of flanking structures: a source of quantitative information. Journal of Structural Geology 27, 1346-1354.

Kocher, T., Mancktelow, N.S., 2006. Flanking structure development in anisotropic viscous rock. Journal of Structural Geology 28, 1139-1145.

Kocher, T.O., 2006. Flanking structures and single layer fold development in isotropic and anisotropic rock. Ph.D. Thesis. Diss ETH No. 16413.

Kohn M.J., Wieland, M.S., Parkinson, C.D. Upreti, B.N., 2004. Miocene faulting at plate tectonic velocity in the Himalaya of central Nepal. Earth & Planetary Science Letters. 228, 299-310.

Langlois, W.E., 1964. Slow Viscous Flow. The McMillan Company. Chapter IV: Exact solutions to the Equations of Viscous Flow. pp. 96-104.

Law, R., Searle, M.P., Simpson, R.L., 2004. Strain, deformation temperatures and vorticity of flow at the top of the Greater Himalayan Slab, Everest Massif, Tibet. Journal of the Geological Society, London 161, 305-320.

LeCureux, F., Burnett, J., 1975. Graphical methods used in the numerical solution of Jeffery-Hamel flow at fixed flow rates. Computer & Graphics 1, 233-238.

Lister, L.S., Snoke, A.W., 1984. S-C Mylonites. Journal of Structural Geology 6, 617-638.

Liu, P.-C., 1977. Introduction to the mechanics of viscous fluids. Hemisphere publishing Company. Washington. pp. 61-67.

Mandl, G., 2005. Rock Joints The Mechanical Genesis. Chapter 7. Joints in Faulting and Folding. Springer. Berlin. 156-157.

Manickavasagam, R.M., Jain A.K., Singh, S., Asokan, A., 1999. Metamorphic evolution of the NW-Himalaya, India: Pressure temperature data, inverted metamorphism, and exhumation in the Kashmir, Himachal and Garhwal Himalaya. In Macfarlane, A., Sorkhabi, R.B., Quade, J. (Eds.), Himalaya and Tibet: Mountain roots to mountain tops. Geological Society of America Special Paper 328, 179-198.

Manohar, M., Krishnamachar, P., 1982. Fluid Mechanics. Third Edition. Vikas Publishing House. New Delhi. p. 274.

Marchildon, N., Brown, M., 2003. Spatial distribution of melt-bearing structures in anatectic rocks from Southern Brittany, France: implications for melt transfer at grain- to orogen-scale. Tectonophysics 364, 215-235.

Massey, B.S., 1975. Mechanics of fluids. Third Edition. Van Nostrand Reinhold Company. New York. pp. 145.

McClay, K.R., Insley, M.W., 1986. Duplex structures in the lewis thrust sheet, crowsnest pass, rocky mountains, Alberta, Canada. Journal of Structural Geology 8, 911-922.

Montgomery, C.W., 1987. Physical Geology. Second Edition. Wm.C. Brown Publishers.

Mukherjee, B.K., Sachan, H.K., 2001. Discovery of coesite from Indian Himalaya: A record of ultra-high pressure metamorphism in Indian Continental Crust. Current Science 81, 1358-1361.

Mukherjee, S., Chakraborty, R., 2007. Pull-apart micro-structures and associated passive folds. In: Aho, J. (Ed), Annual Transactions of the Nordic Rheology Society Volume 15, 247-252. 16th Nordic Rheology Conference, Stavanger, Norway, June 13-15, 2007.

Mukherjee, S., Koyi, H.A., 2007. Microflanking Structures And Their Rheological Significances. In: Aho, J. (Ed) Annual Transactions of the Nordic Rheology Society Volume 15, 243-246. 16th Nordic Rheology Conference, Stavanger, Norway, June 13-15, 2007.

Mulchrone, K. F., 2007. Modelling flanking structures using deformable high axia ratio ellipses: Insights into finite geometries. Journal of Structural Geology 29, 1216-1228.

Munson, B.R., Young, D.F., Okiishi, T.H., 2002. Fundamentals of Fluid Mechanics. 4th Edition. John Wiley & Sons. New York. pp. 354-355.

Nelson K.D. et al 1996. Partially molten middle crust beneath Southern Tibet: synthesis of project INDEPTH results. Science 274, 1684-1696.

Odonne, F., 1994. Kinematic behaviour of an interface and competence contrast: analogue models with different degrees of bonding between deformable inclusions and their matrix. Journal of Structural Geology 997-1006.

Pai, S.-I., 1956. Viscous Flow Theory I- Laminar Flow. D. Van Nostrand Company Inc. New Jersey. p. 51.

Papanastasiou, C.T., Georgiou, G.C., Alexandrou, A.N., 2000. Viscous Fuid Flow. CRC Press. Florida, 253.

Passchier, C.W., 2001. Flanking Structures. Journal of Structural Geology 23, 951-962.

Passchier, C.W., and Trouw, R.A.J., 2005, Microtectonics: Berlin, Springer-Verlag.

Passchier, C.W., Coelho, S., 2006. An outline of shear-sense analysis in high-grade rocks. Gondwana Research 10, 66-76.

Passchier, C.W., Mancktelow, N.S., Grasemann, B., 2005. Flow perturbations: a tool to study and characterize heterogeneous deformation. Journal of Structural Geology 27, 1011-1026.

Patel, R.C., Kumar, Y., 2006. Late-to-post collisional brittle ductile deformation in the Himalayan orogen: Evidences from structural studies in the Lesser Himalayan Crystallines, Kumaon Himalaya, India. Journal of Asian Earth Sciences 27, 735-750.

Patel, R.C., Singh, S., Asokan, A., Manickavasagam, R.M., Jain, A.K., 1993. Extensional tectonics in the Himalayan orogen, Zanskar, NW India. In: Treloar, P.J., Searle, M.P., (Eds.) Himalayan Tectonics. Geological Society of London Special Publication No. 74. pp. 445-459.

Pognante, U., Castelli, D., Benna, P., Genovese, G., Oberli, F., Meier, M., Tonarini, S., 1990. The crystalline units of the High Himalayas in the Lahul-Zanskar region (northwest India): metamorphic-tectonic history and geochronology of the collided and imbricate Indian plate. Geological Magazine 127, 101-116.

Pozrikidis, C., 2001. Fluid Dynamics Theory, Computation and Numerical Simulation. Kluwer Academic Publishers. Boston. Chapter-7, pp. 306-354.

Rajesh, H.G., Chetty, T.R.K., 2006. Structure and tectonics of the Achankovil Shear Zone, southern India. Gondwana Research 10, 86-98.

Ramberg, H., 1981. Gravity, Deformation and the Earth's Crust In theory, experiments and geological applications. Second Edition. Academic Press. London. pp. 5-6.

Ramsay, J.G., Huber, M.I., 1987. The Techniques of Modern Structural Geology. Volume 2. Folds and Fractures. Academic Press. London.

Rice, A.H.N., 1986. Structures associated with superimposed inhomogeneous shearing of basic dykes from Finnmark, Norway. Tectonophysics 128, 61-75.

Robyr, M., Vannay, J.C., Epard, J.L., Steck, A., 2002. Thrusting, extension and doming during the polyphase tectono-metamorphic evolution of the Higher Himalayan Crystalline Zone in NW India. Journal of Asian Earth Sciences 21, 221-239.

Rogers, R.H., 1978. Fluid Mechanics. Routledge & Kegan Paul. London. pp. 93-109.

Schlichting, H., 1955. (Translated by Kestin, J.) Boundary Layer Theory. McGraw Hill. New York. pp. 60.

Schlichting, H., 1955. Boundary Layer Theory. New York. McGraw Hill. pp. 61.

Schlichting, H., 1968. Boundary Layer Theory. (Translated by Kestin, J.). Sixth Edition. McGraw Hill. New York. pp. 99-101.

Schlichting, H., Gersten, K., 1999. Boundary Layer Theory. 8th Revised Enlarged Edition. Springer, Berlin. pp. 101-104.

Searle, M.P., 1999. Extensional and compressional faults in the Everest-Lhotse massif, Khumbu Himalaya, Nepal. Journal of the Geological Society, London 156, 227-240.

Searle, M.P., Rex, A.J., 1989. Thermal model for Zanskar Himalaya. Journal of Metamorphic Geology 7, 127-134.

Searle, M.P., Simpson, R.L., Law, R.D., Parrish, R.R., Waters, D.J., 2003. The structural geometry, metamorphic and magmatic evolution of the Everest massif, High Himalaya of Nepal-South Tibet. Journal of the Geological Society, London 160, 345-366.

Searle, M.P., Waters, D.J., Rex, D.C., Wilson, R.N., 1992. Pressure, temperature and time constraints on Himalayan metamorphism from eastern Kashmir and Western Zanskar. Journal of the Geological Society, London 149, 753-773.

Shelley, D., 1994. Spider texture amphibole preferred orientation. Journal of Structural Geology 16, 709-717.

Singh, S., 1993. Collision Tectonics: Metamorphic and Geochronological Constraints from Parts of Himachan Pradesh, NW-Himalaya. Unpublished Ph.D. Thesis. University of Roorkee. India. pp. 1-289.

Singh, S., Jain, A.K., 1993. Deformational and strain pattern of the Jutogh Nappe along the Sutlej Valley in Jeori-Wangto region, Himachal Pradesh, India. Journal of Himalayan Geology 4, 41-55.

Spurk, J., 1993. Fluid Mechanics Problems and Solutions. Springer. Berlin. pp. 58-60.
Srikantia, S.V., Bhargava, O.N., 1998. Geology of Himachal Pradesh. Geological Society of India. Bangalore. pp. 1-406.

Srikantia, S.V., Bhargava, O.N., 1998. Geology of Himachal Pradesh. Geological Society of India. Bangalore. pp. 1-406.

Stephenson, B.J., Searle, M.P., Waters, D.J., Rex, D.C., 2001. Structure of the Main Central Thrust zone and extrusion of the High Himalayan deep crustal wedge, Kishtwar-Zanskar Himalaya. Journal of the Geological Society, London 158, 637-652.

Stephenson, B.J., Waters, D.J., Searle, M.P., 2000. Inverted metamorphism and the Main Central Thrust: field relations and thermobarometric constraints from the Kishtwar Window, NW Indian Himalaya. Journal of Metamorphic Geology 18, 571-590.

Sykes, J.B., Reid, W.H., 1984. Fluid Mechanics. Second Edition. Pergamon Press. Oxford. pp. 76-81.

Talbot, C.J., Aftabi, P., 2004. Geology and models of salt extrusion at Qum Kuh, central Iran. Journal of the Geological Society, London 161, 321-334. DOI: 10.1133/0016-764903-102.

ten Grotenhuis, S.M., Passchier, C.W., Bons, P.D., 2002. The influence of strain localization on the rotation behaviour of rigid objects in experimental shear zones. Journal of Structural Geology 24, 485-499.

Thakur, V.C., 1993. Geology of Western Himalaya. Physics and Chemistry of the Earth Volume 19, Pergamon. Oxford. pp. 1-366.

Tripathi, A., Gairola, V.K., 1999. P-T conditions of metamorphism in the Garhwal Nappe. In: Jain, A.K., Manickavasagam, R.M. (Eds.), Geodynamics of the NW Himalaya. Gondwana Research Group Memoir 6, Field Science Publishers, Osaka. 167-172.

Unsworth, M.J., Jones, A.G., Wei, W., Marquis, G., Gokarn, S.G., Spratt, J.E. & the INDEPTH-MT team. 2005. Crustal rheology of the Himalaya and Southern Tibet inferred from magmetotelluric data. Nature 438, 78-81. doi: 10.1038/nature04154.

Valdiya, K.S., 2001. Reactivation of terrane-defining boundary thrusts in central sectors of the Himalaya: Implications. Current Science 81, 1418-1431.

Vannay J.-C. Sharp, D.Z., Grasemann, B., 1999. Himalayan inverted metamorphism constrained by oxygen thermometry. Contribution to Mineralogy and Petrology 137, 90-101.

Vannay, J.-C., Grasemann, B., 1998. Inverted metamorphism in the High Himalaya of Himachal Pradesh (NW India): phase equilibria versus thermobarometry. Schweizerische Mineralogische und Petrographische Mitteilungen 78, 107-132.

Vannay, J.C., Grasemann, B., Rahn, M., Frank, W., Carter, A., Baudraz, V., Cosca, M., 2004. Miocene to Holocene exhumation of metamorphic crustal wedge in the NW Himalaya: Evidence for tectonic extrusion coupled to fluvial erosion. Tectonics 23, TC1014, 1-24.

Vannay, J-C., Grasemann, B., 2001. Himalayan inverted metamorphism and syn-convergence extension as a consequence of a general shear extrusion. Geological Magazine 138, 253-276.

Vernon, R.H. 2004. A Practical Guide to Rock Microstructure. Cambridge University Press, Cambridge.

Walker, J.D., Martin, M.W., Bowring, S.A., Searle, M.P., Waters, D.J., Hodges, K.V., 1999. Metamorphism, melting and extension: age constraints from the High Himalayan slab of southeast Zanskar and northwest Lahul. The Journal of Geology 107, 473-495.

Wennberg, O.P., 1996. Superimposed fabric due to reversal of shear sense: an example from the Bergen Arc Shear Zone, western Norway. Journal of Structural Geology 18, 871-889.

Whipp, D.M. Jr., Ehlers, T.A., Blythe, A.E., Ruhl, K.W., Hodges, K.V., Burbank, D.W., 2005. Kinematic and Erosion History of the Greater Himalayan Sequence, Central Nepal from Integrated Thermochronology and Numerical Modeling. Salt Lake City Annual Meeting. Oct 16-19. Geological Society of America Abstracts with Programs 37, 7, pp. 346.

Wiesmayr, G., Grasemann, B., 2005. Sense and non-sense of shear in flanking structures with layer-parallel shortening: implications for fault-related folds. Journal of Structural Geology 27, 249-246.

Wiesmayr, G., Hinsch, R., Grasemann, B., 2004. 3D-visualization and analysis of mesoscale fault drag effects. Geophysical Research Abstracts 6, 05140. S-Ref-ID: 1607-7962/gra/EGU04-A-05140. European Geophysical Union.

Wobus, C., Heimsath, A., Whipple, K., Hodges, K., 2005. Active out-of-sequence thrust faulting in the central Nepalese Himalaya. Nature 434, 1008-1011. doi: 10.1038/nature 03499.

Wu, C., Nelson, K.D., Wortman, G., Samson, S.D., Yue, Y., Li, J., Kidd, W.S.F., Edwards, M.A., 1998. Yadong cross structure and South Tibetan Detachment in the east central Himalaya (89^0-90^0E). Tectonics 17, 28-45.

Yin, A. 2006. Cenozoic tectonic evolution of the Himalayan orogen as constrained by along-strike variation of structural geometry, exhumation history, and foreland sedimentation. Earth Science Review 76, 1-131.